Kent Academic Repository

Dignam, Aishling (2023) *Development and calibration of a passive space dust collector for low earth orbit.* **Doctor of Philosophy (PhD) thesis, University of Kent,.**

Development and Calibration of a Passive Space Dust Collector for Low Earth Orbit

by

Aishling Dignam

Thesis

Submitted to the University of Kent

For the degree of

Doctor of Philosophy

School of Physical Sciences

September 2022

Declarations

This content herein was composed by the author, and has not been submitted for the purposes of a qualification at any other institution or for any other degree.

The content comprising Chapter 4 was adapted and extended from work which has been accepted for publication.

All data is the author's own, unless explicitly stated otherwise. All instances where use has been made of other work has been cited.

List of Figures

Figure 3.4. Tracking the locations of the impact features on the map created of the foil post-impact. This is the 50 nm palladium coated 25 µm Kapton shot at approximately 5 km/s with a total of 62 features measured.

Figure 3.5. Measurement locations on circular and elliptical holes. The red outlines are the outer through hole measurement locations and the yellow outlines are the rim locations. The white arrows show example typical measurement locations. For the circular hole, the measurements are taken 60° apart for both the hole and rim measurements. For the elliptical hole, the semi-major and semi-minor axes are measured with the addition of a measurement at the midpoint between the two axes.

Figure 3.6. Impact on the 25 µm Kapton foil coated with 30 nm of palladium shot at 1 km/s. The top image is an SEM image of the hole and the predefined hole measurement location can be identified. The bottom image shows the palladium coating around the edges which can be seen to be cracking.

Figure 3.7. A large tear on the foil sample from a 10 nm palladium coated 13 µm Kapton foil shot at 5 km/s which spread through the multitude of impact features on the foil, making it unsuitable for measuring the impact feature size and shape.

Figure 3.8. Typical craters on 25 µm, 75 µm and 125 µm shot at 1 km/s and 5 km/s. Most holes are similar except for the 125 µm foil at 1 km/s where the soda lime glass projectiles become embedded in the foil.

Figure 3.9. The new measurement location chosen for the impact features which had embedded projectiles on the 125 µm Kapton foil coated with 10 nm of palladium shot at 1 km/s.

Figure 3.10. SEM BSE image showing some of the molybdenum spheres (the very bright white spheres) charging and becoming coated in the small silica particles, clearly seen in the bottom right corner with the yellow arrow pointing at a molybdenum sphere that is completely covered in silica.

Figure 3.11. The normalised diameter measurements for the 25 µm, 75 µm and 125 µm thickness Kapton foils all coated with 10 nm palladium shot at ~5 km/s. The original projectile sizes are shown in black. It can be seen that all foils have components measured in the $150 - 250$ µm range.

Figure 3.12. The normalised diameter measurements for the 25 µm, 75 µm and 125 µm thickness Kapton foils all coated with 10 nm palladium shot at ~1 km/s. The original projectile sizes are shown in black. Notably, the 25 µm Kapton foil has considerably smaller diameter measurements than the original projectiles.

Figure 3.13. Plot of projectile diameter divided by the foil thickness (D_P/T) versus the hole diameter divided by the foil thickness (D_H/T). The blue line is that of $y = x$ and the green line is the line of best fit, showing that it is almost the same.

Figure 3.14. Taken from Neish and Kibe (2001), this is the D_P/T versus D_H/T plot obtained from their shots in addition to previous other studies (Neish and Kibe, 2001). The 5 km/s LGG data points represent impacts into Kapton film.

Figure 3.15. The D_P/T versus D_H/T plot for the diameter data of foils shot at 1 km/s with the 25 µm Kapton dataset included (top) and excluded (bottom). Red line is the line of best fit through the data and the blue line is the 1:1 line.

Figure 3.16. Histograms of the hole diameter measurements for the different coating thicknesses shot at 5 km/s. There are two distinct peaks on all plots except the 30 nm coating. The black line is the mean of the soda lime glass projectiles.

Figure 3.17. Histograms of the various coating thicknesses shot at 5 km/s with the larger population removed. The vertical black line represents the mean of the soda lime glass projectiles.

Figure 3.18. Plot of the hole diameter measurements for the different coating thicknesses shot at 1 km/s. The diameters measured are much less than those shot at 5 km/s.

Figure 3.19. The various coating thicknesses were shot and the diameter measurements were taken from the rim location. This produces notably larger measurements of the impact feature than the original projectile size and the hole measurements.

Figure 3.20. The rim measurements with the population from the larger portion of the soda lime glass projectiles removed.

Figure 4.1. An SEM image of the coating to show the quality of said coating. Note the long, straight features present on the foil, these appear to be from the coating method.

Figure 4.2. A foil that has been impacted in the photographic slide target holder. The circular area of impacts can be seem in this image.

Figure 4.3. A region of a foil that was shot at 5 km/s that became contaminated with gun residue (the large chunks scattered across the foil) and also had many irregularly shaped holes which may be the result of projectiles shattering in flight.

Figure 4.4. Example of a feature with cracking/delamination surrounded by smaller impacts potentially caused by a mixture of the projectile mix and gun debris.

Figure 4.5. All the coating thicknesses and the delamination/cracking present on the foils shot at 5 km/s. The cracking gets worse with thicker coatings. Left column SEM and right column BSE images.

Figure 4.6. Cracking effect around small features, predominately with radial cracking. Scalebar represents 10 µm.

Figure 4.7. Holes created by 1 km/s impacts on various thicknesses of palladium coating imaged with SE (left) and BSE (right). There is a strong tendency towards concentric cracking after 30 nm in thickness.

Figure 4.8. A schematic diagram of the mounting of the atomic oxygen samples. The outer blue ring represents the copper ring used to hold the foil in place and was taped down. The grey square is the sample to be analysed with the dark inner grey circle as the area previously exposed to atomic oxygen. The mounting was such that a boundary line between exposed and unexposed could be seen, the top corner shown here.

Figure 4.9. Photo of uncoated Kapton after exposure to atomic oxygen. The exposed area (central circle) has been completely eroded leaving behind only the four corners which pinned it in place within the holder and were therefore covered by a metal frame. Scalebar represents 1 cm.

Figure 4.10. Optical images of the returned exposed palladium coated samples. The darkened ring in the centre is the area of the sample that was exposed to atomic oxygen. Scalebar represents 1 cm.

Figure 4.11. SE image showing the boundary line between atomic oxygen exposed and unexposed Kapton on the 10 nm and 100 nm Palladium-coated foils (location highlighted pointed by the white arrow).

Figure 4.12. A wide view of the exposed area on the 10 nm coated foil. There are many different holes and line features visible on the foil.

Figure 4.13. A hole created on the 10 nm coated foil by atomic oxygen. Notably, the hole is an irregular shape.

Figure 4.14. SEM SE (left) and BSE (right) images of long erosion features that spanned a large distance on the foil. Filaments can be seen in the lower images where the Kapton fibres are being eroded and some of these filaments broke under the SEM electron beam.

Figure 4.15. SE (left) and BSE (right) SEM images showing the boundary between the covered and exposed regions of the 10 nm palladium-coated foil. Only the boundary line can be seen clearly and the difference between the two sides is evident in the increased numbers of erosion features present on the upper exposed portion. The BSE image (right) show no change across the boundary.

Figure 4.16. Two long scrapes present on the foil. These may be from tweezers or some other handling effect as there is a build-up of the coating that was removed at the bottom of the feature. This probably occurred before exposure as there is some atomic oxygen erosion of the exposed Kapton.

Figure 5.7. The target holder for the blast tank that was used for the LGG shots. This holder has many slots that can be used for the photographic slides at different locations.

Figure 5.8. One example of a pointing configuration within the MASTER simulation. This is modelled for a satellite to maintain Earth pointing (ESA, 2022b).

List of Tables

Figure 5.3. Model of the Lunar Gateway space station that is planned to be launched in the late 2020s which would present an ideal location for the deployment of ODIE.

Acknowledgements

I wish to thank my supervisor, Dr. Penny Wozniakiewicz, for her continued guidance and support during this project, especially through a pandemic, and who was always there to help out in making many, many samples. I would also like to thank the three second supervisors I have had during this project, Dr. Mark Price, Dr. Mark Burchell and Dr. James Urquhart, whose outside perspective was a breath of fresh air when staring too close at a problem. For operating the gun and helping with my often troublesome shots I would like to thank Mike Cole and Dr. Luke Alesbrook.

Thank you to all the wonderful fellow PhD students throughout the School of Physical Sciences who have been a constant source of support, laughter and joy both online and in-person over these past few years. I would also like to thank the other members of technical and academic staff that have been very kind with their time in helping me out over the years. Thanks to Student Support and Wellbeing as without their support after injury I would probably still be measuring the diameters of that first dataset. A special thanks to Libby Peatman and Stuart Howie who took on the long, arduous job of measuring thousands of diameters and made this thesis possible.

I would also like to thank my friends, housemates, the drummers at Kensei Taiko and the salsa society for always believing in me and being a positive presence in my life. You all have made the past three years an fantastic experience.

And finally, my gratitude goes out to my family who probably never understood why I have only spoken about measuring holes for the past three years, but who have been supportive and enthusiastic about my hole measuring endeavours nonetheless.

Contents

Abstract

Observation of dust and debris in the near Earth environment is a field of great commercial and scientific interest, vital to maximising the operational and commercial life-cycle of satellites and reducing risk to increasing numbers of astronauts in Low Earth Orbit. To this end, monitoring and assessment of the flux of particles is of paramount importance to the space industry and wider socio-economic interests that depend upon data products/services from orbital infrastructure. A passive space dust detector has been designed to investigate the dust environment in LEO—the Orbital Debris Impact Experiment (ODIE). ODIE is designed for deployment in LEO for ~1 year, whereupon it would be returned to Earth for analysis of impact features generated by dust particles. The design emphasises the ability to distinguish between the orbital debris (OD) relating to human space activity and the naturally occurring micrometeoroid (MM) population at millimetre to submillimetre scales. ODIE is comprised of multiple Kapton foils, which have shown great potential to effectively preserve details of the impacting particles' size and chemistry, with residue chemistry being used to interpret an origin (OD vs. MM). LEO is a harsh environment—the highly erosive effects of atomic oxygen damage Kapton foil—requiring the use of a protective coating. Common coatings available for Kapton (e.g., Al, SiO_2, etc.) are problematic for subsequent analysis and interpretation of. OD vs. MM origin, being a common elemental component of MM or OD, or having X-ray emission peaks overlapping with those of elements used to distinguish MM from OD. Thus palladium coatings are proposed as an alternative for this application.

To develop this technology to a flight-ready level much testing and calibration of the instrument is required to ensure it retains impactor residue and size whilst being exposed to the LEO environment. In this thesis the ODIE detector foils, Kapton coated with palladium, are evaluated to find the optimum thickness of Kapton and palladium that survives both hypervelocity impact and exposure to atomic oxygen. The hypervelocity impact experiments were performed with the Light Gas Gun at the University of Kent at 1 and 5 km/s and showed that the 25 µm Kapton foil established the best relationship between the size of the projectile and the size of the impact feature created on impact. The palladium coating was found to delaminate at thicknesses great than 30 nm and hence coatings thinner than 30 nm are recommended for remaining adhered to the Kapton post-impact. The 25 µm Kapton foil with various thicknesses of palladium coating were exposed to atomic oxygen and, based on the mass loss of the samples due to exposure, the 75 nm palladium coating performed the best with the least mass lost during exposure, although the defects on the surfaces of the foils may have affected this result.

For the ODIE detector to be deployed in LEO, a Kapton foil thickness of 25 µm and a palladium coating thickness of 30 nm are the recommended parameters for the detector to address the flux of the sub-millimetre orbital debris and micrometeoroid populations.

Chapter 1: Introduction

The increasing accessibility of space has seen the near Earth environment change significantly since the beginning of space exploration - the occasional meteoroid is now accompanied by the thousands of satellites in orbit, plus the debris associated with them. Humans are populating the area with dead rockets, spent fuel and fragmentation debris, culminating in large numbers of orbital debris (OD) (Pardini, 2005). The natural dust population, meanwhile, is largely derived from comets and asteroids: comets leave behind a trail of dust on their orbits around the solar system, while asteroids can collide and also add to the natural dust population of micrometeoroids (MMs) (Trigo-Rodríguez and Blum, 2021). The composition of debris around the Earth is complex and ever-changing, creating the necessity for exploration and observation to evaluate the hazard it poses to spacecraft.

The total flux of all objects in LEO is important as all particles, regardless of origin, pose some threat. The individual flux within the OD and MM populations is, however, crucial for assessing the level of hazard posed as, for example, the OD population typically travels at much lower velocities than that of the MM population leading to higher impact velocities (Wozniakiewicz et al., 2019). Insights into the makeup of the different populations can help refine current dust models to extrapolate the state of the orbital environment in the future. Furthermore, measuring the OD flux helps us to understand the damage we are doing to the near Earth environment and thus the importance of minimising our debris to prevent creating serious problems for future spacecraft and astronauts alike.

1.1 Sources of Dust

Dust and debris in the solar system originate from a variety of sources, but can be designated as either manmade (orbital debris, OD) or naturally occurring (micrometeoroid, MM or meteoroid, M). Their size ranges vary greatly from sub-micron to metre-scales.

1.1.1   Meteoroids, Micrometeoroids and Interstellar grains

In the vicinity of the Earth, naturally occurring meteoroids (rock-sized) and micrometeoroids (dust sized) are thought to originate from a variety of sources, but particularly from comets and asteroids (Hoppe and Zinner, 2000). Insights can be gained from these objects on the dynamical evolution of the solar system and the threats they pose to spacecraft based on their trajectory, velocity and composition. If sampled and returned for analysis, they can also provide information regarding the evolution of their parent bodies and, in those cases where primitive bodies are sampled, the formation of the solar system (Hoppe and Zinner, 2000).

The primary mechanisms for dust production from asteroids is via collisions, while for comets it is through the sublimation of volatiles when close to the Sun which ultimately liberates the dusty particles they held in place. As the Earth travels through space it encounters these dust streams and thus is bombarded by sporadic meteoroids/micrometeoroids. Modelling of particles produced by asteroidal collision suggests that these particles make up a negligible proportion of the meteoroid environment at the Earth (Jones, 2004; Moorhead et al., 2019). Instead, modelling suggests that it is comets that produce the majority of interplanetary dust which we observe as meteoroids/micrometeoroids (Hoppe and Zinner, 2000). Contrary to this, however, the majority of extraterrestrial material identified on the surface of Earth as meteorites and micrometeorites is believed to be asteroidal in origin (Hoppe and Zinner, 2000).

The zodiacal cloud, a cloud of debris that surrounds the Sun between the planets, is believed to be composed of particles that are mostly formed by the outgassing of comets and collision of asteroids (Nesvorný et al., 2010). Small particles, with a typical cross-section around 100 µm (Nesvorný et al., 2010), created in this way decouple from the parent body and are dispersed by solar radiation pressure (Koschny et al., 2019). The cloud can be seen in the night sky along the ecliptic plane (Nesvorný et al., 2010). From Infrared Astronomical Satellite (IRAS) observations the population is estimated to be comprised of 85%-95% particles from Jupiter family comets, <10% from long-period comets and <10% from asteroidal dust (Nesvorný et al., 2010).

Dust particles pervade even the seemingly empty space between solar systems, as well as between planets. Such interstellar grains are identified and can be studied in primitive meteorites. The indicators for the grains being of interstellar origin are that they exhibit large anisotropies and comprise elements that were not present at the formation of the solar system. These grains are commonly composed of silicon carbide, silicon nitride and formed by stars during their final stages of stellar evolution. For example, grains containing silicon carbide and corundum are formed through the winds of red giants and stars present on the asymptotic branch of the Hertzsprung-Russell diagram, while supernovae create all silicon nitride grains (Hoppe and Zinner, 2000). Using data collected by Ulysses on its highly inclined orbit, Kruger et al. (2007) constrained the size range of interstellar grains in the heliosphere to 0.05 µm and above. There was a deficiency of small grains below 0.3 µm in the overall size distribution of grains measured within 5 AU of the Sun compared to the dust observed in the interstellar medium, possibly the result of strong heliospheric filtering (Krueger et al., 2007). Grains like these have the potential to inform us of the chemical makeup of the galactic and solar environment before the presence of the Sun and also of the nucleosynthesis inside the stars in which they were formed (Hoppe and Zinner, 2000). Space travel between different solar system bodies and solar systems would also benefit from understanding these different sources of naturally occurring micrometeoroids.

1.1.2 Orbital Debris

Human space activity creates the OD population of objects. These are currently largely restricted to within the vicinity of the Earth where the majority of our activities in space have been focused, but as space activities move further afield to other places in the Solar System OD will also spread to all regions of space that we explore. OD is broadly categorised by its origin and here we will briefly discuss some common sources of debris.

1.1.2.1 Products of Launch

Launching rockets creates a substantial amount of debris. Almost every rocket launched leaves a trail of solid rocket boosters and expended fuel (particulates, frequently HCl and aluminium oxide particles) behind. The upper stages of rockets account for approximately 10% of the objects (by number) in LEO, although due to their sheer size this constitutes 50% of the abandoned mass in LEO (Pardini and Anselmo, 2016). The vast majority of the rocket bodies in orbit (67%) belong to the Russian Federation and Ukraine, with the next largest contributors being the USA (12%) and Europe (10%) (Pardini and Anselmo, 2016).

1.1.2.2 Defunct/Dead Satellites

Satellites at the end of their life are referred to as 'defunct' or 'dead'. These are generally moved to so-called 'graveyard orbits' - an orbit in which they won't interfere with active satellites. For example, for geosynchronous satellites, this orbit is about 300 km higher than geosynchronous orbit (Skinner et al., 2014). Despite the precautions taken, satellites in graveyard orbits still have the potential to increase the OD population through the eventual breakup of the materials that comprise them or by spontaneous combustion. For example, in 1975 a Delta II second stage experienced a fragmentation event, an occurrence whereby the satellite breaks into any number of pieces, due to the spontaneous combustion of 150 kg of residual propellants onboard (Anz-Meador et al., 2018). The cause of many Delta II second stage's fragmentations to date has been put down to rupturing of the common bulkhead of the hypergolic fuel/oxidiser tanks due to over-pressurisation caused by solar heating (Anz-Meador et al., 2018). As a result, since 1982 the remaining Delta II second stages have all been fully passivated, i.e. the fuel has been vented (Anz-Meador et al., 2018). Venting the fuel from leftover rocket bodies, or propulsive passivation, is now common practice to prevent these stages from exploding and creating enormous amounts of debris, although the vented particles themselves become debris also (Rex, 1997).

Defunct satellites have also contributed significantly to the small debris population in the form of coolant particles, in particular sodium-potassium (NaK), which are centimetre-sized, electrically

conducting spherical objects observed by Goldstone and Haystack radar facilities in the 1990s (Matney et al., 2019). The population reside in 65° inclination orbits predominately between the altitudes of 850 km and 1000 km (Matney et al., 2019). The densities of the observed particles was consistent with that of NaK coolant used in Radar Ocean Reconnaissance Satellite (RORSAT) nuclear reactors (Matney et al., 2019). These Soviet Union satellites used Buk reactors which were jettisoned at the end of operations in the 1980s into the same orbits as this observed population which led to the venting of the NaK coolant in the reactor. Similarly, the two Plazma-A spacecraft, Cosmos 1818 and Cosmos 1867, used TOPAZ nuclear power reactors with the same NaK coolant for the system (Anz-Meador et al., 2018). Although not used anymore, the population is not dwindling as expected over time, suggesting that old reactors are still leaking coolant and adding to the population (Matney et al., 2019).

1.1.2.3 Satellite Breakup Events

A satellite breakup is defined as "the usually destructive disassociation of an orbital payload, rocket body, or structure, often with a wide range of ejecta velocities" (Anz-Meador et al., 2018). In many cases the cause for the breakup can be easily determined such as a battery malfunction, accidental collision with OD or MM, or anomalous events which occur when there is an unplanned separation of an object from a satellite, usually with the satellite remaining intact (Anz-Meador et al., 2018). A common result of satellite breakups and anomalous events is the production of thousands of smaller particles which further congest the space environment, with satellite breakups and anomalous debris making up 47.7% and 1.9% respectively of the catalogued in-orbit Earth debris population (Anz-Meador et al., 2018). Payloads, the main satellite bodies or bodies released from satellites as functional experiments, are the source for up 58.4% of all catalogued satellite breakup debris as once a satellite, payload or experiment becomes non-functional it becomes a debris object itself. Despite this, the debris formed from the payload breakups is usually much shorter lived than that of the rocket bodies due to the lower altitude and inclination, on average, of the payload orbits (Anz-Meador et al., 2018). The largest contributor to the debris population is without a doubt the collision and explosion of fully intact satellites which create large quantities of fragmentation debris.

1.1.2.3.1 Accidental Satellite Collision

The accidental collision between Iridium 33 and Cosmos 2251 (two intact spacecraft) was recorded on the 10th February 2009 (Pardini and Anselmo, 2011). Iridium 33 was in a polar orbit as part of the Motorola Iridium constellation – a network used for worldwide voice and data communications using handheld satellite phones (Barrows et al., 1995). Cosmos 2251 was a Russian military communications satellite which was decommissioned 10 years before the collision. In the hours prior to the collision it

was noted that the Cosmos satellite was close to the path of the Iridium satellite but the likelihood of collision was slim. Due to its constellation nature, however, Iridium 33 coordinated with the other satellites in the network and its in-built system performed some automatic adjustments to maintain the constellation. Unfortunately, these minor adjustments placed Iridium 33 on a collision course with Cosmos 2251 (Pardini and Anselmo, 2011). The resulting collision produced a large debris cloud; A dedicated NASA campaign using Goldstone and Haystack radar observations measured the quantity of debris created, finding that over 70,000 fragments larger than 1 cm were generated (Pardini and Anselmo, 2011).

1.1.2.3.2 Deliberate Destruction

Satellite breakups can be, and have been, caused intentionally resulting in their deliberate destruction. The self-destruction of Cosmos 50 is considered the first example of deliberate destruction of a spacecraft by its operator. The 5th November 1964 was the re-entry date of the Russian reconnaissance satellite, however, on that day it experienced a malfunction which prevented the satellite from landing in Russia (Anz-Meador et al., 2018). Due to the sensitive nature of the surveillance data which Cosmos 50 collected, they armed the self-destruct and blew up the satellite on that same day (Anz-Meador et al., 2018). The explosion produced 96 tracked pieces of debris at altitudes between 220 – 175 km (Anz-Meador et al., 2018). This debris has since decayed and re-entered the atmosphere.

More common attempts at deliberate destruction have centred around testing of anti-satellite missiles. For example, the United States Department of Defence (DoD) performed an anti-satellite weapons test in September 1985 (before the introduction of a congressional ban on such tests in October 1985) on the Solwind P-78 satellite, a gamma ray solar physics instrument (Portree and Loftus, 1999). This choice of target was contested by NASA as it was in a high-altitude orbit (515-545 km) that would produce long-lived debris which their models showed would pose a threat to the planned space station in the 1990s (Kessler, 1993). Despite NASA's protestations, the DoD continued with their original choice of target due to the time constraints. The destruction of Solwind P-78 produced 285 catalogued debris objects (Anz-Meador et al., 2018). The 1989-1991 solar maximum expanded the atmosphere much more than NASA's models had predicted in 1985 which accelerated the decay of the debris from this explosion, alleviating concerns for the impact-shielding on the proposed space station at the time (Portree and Loftus, 1999). There are currently no more catalogued objects left in orbit from this event (Anz-Meador et al., 2018).

A more recent example of deliberate destruction of a satellite by a weapons test is the destruction of the Chinese satellite Fengyun 1C on 11th January 2007 by the Chinese government in a test of their anti-satellite missile capabilities (Pardini and Anselmo, 2009). Fengyun 1C was a weather satellite that was launched on 10th May 1999 but had become non-operational, thus was an ideal target for such a test.

The ensuing explosion of this satellite produced 3,442 catalogued pieces of space debris, considerably more than other anti-satellite weapons tests (Anz-Meador et al., 2018). Current predictions of the evolution of the debris cloud generated by the event predict there will be over 250 catalogued pieces of debris still left in orbit after one century (Pardini and Anselmo, 2011). This event is the highest recorded impact in orbit at an altitude of 895 km (Anz-Meador et al., 2018). More recently, the Russian satellite Cosmos 1408 was destroyed by a kinetic anti-satellite test in November 2021, creating a debris cloud of around 1,500 trackable pieces of debris (Williams, 2022).

These are several incidents that have created OD adding to the congestion of the Earth environment. The significant clouds of debris produced by the destruction of Fengyun 1C, Iridium 33 and Cosmos 2251 have drastically increased the amount of debris objects in the low Earth orbit environment. The probability of collision at altitudes of around 800km was increased by a factor of two by these breakup events (Barrows et al., 1995). The intentional destruction of Fengyun 1C marked the most extreme rise in the debris population to date (Anz-Meador et al., 2018). Despite best efforts to minimise the likelihood of collision, the accidental collision of Cosmos 2251 and Iridium 33, two categorised and hence tracked objects, showed the fallibility of our current efforts to avoid collisions and highlighted the importance of monitoring debris and its production in LEO. Of the debris clouds, the Fengyun 1C cloud will disperse more slowly due to its high inclination (Pardini and Anselmo, 2011). The density of the debris clouds is a growing concern as impacts from debris, can have devastating effects on satellites.

1.1.2.3 Managing Break Up Events Beyond LEO

The large-scale debris generating fragmentation events discussed earlier all occurred below 900 km in altitude. On orbits higher than this, especially around geosynchronous orbit (GEO – approximately 35,786 km), more care is taken to avoid congestion. This orbit is a valuable resource for satellite positioning and great care is taken when inserting satellites into orbit there (ESA, 2022a). Indeed, in 1997 the Inter-Agency Space Debris Coordination Committee (IADC) proposed and endorsed a policy of de-orbiting all dead satellites left in a torus around GEO to free up space and reduce the likelihood of collision here (Anselmo and Pardini, 2008). This has been instrumental in the maintenance of this orbit as the density of satellites is on average 3.3 satellites per degree in longitude (Luo et al., 2019).

Despite these efforts, however, debris is still found in GEO and largely consists of rocket bodies and mission related debris, which observations with the Michigan Orbital Debris Survey Telescope (MODEST) have shown a population of small objects between 25 – 100 cm in size. The number of objects between 10 – 100 cm in size is thought to be twice that of the objects greater than 1 m (Johnson, 2012). While far less than in other orbits, over time there will be an increase in the debris population as space activity increases and in GEO this debris will be much longer-lived than that in LEO as there are

negligible dampening effects, such as atmospheric drag, to speed up the decay of this debris (Luo et al., 2019).

There have been no known unintentional collisions or impacts of OD further beyond GEO with any satellites although it is highly likely that the satellites around our solar system and those orbiting other planets have experienced impacts by MM and small particles.

1.1.2.4 Dropped Objects and Miscellaneous Debris

Not all space debris is derived directly from satellites and the rockets that launched them. Over the years there have been some more unusual items added to the debris population by astronauts performing extra vehicular activities. One such item was the "favourite spatula" of astronaut Piers Sellers that he dropped in 2006 during tests for new emergency repair techniques on the International Space Station (The Sydney Morning Herald, 2016). However, Sellers was not the first or last astronaut to drop items during a spacewalk. The trend started with the first American spacewalker, Ed White. During his first spacewalk on Gemini 4 in 1965 he let go of a glove which orbited Earth for around a month before re-entry (Wired, 2009). Since then several items including Sellers' spatula have been added to the OD population by astronauts, including pliers and a camera (see Table 1). While such objects are not dropped very frequently and do not stay in orbit very long, they still contribute to the debris population and increase risks for impact with other objects.

Date	Catalog	Object	Astronaut
2006	29257	Spatula	P. Sellers
2006	29677	Camera	S. Williams
2007	32286	Pliers	S. Parazynski
2008	34442	Crew Lock Bag	H. Stefanyshn-Piper
2017	42434	Node 3 Shield	S. Kimbrough
2018	43498	Wire tie	A. Feustel

Table 1.1. Objects that have been dropped by astronauts which have been catalogued as satellites (Fernholz, 2018).

Another unusual item to find in space are the ashes of people finally fulfilling their dreams of spaceflight. The company Celestis provides this service and one of the most notable participants is Star Trek creator Gene Roddenberry whose ashes were shipped to space in 1992 (Celestis, 2022).

1.2 Hazards Posed by Micrometeoroids and Orbital Debris

Both MM and OD are dangerous to any satellite or vehicle in orbit due to the potential for extremely high impact velocities. With the ability to track the larger objects in orbit this allows the use of avoidance manoeuvres, most notably, the International Space Station regularly needs to perform evasive manoeuvres to avoid any possibility of collision with large debris to safeguard the astronauts within the space station although there is not any tracking available for smaller pieces and thus impact with these are unavoidable. Shielding is present on many spacecraft, in particular around any coolant piping as if they suffer an impact the coolant within can escape and form debris itself, as mentioned previously with passivation. Despite the presence of shielding, impact with a large object could have catastrophic results on the satellite, ending the mission and adding to the debris in orbit.

1.2.1 Collision with a Meteoroid

The Olympus satellite was launched by the ESA in July 1989 with the goal of conducting experiments into many different areas of communications (Caswell et al., 1995). On the 11th August 1993, during the peak of the Perseid meteor shower, the satellite lost its Earth pointing and began spinning slowly. The spacecraft was equipped with an automatic control system to maintain the pointing regime of the satellite and this system was brought online by the anomaly, attempting to de-spin and reorientate the satellite. By the time Olympus was brought under manual control, these attempts had depleted a significant amount of the satellite's fuel leaving insufficient fuel remaining to execute its end of life plan of moving to a graveyard orbit above GEO. The anomaly had also lowered the orbit of Olympus so its missions were aborted and the satellite was immediately placed in a graveyard orbit more than 200km below GEO. Given that the timing of the anomaly coincided with the peak of the Perseid meteor shower it is suspected that a Perseid meteoroid impacted Olympus and caused the event that followed. These particles are not tracked due to their small size and therefore it is impossible to prove a Perseid meteoroid caused the anomaly that ultimately led to the demise of Olympus (Caswell et al., 1995).

1.2.2   Collision with Orbital Debris: Example 1

The French microsatellite Cerise experienced a sudden loss of attitude on the 24th July 1996. An investigation was launched into the source of the problem since preliminary results showed that the

satellite subsystems were working perfectly. It was suggested that the cause was external with the investigation hypothesising that Cerise had most likely collided with space debris. The approach used to explore this hypothesis was to first look at the database of catalogued debris and determine if any known objects had a possible collision course with Cerise. It was discovered that debris object number 18208 experienced a sudden change in trajectory at the same time on the same day as the satellite. Object 18208 was created along with hundreds of other pieces of tracked debris in November 1989 after the breakup of ESA's SPOT 1 rocket (Anz-Meador et al., 2018). A new debris object, number 23994, was discovered a few days after the anomaly with Cerise and by extrapolating the path of this object it was determined that it had originated at the site of the collision (Alby et al., 1997). The simultaneity of the creation of object 23994 and the change of trajectory of Cerise and object 18208 led to the conclusion that a collision with object 18208 had occurred. This was the first known accidental collision between two objects documented in the U.S. satellite catalogue and led to severe damage of the gravity-gradient boom onboard Cerise (Anz-Meador et al., 2018).

1.2.3   Collision with Orbital Debris: Example 2

The Sentinel-1A spacecraft is part of the Copernicus Earth observation program operated by the ESA and is in a sun-synchronous orbit of 700 km. On the 23rd August 2016 an anomaly occurred causing partial power loss and it experienced a notable change in the impulse and orbit of the satellite. This led to an investigation into the cause of the simultaneous anomalies which concluded the most probable cause was that a micrometeoroid and/or orbital debris (MMOD) impacted the solar array (Figure 1.1) (Krag et al., 2017).
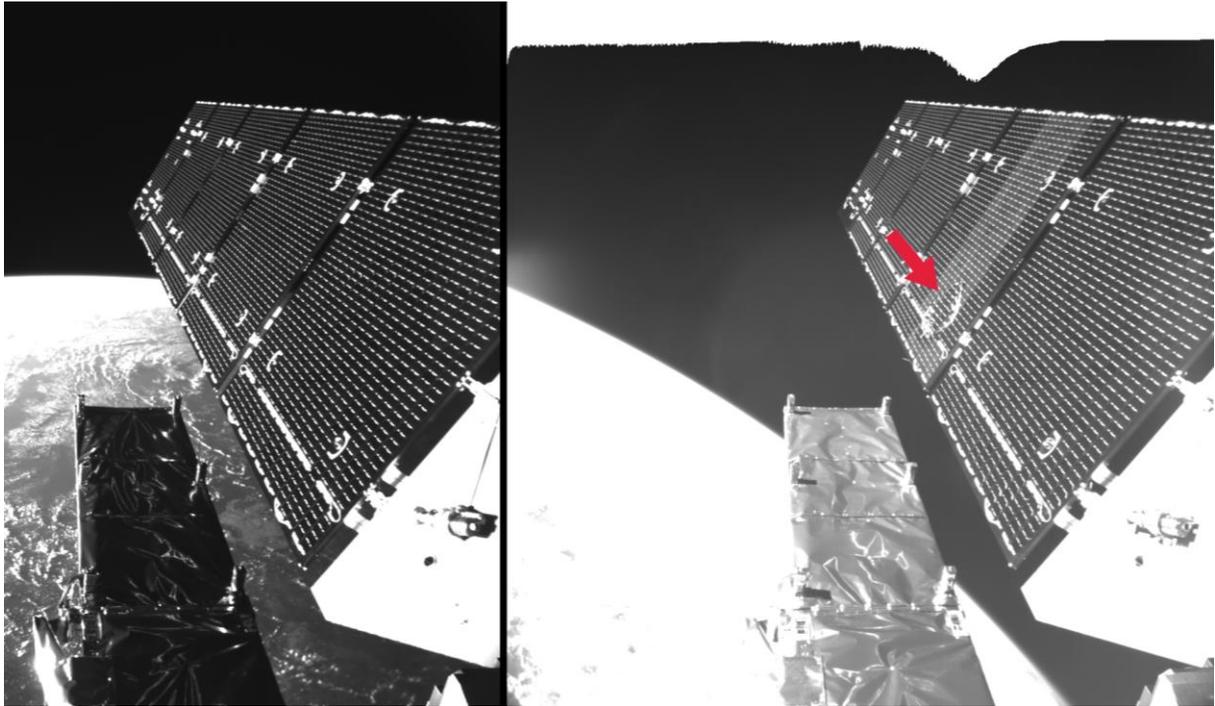
Figure 1.1. Before (left) and after (right) impact on the Sentinel-1A solar array (Krag et al., 2017). The red arrow points to the location of the impact.

The spacecraft function was not greatly affected by the impact and it could continue Earth observation. The United States Joint Space Operations Centre identified 8 fragments that are considered to be created as a result of this impact (Krag et al., 2017).

1.3   Flux Measurements: Quantifying the Hazard

We can observe the population of objects larger than 3 mm using ground-based optical and radar observations (Lederer et al., 2017). As can be seen in Figure 1.2, and discussed in Section 1 of this chapter, the population of objects that are generated by our activities in space and tracked by the United States Space Surveillance Network are created through many avenues, with this number having increased drastically over the past twenty years, largely as a result of two major debris generating events (the destruction of Fengyun 1-C in 2007 and collision of Iridium and Cosmos satellites in 2009).

Monthly Number of Objects in Earth Orbit by Object Type
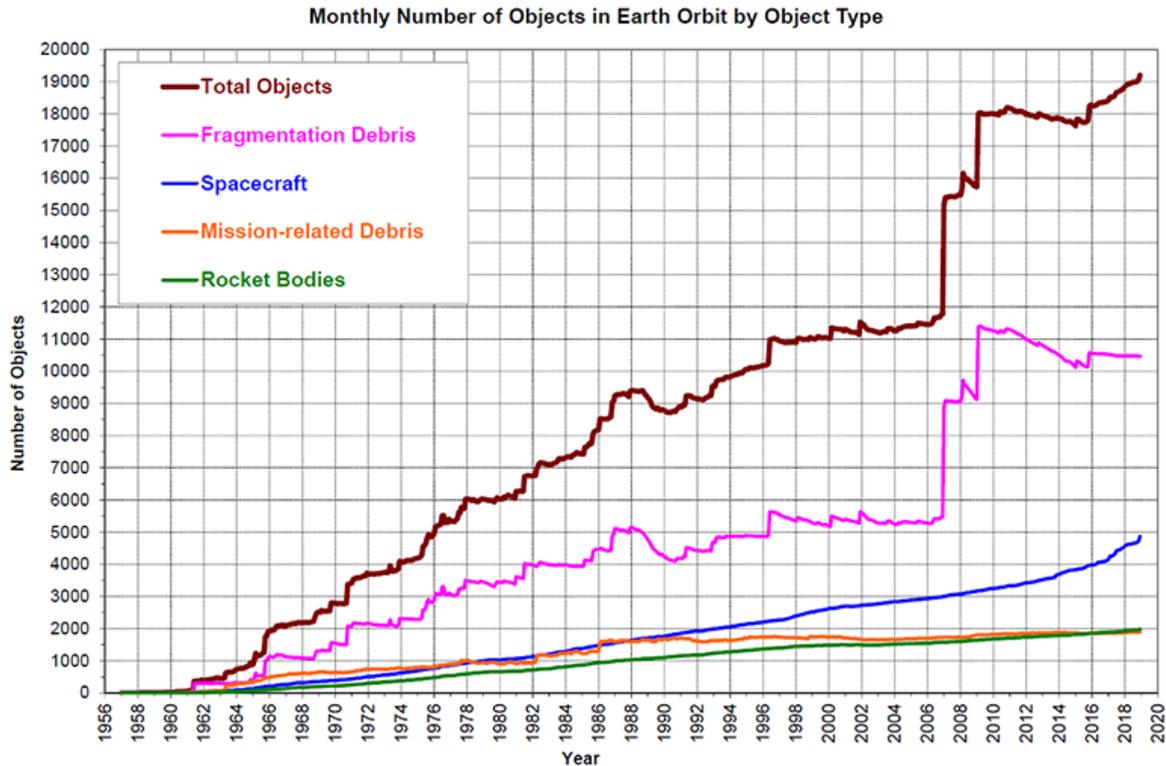
Figure 1.2. The monthly number of catalogued objects tracked by the United States Space Surveillance Network by object type. Both satellite breakup debris and anomalous debris are included in "Fragmentation Debris"("ARES Orbital Debris Program Office Optical Measurements," 2019).

Given the increasing reliance of daily life on orbiting satellites, assessing and monitoring the flux of OD and MM populations in LEO is of vital importance since they can pose a serious hazard to spacecraft and astronauts alike.

To date, various methods have been used to try determine the flux and size distribution of objects in the LEO environment, in particular radar and optical observations provide information on larger sizes, while smaller sized particles have been investigated by examining returned space-exposed surfaces or by dedicated detectors designed to be impacted by dust particles. The results from these experimental methods are fed into computational models of the space environment, resulting in the current limited understanding of particle flux which usually does not distinguish between OD and MM populations. The distinction between the two populations is important for assessing the hazard that they pose as, for example, the OD population typically travels at much lower velocities than that of the meteoroid and micrometeoroid population (Wozniakiewicz et al., 2019).

1.3.1 Measuring the Flux: Ground-Based Observations

Remote sensing is a method by which we observe the OD population from Earth using radar and optical telescopes. The Goldstone Radar, a ground-based tracking station operated by NASA, is a powerful radar capable of detecting a conducting sphere 3 mm in diameter up to an altitude of 1000 km (Goldstein et al., 1998). The Haystack radar operated by MIT Lincoln Lab, upgraded in 2010 to the Haystack Ultra-wideband Satellite Imaging Radar (HUSIR), is able to identify small debris objects of approximately 5 mm up to 1000 km in altitude (Matney et al., 2019). The HUSIR radar utilises "beam-park" mode for observations of OD. In this mode the radar antenna points at a fixed elevation and azimuth and surveys the objects which pass through the radar beam. By doing this the calculations of conductive debris flux is simplified although this short observation time limits the ability to precisely measure the orbital parameters of the debris (Matney et al., 2019).

Optical telescopes are also used in the terrestrial monitoring of OD. The 1.3 m Eugene Stansbery Meter-Class Autonomous Telescope (ES-MCAT) on Ascension Island has been used by NASA since 2015 to observe and track OD. Its primary observing goal is to monitor and assess the orbital environment with a focus on the GEO debris belt and the density and size range of the debris there (ARES Orbital Debris Program Office Optical Measurements, 2019). Its estimated detection limit is in the range $20 - 35$ cm in GEO. ES-MCAT has five-times more light-collecting power than its predecessor MODEST (Lederer et al., 2017). Between $2001 - 2014$ MODEST was NASA's main optical detector for GEO debris and could detect objects of 25 and 17 cm in size (ARES Orbital Debris Program Office Optical Measurements, 2019).

1.3.2 Measuring the Flux: In Situ

To circumvent the detection limits in radar and optical observations, on-orbit observations are ideal to sample a wide size range, especially the smaller particles that are not observable by remote techniques. Such detectors provide information for the debris in orbit at that specific altitude and can be either active or passive.

1.3.2.1 Active Detectors

Active dust detectors are designed to respond to impact by particles, and designs to date have measured velocity, impact angle and estimated particle size to determine the total flux of particles. These require power and data connections. Some examples of active detectors are the Geostationary Orbit Impact Detector (GORID), the Debris In Orbit Evaluator (DEBIE), and the Space Debris Sensor (SDS). Launched onboard the Russian Express-2 telecommunications spacecraft in 1996, GORID, an impact

ionisation detector, was designed to measure the sub-micron to millimetre sized particle population in GEO (Figure 1.3) (Drolshagen et al., 1999).
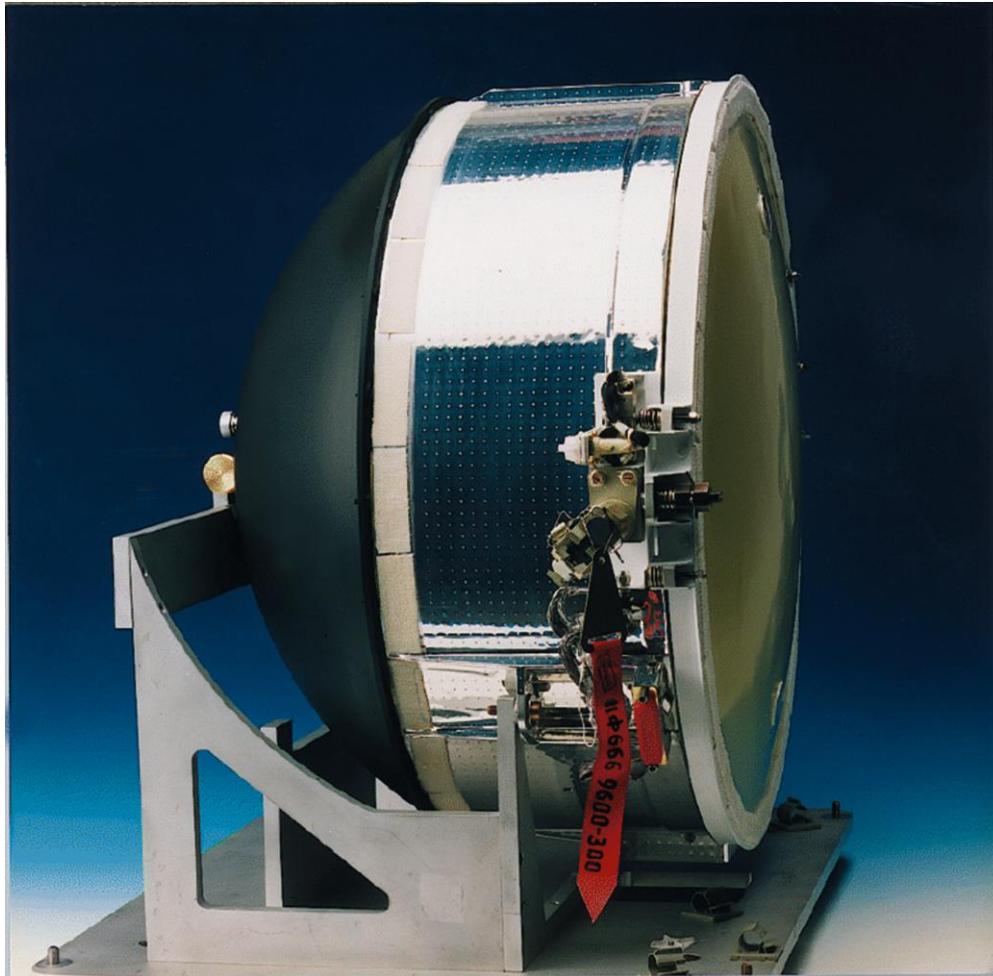
Figure 1.3. The Geostationary Orbit Impact Detector, one of the first active impact detectors in GEO (ESA, 2009)

Two DEBIEs were launched onboard the ESA PROject for On-Board Autonomy (PROBA) satellite in October 2001, into a polar low Earth orbit and used several sensors to detect and calculate the direction of impacting particles (Schwanethal et al., 2005). Other DEBIEs were installed on the exterior of the Columbus module on the International Space Station in February 2008, shown in Figure 1.4, as part of the European Technology Exposure Facility (EuTEF) (Menicucci et al., 2013). While in operation, DEBIE was sensitive to objects in the sub-millimetre range (Schwanethal et al., 2005).
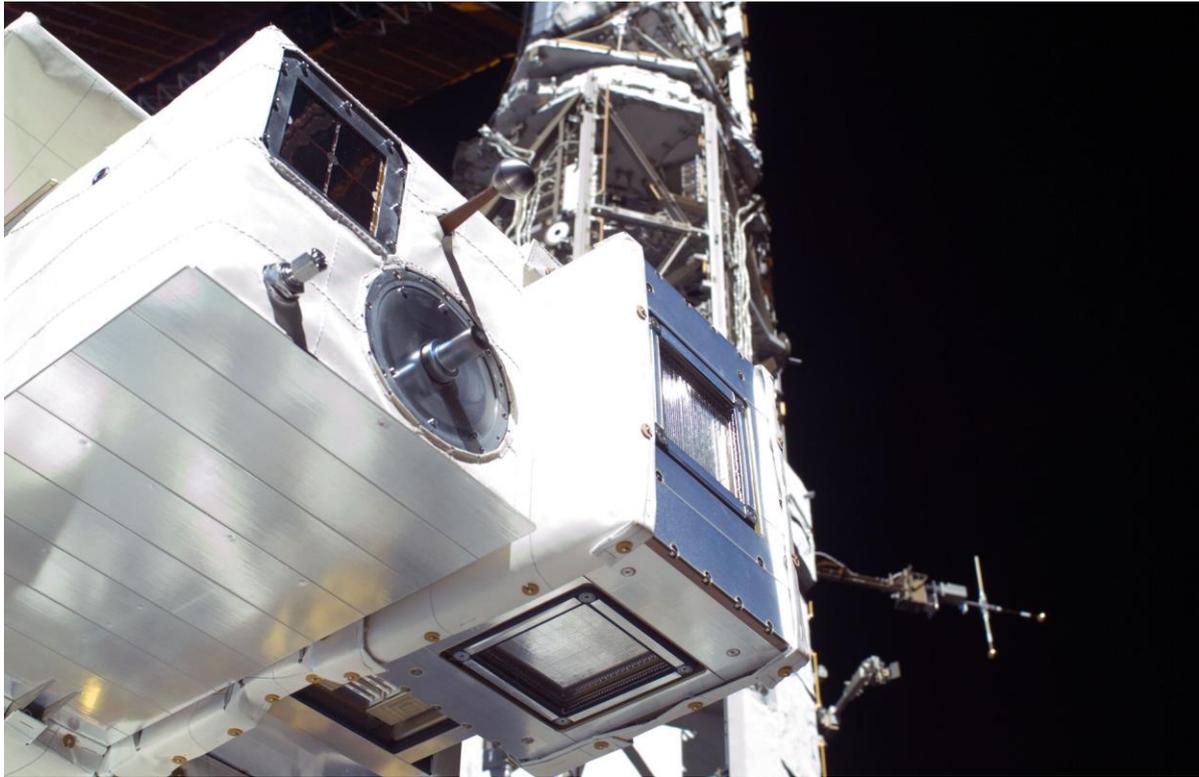
Figure 1.4. DEBIE detectors deployed on the Columbus module of the International Space Station to collect data on the dust population in orbit (ESA, 2009).

NASA's SDS was an experiment located on the outside of the International Space Station (ISS) in 2018. The detector used the Debris Resistive/Acoustic Grids Orbital NASA-Navy Sensor (DRAGONS) to determine impacting particles' size, speed, direction and density for particles in the 50 µm to 100 µm range (Hamilton et al., 2017). This experiment was intended to operate for 3 years but unfortunately it experienced multiple anomalies leading to it becoming inoperable after only 26 days (Anz-Meador et al., 2019). These methods are effective in measuring particle flux in real-time but most active detectors are not able to measure chemistry of the incoming particle and, hence, are incapable of making the distinction between man-made debris and the natural meteoroids and micrometeoroids (Wozniakiewicz et al., 2019). Time of flight mass spectrometer based dust detectors, such as those 189 detectors used onboard Cassini, are capable of measuring the chemistry of impacting particles, however, these typically have small collection/ionisation surfaces which limits them to analysing small particles (Wozniakiewicz et al., 2021).

1.3.2.2 Passive Detectors

Passive dust detectors are those with no inputs or outputs during deployment, and are typically surfaces that simply capture impacting particles and enable the determination of details of the impactor (e.g. the size, shape and composition of the impacting particle) after being returned to the Earth for analysis in the laboratory. These can be dedicated or opportunistic in nature.

1.3.2.2.1   Dedicated Detectors

Dedicated collectors are those that have been designed specifically to collect and measure dust particles. The Long Duration Exposure Facility (LDEF), shown in Figure 1.5, spent 69 months in orbit at 465 km mean altitude and was retrieved in 1990 (Drolshagen et al., 1996). The satellite contained 57 experiments to survey the LEO debris environment (Bernhard et al., 1993).

Figure 1.5. The Long Duration Exposure Facility in orbit. The various experiment trays can be seen as the individual squares on every side of the detector. The pointing of the spacecraft was maintained thus the 12 sided spacecraft allowed for experiments to be on the ram or wake facing side during the whole mission (ESA, 2009).

The impact features ranged from a few micron to 5 mm (Drolshagen et al., 1996). The European Retrievable Carrier (EURECA) was exposed for nearly 11 months and retrieved in 1993, although impact features were mainly observed on the solar arrays and multi-layer insulation (MLI) rather than the dedicated collector surface. The impactors were between 30 μm to 6.5 mm. With both of these detectors being retrieved over 25 years ago the current population and composition of the LEO environment is becoming more of an unknown due to the increase in space traffic and, consequently, many large breakup events that have taken place since the completion of these missions.

1.3.2.2.2 Opportunistic Returns

With respect to the smaller population, much of the available data on flux has come from non-dedicated surfaces – those whose primary function was not the capture of impacting particles, that have subsequently been returned to Earth during, for example, service missions whereupon examination revealed impact features that could be analysed and interpreted. Since these are not purpose-built for the study of impact features, this often leads to difficulties in their analysis (e.g. distinguishing chemistry of impactor and that of spacecraft surface, difficulty determining impactor size from impact feature size, Kearsley et al., (2005a)) which lead to uncertainties or poor statistics in the flux determined.

Examples of such opportunistic samples include the heat-shield windows from Apollo 7 to 17, excluding Apollo 11, which were used in studies of meteoroid impacts (Cour-Palais, 1974). Impact features have also been studied on solar arrays (Figure 1.6) and a radiator shield from the Hubble Space Telescope (HST) returned by the Space Shuttle Orbiter program (e.g. Kearsley et al., 2005a) and, as mentioned above, solar cells and MLI from EURECA (Herbert et al., 1997).
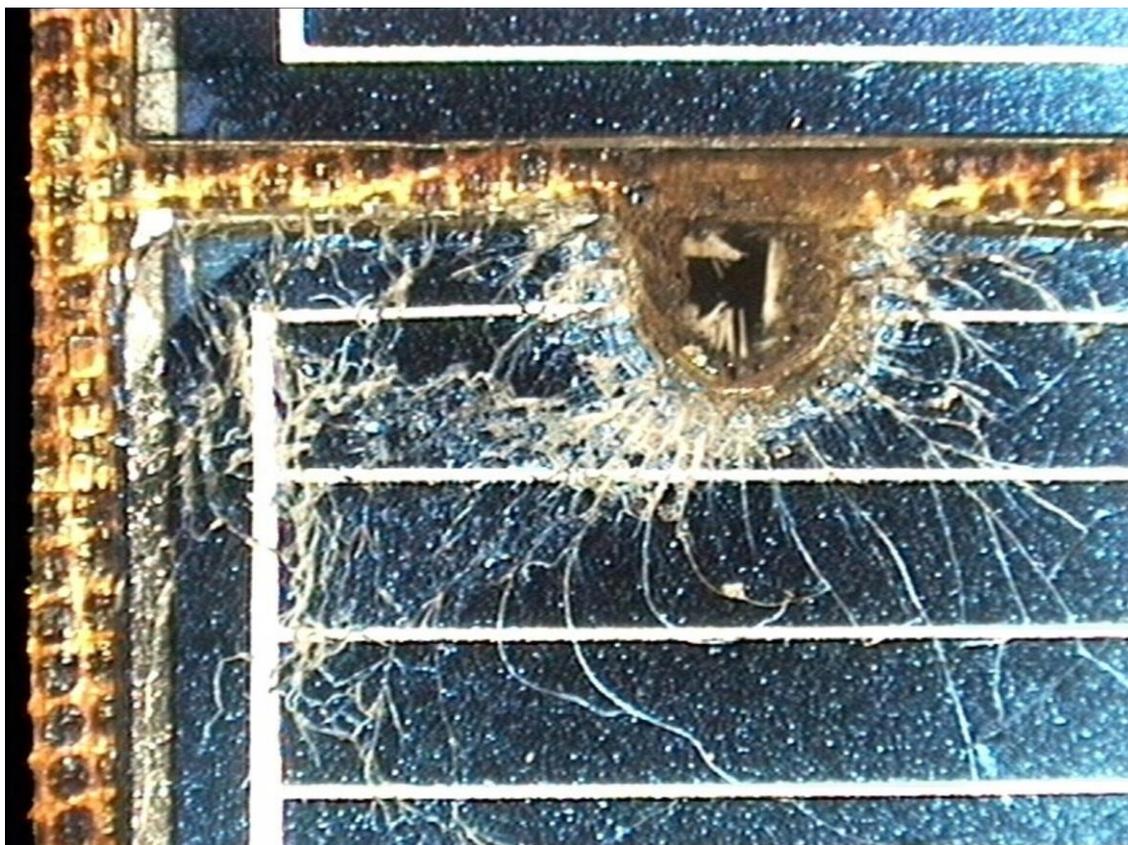
Figure 1.6. An impact on the returned Hubble Space Telescope solar array. The damage extends past the impact hole, cracking the solar cell (ESA, 2009).

The Solar Maximum spacecraft was repaired on the 11th Challenger space shuttle flight, with aluminium thermal control louvers and multilayer thermal blankets recovered for analysis of 1908 impacts features produced during 4.15 years in orbit (Warren et al., 1989). Tray clamps, which held experiment trays in place on LDEF were also returned for study of impact features (Bernhard et al., 1993). The Space Flyer Unit, retrieved after 10 months in space, had Kapton multi-layer insulation foils (MLI), as shown in Figure 1.7, and Teflon radiators returned for study of impact features (Yano et al., 1997).
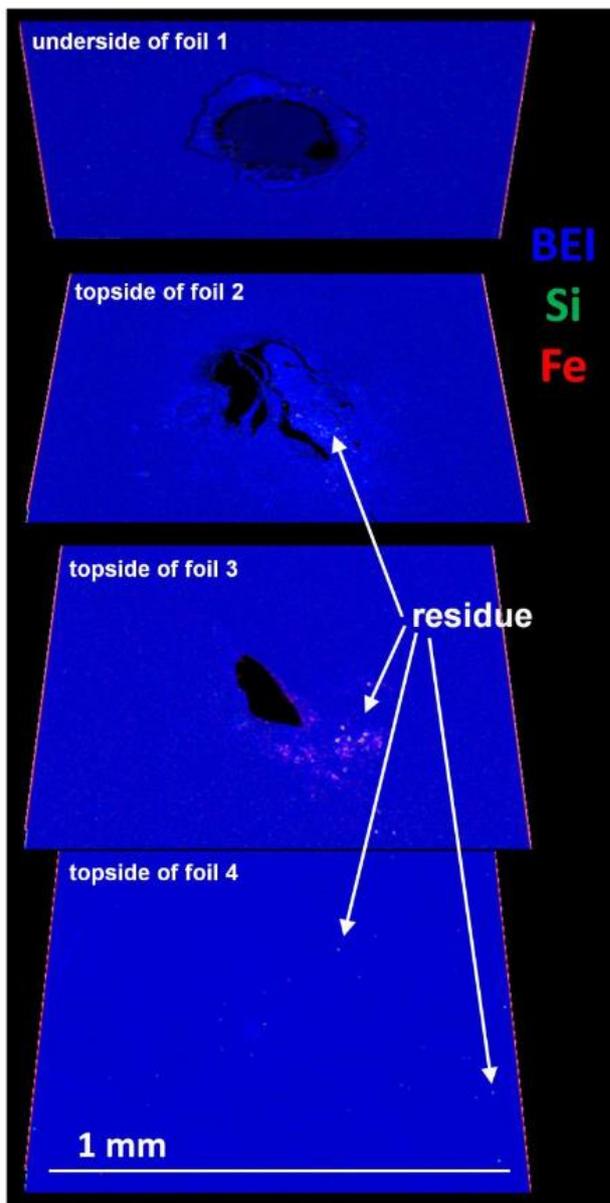
Figure 1.7. Multi-layer insulation from the Space Flyer Unit. The particle that impacted the insulation left residues on the foils it passed through that was identifiable with SEM elemental maps. This finding is key for identifying the types of particles that can be encountered in the interplanetary environment despite this not being a perfect detector surface (Kearsley et al., 2005b).

However, these surfaces were not created for the study of impact features, hence they hinder analysis efforts as they are made of materials whose elemental components are also present in OD and MM.

From previous studies of the LEO environment with active and passive detectors as well as opportunistic returns, a gap in measurement data has been identified for particle sizes between approximately 200 µm and 2 mm (Wozniakiewicz et al., 2019). The particles smaller than 200 µm have been identified through returned surfaces for OD and MM alike and particles larger than 2 mm can be tracked and identified using ground-based observations. Additionally, the aforementioned returned surfaces and passive detectors, for the majority, are outdated and were retrieved over 25 years ago, long before the increased use of space and the more recent large breakup events such as the destruction of Fengyun-1C or the collision of Cosmos 2251 and Iridium 33. The impacts that occurred to Cerise and Olympus were examples of both man-made and natural debris impacts. The majority of these events are unlikely to have been avoidable due to the high velocities and small size of impacting particles. It follows that new observations of the debris environment are required to fill this void in current understanding of LEO to improve our environment models and inform our decisions on risks present in orbit for satellites.

1.4 Flux Models and Modelling

Understanding and predicting the flux of space dust is necessary to ensure the safety of spacecraft, for example, the design of a spacecraft deemed at high risk of impact during its mission will incorporate adequate shielding and avoidance manoeuvre capabilities (e.g. thrusters and extra fuel). The substantial amount of data collected through the various forms of dust environmental observations can be extrapolated to create models that represent the orbital environment. Various models have been created to propagate the evolution of space dust (both OD and MM populations) through time both in the vicinity of the Earth and interplanetary space. Two notable models of the near Earth dust environment are ESA's Meteoroid and Space Debris Terrestrial Environment Reference (MASTER) model and NASA's Orbital Debris Engineering Model (ORDEM). Both models incorporate a plethora of modelling techniques and theories of the distribution of particles to attempt to best encapsulate the variation in the debris population now and for decades to come.

1.4.1   Meteoroid And Space Debris Terrestrial Environment Reference (MASTER)

ESA's Meteoroid And Space debris Terrestrial Environment Reference (MASTER) model assesses the space dust flux imparted on a spacecraft in orbit around the Earth up to 36,786 km in altitude (GEO) (Horstmann and Stoll, 2017). MASTER 8.0.3 is the current release of the software with five predecessors since the first release in 1995. The current lower limit on the size range is 1 µm. Of key

interest to the MASTER team are objects in the range of 1 – 10 cm as these particles are highly dangerous to spacecraft due to both to the difficulty in tracking these particles and the destructive power upon impact with a spacecraft (Horstmann and Stoll, 2017).

MASTER categorises its inputs and outputs based on the origin of the debris fragments. These different sources are shown in Figure 1.8 along with their corresponding size ranges. For each debris source there is a generation model with the mass and diameter of the objects in addition to their velocities and the directional spreading (ESA, 2022b). Objects greater than 1 µm are propagated into the future.

The events which generated large numbers of debris less than 1 mm in size such as degradation of surfaces, solid rocket motor (SRM) firings and secondary ejecta are simulated individually. As each SRM firing can be traced to its source these events are modelled deterministically. As for the other events, they are simulated statistically. Tracking and Imaging Radar (TIRA) and European Incoherent Scatter Scientific Association (EISCAT) radar data is used to validate the resulting populations based on observational data.
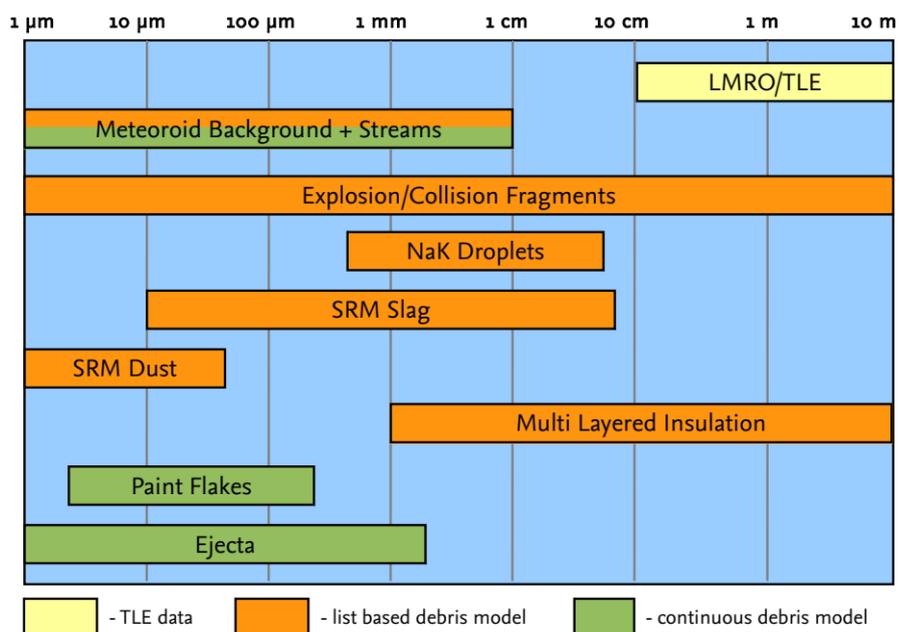
Figure 1.8. The categories for sources and corresponding size ranges used by the MASTER model (ESA, 2022b).

1.4.1.1 MASTER Meteoroid Models

MASTER incorporates several different models of natural dust populations in an effort to accurately simulate their abundances over time: the Divine-Staubach meteoroid model, the Grün meteoroid model,

the Cour-Palais model and the Jenniskens/McBride model (ESA, 2022b). The isotropic Grün meteoroid model is implemented throughout MASTER for the background interplanetary flux.

1.4.1.1.1 Divine-Staubach

The Divine-Staubach meteoroid model is used to model the steady state natural meteoroid environment in MASTER. This is centred around Divine's theory using five populations (core, eccentric, halo, inclined and asteroidal) distinguished by their mass spectrum, eccentricity, inclination and perihelion distance (Divine, 1993). Staubach updated the Divine model utilising data from the Ulysses and Galileo dust detectors to constrain the distribution parameters. The distinct populations of eccentric, halo and inclined were redefined to the A, B and C populations whilst the core and asteroidal population categories remained unchanged (Divine, 1993).

1.4.1.1.2 Grün Meteoroid Background Flux Model

MASTER also incorporates the Grün Meteoroid Background Flux model to describe the interplanetary dust population in terms of background meteoroids with an averaging of the seasonal streams. This is an analytical model which describes isotropic flux dependent only on the meteoroid mass. The radial distance from the sun is the only factor necessary when calculating velocity (in the vicinity of the Earth this is found to be 20 km/s), although for the MASTER model the Taylor Velocity Distribution is used to more accurately reflect the MM environment giving meteoroids velocities between $10 - 20$ km/s (ESA, 2022b).

There are two additional options for the user to choose from to model seasonal meteoroid stream events; the Cour-Palais model and the Jenniskens/McBride model.

1.4.1.1.3 Cour-Palais Model

The Cour-Palais model describes the activity of seasonal meteoroid streams using a flux ratio of the cumulative flux of every stream to the average cumulative sporadic flux. However, this model is intended for engineering purposes and is thus highly idealised. For example, it does not include any gravitational focusing or Earth shielding effects when modelling the streams. Simple rectangular and triangular profiles are used as analogues for spacecraft when describing the time profile for any given stream.

1.4.1.1.4   Jenniskens/McBride Model

Like the Cour-Palais model, the Jenniskens/McBride model also describes the activity of seasonal meteoroid streams. This model is derived from observations of meteor streams by amateur astronomers from both the northern and southern hemispheres between 1981 to 1991. These were used as the first set of observations of about 50 meteoroid stream activity curves including minor and major streams. As these observations are ground-based, and made purely based on positive detections, the mass-flux relationship is missing from this model. However, a conversion of the activity of the streams to a mass influx profile is possible to produce the particle mass by making assumptions about the perpendicular distribution density with respect to the Earth (Jenniskens, 1993).

1.4.2 Orbital Debris Engineering Model (ORDEM)

The Orbital Debris Engineering Model (ORDEM) is a NASA Orbital Debris Program Office (ODPO) tool developed for spacecraft designers to identify the long-term risks posed by human-made OD, unlike MASTER, the MM modelling is a separate library and no included in the basic package. The development of ORDEM began in the mid-1980s. The first computer-based version of this tool was released in 1996 called ORDEM96, followed by ORDEM2000 which improved upon the curve-fitting function by replacing it with a finite element representation of the debris environment. The successor to this model was ORDEM 3.0 in 2015 which was a major upgrade to the model. The features and capabilities were extended to include the GEO region, enabling analysis of the Geosynchronous Transfer Orbit (GTO) and highly-elliptical orbits (Matney et al., 2019). Uncertainties in the OD flux were added as well as the material densities. ORDEM includes the most recent data available to NASA and has applied novel analysis techniques to both new and legacy data to improve the models of the OD population and spans the years 2016-2050 (Matney et al., 2019). Table 2 shows the various sources that have been used in the ORDEM model including their limiting size ranges for detection. This model benefitted greatly from post-flight analysis of the Space Shuttle (STS) surfaces for impact features (Matney et al., 2019).

Data Source	Source Type	Orbit Region	Detection Size Range (approximate)	Calendar Year(s): Model Build	Calendar Year(s): Model Validation
STS windows, excluding cargo bay windows	*in situ*	LEO	10 – 300 μm	1995-2011	N/A
STS radiators	*in situ*	LEO	300 μm – 1 mm	1995-2011	N/A
HST Bay 5 MLI cover	*in situ*	LEO	10 – 300 μm	N/A	1990-2009
HST WFPC-2 radiator	*in situ*	LEO	50 – 300 μm	N/A	1993-2009
HUSIR, 75˚E	Radar	LEO	>5.5 mm	2007*, 2009*, 2013-2015	2016-2017
HUSIR, 20˚ S	Radar	LEO	>2 cm	2015	N/A
Goldstone	Radar	LEO	2 – 8 mm	N/A	2016-2017
SSN	Radar, Optical	LEO, GEO	>10 cm (LEO), >1 m (GEO)	1957-2015	2016
MODEST (UCTs and CT debris)	Optical	GEO	>30 cm	2004-2009	2013-2014

* Datasets used for characterization of large breakups (Fengyun-1C [FY-1C], Iridium 33, and Cosmos 2251). Data from special Haystack observation campaigns around the time of the event were used.

Table 1.2. Datasets used to build and validate ORDEM (Matney et al., 2019) The U.S. Space Transportation System (STS), commonly known as the Space Shuttle, the Hubble Space Telescope (HST), the Haystack Ultrawideband Satellite Imaging Radar (HUSIR), the Goldstone radar, the Space Surveillance Network and the Michigan Orbital DEbris Survey Telescope (MODEST) were all used as inputs in building the ORDEM model.

The particles in LEO approximately 5 mm to 10 cm are modelled using HUSIR data. Particles smaller than 3 mm in size are constrained using analysis from in situ impacts on the Space Shuttle and from the Hubble Space Telescope, particularly for the sub-millimetre range. In GEO, objects in the range of 10 cm to 1 m are modelled using optical observations from the Michigan Orbital Debris Survey Telescope (MODEST). The NASA LEO-to-GEO Environment Debris Model (LEGEND) is used in the modelling of the populations greater than 1 mm (Matney et al., 2019). Specific, historical fragmentation events (e.g. Fengyun 1C) were later added after they were modelled using a special version of the NASA Standard Satellite Breakup Model (SSBM) which incorporates material density for fragments less than 10 cm. This model comes from analysis of fragments generated by the Satellite Orbital Characterisation Impact Test (SOCIT) series and also breakdowns of the known satellite material (Matney et al., 2019).

The essential dataset in the model is the ODPO-maintained space traffic database which typifies satellites launched with their orbital parameters in addition to information on previous breakups and manoeuvres (Matney et al., 2019). This database is built upon the SSN catalogue which contains almost all information on objects larger than 10 cm in LEO and 1 m in GEO. To expand the dataset to include smaller size ranges than the observational limits and orbital regions that are not well documented by the SSN catalogue the data obtained from radar, in situ and optical observations are extrapolated. The

space traffic database is used as an input to the LEGEND model to predict the evolution of the debris environment (Matney et al., 2019).

The breakdown of material densities is a major development in ORDEM which paves the way for more accurate assessments of the danger of debris objects. There are five density categories for the debris populations: intact spacecraft and rocket bodies; low-density (1.4 g/cc) fragments; medium-density (2.8 g/cc) fragments and microdebris; high-density (7.9 g/cc) fragments and microdebris; and sodium-potassium (NaK) coolant droplets from the Radar Ocean Reconnaissance Satellite (RORSAT) class of spacecraft (0.9 g/cc) (Matney et al., 2019).

ORDEM covers 2016 to 2050 with its models by making a few assumptions about how the debris population will grow, evolve and change over time. Firstly, it is assumed that the traffic from launches will follow the same cycle as the previous 8 years and that the success rate for disposal of post-mission debris is 90% for rocket bodies and spacecraft (Matney et al., 2019). The occurrence of future collisions and explosions is statistically modelled. For the population in LEO are modelled using LEGEND down to 1 mm in diameter with material densities designated dependent on the fragment size and area-to-mass ratio while in GEO objects down to 10 cm in size are modelled (Matney et al., 2019).

1.4.3   Comparison of ORDEM with MASTER

A comprehensive comparison of the ORDEM 3.0 and MASTER-2009 models was undertaken by Krisko et al. (2015) as at this point the two models were at similar stages of completion. The sizes of debris used in the comparison were 1 m, 10 cm and a range of 1 cm to 1mm. The cumulative fluxes of these debris were compared at four different orbits; that inhabited by the International Space Station (ISS); Sun-synchronous Orbit (SSO); Geosynchronous Transfer Orbit (GTO); and Geosynchronous Orbit (GEO). This size range investigated includes those larger particles that are of great concern to both crewed and robotic missions as well as those smaller sizes that cannot be tracked by ground-based radar and optical methods and are thus the populations for which modelling to assess hazard are most important.

The comparison of the two models for 1 m objects is in good agreement, as expected due to current thorough ground-based observations of the LEO and GTO orbits for objects of that size. The two models differ for the 10 cm population, with the MASTER model having a higher flux. Within the critical size range MASTER also shows a higher population by nearly an order of magnitude at 1 cm and over an order of magnitude at 1 mm, a result that was also found when comparing the predecessors of both models. In SSO, similar results to LEO were also found in the comparison. ISS orbit had highly similar results to GTO in both models. These differences could perhaps be due to a variation in how the two

models include unconfirmed events, propagate debris objects and calculate size from radar observations.

Analysis of the debris populations created by both models is somewhat difficult due to the different categorisations used for the outputs from each model, as previously discussed MASTER splits the outputs into classes based on the source of the fragment and ORDEM categorises fragments based on their densities. Another hinderance to the comparison is that the source populations used for the development of each model are different. ORDEM made use of returned surfaces from the Space Shuttle in their analyses and this indicated a low frequency in Al_2O_3 impactors thus they did not include an explicit SRM slag population. The MASTER model used data from Interplanetary Dust Experiment (IDE) onboard LDEF which measured the time of impact on the detector and noted multiple orbital event sequences occurring, which are observed high numbers of impacts for particular locations on the orbit (Oliver et al., 1995). The data showed that the impacts could be directly linked to SRM firings therefore making it imperative that this population was included in the model. Potentially this difference in noting the significance of SRM firings on the population could be explained by the difficulty in analysing materials that are not designed for identification and categorisation of debris as they likely contained traces of the debris components themselves, thus hindering identification (Stabroth et al., 2008).

These various models and modelling techniques are essential in understanding the OD environment. Despite both the MASTER and ORDEM models using the most innovative models for OD, they are in poor agreement with each other requiring further research to improve this disparity. The most likely reason for this is that the models used different input populations, especially for objects less than 1 cm in size due to the lack of data as well as the rapid increase in space traffic necessitating improved predictions for the environment while still only using this limited input population. A reliable model requires high-quality data as an input so it follows that improved observation techniques and more in situ measurements would provide data necessary for constraining the micro-debris population further, in turn improving the input data for both models.

1.5. Orbital Dust Impact Experiment (ODIE)

The Orbital Dust Impact Experiment (ODIE) has been designed with the aim of addressing the identified data gap in the smaller size regime to enhance the current understanding of the near Earth dust environment (Wozniakiewicz et al., 2019). Based on the previous studies of the LEO environment, ODIE is designed as a passive detector as this is optimal for discerning the particle composition, thus allowing for the flux of the individual OD and MM populations to be assessed. This detector works in the same way as a Whipple shield, with the incoming particle loosing energy and, potentially, being

disrupted as it impacts with the front foil, with further loss of energy and fragmentation occurring on successive foils until the particle is stopped (also similar to the capability of multilayer insulation to capture orbiting particles). As shown in Figure 1.9, the detector is modular in design, allowing for the exact size to be based on the location at which ODIE would be deployed.
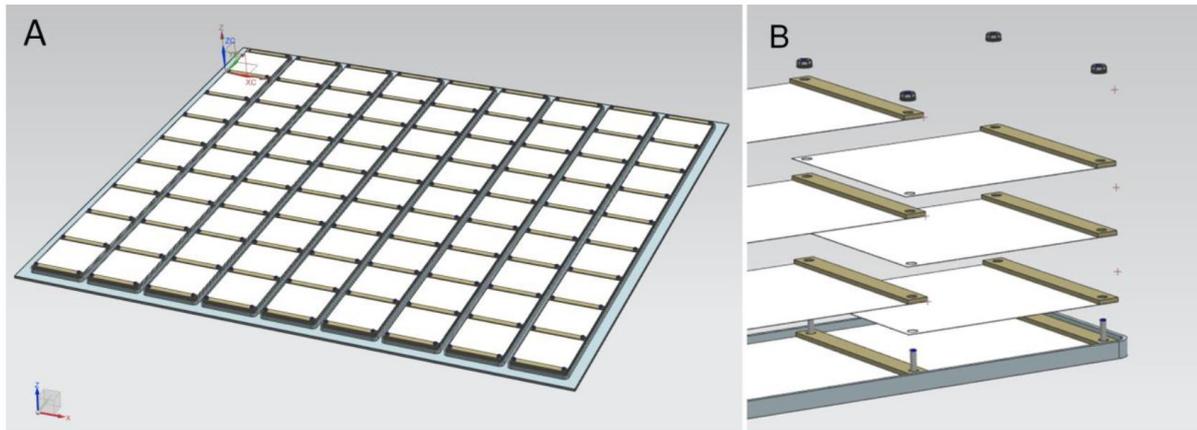
Figure 1.9. A CAD rendering of the ODIE detector configuration for a capture area of 1 m²(Wozniakiewicz et al., 2019). Image A) shows the full scale of the detector comprised of small modules. Image B) indicates one potential method of constructing the modules with minimal materials used.

Using a thin sheet of Kapton gives the front foil the ability to preserve the shape of the impactor and calibration experiments (e.g. performed using a light gas gun) with well characterised projectile materials may enable relationships between the impacting particle and resulting impact feature to be determined (Kearsley et al., 2005b). As the particle travels through the foils, it deposits residue on or around each impact feature (hole or crater) it creates. Upon retrieval of the detector, the residues present on the impact features can be analysed using the wide range of analytical techniques available on the ground, for example scanning electron microscopy (SEM) with energy dispersive X-ray (EDX) microanalysis capabilities.

The Kapton foil is coated to protect from atomic oxygen erosion. Choosing a metallic coating for this purpose has the added benefit of aiding in dispelling the charge accumulation that occurs on Kapton foils during SEM examination, and making the location of penetration holes easier to locate (since the hole appears black against the bright (high atomic number) background in back scattered imaging mode). By analysing residues, the composition of the impactor can be determined and allocated an OD or MM origin according to the presence of specific elemental indicators compared with a knowledge of mineralogy and commonly used materials in space (e.g. presence of metallic elements other than Fe and Ni indicate OD origin, presence of S with Fe, Ni, Mg and I indicate an MM origin). This design

was first proposed by Kearsley et al. (2005b) having noted the preservation of particle residues on the SFU MLI and thus the potential for such thin layered foils to act as a dedicated capture surface. Due to the novel techniques applied in this detector the technology readiness level needs to be advanced to ensure this design will function in the harsh LEO environment conditions, especially with regard to atomic oxygen.

1.5.1 ODIE Palladium-Coating for Protection Against Atomic Oxygen

Atomic oxygen is present in the LEO environment, produced by solar radiation incident on the oxygen molecules present in the upper atmosphere. Collisions with spacecraft are at relative velocities of ~7.4 km/s with fluxes in the range of 10^{13} to 10^{15} atoms cm^{-2} s^{-1}, potentially causing catastrophic damage to the craft, thus motivating studies of the extent of damage this can cause (Cooper et al., 2008). The Long Duration Exposure Facility (LDEF) carried a number of experiments designed to investigate the performance of materials, and hence their suitability for use, in space. Deployed in April 1984 for 69 months, the atomic oxygen fluence in its circular orbit at 28.5° inclination was investigated with the ram-facing fluence 9.02 x 10^{21} atoms cm^{-2} s^{-1} and wake-facing found to be ~10^3 atoms cm^{-2} s^{-1} (Silverman, 1995). LDEF (experiments AO134 and A0114) and Space Shuttle flight data (STS-41-G mission) show that the AO erosion of Kapton is linearly predictable with AO fluence (Silverman, 1995). The erosion of polymeric materials was prevented through the use of coatings with even extremely thin coatings on the orders of nanometres providing adequate protection from atomic oxygen degradation. Sputter-deposited coatings on polymers, such as Kapton, were found to be effective at preventing mass loss in LEO (experiment A0134) (Silverman, 1995).

A common coating utilised for Kapton foil is aluminium, which has been found to be effective at protecting against atomic oxygen (Cooper et al., 2008). Silicones are useful coatings that have the ability to form a SiO$_x$ glass-like film which can protect itself from AO attack (Silverman, 1995). Germanium coated black Kapton is used as a thermal control on the sunshield of satellite antennae as the germanium coating is transparent in radio frequencies whist performing its protective function (Prajwal et al., 2018). This combination is widely utilised although it is particularly vulnerable to oxygen degradation during storage on ground, with a typical shelf life of only ~6 months (Esther et al., 2015).

While these coatings are useful in their applications, for the purposes of ODIE they each have large drawbacks. The main mode of analysis for the returned samples would be by SEM, which requires the sample to not degrade in the presence of oxygen, hence germanium cannot be used. The other common coatings of aluminium, gold, platinum and silicones all have the disadvantage of being a common elemental component of MM (silicon) or OD (aluminium), or of having X-ray emission peaks that overlap with peaks for elements that can be used to distinguish an MM from OD particle (gold and platinum overlap with peaks for sulphur which is a common diagnostic element present in MMs but not

OD) (Kearsley et al., 2005b). Thus, the detector requires an alterative coating that can provide the necessary protection from atomic oxygen damage whilst having an X-ray emission peak that does not coincide with any of the peaks of interest for the identification of residue on the detector. Palladium was chosen as this coating as its X-ray peak does not overlap with the relevant peaks, as shown in Figure 1.10, where palladium and rhodium are the only two elements that would be suitable for such a detector (Kearsley et al., 2005b).
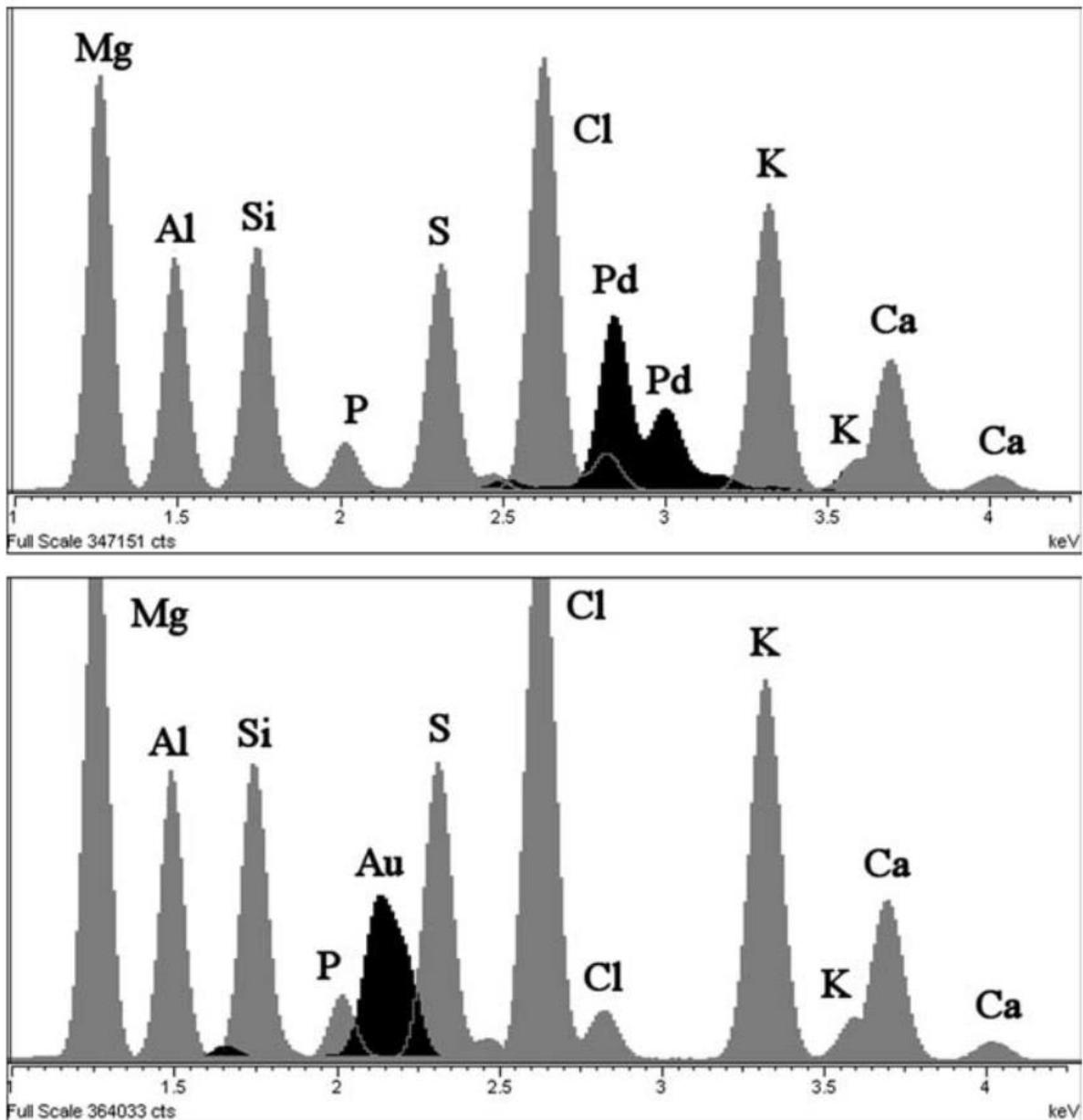
Figure 1.10. EDX spectra showing the positions of the peaks of the area of interest (Kearsley et al., 2005b). The top spectrum indicated the location of the palladium (Pd) peak and shows there is no clear overlap with any nearby elements. In contrast, the bottom spectrum shows the position of the gold (Au) peak where it has an overlap with the sulphur (S) signal which is a key indicator for MM residue and hence gold would hinder identifying this signifier.

Using the thinnest layer of coating possible is optimal as thick coatings are more likely to produce cracks, creating a point of entry for the atomic oxygen (Cooper et al., 2008). Only the exposed side of the polymer is coated to prevent the atomic oxygen undercutting; A process by which the atomic oxygen enters the polymer through a crack, bouncing between the two layers of coatings and causing more

damage than having an exposed back surface (Cooper et al., 2008). Any defects in the surface of the coating present an opening for the atomic oxygen to attack the protected polymer beneath leading to atomic oxygen undercutting with the potential to increase the size of the original defect. Therefore, preparation of the polymer in a clean environment is required to reduce likelihood of defects and the coating deposition must be smooth and thin (de Groh and Banks, 1994).

For ODIE, palladium was applied to the Kapton foils by sputter coating. This easy to use and relatively inexpensive method provides thin, smooth coatings. Sputter coating consists of using a high voltage to produce a plasma of the materials to be deposited onto a surface. This plasma is then accelerated towards the surface to be coated and each individual atom creates small indents in which they reside (Simon, 2012). The thickness is built up through many of these atoms being deposited onto the surface. The coating created is susceptible to being rubbed off mechanically as the atoms can be disturbed from the places in which they sit.

1.6. Aims of this Thesis

The overall aim of this thesis is to advance the Technology Readiness Level (TRL) of the ODIE detector. The TRL of a new material or technology is used to determine its flight-worthiness for use in space as the space environment is a harsh one and many materials or technologies may not survive the launch, the exposure to atomic oxygen or radiation in orbit as well as the thermocycling experienced by satellites which requires the ability to survive both extreme low and high temperatures alongside rapid switching between these temperatures. In order for ODIE to be used as a dust detector it must satisfy the TRL requirements to remain operational in the LEO conditions. To this end, the efficacy of palladium as a protective coating is paramount to advancing the TRL of ODIE. In addition to this, the overall function of the detector, that is, to measure the impacting particle size and composition, must remain unhindered by the application of the protective coating. Therefore, there are two main investigations within this thesis; to study the palladium coating and to evaluate the impact feature and projectile relationships.

The main concerns with the coating are to determine what thickness is best to protect the Kapton foil from erosion from atomic oxygen during exposure in LEO, if the coating has any effect on the impact features observed on the foils and if that varies with thickness. As palladium has only a single report of exposure to atomic oxygen on LDEF (Silverman, 1995), conducting a range of experiments to study the reaction of different thicknesses of palladium to atomic oxygen will give a new insight into the protection capabilities of the coating. In this study, sputter coating is used as the method for coating all thicknesses of the Kapton foils. The foils were then used for atomic oxygen exposure experiments and LGG hypervelocity impact experiments.

The relationship between the impact feature size and the size of the original projectile for different thickness Kapton foils and different thickness coatings are explored in Chapter 3. This chapter covers a range of LGG experiments shooting the palladium-coated Kapton at 1 km/s and 5 km/s with a range of projectiles, with measurements taken on the impact features formed. Different thicknesses of Kapton foil (13 µm, 25 µm, 75 µm, 125 µm) with 10 nm of palladium coating are shot to assess the optimum thickness of Kapton foil for extrapolating a relationship between the impact feature and the size of the projectile, and to assess whether the thickness of the Kapton has any effect on the relationship. The next experiments determine whether the palladium coating itself has any effect on the relationship by varying the thickness of the palladium coating (10 nm, 20 nm, 30 nm, 40 nm, 50 nm, 100 nm) whilst using the same Kapton thickness of 25 µm for all targets.

Following on, the performance of palladium as a protective coating is the focus of Chapter 4 with regards to how it withstood the hypervelocity impacts and exposure to atomic oxygen. Samples prepared for the impact feature experiments of Chapter 3 were studied with the aim of determining the extent of damage that hypervelocity impact had on the coating and which coating thickness suffered the least amount of damage (i.e. remained intact on the Kapton foil). Additional samples of the 25 µm Kapton foil with a range of palladium coating thicknesses (0 nm, 10 nm, 25 nm, 50 nm, 75 nm, 100 nm) were exposed to atomic oxygen and surveyed for defects and erosion features caused by the exposure.

The development of any technology is a long process with many specific tests required to advance the TRL to a flight ready status, thus Chapter 5 describes many additional avenues of investigation that have been initiated but that, due to time constraints, have not been completed. Vacuum, vibration and thermocycling tests are also required to advance the TRL of ODIE, all of which use specific instrumentation unavailable during this project. Additionally, ODIE is a recently conceived detector and, as such, requires substantial testing to fine tune the parameters for observing sub-millimetre impact features, which initial progress has been made on many aspects of the subsequent calibrations of ODIE discussed in this chapter. Some of the topics therein include conducting further experiments with the LGG (e.g. inclined impact experiments as dust may not impact perpendicularly), the use of computer modelling using Ansys Autodyn to explore the impact feature and projectile relationships beyond the current capabilities of the LGG (e.g. at higher velocities than are currently possible with the LGG).

Through these experiments this thesis will determine the relationships between the impact feature size and projectile for different thicknesses of Kapton foil and of palladium coating, concluding Chapter 3 with an evaluation of the influence of palladium coating on this relationship, and a recommendation for the optimum Kapton thickness for preserving this relationship. The minimum palladium coating required for the protection of Kapton against atomic oxygen in LEO also will be determined in Chapter 4 and, combined with results from Chapter 3, result in a recommendation for optimum palladium

coating thickness for use on ODIE. Future testing and calibration avenues are discussed in Chapter 5 with the aim of either improving the ability of ODIE to determine the size and composition of impacting particles or to improve the TRL of the detector in order to prepare it for flight.

Chapter 2: Methods

This chapter describes the methods used to prepare and analyse the samples created and studied in this thesis. All samples were made following the same procedure - using Kapton as the material for the foil and coating this with palladium. The samples were then subjected to hypervelocity impact using a light gas gun, simulating the impact events experienced by materials in LEO. A set of samples were exposed to atomic oxygen to simulate the erosive conditions of LEO. The samples were then analysed using SEM to assess the damage by impact and exposure to atomic oxygen, and determine how well the foil survived and preserved the impactor size dimensions, as well as how these dimensions relate to the size of the initial projectiles.

2.1 Coating of Kapton Foils

Polymeric materials in LEO are highly susceptible to erosion by atomic oxygen created in the upper atmosphere that is present in quantities that can have large erosive effects up to an orbit of around 800 km. Consequently, these materials require protection from erosion which is done through coating the polymer to build a protective barrier to erosion. For the ODIE detector, this requisite coating is critical as the detector is constructed of polymer foils as the main detector material. The coating on the detector needs certain attributes to facilitate the objectives of the detector – to preserve the impact feature size and any residue it may deposit in order to determine the OD or MM nature of the impacting particle. Thus, we need a coating that does not consist of any materials that are present in OD or MM, which could lead to a conflict in origin determination. Additionally, the coating needs to be capable of dispelling charge on the sample when undergoing SEM analysis as the Kapton foil is an insulator and hence cannot perform this function. Due to these considerations, the commonly employed coatings of aluminium and gold are unsuitable as they conflict with the composition of OD and MM, therefore palladium was selected for this purpose. Today, the most common coating method is sputter coating, which is the method chosen for this investigation.

Sputtering is a commonly used coating method in a variety of industries including semiconductor processing, jewellery making and aerospace (Simon, 2012). Sputtering is a process whereby ionised atoms from the coating material get accelerated and impact the surface to be coated, termed the target surface, in turn ejecting atoms from the surface which then condense onto a sample to create a thin film of the material. The other physical vapour deposition method that was used commonly until sputter deposition dominated the market was evaporation. Evaporative methods include many different processes by which a liquid is vapourised by either heat or low pressure and this vapour is then directed towards the target to be coated (Rossnagel, 2003). The kinematics of the particle emission process between the two methods has fundamental differences whereby the atoms are emitted thermally in

evaporation techniques after heat is applied to a large region of the source material to be used as the coating, whereas sputtering is a nonequilibrium process that takes place within the energy range of interest for deposition of the film (Rossnagel, 2003). This difference between the sputtering and evaporation methods is that sputtering creates a high-energy flux leading to a high surface mobility that produces "smooth, dense, conformal, and continuous films" in a more effective manner than evaporation (Simon, 2012).

Sputtering is induced when an energetic particle, typically an ion, collides with atoms present in the target material. A common ion used in this process is argon (Ar^+) as it is chemically inert and inexpensive (Simon, 2012). The impact of this ion dislodges one or more of the target palladium atoms and, with the kinetic energy gained through this process, these atoms move deeper into the material and spread the energy throughout the material, dislodging atoms as it goes, until the energy is dissipated so that no more atoms can be dislodged (Rossnagel, 2003). During this collisional process, atoms near the surface can become dislodged with sufficient energy to overcome the binding forces in the target and be emitted from the surface. Sputter deposition occurs when these atoms deposit on the surface of the sample (Rossnagel, 2003). In our case, this would be when the palladium atoms have been emitted from the palladium target by the argon ions and then condensed on the surface of the Kapton to form the thin palladium coating.

The samples for testing the design of the ODIE detector were constructed of Dupont Kapton HN (referred to as Kapton herein) coated with palladium. The coaters used in coating our samples were the Quorom Technologies Ltd Q150T ES and Q150V Plus which operated similarly to one another. The Q150TS ES is shown in Figure 2.1. The Q150V Plus was acquired after the Q150TS ES developed a fault and could no longer effectively evacuate the target chamber thus preventing sputtering from occurring.

Figure 2.1. Image of the Quorum Technologies Q150T ES sputter coater with the lid of the target chamber opened.

Prior to coating, the samples were prepared for coating by cutting the Kapton to the same size as the photographic slides they will be mounted on, 3 x 4 cm. The edges of the Kapton rectangles were then rimmed with copper tape to aid with handling (Figure 2.2). To prevent the foil moving when experiencing a vacuum, the foil was held to the photographic slide with rubber bands. Mounting the foils this way ensured a flat surface was maintained throughout the coating process and thus optimal palladium deposition occurred.
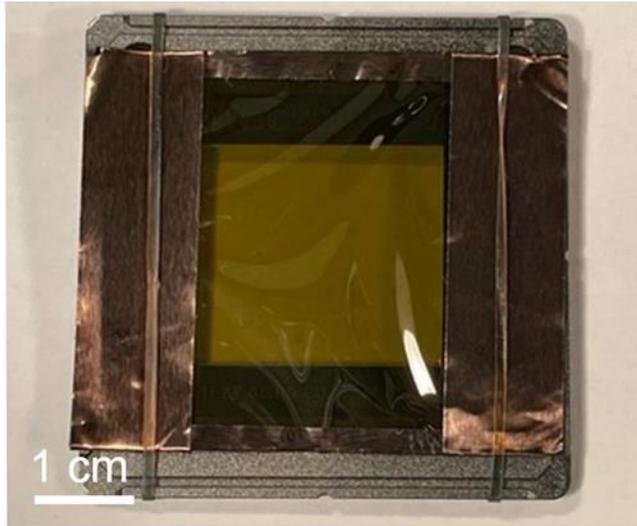
Figure 2.2. Kapton foil with a copper tape edge held down with rubber bands in preparation for coating.

The sputter coater was set up such that the material information on palladium was saved and the only change required was to change the coating thickness when needed. Different coating thicknesses were applied; 10 nm, 20 nm, 25 nm, 30 nm, 40 nm, 50 nm, 75 nm and 100 nm. The coatings were examined for uniformity and defects on the surfaces by SEM prior to impacting or exposing to atomic oxygen.

2.2 Impact Experiments Using the Two-Stage Light Gas Gun

Experiments which are analogous to impacts in LEO are conducted in many different ways. Van de Graff accelerators can accelerate charged particles to speeds of 90 km/s or more (Burchell et al., 1999). The particles are placed in a chamber and the accelerator initiates a charge that accelerates the particles. This method can achieve high velocity impacts but only works with charged particles that are small dust, typically much less than a millimetre which would not be appropriate for our investigation. Light gas guns (LGGs) are more commonplace recently with maximum speeds around 13 km/s (Rogers et al., 2022). LGGs can accelerate larger and uncharged particles to hypervelocity speeds. Each of these methods have their benefits and drawbacks and for our investigation we require particles up to 1 mm in size so for that reason and also the availability of instrumentation we used a LGG for this study.

The velocity of the projectile shot by the LGG is dependent of the velocity of expansion of the light gas used and, therefore the velocity can be chosen using specific combinations of pressure and temperature of the gas. For the two-stage LGG, the gas is compressed by a piston that is accelerated by igniting a propellant, in our case this would be gunpowder. The velocity is calculated using equation 2.1 where V_{max} is the maximum velocity of the projectile (m/s), γ represents the specific heat ratio of the gas used, P is the gas pressure (Pa) and ρ is the density of the gas (kg/m^3) (Doolan 2018).

$$V_{max} = \left(\frac{2}{\gamma - 1}\right)\sqrt{\gamma\frac{P}{\rho}}$$

Equation 2.1

From this equation, it is evident that the lowest density of gas would produce the highest velocities. Hence, the common gases used in LGG facilities are hydrogen and helium, the two lightest elements.

Hypervelocity impact experiments were conducted for this thesis using the two-stage LGG at the University of Kent, Canterbury, UK to assess the performance of the detector under hypervelocity impact (Figure 2.3 and 2.4). Following from one of the first proposed guns by Crozier and Hume (1957), LGGs have become commonplace in testing the ballistic limits of materials and for performing analogue impacts to those experienced by objects in space travelling at velocities greater than a few kilometres per second (Crozier and Hume, 1957; Kearsley et al., 2006). LGGs function off the principle of compressing a light gas and the resultant pressure ruptures a burst disk which then accelerates the projectile to higher speeds than achievable with conventional methods of acceleration such as using gunpowder alone for acceleration (Burchell et al., 1999).
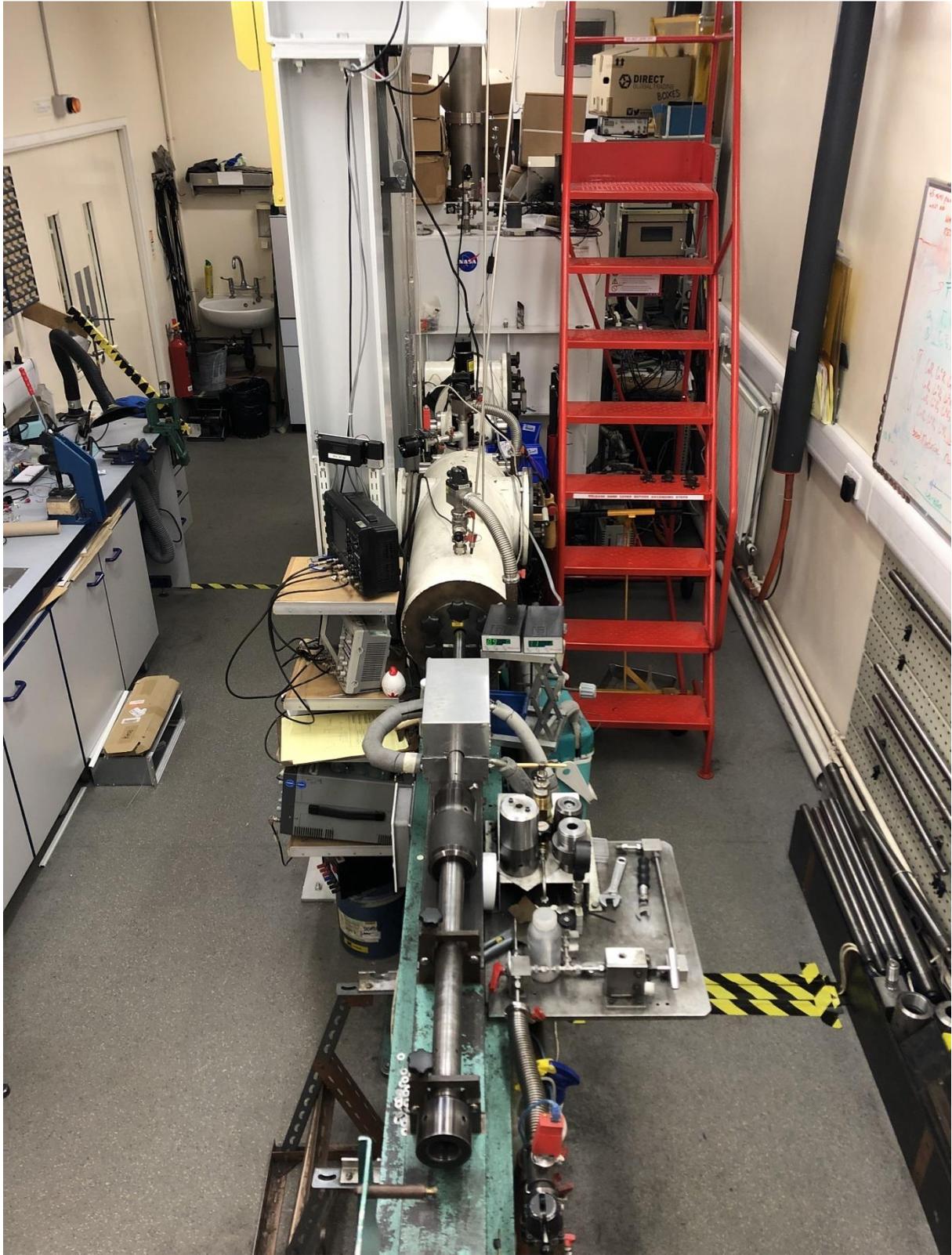
Figure 2.3. Photo of LGG at the University of Kent. The pump tube is visible as the dark grey tube in the foreground which connects to the white chamber of the blast tank and lastly, the large target chamber in the background.
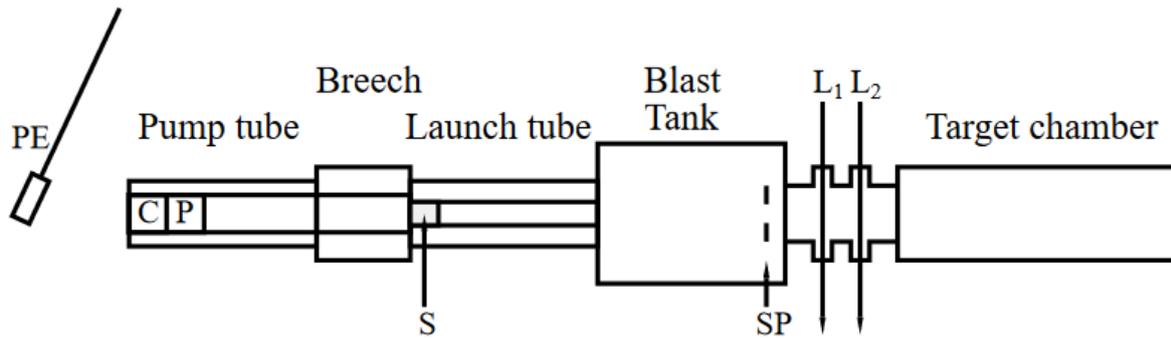
Figure 2.4. Schematic diagram of the two-stage light gas gun with the pendulum (PE), cartridge (C), piston (P), sabot (S), stop plate (SP) and lasers (L₁ and L₂) (Burchell et al., 1999). The targets for our investigations were placed in the blast tank.

The general operation of this facility can be described as follows: The projectiles are loaded into a split sabot, this is a hollow cylinder comprised of four sections which is filled with the projectiles. The targets are placed in a target holder and are typically placed in the target chamber, which is sealed along with the rest of the gun for shooting. The process of shooting the gun begins with evacuation of the entire assembly to a vacuum of typically 0.5 mbar. Following this, the light gas, generally hydrogen, helium or nitrogen, is pumped into the pump tube. The choice of gas is dependent on the desired velocity as the velocity of the expansion of the compressed gas is proportional to the inverse of the square root of the mean relative molecular mass of the gas, hence the lighter the gas the higher the possible velocity (Burchell et al., 1999). For the single stage configuration, the gas is injected continuously such that it is compressed to the point of breaching the burst disk, ultimately accelerating the sabot located on the other side. In the case of the two stage configuration, the compression of the gas is achieved using a piston accelerated by a gun cartridge. A pendulum is dropped such that it impacts the firing pin of the cartridge, igniting the gunpowder contained within the cartridge which accelerates the piston to compress the gas in the pump tube. This then initiates the burst disk to rupture and the sabot is accelerated in the launch tube, splitting as it travels to expose the projectile inside (Schneider and Schäfer, 2001). Splitting of the sabot is necessary so that only the projectile impacts the target. In order to achieve this the sabot is comprised of four separate sections that slot together leaving space for the projectile inside. Due to the rifling of the barrel, a technique that induces a spin on the sabot, this causes the sabot sections to separate and these sections of the sabot impact the stop plate at the exit of the blast tank with the projectile continuing on down the gun to reach the target chamber. The speed of the projectile is determined using two light gates which detect the sabot as it travels along the gun and this

signal, displayed on an oscilloscope, is used to calculate the projectile velocity with a typical error of 5%.

Both the single-stage and two-stage configurations of the LGG were used in this work in order to perform impact experiments at both 1 and 5 km/s. Although the target to be impacted is generally placed within the target chamber, for the shots of this thesis, the target was instead placed in the blast tank (Figure 2.5). The blast tank generally produces the least amount of excess shot residue on the target which is optimal for our purposes of examining impacts that are solely from the projectiles and not from any other source within the gun. When using particularly small projectiles, there is a higher likelihood that they would miss the target or go missing the farther the projectile has to travel along the barrel hence the target is placed in the blast tank to mitigate this risk. As the blast tank was the mounting location, the main time of flight system was unable to be used and thus, speed measurements were taken using the secondary muzzle laser and exit aperture PVDF sensor system. The changes in the target mounting locations also necessitated a corresponding change in the separation of the two detectors from 0.8475 m (as described in Burchell et al. (1999)) to 0.6595 m to enable the mounting of the target behind the exit aperture. Therefore the errors in speeds are slightly above those stated at ±5%.
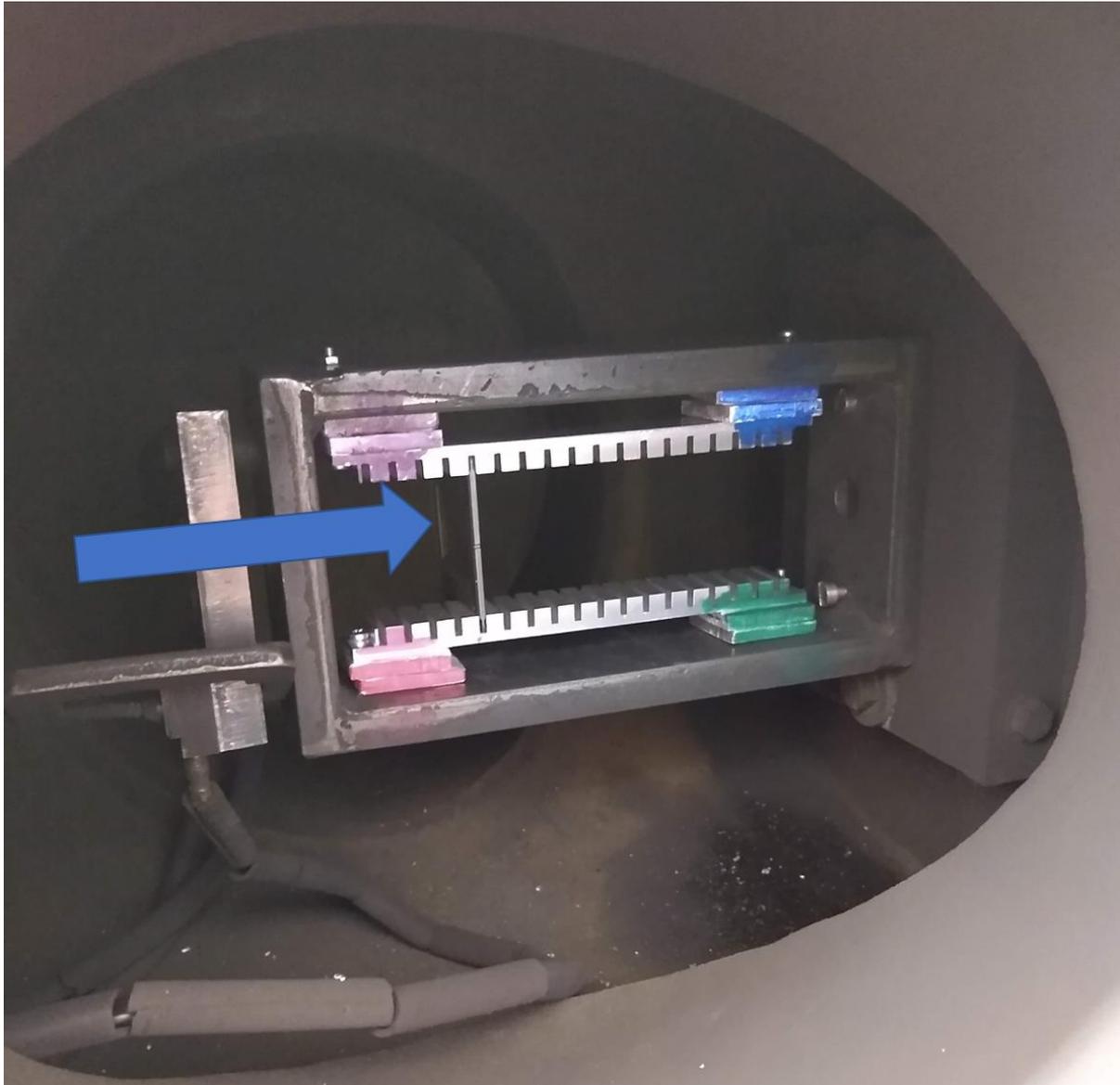
Figure 2.5. The target holder placed in the blast tank. The blue arrow depicts the direction of travel of the projectiles and points to where the target is placed in the holder.

The LGG at the University of Kent is capable of shooting single solid projectiles up to 3 mm in diameter or a buckshot comprised of many small projectiles, typically in a powder form (Burchell et al., 1999). For our purposes, we used the buckshot option to maximise the variety of compositions and sizes we could shoot in a single shot for efficiency. A projectile mix was produced comprising several monodisperse components that are analogues for MMs or OD: 1 ± 0.005 mm basalt (MM), 108 ± 0.2 µm soda lime glass (MM), 50 ± 1 µm molybdenum (OD) and 7 ± 0.5 µm silica (MM) (Figure 2.6). Details of all shots performed for this thesis are provided in the Appendix.
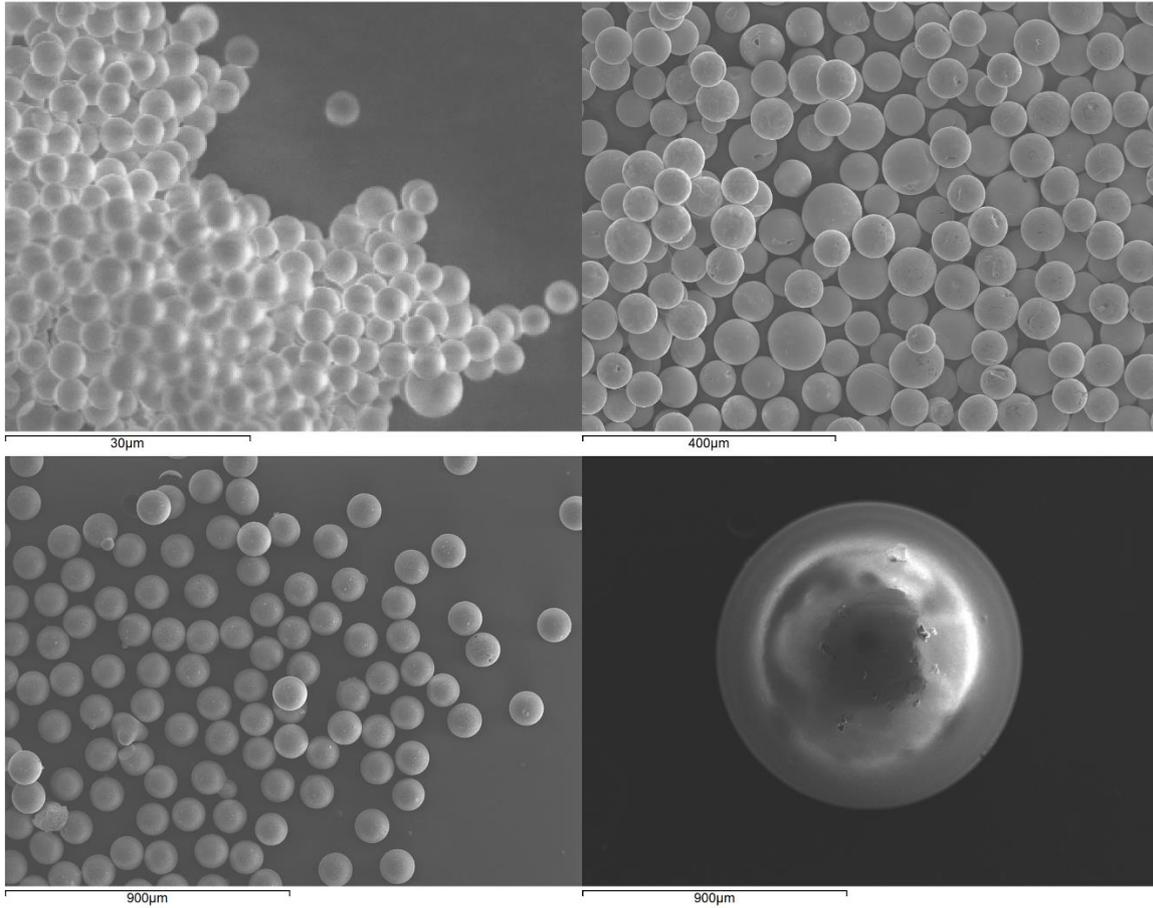
Figure 2.6. Projectile mix of 7 ± 0.5 μm silica (upper left), molybdenum 50 ± 1 μm (upper right), 108 ± 0.2 μm soda lime glass (lower left) and 1 ± 0.005 mm basalt (lower right).

This mix was placed in the sabot with the 1 mm basalt sphere holding the powder in place in the sabot. The monodisperse nature of each projectile, and substantial gap in sizes between projectile types was chosen to ensure impact features could be ascribed to an individual projectile type based solely on the impact feature size. Although it is noted in the SEM images of Figure 2.6 that there is a broad variations in the size ranges for some of the projectiles and irregularities in the projectiles shapes are also evident.

2.3 Low Earth Orbit (Atomic) Oxygen Space Environment Simulation Facility (LEOX)

The LEOX facility at the European Space Research and Technology Centre (ESTEC) was used for testing the level of protection provided by palladium to the Kapton of the samples. A high density oxygen plasma is created and the thermal energy contained within is converted to kinetic energy, accelerating the atomic oxygen which is directed at the target (Tighe 2010).

Before and after the test the mass was measured, optical and SEM images were taken and thermos-optical properties were measured. An average atomic oxygen fluence of 2×10^{21} atoms/cm^2 is targeted in the tests with the fluence measured by evaluating Kapton witness plates that are additionally placed in multiple locations in the sample holder.

The experiments were run remotely by the team at ESTEC due to COVID restrictions. The samples to be tested were made similarly to those for the gun shots but were cut to a smaller size to fit in the sample holder (Figure 2.7). All of these samples were 25 µm thick Kapton coated with different thicknesses of palladium coating: 0 nm, 10 nm, 25 nm, 50 nm, 75 nm and 100 nm with an additional 10 nm coated sample that had been shot at 5 km/s prior to exposure. This was to determine the effects of atomic oxygen on the foil after impacts have disturbed the palladium coating.
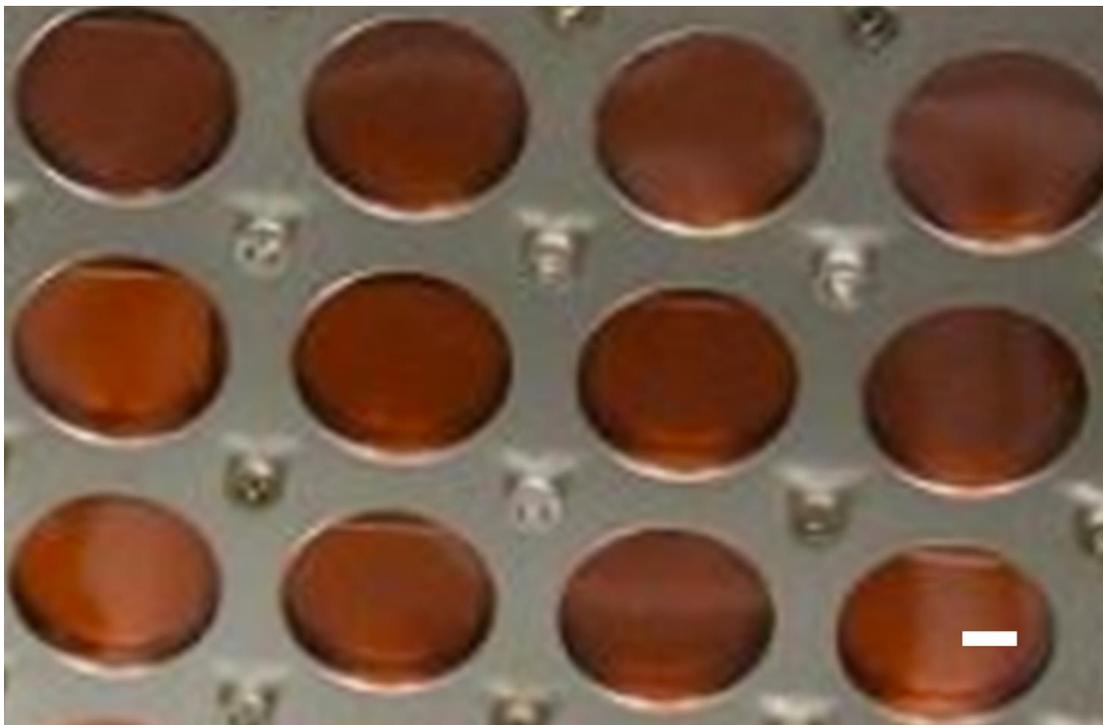
Figure 2.7. Section of the ATOX facility sample holder showing a circular region of each sample for exposure to atomic oxygen. Scalebar represents 0.5 cm.

2.4 Sample Analysis by Scanning Electron Microscopy

Impacted and atomic oxygen exposed samples were analysed by Scanning Electron Microscopy (SEM). Used in many post-retrieval studies of impacted surfaces (e.g. HST solar arrays (Kearsley et al., 2005), EURECA solar arrays (Herbert et al., 1997)) SEM is a common analytical technique applied to the categorisation of hypervelocity impact craters due to its imaging capabilities at sub-millimetre size

scales and the ability to create maps of the elemental data present on the samples using Energy Dispersive X-ray Spectroscopy (EDX). SEM and EDX are (largely) non-destructive techniques which is of high importance for the unique and rare samples that are returned from orbit. Both of the SEMs at the University of Kent were used in this study; the Hitachi 3400N SEM with an Oxford Instruments 80 mm^2 X-max Energy Dispersive X-ray Spectrometer and the Hitachi 4700 cold field emission SEM with a Bruker X-flash Energy Dispersive X-ray Spectrometer, herein termed FEG-SEM.

Figure 2.8. Image of the Hitachi 3400N SEM with an Oxford Instruments 80 mm2 X-max Energy Dispersive X-ray Spectrometer at the University of Kent.

Figure 2.9. Image of the Hitachi 4700 cold field emission SEM with a Bruker X-flash Energy Dispersive X-ray Spectrometer at the University of Kent.

The design of an SEM is centred around the electron beam. This beam interacts with the sample in many scattering events and produces the secondary electrons (SE) and backscattered electrons (BSE) used to create images as well as X-rays used to create elemental maps.

The most common method of creating the electron beam is using a thermionic gun comprising a tungsten filament with a narrow tip that spontaneously emits thermionic electrons through heating to a temperature of 2700 K (Bogner et al., 2007). This is the source type employed by the Hitachi 3400N SEM. The width of the filament limits the resolution of the instrument, requiring as narrow a tip as possible for optimal resolution. Different lenses are used to direct the beam and these can also have an effect on the resolution of the instrument. These tungsten filaments are inexpensive and are easy to use but have the main drawback of a short lifetime, typically 100 hours (Bogner et al., 2007). The electron beam scans the sample along parallel lines (Bogner et al., 2007).

Another method of emission is using a field emission gun (FEG). This is a sharp, pointed wire that is supported by a hairpin wherein the tip the brought near to a positively biased extraction electrode

causing the emission of electrons through the quantum mechanical tunnelling process (Bogner et al., 2007). The FEG-SEM used in these studies (the Hitachi 4700) works through cold field emission; an effect created when a high electric field induces the tunnelling of electrons through the potential barrier and exit the barrier of the cathode at room temperature (Bogner et al., 2007).

When the beam interacts with a sample, the resultant electrons can be scattered in many different directions with some electrons experiencing sufficient scattering events within the sample to travel back in the direction from which they came and leave the surface of the sample, termed backscattered electrons (BSE). These electrons can carry information on the sample composition and topography (Giannuzzi et al., 2018).

The weakly bound valence electrons within the sample can be ejected by the electron beam. These ejected electrons are secondary electrons (SE) and have notably low kinetic energy. The lower kinetic energy translates to a smaller escape depth for SE rather than BSE and therefore typically only surface electrons can escape, hence it is a powerful tool for surface topography (Giannuzzi et al., 2018).
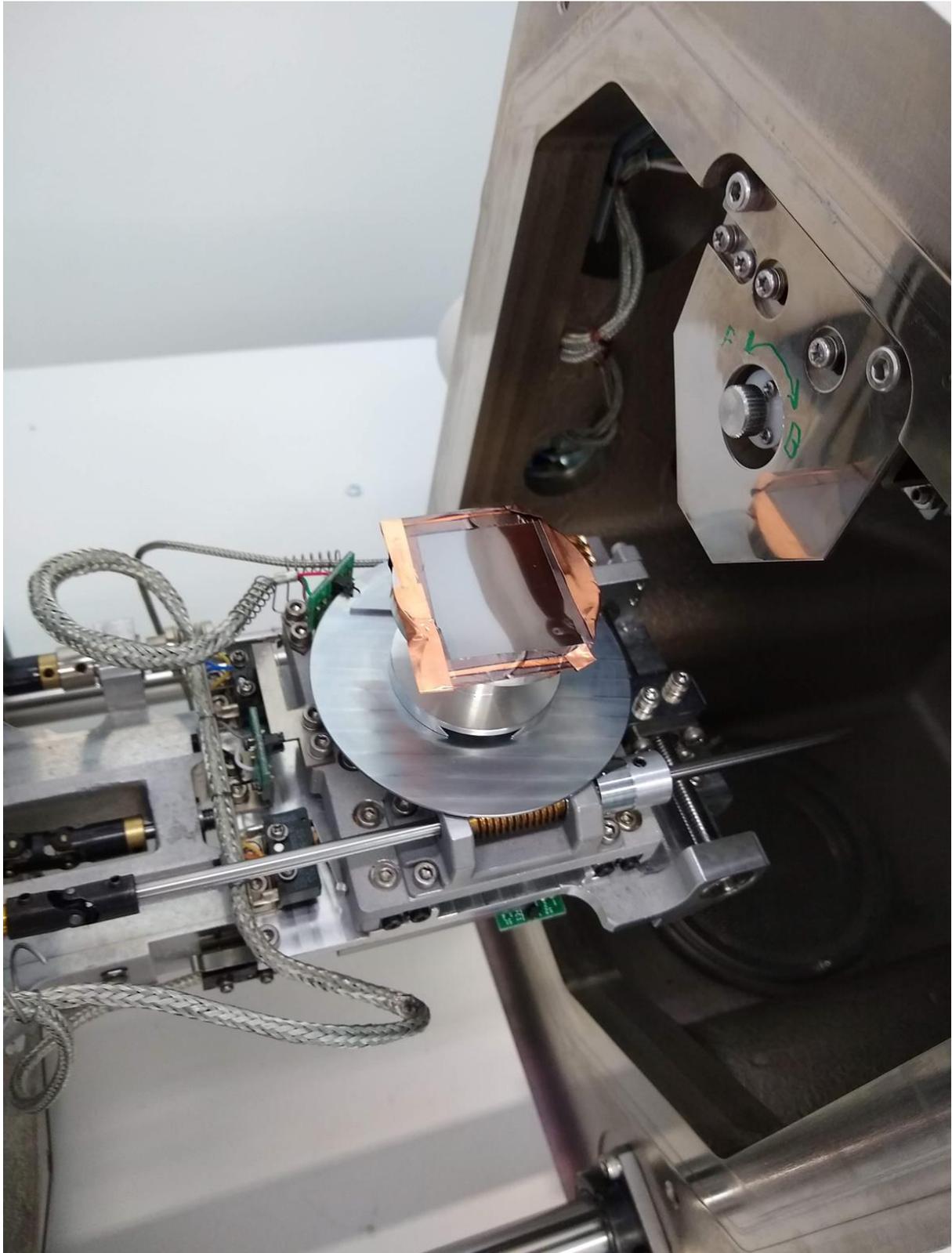
Figure 2.10. Sample mounted for SEM analysis using copper tape to hold the sample flat on an SEM stub.

For most of the studies, the accelerating voltage was set to 20 kV, the working distance was 10 mm and a dwell time of 10 µs used in SEM mode. The samples were mounted on SEM stubs using copper tape to hold the sample flat as shown in Figure 2.10. The SEM was used for imaging samples and preliminary assessment of the presence of residue although the resolution was not appropriate for the samples we had. The callipers function on the INCA software was used to measure the dimensions of impact features on the samples.

Chapter 3: Studying the Size Relationships Between Impactors and Impact Features

3.1 Introduction

The ODIE detector design aims to preserve the impact features in such a way that it will be possible to determine the size of the impacting particle from the size of the impact feature. This would be an invaluable resource in monitoring the LEO environment at small (sub-mm) size ranges to assess the modern day flux in orbit. Impact features have been studied on various space-exposed surfaces such as LDEF and SFU with difficulty arising from not having predetermined relationships between the surface materials and the impacting particles before exposure. These size relationship difficulties commonly arise as many surfaces are opportunistic returns that were not optimised for this purpose. Hence, establishing the relationship between impact feature size and original projectile size is vital for the ODIE detector before flight and is the aim of this chapter.

The measurement of impact holes is a subject that has many differing ideas with no clear consensus on a single method as every technique has individual merits for specific materials, but may not work well for all materials. Some studies measure only the inner hole of the feature, others measure every clear distinct diameter that can be identified. The variety of measurement types and evolution of novel technologies allowing for different measurement parameters to be used creates a field that is constantly evolving and expanding capabilities without yet agreement on a standard method for feature measurement. Difficulties in the field also arise from non-ideal materials often becoming the objects of study comprised of many layers and complex materials adding extra challenges in identifying the object type and origin. Before studying the size relationships between impactor and impact feature here, we must consider these different method and choose those most appropriate for Kapton foils.

Hörz et al. (1995) measured impact features on Teflon through a series of hypervelocity impact experiments firing 3.175 mm soda lime glass impactors at a wide range of velocities. The location chosen for measuring the features created was the inner hole of the impact feature (D_h shown in Figure 3.1). The difficulty with this method is that Teflon is observed to fray at the edges of the impact features and hence the measured diameters of the inner hole exhibit large variations (Hörz et al., 1994). This ragged edge also led to different measurements being obtained by different measurement operators with a substantial difference of 15% between operators (Hörz et al., 1994). It was also not taken into account that these frayed edges could potentially change position during analysis by SEM as they are not rigidly fixed to the same locations in the hole.
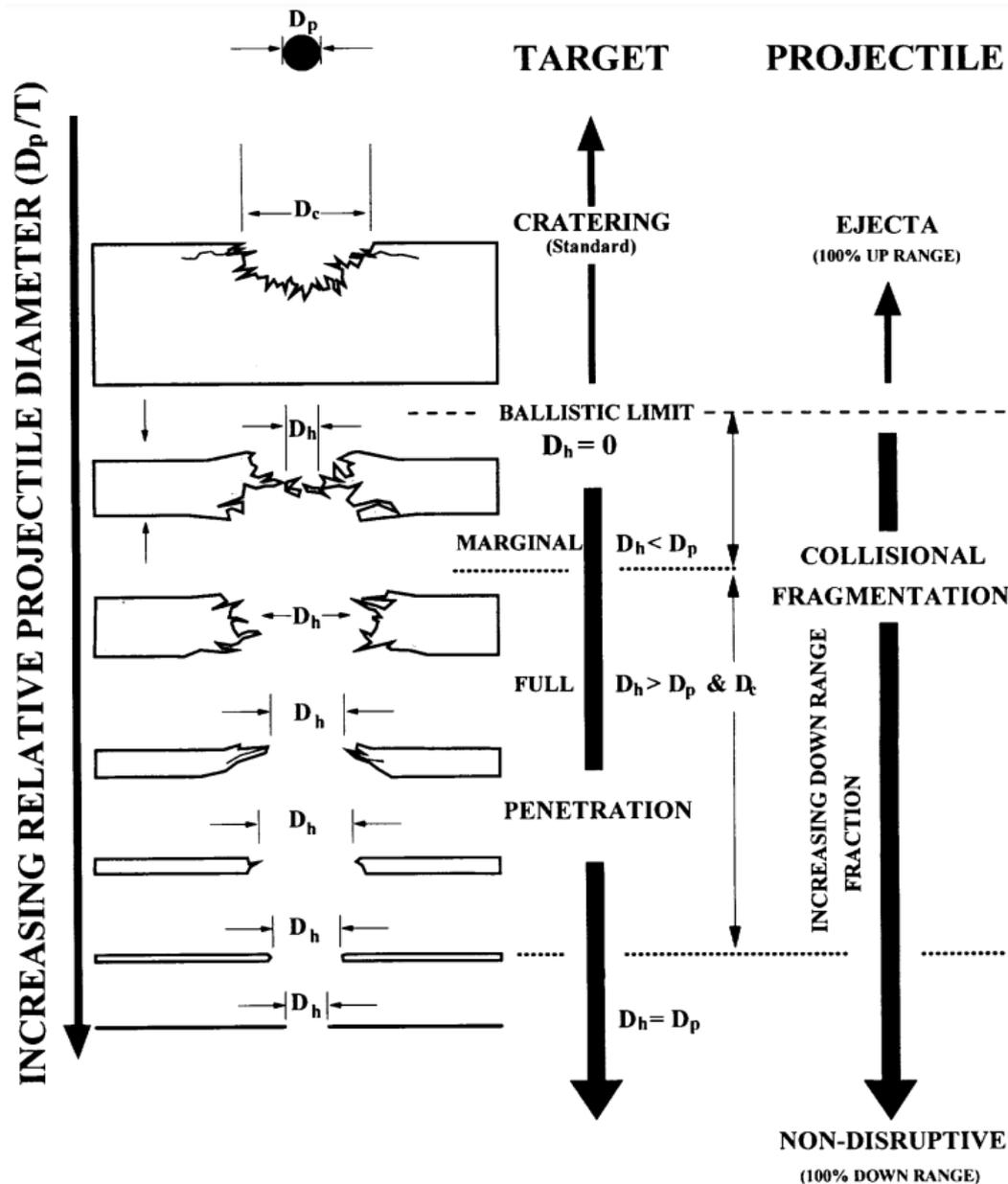
Figure 3.1. Measurement locations adopted by Hörz et al. (1995). The diameter of the hole, D_H, is shown for different film thicknesses and penetration depths.

Following on from the Hörz et al. (1995) study, Neish and Kibe (2001) performed similar experiments with aluminised Kapton MLI and silverised Teflon as targets to compare to and calibrate the materials present on the SFU (Neish and Kibe, 2001). The aluminium coating on the 75 µm Kapton was applied on the back surface of the MLI which they posited would have a negligible effect on the cratering process upon impact (Neish and Kibe, 2001). The shots used 100 µm soda lime glass projectiles shot as a buckshot for practicality and to minimise cost with a chosen speed of 5 km/s. The measurement method for this study was through tracing the edge of the impact hole and calculating the number of

pixels within this traced out area. This value of pixels was then converted into a circle which enclosed the same area. This method has the advantage of compensating for the irregularities in the frayed edges of impact holes in polymeric materials. A major drawback of this method is that it does not account for any possibility that the inner wall of the impact hole could have some frayed edges which are loose and not in fixed positions and hence do not make up part of the hole wall that was created by the impacting particle. It is also highly dependent on the consistency of the measuring operators and, as mentioned previously, errors with this can be in the range of 15%.

One study to establish diameter measurement locations by Ward and Anz-Meador (2019) analysed MLI blankets from the HST electronics bays to characterise the impact features and determine an estimate of flux. Through-holes and craters greater than 10 μm were imaged using a digital microscope to record the shape, size, depth and volume of the features. Difficulty in the identification of measurement locations was noted as the edges of the features presented no clear boundary and colour filter gels were required to aid in sharpening this boundary. Diameter measurements were taken as a radius for circular features and the minor and major axes for elliptical features. One significant observation was that the measurement locations available on the impact features changed depending on the lighting conditions. In total, six different measurement locations were identified by this team; the inner through-hole (ITH), outer through-hole (OTH), opaque erosion zone (OEZ), transmission zone (TZ), inner coating melt (ICM) and outer coating melt (OCM) (Figure 3.2). From a comparison of the returned surface to a similar test campaign with LGG impacts, it was the outer-through hole which excludes the loose, frayed edges that was identified as the most accurate measurement location on the impact features of the projectile diameter (Ward and Anz-Meador, 2019).
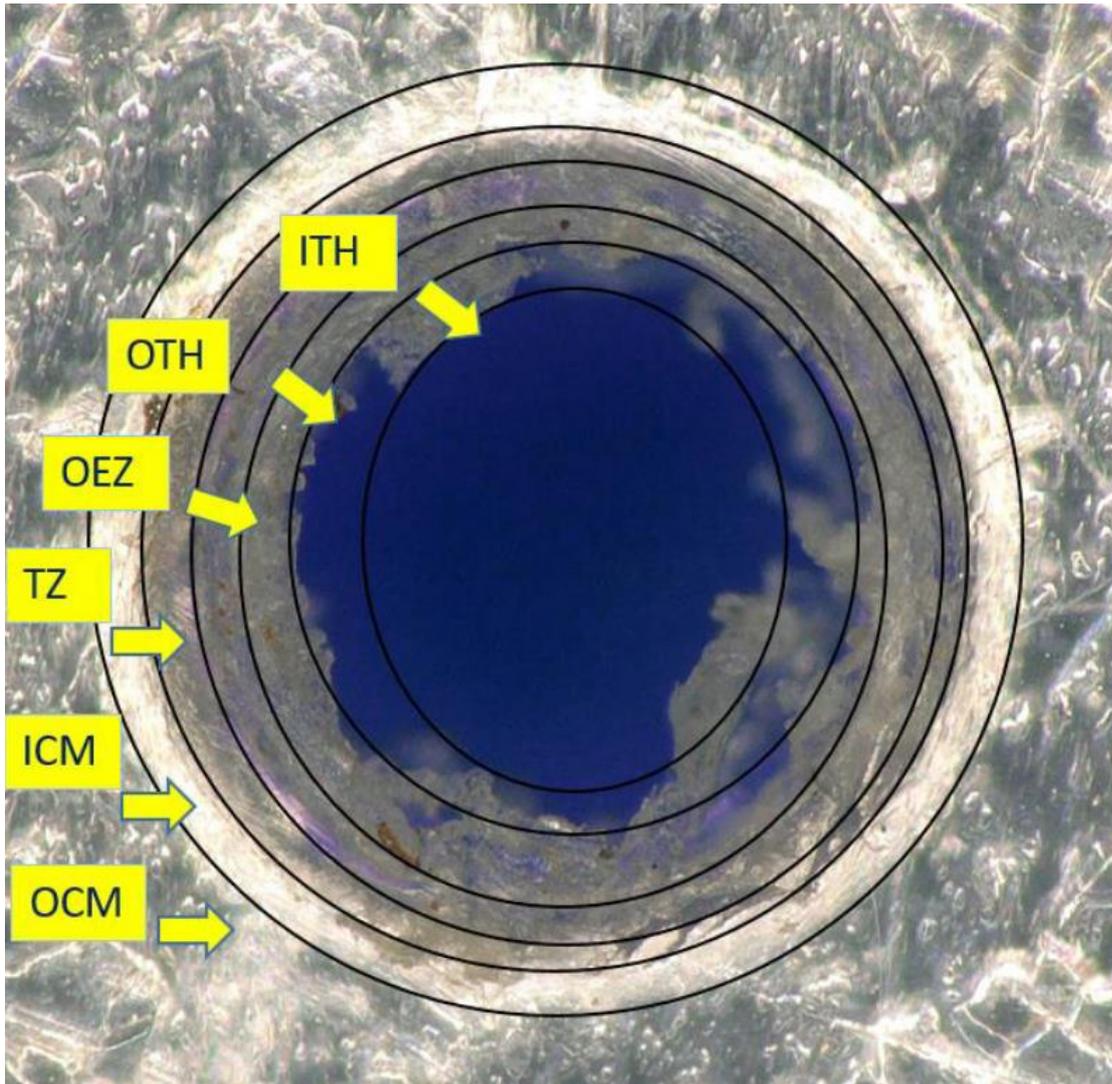
Figure 3.2. Different measurement locations identified by Ward and Anz-Meador (2019) on the impact hole. Acronyms are as follows; the inner through-hole (ITH), outer through-hole (OTH), opaque erosion zone (OEZ), transmission zone (TZ), inner coating melt (ICM) and outer coating melt (OCM). The multitude of locations were identified by any clear edges that make a continuous circle at a given location (Ward and Anz-Meador, 2019).

From these assorted studies it is clear that there is no consensus regarding measurement location for calculating the size of impact features on foils. Neither of the methods employed by Hörz et al. (1995) and, subsequently, Neish and Kibe (2001) considered that the frayed edges can move and may influence the diameter measured for the impact features. This is highlighted by Ward and Anz-Meador (2019) as they noted that the inner through-hole (ITH), the location the other studies used for measurements, was not the most reliable location. Indeed they found the outer through-hole (OTH), which would account for the small, frayed pieces not having a major effect, to be the most accurate location for measurement of the diameter).

A previous study of impact feature dimensions into aluminium by Kearsley et al. (2006) highlights that choosing the location for measuring the impact feature diameter presents an interpretive hurdle in the study and comparison of impact feature dimensions (Kearsley et al., 2006). Not clearly defining the feature dimension measurements to be taken causes complications in the reproducibility of data as it is left largely up to the interpretation of the individuals as to the positions of the start and end of the crater. They can appear ambiguous, especially when studied by SEM, as the depth of focus, which is normally viewed as an advantage of SEM, can make it problematic to determine a precise boundary between the sample surface and that of the inner slope of the impact feature (Kearsley et al., 2006). They suggest choosing the crest of the lip of the impact feature, be it a crater or hole, as the measurement location as this morphological feature is easily identifiable with SEM as the curvature of the lip makes it bright and ensures reproducibility across many observations. This top lip is taken as the highest point on the feature, as though a flat surface were placed atop the feature, and the points where it touches the lips are to be taken as the measurement locations (Fig 3).
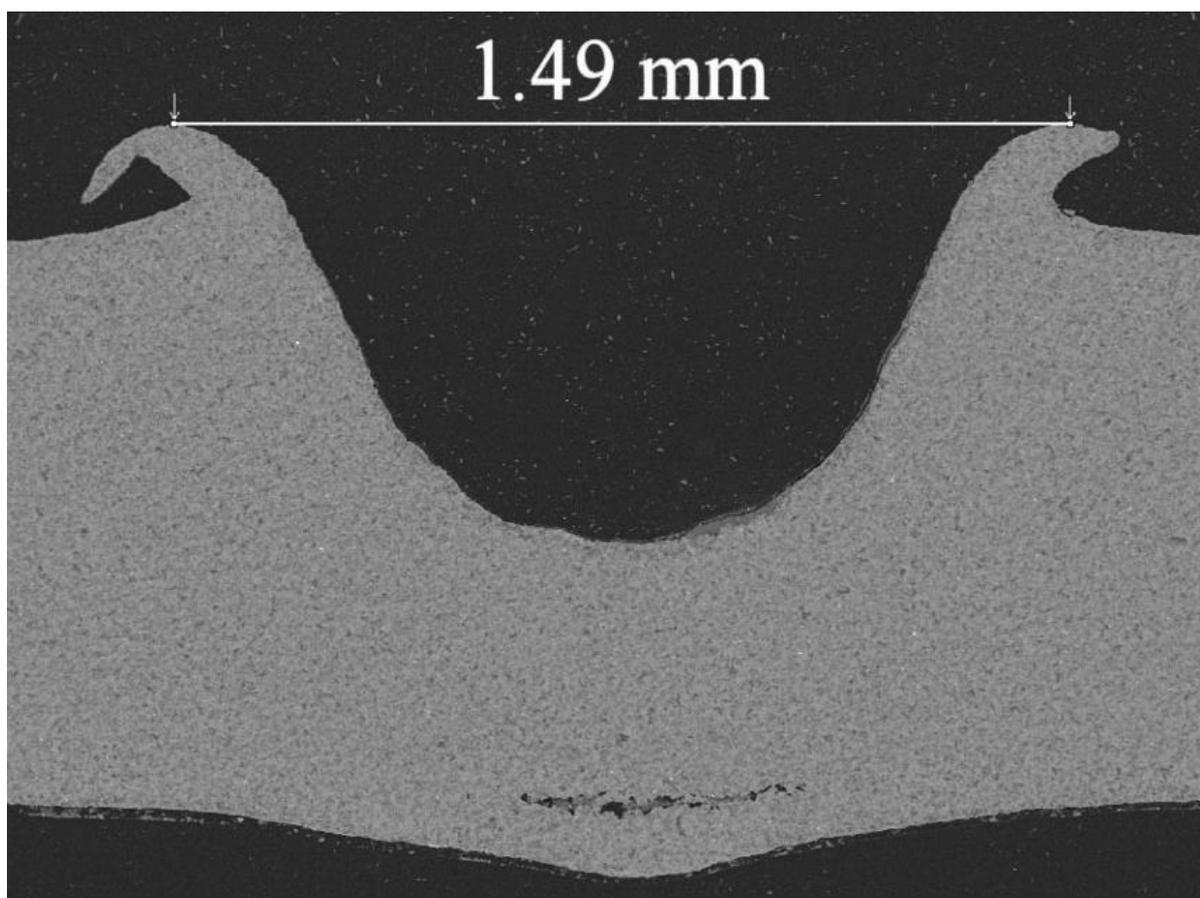
Figure 3.3. Example measurement location from Kearsley et al. (2006) where the highest point of the lip of the impact feature is taken as the position to measure. This was chosen as it was considered an easily identifiable position with SEM (Kearsley et al., 2006).

In our study, we investigate different measurement locations on the impact features created through hypervelocity impact experiments. As Teflon is similar to Kapton in density and composition, all the previous studies mentioned which are primarily based on Teflon are comparable to the outcome of impacts on Kapton. The aforementioned investigations conclude that the outer through-hole has proven to be the most accurate measurement when compared with similar hypervelocity impact experiments. However, reproducing these exact measurements is severely limited by the subjective nature of determining the measurement locations. Hence, it was also necessary to consider the method proposed by Kearsley et al. (2006) of measuring the top of the impact feature lip with SEM with emphasis on reproducibility in this study, although their experiments were with aluminium. Both locations, the outer through-hole and lip, are found to be the most suitable measurement locations to consider when calibrating detector materials for the purpose of impact feature size measurement and, hence, were chosen as the locations for our study.

3.2. Method

In optimising the design of ODIE the material thicknesses play a key role in the calibration of the detector. Choosing the thicknesses of the Kapton substrate and palladium coating for preserving impact feature size is a key factor in this investigation and so the experimental design is based on determining the optimal thicknesses of materials. The different thicknesses of Kapton to be investigated (13 µm, 25 µm, 75 µm, 125 µm) were chosen primarily due to availability but also to determine the optimum front foil thickness (the thickness for which the relation between impactor size and impact feature is most consistent between features) for the detector design. The different thicknesses of palladium (10 nm, 20 nm, 30 nm, 40 nm, 50 nm, 100 nm) used were to assess whether this novel coating had any apparent effect on the impact feature size, or ability to measure it, as it is to be the protective coating for the detector.

The various thicknesses of Kapton were cut to the required size for the photographic slide holders and then coated. These foils were then shot at 1 km/s and 5 km/s with the buckshot of projectiles described in Chapter 2. The foils were then removed from the LGG and analysed by SEM.

Firstly, a map was taken of the foil surface with the INCA montage feature to use as a reference for the impact feature locations on the foil (e.g. Figure 3.4). The region of impacts on each foil was roughly circular and was typically concentrated over an area a little over 1 cm in diameter. Time constraints, combined with issues pertaining to the behaviour of the projectiles (clumping, see later section 3.3) resulted in our focus on the fate of the larger, 108 ± 0.2 µm glass projectiles. The diameters of up to 100 impact features over 80 µm in diameter were then measured on the pre-defined diameter

measurement locations, although for the 1 km/s shots the largest diameter population of features was measured which included features smaller than 80 µm, whilst marking the feature positions on the map as in Figure 4. Only features that were predominately circular (did not have multiple lobes indicative of impact by multiple or non-circular – possibly broken - impactors) in shape were measured.
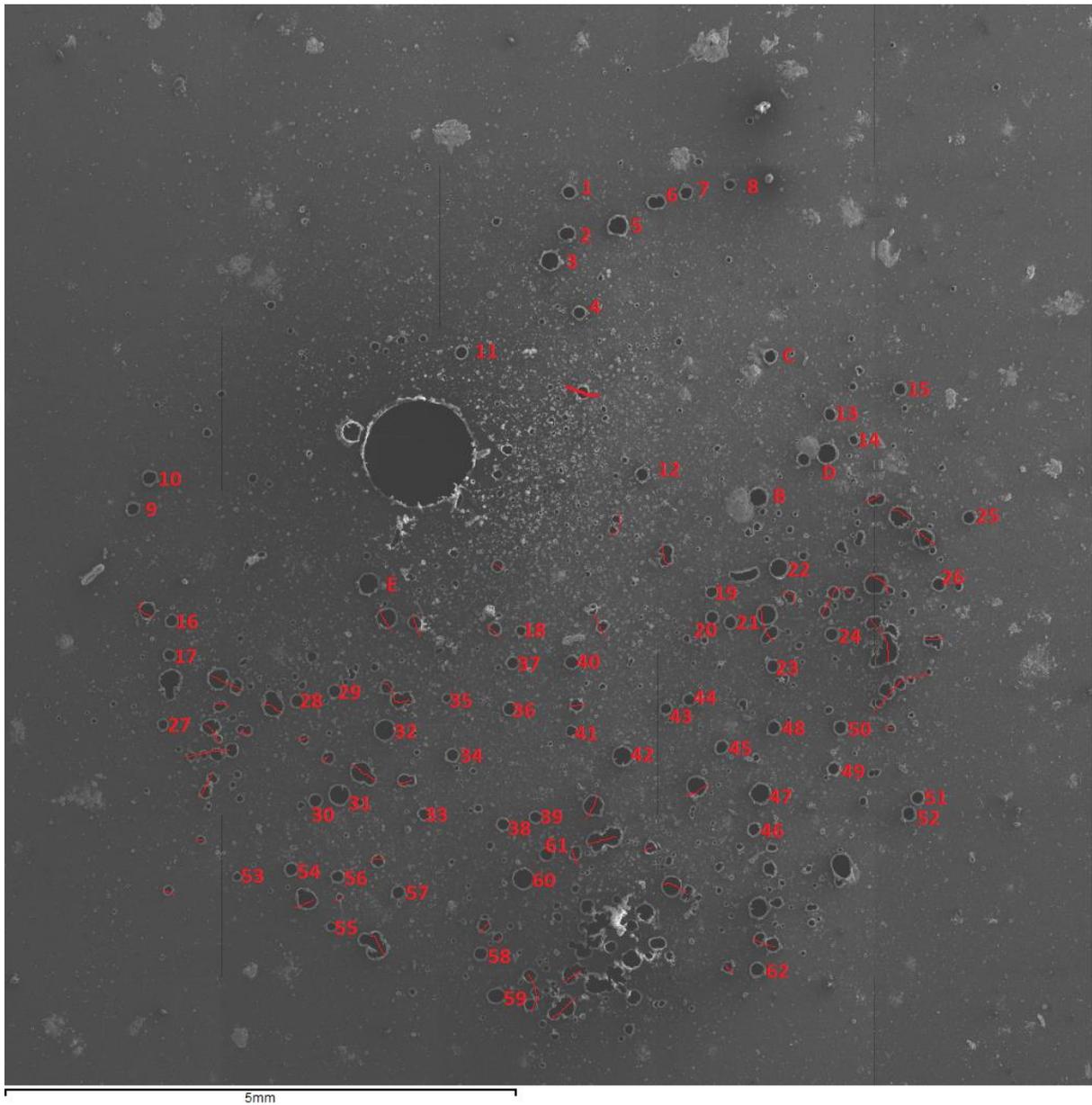
Figure 3.4. Tracking the locations of the impact features on the map created of the foil post-impact. This is the 50 nm palladium coated 25 µm Kapton shot at approximately 5 km/s with a total of 62 features measured.

The diameter measurements were taken at the two previously defined locations, with the outer through-hole (hole) being measured in all cases, and the highest point on the lip (rim) if present. For each measurement location the diameter was measured three times in an attempt to minimise the human error in assessing the precise locations to take the measurement from. This method was suggested by Kearsley et al. (2006) to measure the diameters 60° apart in the case of circular impactors (Kearsley et al., 2006). When the impacts were non-circular the semi-major and semi-minor axes were measured with the addition of a measurement at the midpoint between the axes to maintain consistency in having three measurements for every feature chosen.
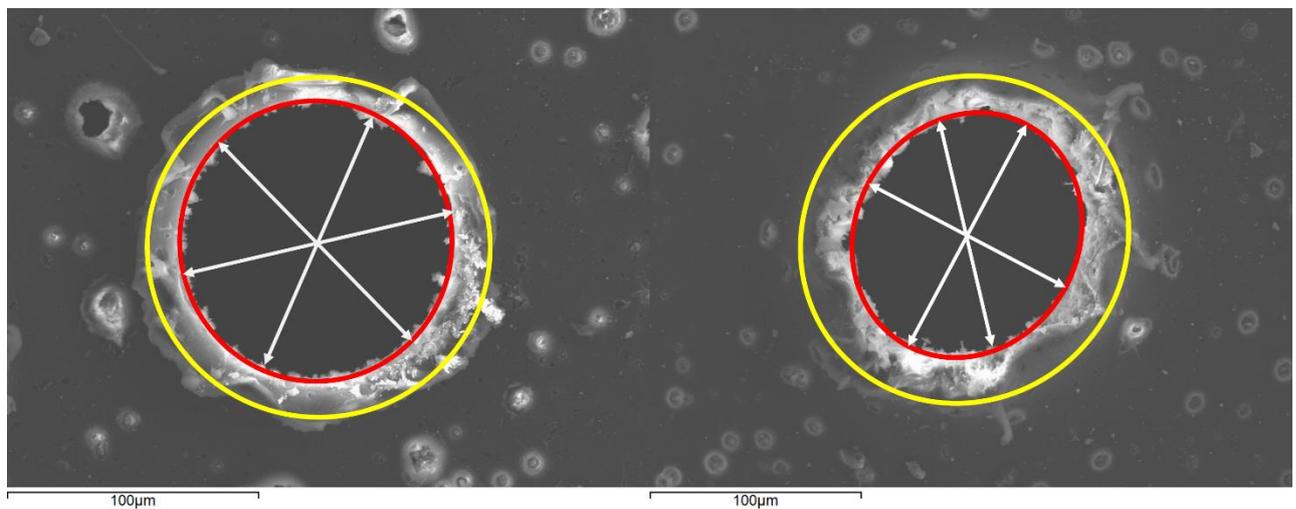
Figure 3.5. Measurement locations on circular and elliptical holes. The red outlines are the outer through hole measurement locations and the yellow outlines are the rim locations. The white arrows show example typical measurement locations. For the circular hole, the measurements are taken 60° apart for both the hole and rim measurements. For the elliptical hole, the semi-major and semi-minor axes are measured with the addition of a measurement at the midpoint between the two axes.

The three measurements of the diameters at the different locations were averaged to produce a single diameter measurement and the datasets produced were analysed using Python 3.9.

3.3 Results

The shots were performed for the majority of planned experiments with difficulties encountered with the 1 km/s shots. For this speed, the single stage LGG is used and presented challenges with the buckshot projectile not reaching the speed required. Many shots had to be repeated as a result of the shots either not having projectiles impact the target or the speeds being much lower than 1 km/s. Due

to limited (time) access to the palladium coaters, the suite of foils were prepared (cut and coated) for these experiments in advance with a number of spare foils produced for each coating and foil thickness combination being studied should there be failed shots. For the 50 nm and 100 nm coated 25 µm foils, the number of failed shots meant that we were unable to get a suitable sample produced at 1 km/s and thus there are gaps in our sample set for these parameters.

Upon initial inspection of the foils, a diameter was identified in BSE as the "halo" around the impact feature. This location was where the palladium coating stopped and could be clearly identified as in BSE the palladium shows up very bright in comparison to the Kapton as in Figure 3.6. This created a potential measurement location on the foils that would be easily identifiable and reproducible, but this BSE palladium halo was not visible on all thicknesses of Kapton and at both 1 and 5 km/s and therefore it was deemed unusable for ODIE as there was no consistency for this location.
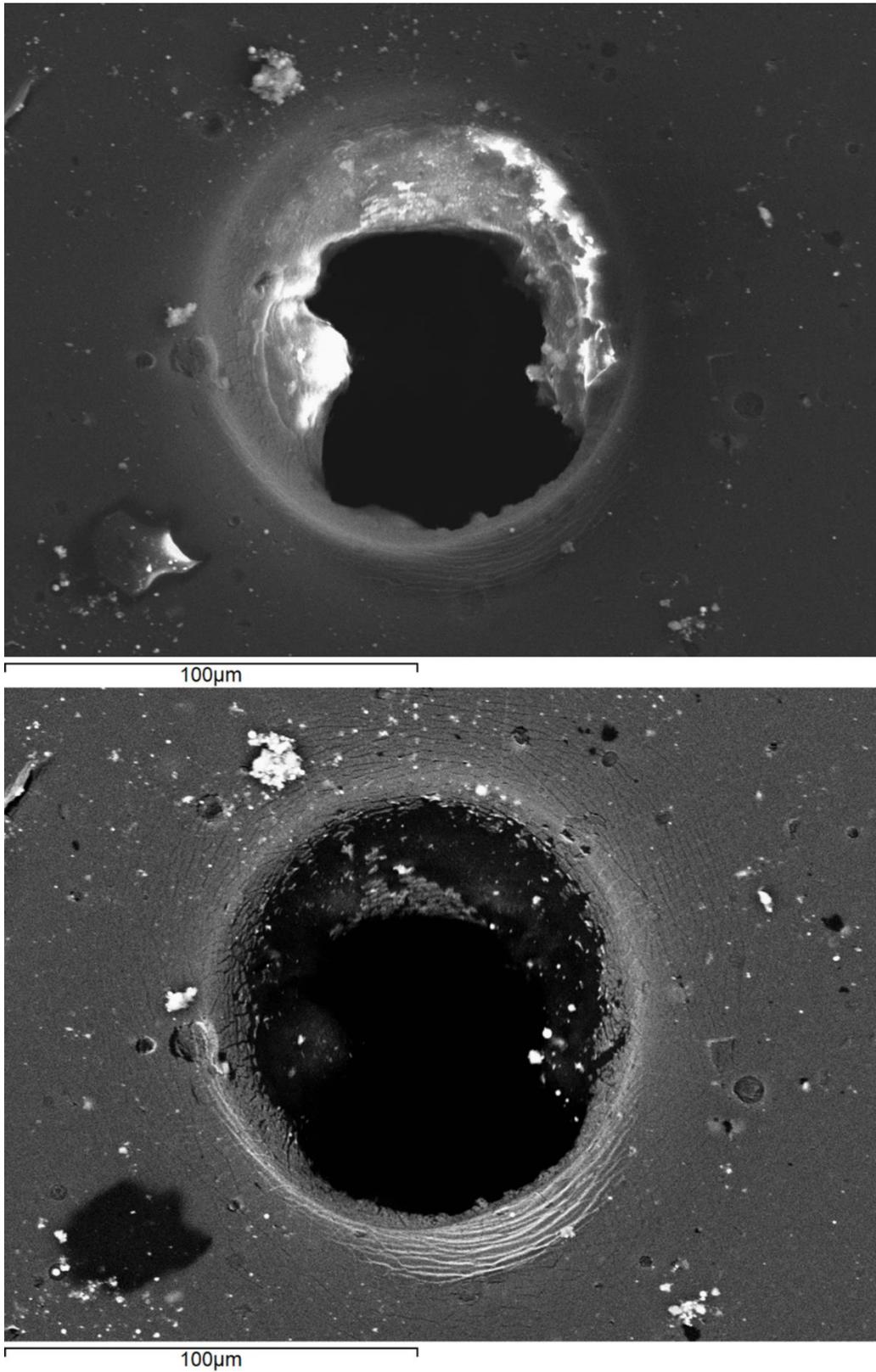
Figure 3.6. Impact on the 25 µm Kapton foil coated with 30 nm of palladium shot at 1 km/s. The top image is an SEM image of the hole and the predefined hole measurement location can be identified. The bottom image shows the palladium coating around the edges which can be seen to be cracking.

The following description of results is split into two sections: the results of impact into different thickness of Kapton foils and the results of impact into different thicknesses of palladium coatings. The aim of shooting the different thicknesses of Kapton is to elucidate the optimal front foil thickness for the detector, that is, the foil which has the best (constrained) relationship between the size of the impact feature and the projectile. Following on from this, the next section aims to address if changing the coating thickness has an impact on this relationship (either by directly affecting the size of impact feature formed, or ability to perform measurements and obtain accurate dimensions). By the end of these sections, it should be possible to present a recommendation on the front foil size and the thickness of palladium coating to be applied to said foil, creating the optimum configuration for preserving feature size and establishing a potential size for the impacting particle.

3.3.1. Results: Different Thickness Foils

The front foil of the ODIE detector has the role of preserving the impact feature size so that it can be related to the size of the original impactor. In this section, the morphology of the impact feature as well as the impactor size and impact feature size relationship are explored. Every foil in this section is coated with 10 nm of palladium for consistency such that only the thickness of the substrate is varied. This coating also aids analysis by SEM by ensuring the sample is conductive such that charging issues do not hamper imaging and measurements. Different thicknesses of Kapton (13 µm, 25 µm, 75 µm, 125 µm) were all successfully shot at 1 km/s and 5 km/s.

3.3.1.1. The 13 µm Kapton Foil

Initial inspection of the 13 µm foils revealed that it was not possible to investigate this thickness of foil further using the Kent LGG. This conclusion was reached as the foil tore in every shot it experienced (Figure 3.7). This appeared to be intrinsic to the foil properties itself, due to the very thin foil and a large amount of impacts, the impacts did not stay discrete and instead tore the foil leading to large areas becoming unusable for measurement. The tearing of the foil introduced curvature to the sample and exposed the Kapton beneath the coating, making it difficult to analyse with SEM as the Kapton charges. The resulting non-flat geometry of the foil made it nearly impossible to clearly measure the diameters due to the shading on the sample as well as a degree of warping was introduced to the foil by this debris cloud which may have altered the shapes and sizes of the impacts features. As noted by Ward and Anz-Meador (2019), the lighting of the impact feature is key in determining the locations for measurement.
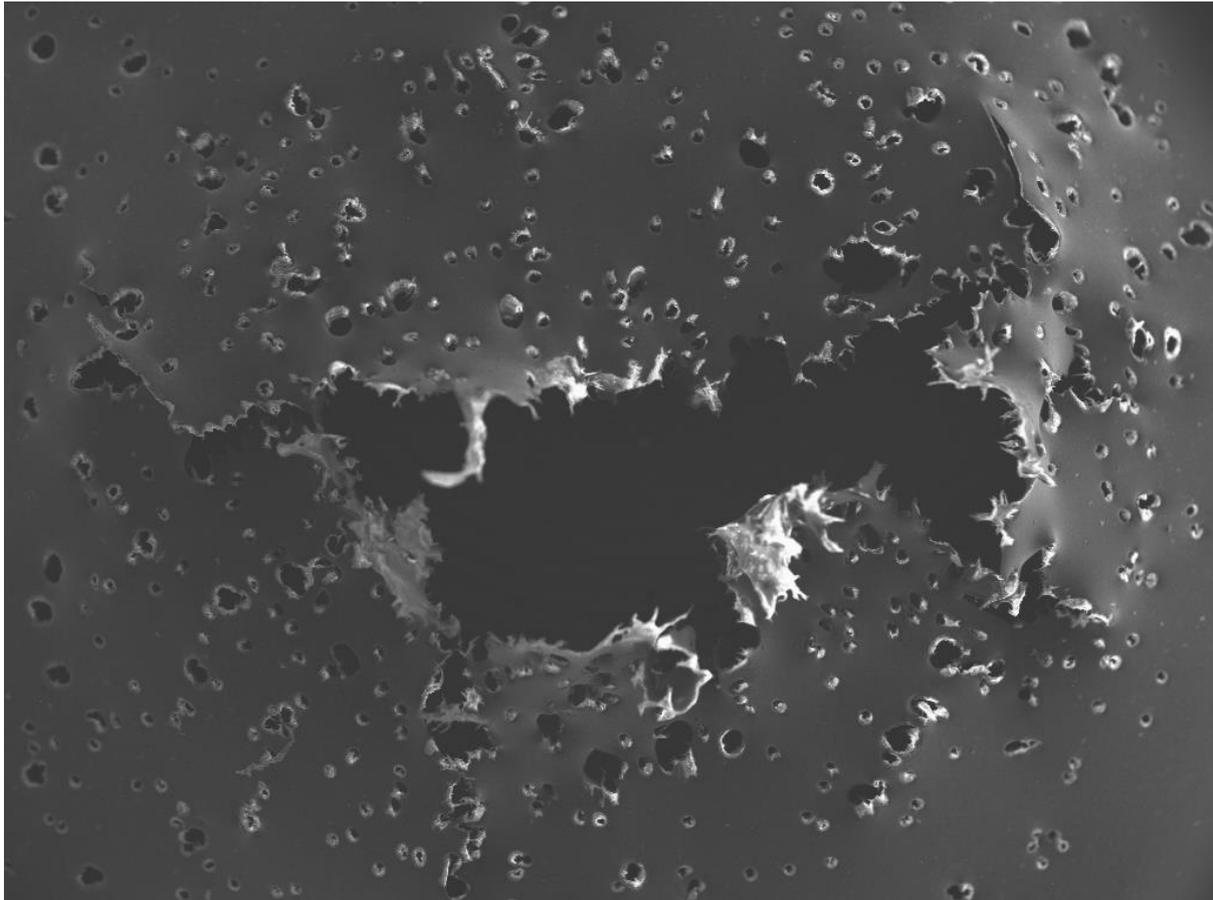
Figure 3.7. A large tear on the foil sample from a 10 nm palladium coated 13 μm Kapton foil shot at 5 km/s which spread through the multitude of impact features on the foil, making it unsuitable for measuring the impact feature size and shape.

It is likely that the tearing of the foil is due to the exceptionally high number of impacts (by both the projectile mix and gun debris) it experienced, which is much greater than expected for LEO. Despite this, the foil is difficult to work with and would be difficult to calibrate a size relationship for the impactors due to this tendency to tear. Additionally, the charging of the Kapton was not limited to the edges of the tears but also to the impact features themselves, resulting in the diameter locations being difficult to determine and measure. Thus, the suitability of a foil this thin for use on ODIE could not be tested at this time.

3.3.1.2. The 25 μm, 75 μm and 125 μm Kapton Foils

Impact features over ~80 µm in diameter were holes in all cases except for the 125 µm foil at 1 km/s. The three thickness foils considered here survived impact without significant damage beyond the site of impact, showing clear retention of the impactor shape which is promising for the ODIE detector. The impact features across the different size foils were largely similar in morphology when shot at 5 km/s (Figure 3.8). When shot at 1 km/s, this same morphology was exhibited on the 75 µm foil, however, impact features on the 25 µm foil typically presented without rims and features on the 125 µm foil often had the soda lime glass particles embed in the foil (Figure 3.8).
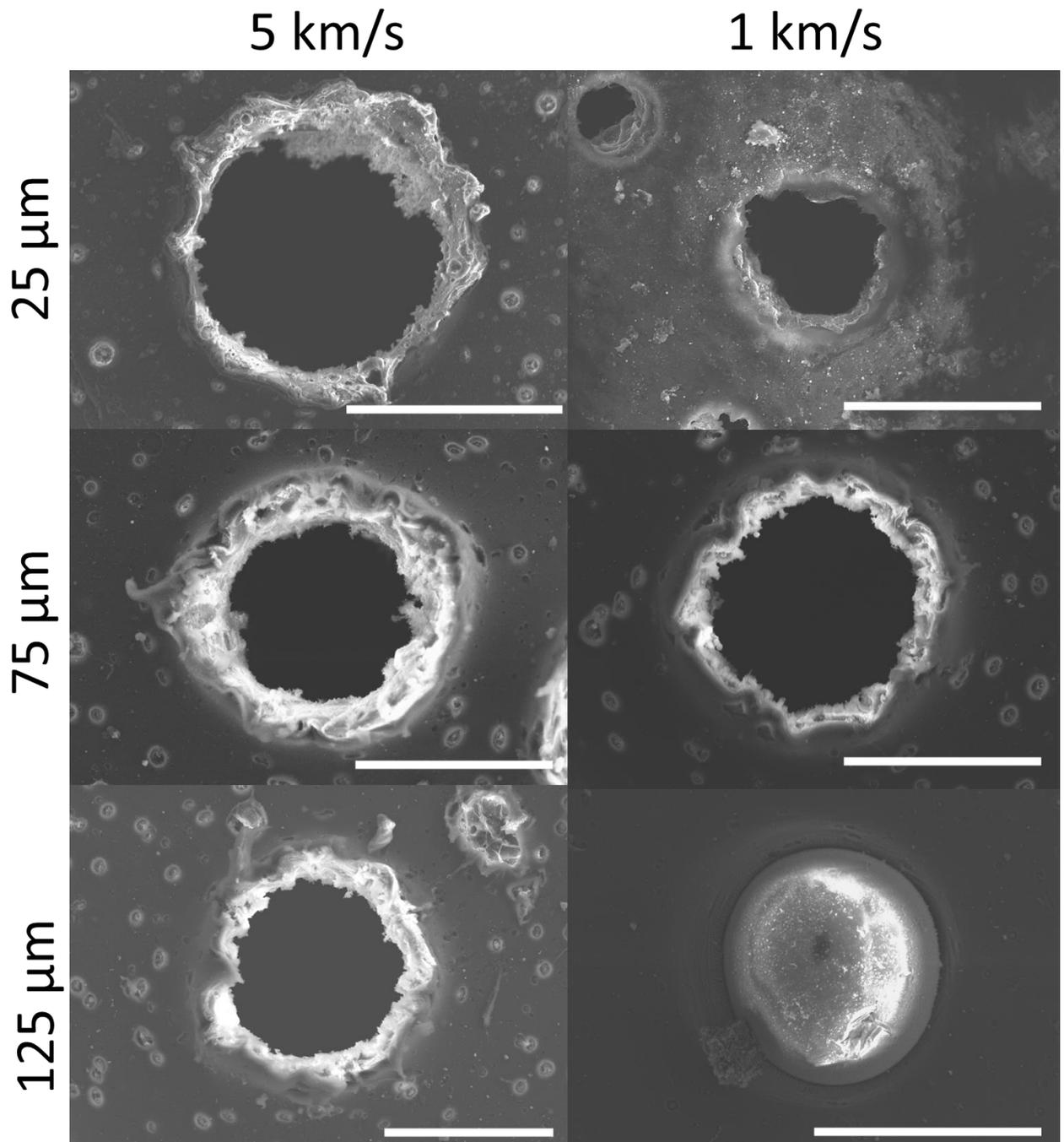
Figure 3.8. Typical craters on 25 µm, 75 µm and 125 µm shot at 1 km/s and 5 km/s. Most holes are similar except for the 125 µm foil at 1 km/s where the soda lime glass projectiles become embedded in the foil.

Despite the absence of a rim, impact features on the 25 µm foil at 1 km/s could still have their hole diameters measured using the standard convention defined earlier. The lack of rim or hole for impacts into the 125 µm foil, with embedded glass projectiles, meant that it was necessary to define a new measurement location. The interface between the impactor and foil were chosen in an attempt to

maintain consistency across the various datasets and in this case it was the red circle seen around the embedded soda lime glass (Figure 3.9). This was chosen as the equivalent to the outer through-hole as it is approximately the size of the impactor.
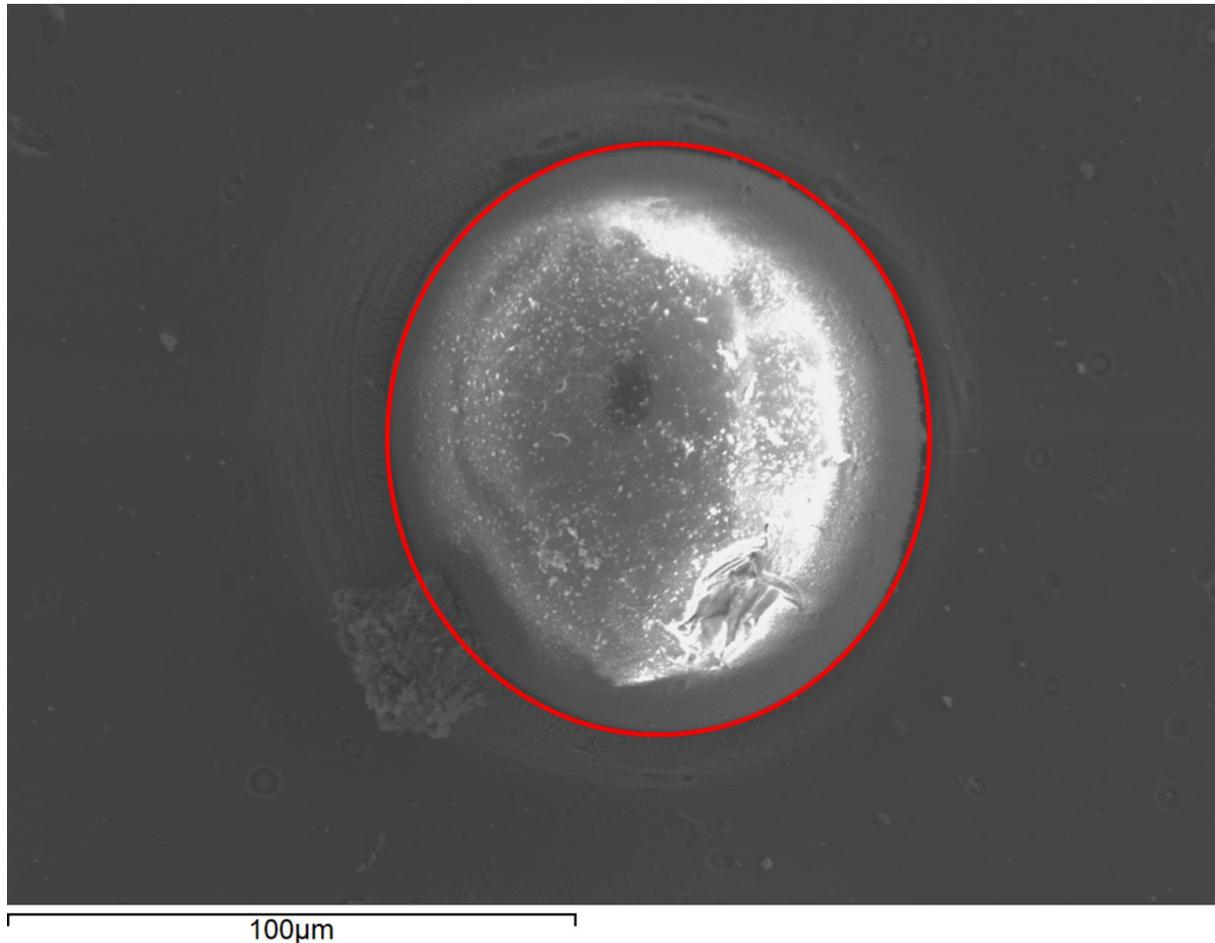
Figure 3.9. The new measurement location chosen for the impact features which had embedded projectiles on the 125 µm Kapton foil coated with 10 nm of palladium shot at 1 km/s.

3.3.1.2.1 Size Measurements

An upper limit of 100 features for measurement was introduced as not all foils showed equally large number of impacts in the predefined size range of diameters greater than 80 µm, particularly for the 1 km/s shots. Our focus was on the 108 ± 0.2 µm soda lime glass spheres and thus measurements were recorded for features greater than 80 µm that were largely circular in shape. Features greater than 80 µm are most likely not created through any of the other projectile particles. The molybdenum projectiles were not used in this case as they varied greatly in size, introducing more uncertainty into the measurements. Also, the molybdenum spheres charged in the projectile mix, which led to the spheres

becoming coated with the small silica spheres (Figure 3.10). It is unknown if the particles remained attached to the molybdenum during flight but this would not be a reliable diameter measurement, thus this was another reason the molybdenum was disregarded.
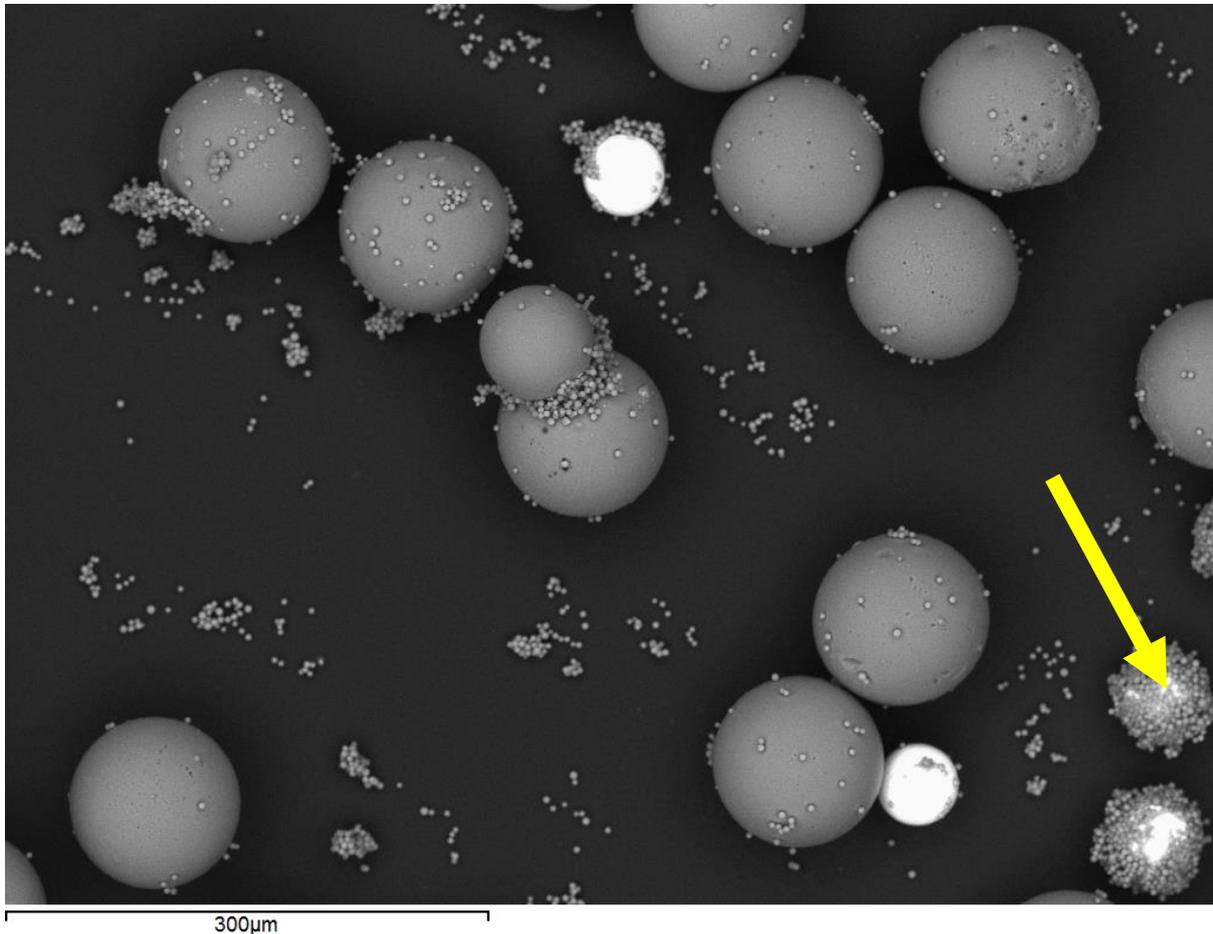
Figure 3.10. SEM BSE image showing some of the molybdenum spheres (the very bright white spheres) charging and becoming coated in the small silica particles, clearly seen in the bottom right corner with the yellow arrow pointing at a molybdenum sphere that is completely covered in silica.

The silica projectiles created features that appeared blurred in the SEM, although different combinations of accelerating voltages, vacuum pressures and any other options available it was not possible to locate the exact edge of these features and thus make confident measurements of their dimensions. They were too small to be measured with the SEM on the 5 km/s shot and bounced off of the foil at 1 km/s. There was also a lot of gun debris present on the foils which is of similar size to the silica therefore the silica impacts could not reliably be identified in surveying the impact feature sizes.

The diameter measurement data is tabulated for each foil and provided in the Appendix and is presented as histograms in Figures 3.11 and 3.12. The average hole diameters determined for each foil were, in general, in good agreement with the measurements of the original projectiles. Due to the differing quantities of impacts on the foils, the data was normalised with respect to the total number of features measured on a foil using the inbuilt normalisation of histogram data in the matplotlib.pyplot library of Python 3.9. This function is a probability density function and normalises the dataset by dividing the total number of measurements by the number of observations times the bin width. This produces a normalised density function that can be plotted as a histogram, which was how the following plots were produced.

As seen in Figure 3.11, impact feature size measurements on foils shot at 5 km/s were similar to that of the glass projectiles which have an average size of 108 ± 0.02 µm but there is a considerable portion of measurements in the range $150 - 250$ µm. The data obtained for the projectiles, however, do show the presence of occasional large projectiles; of the 100 glass spheres measured, a single sphere measuring 146.3 ± 0.05 µm was found. It is therefore possible that such larger spheres produce a population of larger impact features.
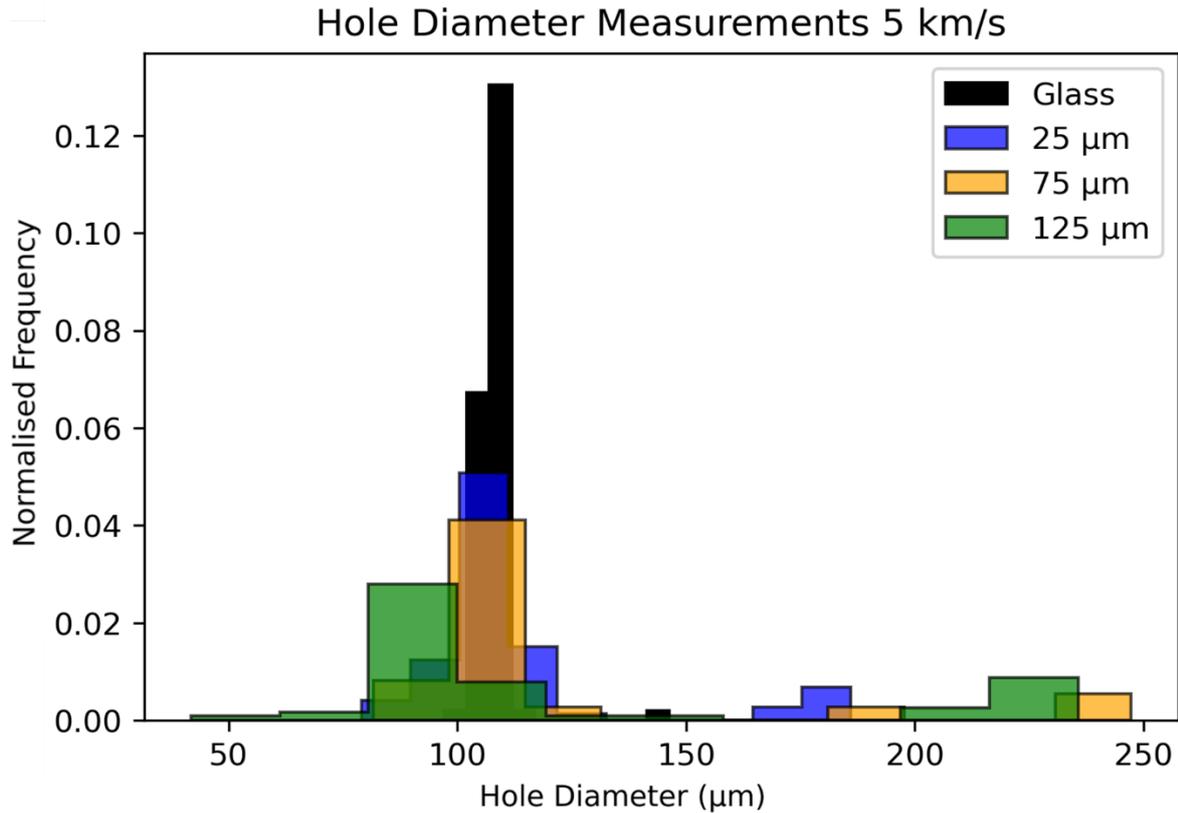
Figure 3.11. The normalised diameter measurements for the 25 µm, 75 µm and 125 µm thickness Kapton foils all coated with 10 nm palladium shot at ~5 km/s. The original projectile sizes are shown in black. It can be seen that all foils have components measured in the 150 – 250 µm range.

In the 1 km/s regime, the datasets for impact features on both the 75 µm and 125 µm foils are also closely distributed around the glass projectile size, and the different speed appears to have had a minimal effect. There is a small portion of the impact features on the 75 µm foil that measure greater than 150 µm, similar to the 5 km/s shots and is also noted that only the 75 µm foil at 1 km/s had similar morphology to the 5 km/s shots (Figure 3.12). Again these outliers are potentially an artefact of the glass projectiles having some outliers. For the 25 µm foil, there are no measurements greater than 80.6 µm, although the impact features look similar to the 5 km/s shots without the rims present on the holes.
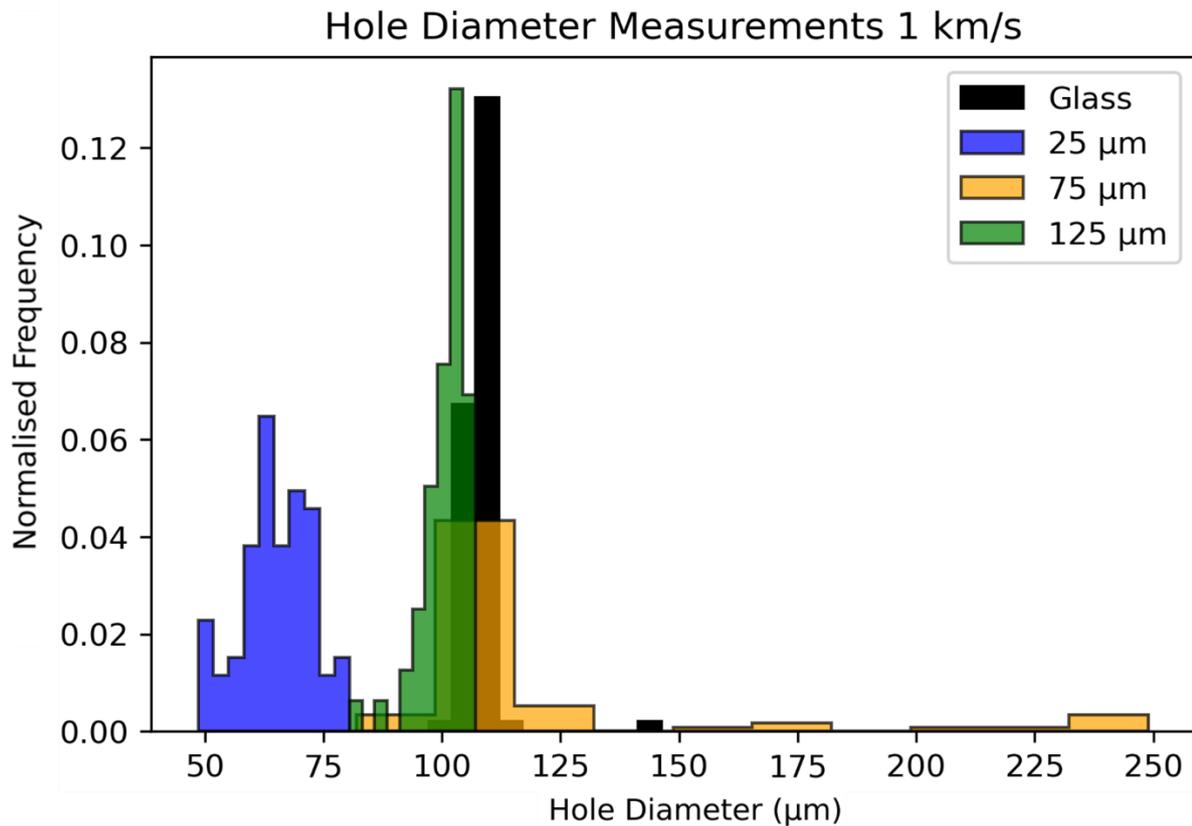
Figure 3.12. The normalised diameter measurements for the 25 µm, 75 µm and 125 µm thickness Kapton foils all coated with 10 nm palladium shot at ~1 km/s. The original projectile sizes are shown in black. Notably, the 25 µm Kapton foil has considerably smaller diameter measurements than the original projectiles.

Since much of the data appear to exhibit a bimodal distribution, with a peak around the original size of the projectile and another, separated population peaking >150 µm, average hole diameters were calculated in two ways – first including all the data, second with the larger population excluded. Doing this assumes that the smaller size range is created by the smaller impactors and that the larger size range is a result of the small proportion of the projectile mix that is much larger in size than the majority of the mix.

Errors on the measurements were calculated using the standard error on the mean whereby the standard deviation is divided by the square root of the number of measurements. The 75 µm thickness foil is in good agreement with the original size range of the projectile powder, whilst the others are slightly out of range. Speed appears to have a minimal impact on the size of the impact features for the foil shot at 5 km/s, with the mean impact feature diameters lying within 98% of the mean projectile diameters for each foil thickness. For the 1 km/s shots however, the 25 µm foil has sizes that are much lower. Table

3.1 shows the hole measurements as a fraction of the original projectile size, D_P, and was only calculated for the "corrected" hole sizes which have the larger portion of the data removed. This illustrates that the 5 km/s shots into the 25 µm and 75 µm foils is almost a 1:1 relationship with that of the original glass projectile sizes. The errors on the measurements is reasonable, if a normal distribution of the error is assumed, the measurements lie within the first confidence interval for the 125 µm foil shot at 1 km/s and the 25 µm and 75 µm foils shot at 5 km/s. This is a good result for the ODIE detector as the range of possible values for the size of the impact features is acceptable for finding the original projectile size.

Kapton Thickness (µm)	Mean Hole	Measurement (µm)			
	1 km/s		Original 5km/s	Corrected 5 km/s	
25	65.1 ± 0.8	0.60 D_P	113 ± 2.9	106 ± 1.1	0.98 D_P
75	121 ± 4.5	1.12 D_P	123 ± 5.1	107 ± 2.0	0.99 D_P
125	101 ± 0.6	0.94 D_P	123 ± 3.1	96.8 ± 1.3	0.90 D_P

Table 3.1. Measurement data for the size of the hole diameters at 1 km/s and 5 km/s. The original sizes are those including the large population of impacts and the corrected sizes are those without the large sizes. The relationship of the 1km/s features and 5 km/s corrected features to the original impactor size are shown as a ratio to the original projectile size D_P.

To aid in the interpretation of these results we can compare these results with those of the previous literature to ascertain if there is acceptable comparison between the experiments and the different materials of Kapton and Teflon. The shots were performed using Kapton while most previous literature consisted of investigations of Teflon and some of aluminium. As mentioned previously, the method employed by Hörz et al. (1995) and Neish and Kibe (2001) was to divide all diameter measurement data by the thickness of the foil it was shot into. Then the data were plotted as the projectile diameter divided by the foil thickness (D_P/T) versus the hole diameter divided by the foil thickness (D_H/T) as shown in Figure 3.13.
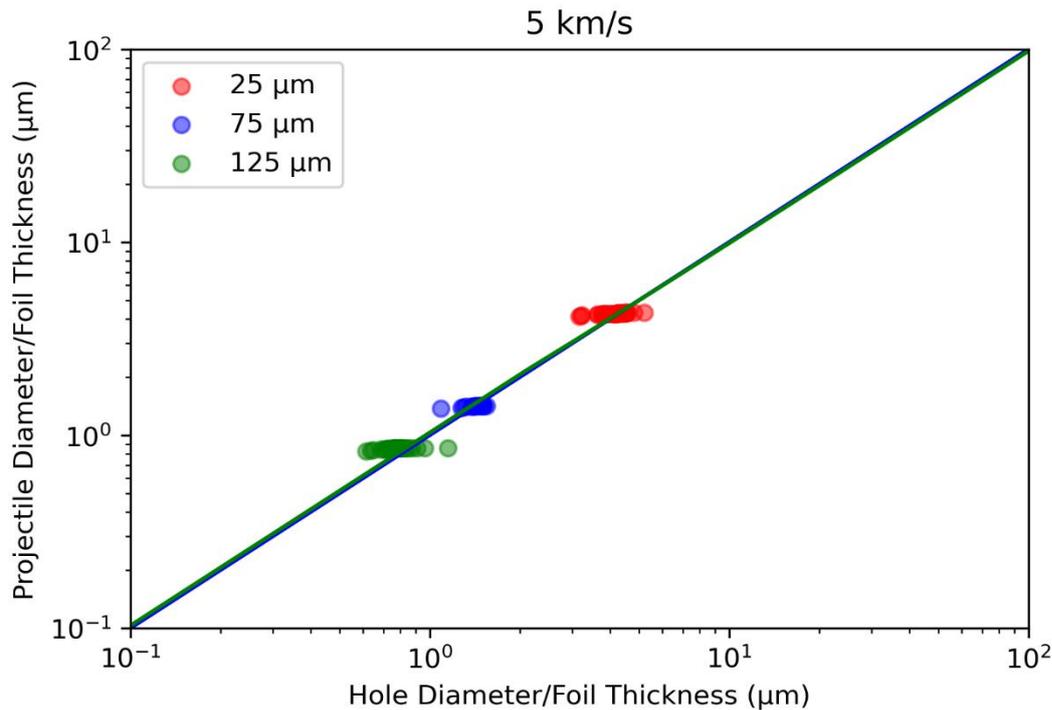
Figure 3.13. Plot of projectile diameter divided by the foil thickness (D$_P$/T) versus the hole diameter divided by the foil thickness (D$_H$/T). The blue line is that of y = x and the green line is the line of best fit, showing that it is almost the same.

In Figure 3.13, a blue line indicates where the D$_P$/T is equal to D$_H$/T, where a projectile of a given thickness will create a hole of that thickness. A green line represents the line of best fit through the measured data. These lines are almost identical with a very slight difference in slope such that the equation of this line is:

$$y = 0.976x + 0.1$$

Eq. 1

The 75 μm foil diameter data has the smallest spread of the data which follows from the previous section that this foil is in the closest agreement with the projectile sizes. This is in contrast to the results of Neish and Kibe (2001), whose data largely lay below the y = x line and was fit with a curve instead of a line (Figure 3.14). This shows a more complex relationship between the projectile and impact feature or perhaps our study requires more data at different speeds across a wider range of projectile sizes in

order to be comparable. One notable difference is that the Kapton film dataset more closely resembles that of Teflon than our data.
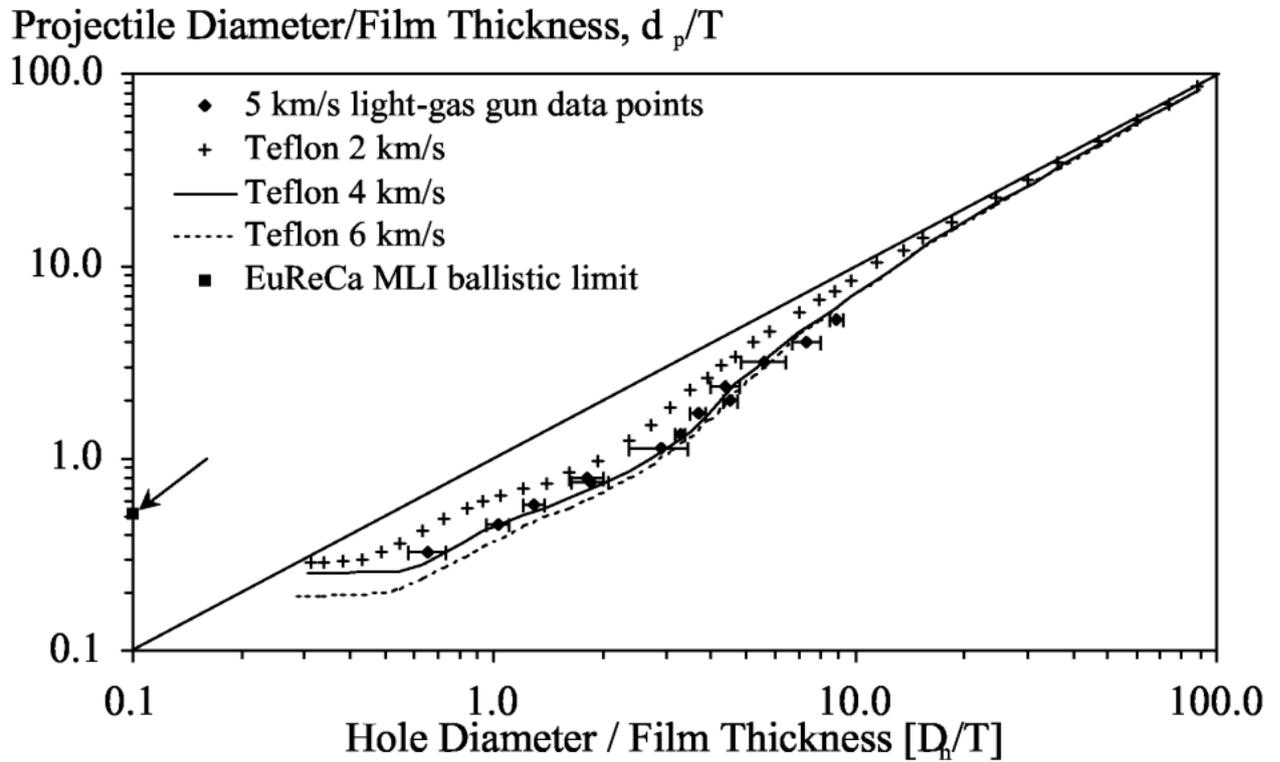
Figure 3.14. Taken from Neish and Kibe (2001), this is the D_P/T versus D_H/T plot obtained from their shots in addition to previous other studies (Neish and Kibe, 2001). The 5 km/s LGG data points represent impacts into Kapton film.

The same process was undertaken with the data from the 1 km/s shots. This data did not show as good agreement with the y = x line with the equation of the line of best fit shown in Equation 2. This implies that there is a speed dependency for the relationship that is found in these investigations.

$$y = 1.664x - 0.565$$

Eq. 2

The trend line fit to 1 km/s data (red line in Figure 3.15) lies above the $y = x$ line (blue line in Figure 3.15), similar to the observed trend from Neish and Kibe (2001) where with a decrease in speed the feature size made with the same size projectile also decreases. The data is heavily skewed by the much lower observed diameters in the 25 μm Kapton. As seen in Figure 3.14, the exclusion of the 25 μm dataset creates a curve which resembles the trend seen by Neish and Kibe (2001) at low speeds.
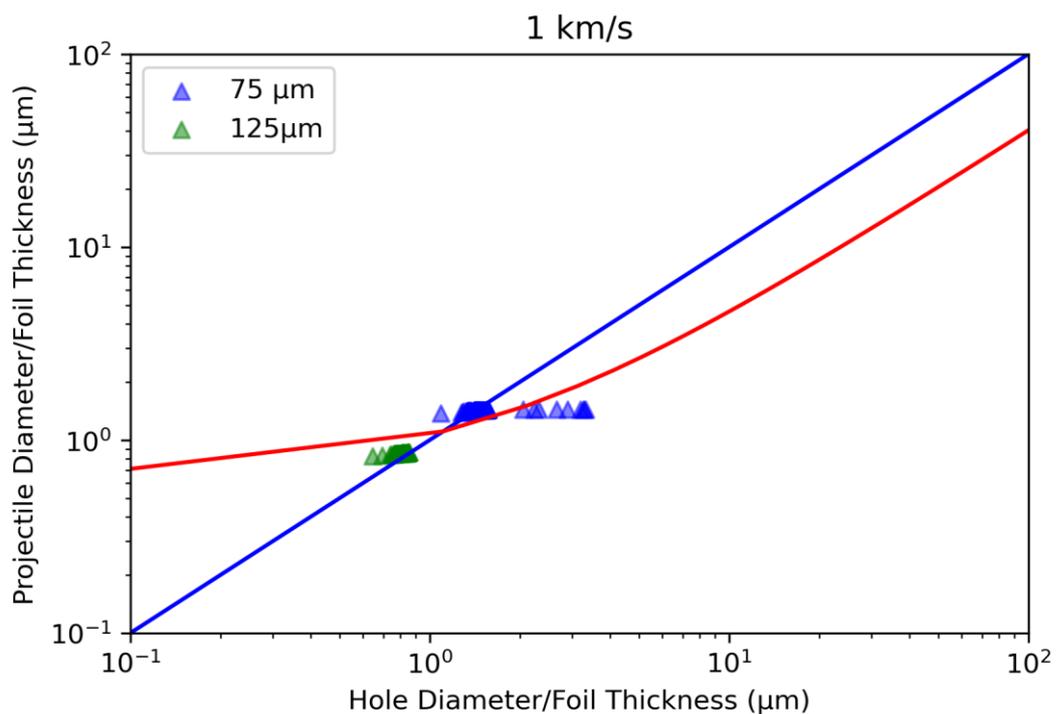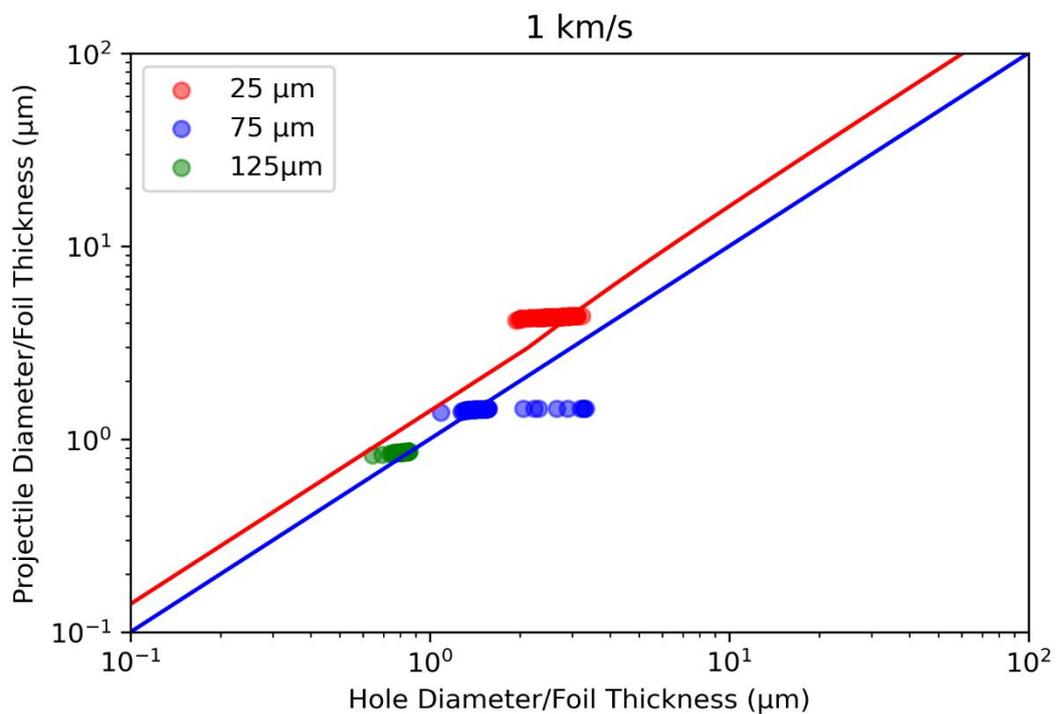
Figure 3.15. The D$_P$/T versus D$_H$/T plot for the diameter data of foils shot at 1 km/s with the 25 μm Kapton dataset included (top) and excluded (bottom). Red line is the line of best fit through the data and the blue line is the 1:1 line.

3.3.2 Results: Different Thickness Palladium Coatings

Hole measurements from up to 100 features >80 µm in diameter were obtained from the 25 µm foils coated with varied thickness coatings and these data are plotted as histograms in Figure 3.17. The mean diameter measurement was calculated (Table 3.2) and the error was again calculated using the standard error on the mean. The "original" and "corrected" measurements are again a result of the bimodality of the data at 5 km/s with the corrected data excluding the larger sized impacts. The relationship of the hole size to the size of the projectile is also calculated in this table. The 50 nm coating shows an exact relationship with the projectile size and the other coatings do not include the 108 ± 0.2 µm glass size in the first confidence interval.

Coating Thickness (nm)	5 km/s Hole	Measurement (µm)	
	Original	Corrected	
10	113 ± 2.9	105 ± 1.1	0.92 D_P
20	99.5 ± 2.3	96.3 ± 1.6	0.89 D_P
30	121 ± 2.3	114 ± 0.5	1.05 D_P
40	144 ± 5.1	112 ± 0.9	1.04 D_P
50	118 ± 3.3	108 ± 1.6	1.00 D_P
100	121 ± 3.7	114 ± 1.4	1.05 D_P

Table 3.2. Diameter measurements of the holes on different thicknesses of palladium at 5 km/s. The original sizes are those including the large population of impacts and the corrected sizes are those without the large sizes. The relationship of the 1km/s features and 5 km/s corrected features to the original impactor size are shown as a ratio to the original projectile size $D_{P.}$

Changing the coating thickness does not appear to have greatly influenced the sizes of the holes measured on the foils. The other coating thicknesses are in good agreement with the projectile dataset although the 40 nm coating appears to have been subjected to a particularly high bombardment by a higher proportion of larger particles in the histogram of Figure 3.16. The 30 µm coating does not seem to have suffered any impacts from the larger population and thus has a small spread of measurements in this instance. All other foils show some impacts from the higher population of impacts although this is much less than the main largest peak in the data which, for all foils, lie relatively close to the black line of the 108 ± 0.2 µm mean of the soda lime glass population.
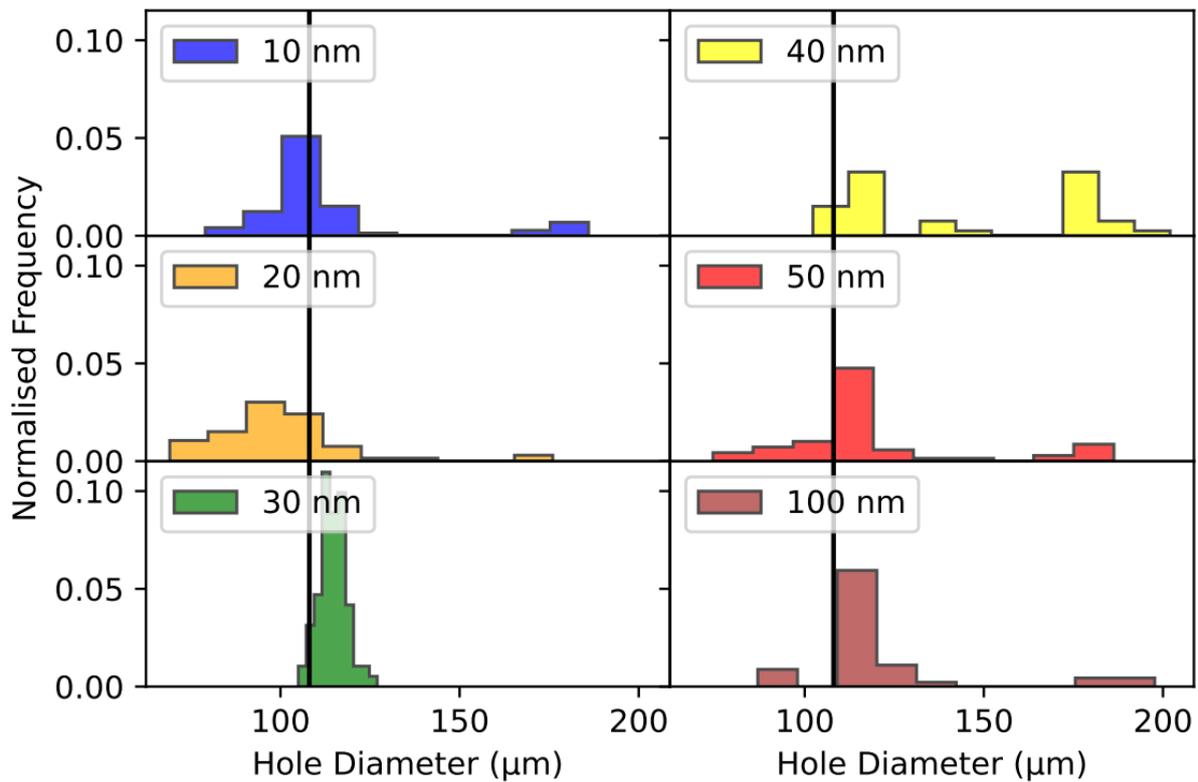
Figure 3.16. Histograms of the hole diameter measurements for the different coating thicknesses shot at 5 km/s. There are two distinct peaks on all plots except the 30 nm coating. The black line is the mean of the soda lime glass projectiles.

Given the presence of the gap between the smaller and larger populations here as before, we have assumed that all impacts above 140 µm in diameter are from the larger population of glass in the projectile mix and have therefore calculated the mean both with and without this population included (Table 3.2). If we disregard them, we see that the majority of impact features measured in this smaller population have diameters between 100 and 130 µm (Figure 3.17), a range which includes the mean diameter of the original projectiles (108 ± 0.2 µm). The hole diameters therefore lie within 99% of the mean projectile diameter. The spread of data varies for the different samples but there appears to be no relation between spread and coating thickness and instead this is likely due to the shot conditions, such as the impact velocity, quantity of projectiles and the cleanliness of the shot.
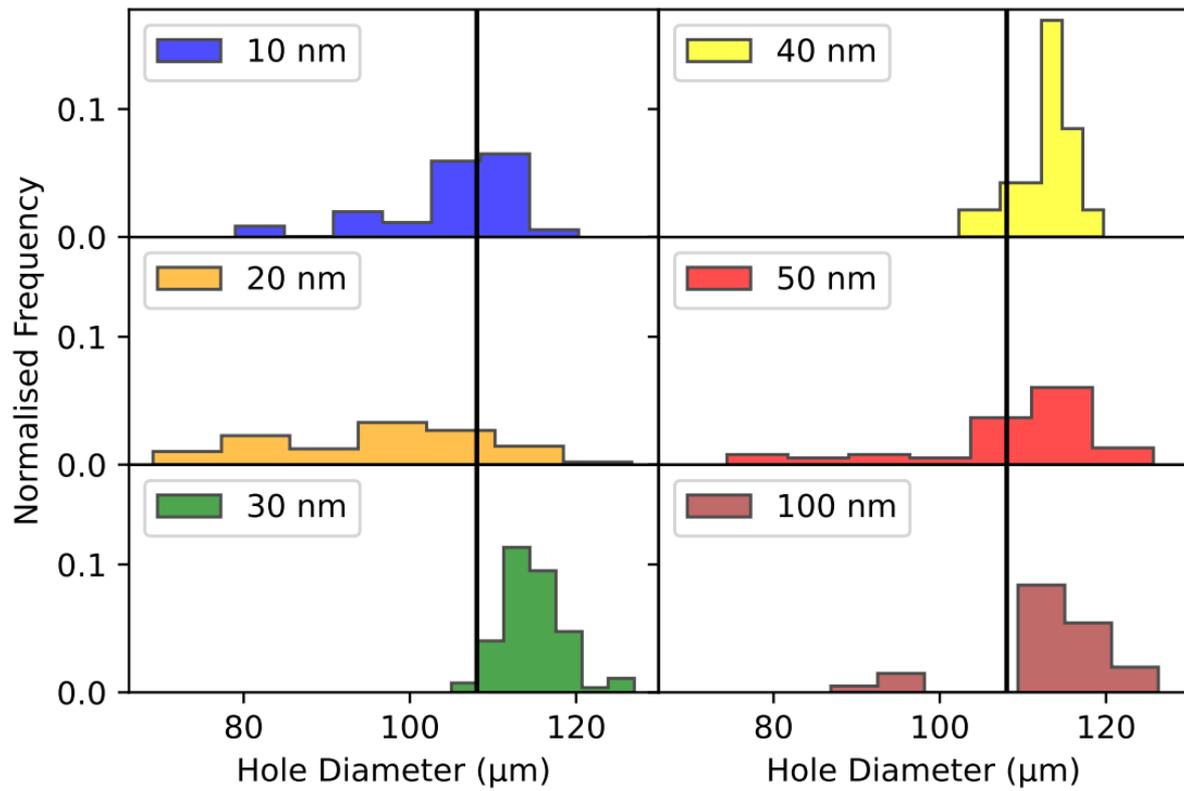
Figure 3.17. Histograms of the various coating thicknesses shot at 5 km/s with the larger population removed. The vertical black line represents the mean of the soda lime glass projectiles.

The foils that were shot at 1 km/s display no bimodality in the data (Figure 3.17). The mean hole sizes for these shots are much smaller than that of the initial projectiles (Table 3.3). This difference highlights the speed dependence of the relationships to be found between impact feature and projectile and verifies the previous finding for the 25 µm foil shot at 1 km/s in Section 3.1 (where features were likewise smaller than the original projectile).

Coating Thickness (nm)	1 km/s Hole Measurement (µm)	
10	65.1 ± 0.09	0.60 D_P
20	67.6 ± 0.02	0.63 D_P
30	69.4 ± 0.11	0.64 D_P
40	64.5 ± 0.08	0.60 D_P

Table 3.3. Hole measurement data of the different coating thicknesses shot at 1 km/s. The relationship of the features to the original impactor size are shown as a ratio to the original projectile size D_P.

The holes are consistently ~38% smaller than the original projectile size for all coating thicknesses. Shown in Figure 3.18, the spread of the hole measurements is constrained and consistent across the different thicknesses of palladium, thus showing the palladium thickness has no effect on the hole size and acting as repeat experiments. This clearly shows that when shot at 1 km/s, the 25 µm foil will produce impact features that are smaller than the size of the original projectile.
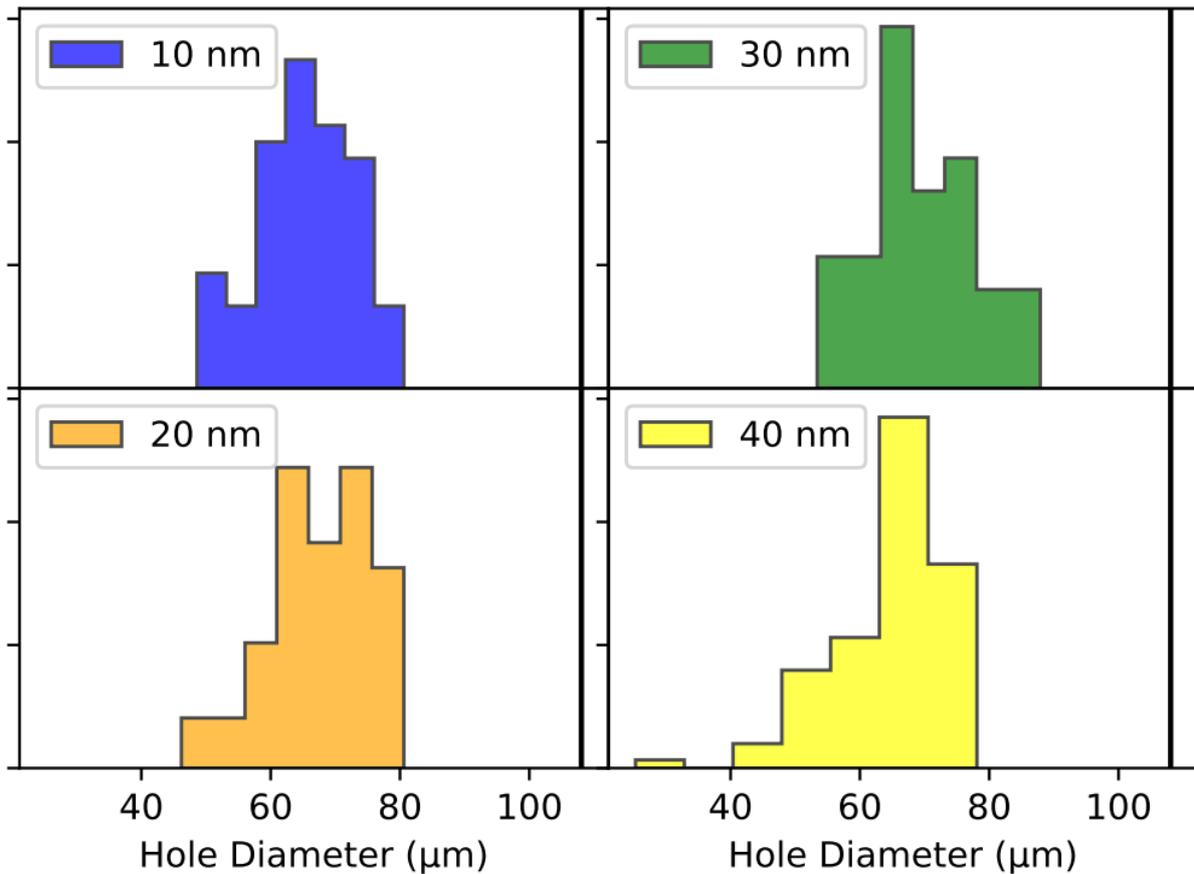
Figure 3.18. Plot of the hole diameter measurements for the different coating thicknesses shot at 1 km/s. The diameters measured are much less than those shot at 5 km/s.

3.3.3 Results: Rim vs Hole Measurements

The rim measurement location was only available across the different coatings on the 25 μm foil as the other thicknesses of foil did not have rims consistently across all features at both speeds. The rim measurement, taken from the highest point on the lip formed around the feature, is generally much larger than that of the hole measurement.

Coating Thickness (nm)	5 km/s Rim	Measurement (μm)	
	Original	Corrected	
10	134 ± 3.3	123 ± 1.4	1.14 D_P
20	120 ± 2.9	117 ± 2.0	1.08 D_P
30	151 ± 2.3	143 ± 0.7	1.32 D_P
40	164 ± 5.1	133 ± 1.3	1.23 D_P
50	142 ± 3.8	130 ± 2.1	1.20 D_P
100	150 ± 3.9	142 ± 2.1	1.32 D_P

Table 3.4. Rim measurement of impact features shot at 5 km/s. Notably much larger than the size of the soda lime glass projectiles. The original sizes are those including the large population of impacts and the corrected sizes are those without the large sizes. The relationship of the corrected features to the original impactor size are shown as a ratio to the original projectile size D_P.

The rim measurements varied greatly in comparison to the hole measurements on the same impact features (Table 3.4). There is no observable trend or consistency in the relationship between the rims and the projectile diameter, D_P. This may be a result of the rim forming post-impact and not necessarily having a direct interaction with the impacting particle. The hole measurement is created by the projectile itself and thus would appear that the rim is created from the displaced material of the impact and is therefore larger than the projectile size. This shows no clear dependency on the coating thickness although the smallest rim measurements, and closest to the projectile diameter, are the two thinnest coatings of 10 nm and 20 nm.
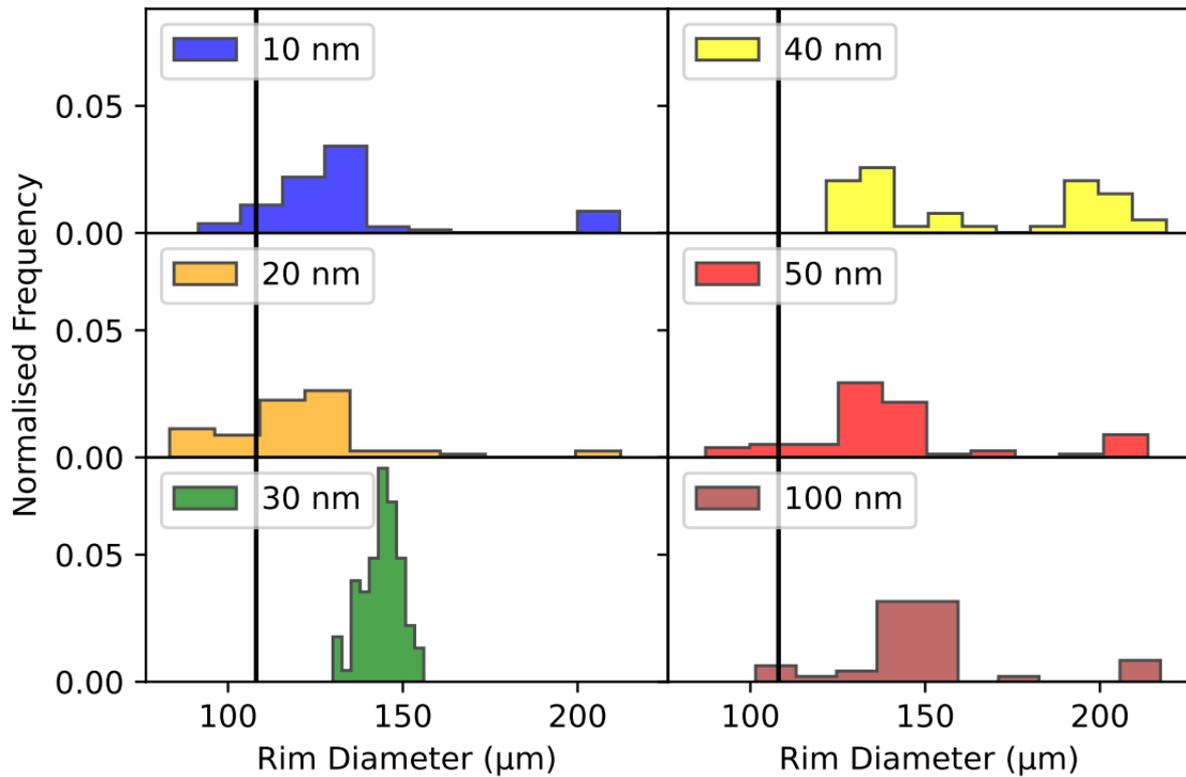
Figure 3.19. The various coating thicknesses were shot and the diameter measurements were taken from the rim location. This produces notably larger measurements of the impact feature than the original projectile size and the hole measurements.

The rim measurements also exhibit a population of larger features (see Figure 3.19), likely again as a result of the larger projectiles within the soda lime glass mix. This measurement location gives a much larger size distribution than that of the holes. As the rim feature only appears consistently on the 25 µm foil this is a feature measurement location that may not be ideal as a main classifier for ODIE as it is not present across the different foil thicknesses and is inconsistent in comparison to the hole measurements.

Removing the larger population of soda lime glass projectiles from the dataset does not change the result of the rim diameters significantly (see Figure 3.20). The rim diameters measured remain much greater than that of the soda lime glass. The rim measurement was originally suggested by Kearsley et al. (2006) when performing shots into aluminium and this could be the case that this measurement location is appropriate for metals but is not useful when working with thin polymer films.
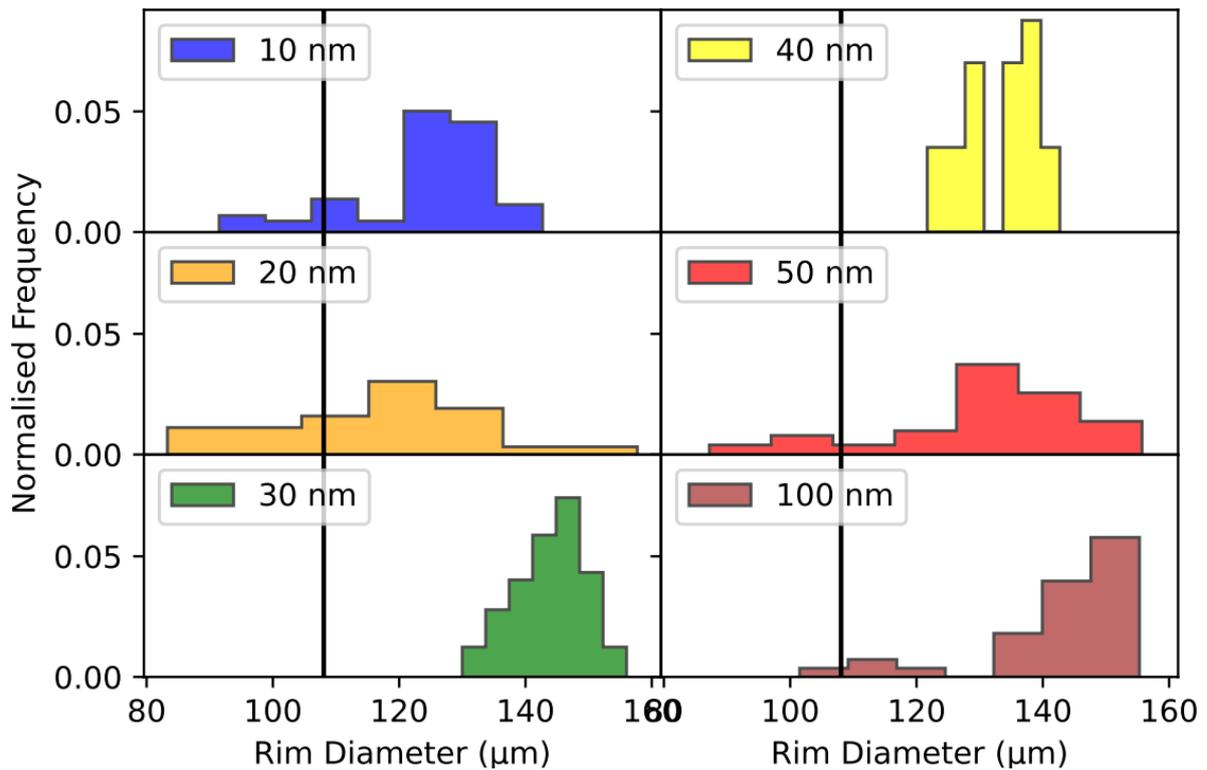
Figure 3.20. The rim measurements with the population from the larger portion of the soda lime glass projectiles removed.

3.4 Conclusions

The impacts into palladium coated Kapton showed how these materials react when subjected to hypervelocity impacts, as would be the case for the ODIE detector in LEO. The aim of the ODIE detector is to be able to discern the original size of the impacting particle and thus it is important to calibrate the instrument to find a relationship between the impacting particles and the impact features. This chapter aimed to determine this relationship for different thicknesses of Kapton, and then to assess whether the palladium coating thickness has an effect on this relationship.

The 13 µm Kapton foils all ruptured when shot at 5 km/s, tearing and not maintaining the shape of the impact feature. The tears also inhibited SEM analyses by creating a curved surface, plunging a half of some features into darkness preventing the identification of the measurement locations. The exposed Kapton in the impact features but also around the torn sections led to severe charging of the sample. This was the same for all impact features but to a lesser extent than the 13 µm foil. The 13 µm foil therefore could not be investigated further here.

Of the remaining foils (25 µm, 75 µm, 125 µm) the 75 µm foil was in best agreement with the glass projectile dataset. The 25 µm and 125 µm datasets had strong relationships between projectile and hole

as well, thus any of these foils would be acceptable for impacts at 5 km/s. The relationship established for the 1 km/s data is in agreement with Neish and Kibe (2001) as the trend they observed also has a trailing edge at a certain projectile to hole ratio. Although our data is generally showing that larger projectiles are creating smaller holes at 1 km/s than Neish and Kibe (2001).

The 25 µm foil at 1 km/s had an interesting phenomenon occur where the impacts, on all thickness of coating, were consistently about 38% below the soda lime glass 108 ± 0.2 µm average diameter. This is something that was not observed in Neish and Kibe (2001) and so is difficult to determine the cause. Also at 1 km/s, the 125 µm foil experienced the embedding of most of the particles in the foil rather than the creation of a hole.

The size preservation and relationships found on all coatings was highly dependent on the number of impacts experienced and the size distribution of those projectiles, as Hörz et al. (2005) endeavoured to have high precision measurements of the projectiles for this reason. All thicknesses showed minor variations in size measurements but overall did not have a major impact. The relationships established between the projectile size and the hole size were near 1:1 (hole diameters within 98% of the mean projectile diameter) regardless of coating thickness, or, in the case of the 5 km/s shots, foil thickness. The rim measurements were consistently much larger than that of the projectile with no apparent trend and thus are potentially not the optimal location for measurement taking.

Of course, we cannot negate the impact that variation in the experiments had. The LGG experiments differed substantially between shots, with more failures than successes, with variable numbers of projectiles being used in each shot. There is also the variation in speed which appears to have an impact on the relationships found between the projectile diameter and the diameter of the impact feature. The SEM measurements were performed using the inbuilt callipers on the INCA software leading to an error induced by operators when determining the exact positions from which to measure the diameters. All measurements were performed by multiple people but under the supervision of one individual thus somewhat mitigating the 15% error reported by Ward and Anz-Meador (2019) between different operators.

The spread of the data was the smallest for the 25 µm Kapton foil shot at 5 km/s and this is a key factor in the development of ODIE. The detector is to be optimised for the preservation of the size data of impacting OD and MM and therefore must have small margins of error on the measurement calibration. The coating that exhibited the smallest spread in errors was the 30 nm coating, although this may be a result of the exceptional shot which it experienced. As previously mentioned, the shot was notably different to the others and could have had an effect on the results.

In future studies of returned surface and passive detectors there is a need for a broadly accepted method or standard for measuring the diameters of impact features. Here we suggest that the hole measurement, which Ward and Anz-Meador (2019) defined as the outer through-hole measurement, is taken as the

measurement location for Kapton. More studies are required to determine if this measurement location is pertinent for all polymeric materials. Potential LGG experiments into Mylar and Teflon may aid in constraining this measurement location. Using different angles for the impacting particles would be useful in ascertaining the applicability of the hole measurement location across a broad range of impact scenarios or if new diameter measurement locations would need identification.

Similarly, investigations with optical microscopy could yield a difference in the observed measurement locations, as shown by Ward and Anz-Meador (2019). In our study no destructive techniques were used as the samples were to be stored and reanalysed many times, but in future it may be advisable to use coloured dyes as Ward and Anz-Meador (2019) noted that the dyes present new locations to measure or provided more definition to already identified locations.

There is also a requirement for experimentation with the velocities of the projectiles, especially for the 25 µm Kapton foil. It would be beneficial to determine the point at which the Kapton stops creating holes of similar size to the impacting projectile and begins to make smaller hole sizes. Investigations into whether this phenomenon occurs with other sized projectiles at different velocities is necessary to determine the exact cause of the smaller hole sizes and the relationship that may be between the Kapton and smaller sizes as to whether this is something that follows a trend.

In conclusion, the projectile size to hole size relationship was a near 1:1 relationship (hole diameter within 99% of the mean projectile diameter) for the 5 km/s shots into all thickness foils regardless of coating thickness. The 75 µm Kapton foil performed the best with regards to size preservation of the original impactor.

Chapter 4: Investigating Palladium Coating Performance

The primary function of the palladium coating proposed for use on the ODIE detector is to protect its Kapton foils from the erosive action of atomic oxygen. It also removes the need to apply a conductive coating to facilitate analysis by SEM and, further, aids the identification of impact features since holes and craters appear much darker against the bright (high atomic number) coated and undisturbed foil surface. However, palladium is not a commonly applied coating to Kapton, and thus its performance as a coating, in particular its effectiveness as a protective coating against atomic oxygen, and its reaction to being impacted, therefore needs to be tested.

Coatings are typically applied on the order of a few to tens of nanometres in thickness, but the optimum thickness must be investigated for palladium. It has been shown that even 3 nm coatings of aluminium can be sufficient for stopping large quantities of atomic oxygen erosion. As ODIE is intended for use in LEO it will experience a high proportion of atomic oxygen as it is concentrated close to the atmosphere. An ideal coating for ODIE is one that remains intact on the Kapton foil post-impact and that protects the Kapton from erosion. These two requirements are dependent on the other as the more damage to the coating the more atomic oxygen can attack the Kapton. Thus, the performance of the coating under hypervelocity impact and atomic oxygen exposure both need to be investigated.

4.1 Performance of Palladium Under Hypervelocity Impact

4.1.1. Method

4.1.1.1. Sample Coating, Shooting and Analysis

The LGG facility at the University of Kent was used to test the coating response to hypervelocity impact. Quorum sputter coaters were used to apply 10 nm, 20 nm, 30 nm, 40 nm, 50 nm and 100 nm thick palladium coatings to 25 µm thick Kapton foils.

The palladium coatings were examined by SEM to ascertain their quality, uniformity and cleanliness. Despite attempts to keep the foils clean (e.g. ensuring the bulk foils remain in sealed containers until use), preparation of the foils (cutting and mounting) for coating could not be performed in a clean room and thus contamination of the surface with particles was inevitable (see Fig. 4.1). Also observed were long, straight features criss-crossing the foil surface. These appear on all foils and appear to be an inherent characteristic of the material, suggesting they derive from manufacture of the foils.
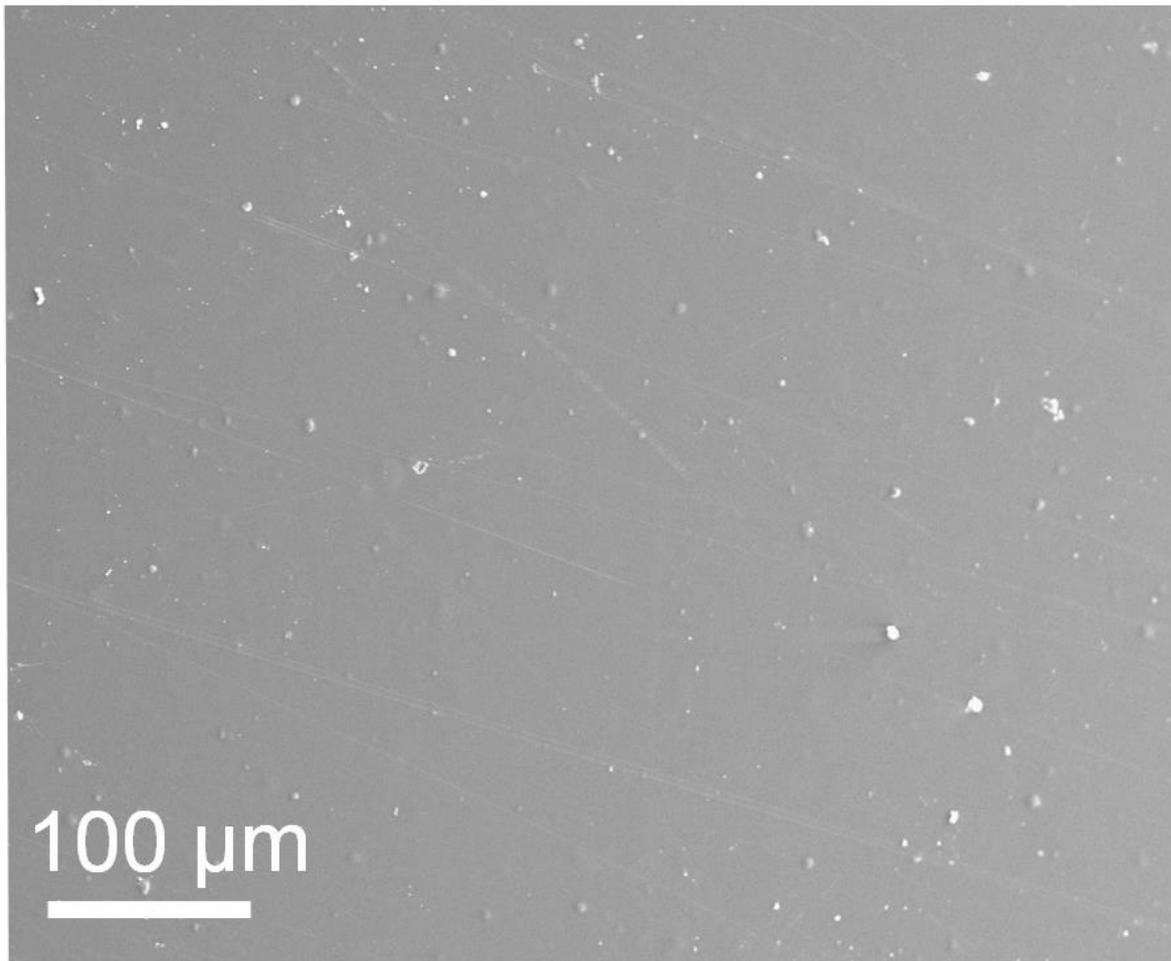
Figure 4.1. An SEM image of the coating to show the quality of said coating. Note the long, straight features present on the foil, these appear to be from the coating method.

Coated foils were then subjected to impacts by the multi-component buckshot (1 mm $\pm$ 0.005 mm basalt (MM), 108 $\pm$ 0.2 µm soda lime glass (MM), 50 $\pm$ 1 µm molybdenum (OD) and 7 $\pm$ 0.5 µm silica (MM)) using both the single (to achieve ~ 1 km/s impact speeds) and two-stage (to achieve ~5 km/s impact speeds) configurations of the LGG. All shots used in this study were performed with the target in the blast tank. These experiments (coating thickness, velocities achieved) are summarised in Table 4.1. Once shot, each foil was studied to look for any signs of damage displayed by the different thickness coatings at different speeds and thus to assess their ability to protect the underlying Kapton foils after impact and to retain information about the impacting particle (i.e. their size).

Coating Thickness (nm)	Velocity Achieved for 5 km/s shots
10	4.72
20	3.91
30	4.22
40	4.62
50	4.23
60	4.45

Table 4.1. Different coating thicknesses used in the experiments and the velocities they were impacted at.

4.1.2 Results

The impact features observed on the foils were a mixture of holes (where the projectile had enough energy on impact to penetrate) and craters (where it did not). The foils created during the shot programmes of this thesis all exhibited a dark, roughly circular area across them after impact – this was gun debris, and varied in extent such as in Figure 4.2 where the gun debris is minimal and the foil remained clean.

Figure 4.2. A foil that has been impacted in the photographic slide target holder. The circular area of impacts can be seem in this image.

Previous studies suggest this gun debris is comprised of a carbon-rich film of material as well as discrete, often metallic particles which can also be accelerated to sufficient speeds to generate their own impacts (Wozniakiewicz et al., 2009) (Fig. 4.2). This posed a significant problem when examining smaller impact features on the foils since it often complicated interpretation of the true nature of the coatings around the impact sites. Where gun debris was deemed excessive, the samples were disregarded due to these complications such as in Figure 4.3.
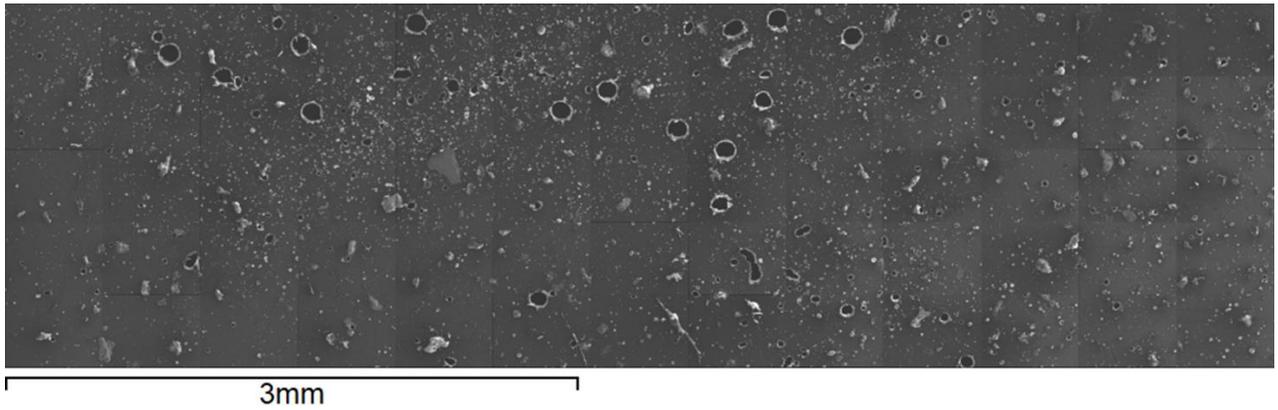
3mm

Figure 4.3. A region of a foil that was shot at 5 km/s that became contaminated with gun residue (the large chunks scattered across the foil) and also had many irregularly shaped holes which may be the result of projectiles shattering in flight.

The successful shots had typical features comprising holes through the foil, generally with rims present around the penetration hole, with some cracking or disturbance of the palladium coating. As shown in Figure 4.4, this BSE image highlights how the palladium, due to its high atomic number, presents as a bright background enabling clear identification of impact features. The central hole in the image is also surrounded by a range of smaller impacts, many of which are irregularly shaped and thus appear to be debris from the gun impacting the foil. This is present throughout all the shots and can provide an avenue for investigation of the reaction of the coating to many different sized impacts.
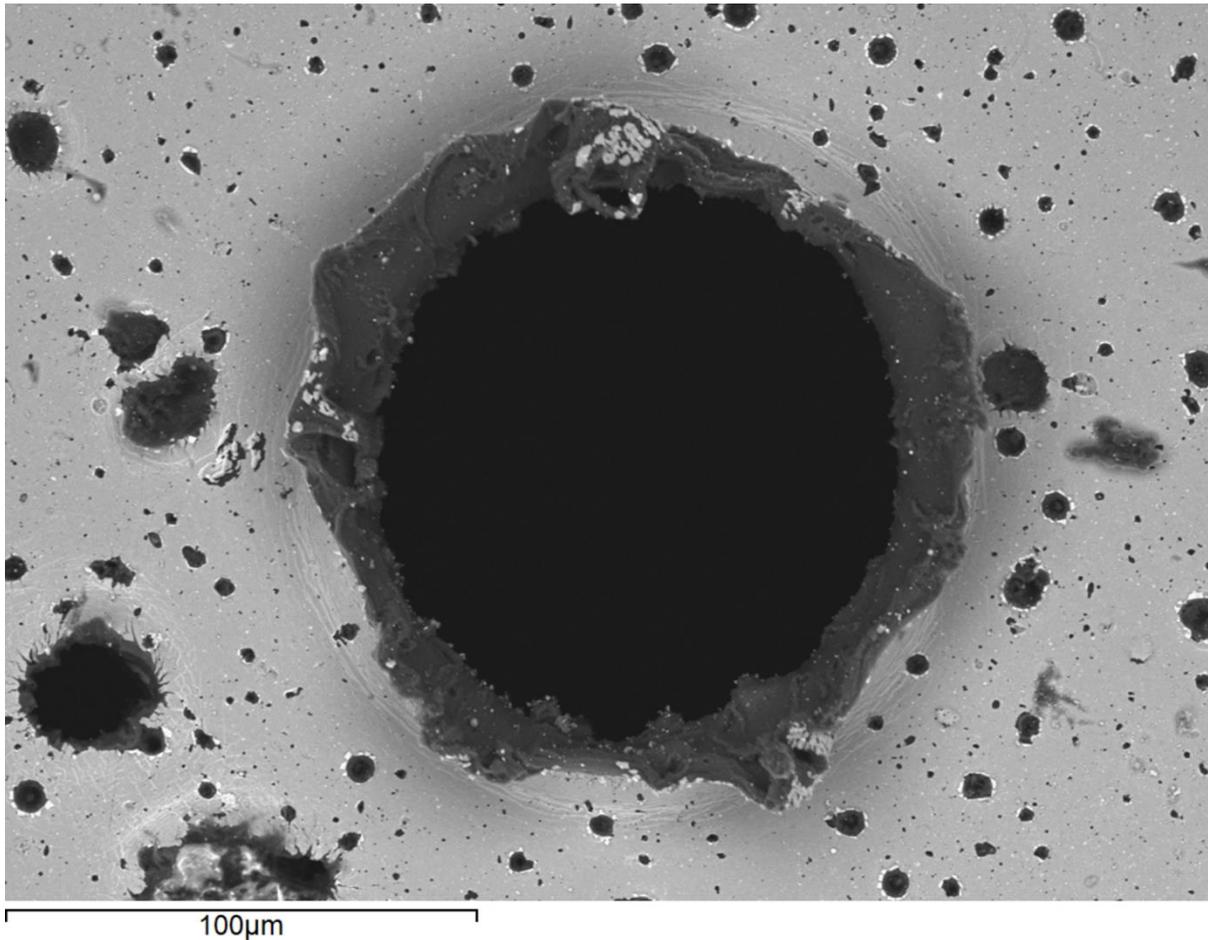
Figure 4.4. Example of a feature with cracking/delamination surrounded by smaller impacts potentially caused by a mixture of the projectile mix and gun debris.

4.1.2.1 5 km/s Shots

For all foils shot at ~5 km/s, similar impact features—a mixture of larger circular penetration holes over ~ 100 µm in size with thin rims and a range of smaller impact craters—are observed on foils coated with different thicknesses of palladium .The coating itself, however, exhibited cracking, delamination and loss of the coating around the impact features (Figures 4.4, 4.5 and 4.6). Loss of the coating is far from ideal for the purpose of ODIE as the palladium must remain attached to the Kapton foil in order to form a protective coating and preserve the original hole dimensions. The larger impact holes show minimal cracking and damage from 10 nm to 40 nm and once the 50 nm coating is reached the extent of the cracking becomes much worse. The 100 nm coating shows the worst result with the coating forming large concentric cracks around the large impact feature.

There is evidence of peeling of the coating away from the Kapton surface which would be highly detrimental to the polymer in LEO. The critical coating thickness for the beginning of delamination present on these impacts is hindered by the limited number of coatings that were used in this study. It

appears that the critical thickness is between 40 – 100 nm and it would be necessary to conduct more LGG experiments with coating thicknesses within this range to narrow down the thickness where the coating changes from cracks occurring as a result of impact to where the coating peels off in large chunks.
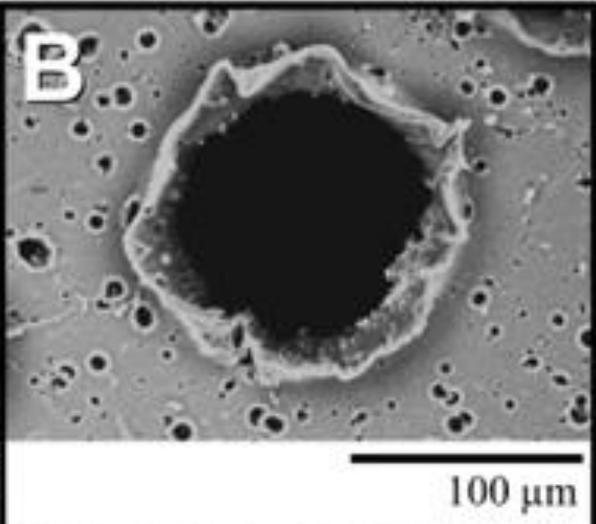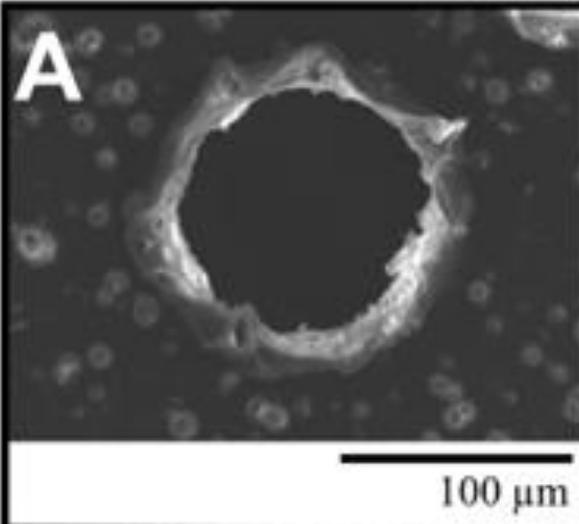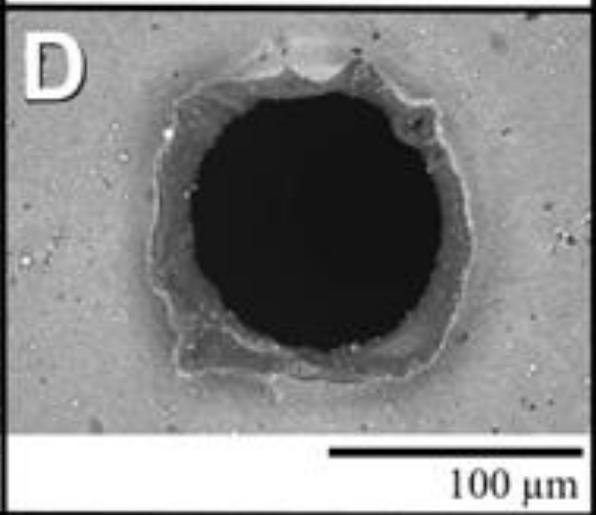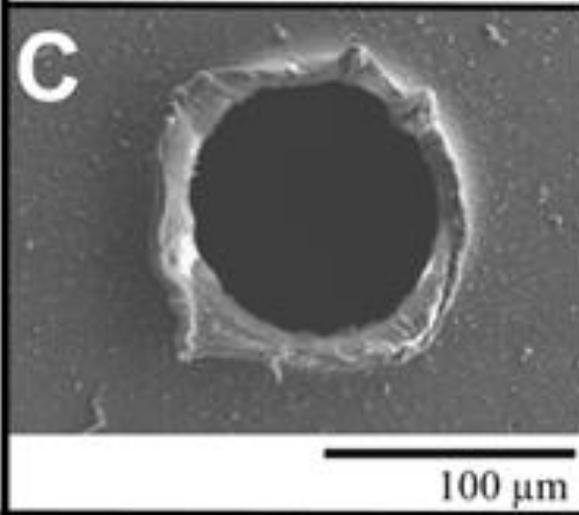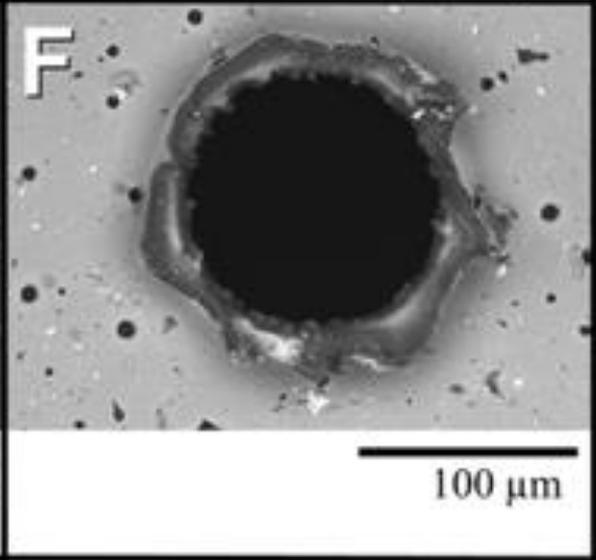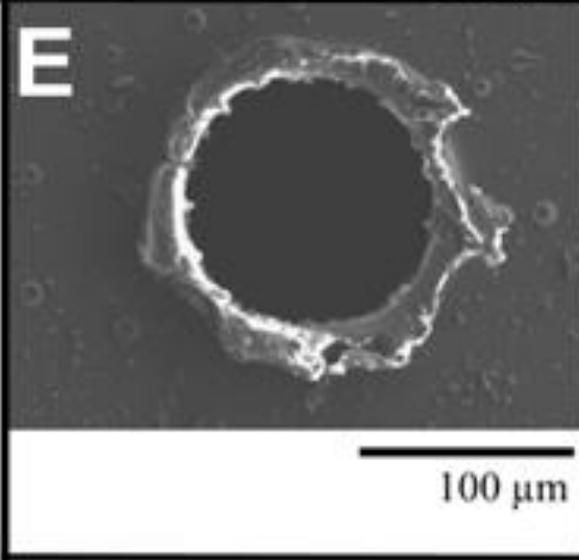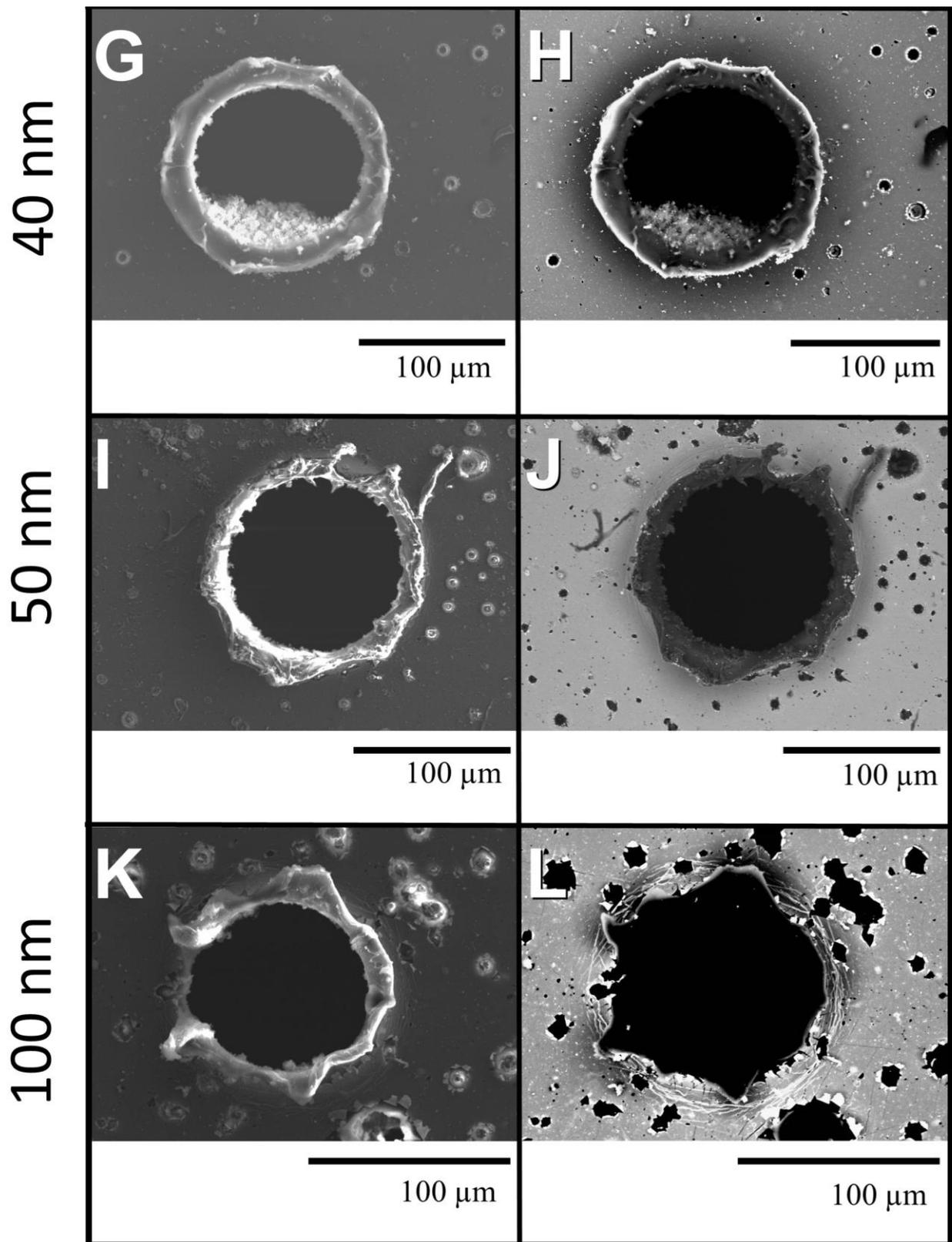
Figure 4.5. All the coating thicknesses and the delamination/cracking present on the foils shot at 5 km/s. The cracking gets worse with thicker coatings. Left column SE and right column BSE images.

Upon initial inspection, smaller impact features exhibit similar degrees of radial cracking regardless of coating thickness with no evidence of concentric cracking around the impact features. It is clear, however, that the thicker coatings suffered the most damage and coating loss due to impact with the cracking around impact features appearing more prominent for the 100 nm coating (Figure 4.5). The small impact features exhibit delamination when coatings exceed ~40 nm, similar to the large impact features. Thinner coatings experienced more radial cracking that expanded outwards leaving petals of palladium around the feature which peel to reveal the Kapton (Figure 4.6).
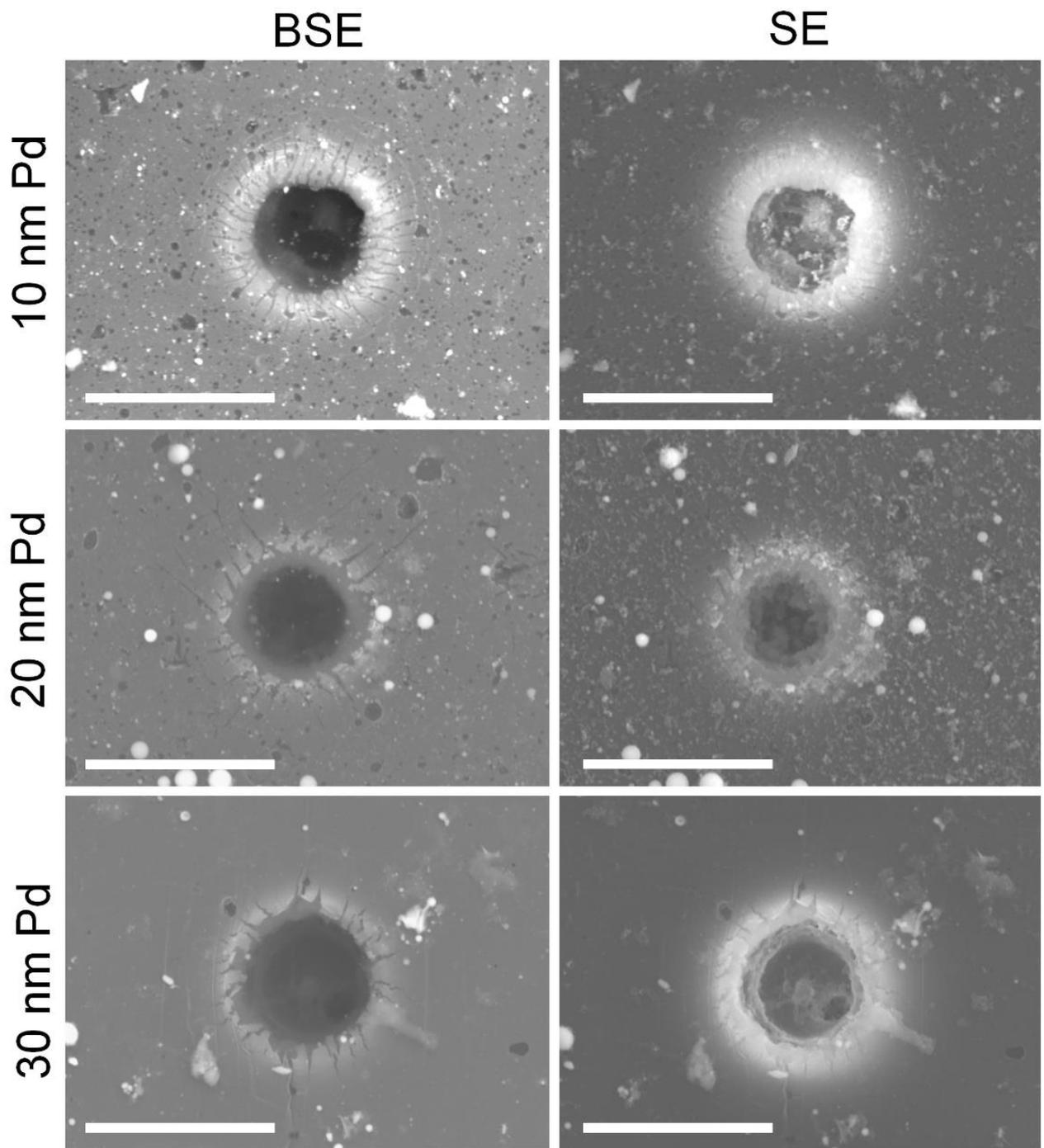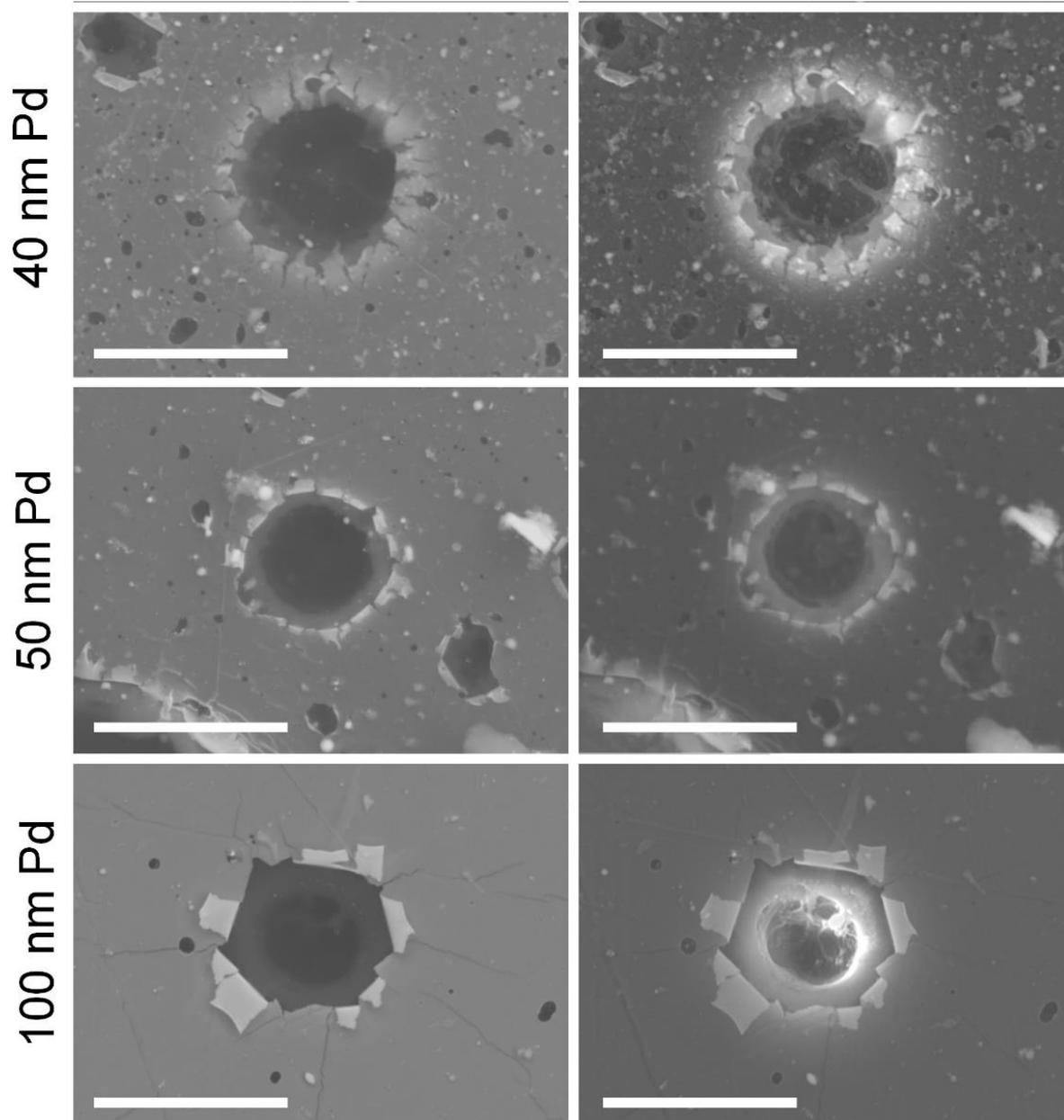
BSE SE

10 nm Pd

20 nm Pd

30 nm Pd

Figure 4.6. Cracking effect around small features, predominately with radial cracking. Scalebar represents 10 µm.

4.1.2.2 1 km/s Shots

It proved much more difficult to get a successful shot at 1 km/s than at 5 km/s. The projectiles often did not reach the target or, if they did make it, there were not that many impacts. This resulted in many repetitions in an attempt to obtain a clean shot that had more than 20-30 impacts. For some thicknesses

of coating this was not feasible with the limited amount of foils and the large amount of attempts (more than 4) to get the optimal conditions.

The large impact features of the soda lime glass projectiles generated on the foils by these slower speeds look different to those at higher speeds, having, in general, no rims and exhibiting more exposed Kapton (since the material that would ordinarily detach upon impact to create a hole seems to have remained attached). Concentric cracking is again observed around the edge of these impact features, becoming prominent for coatings above ~30 nm in thickness although the large petals peeling away from the hole are not evident at these lower speeds.
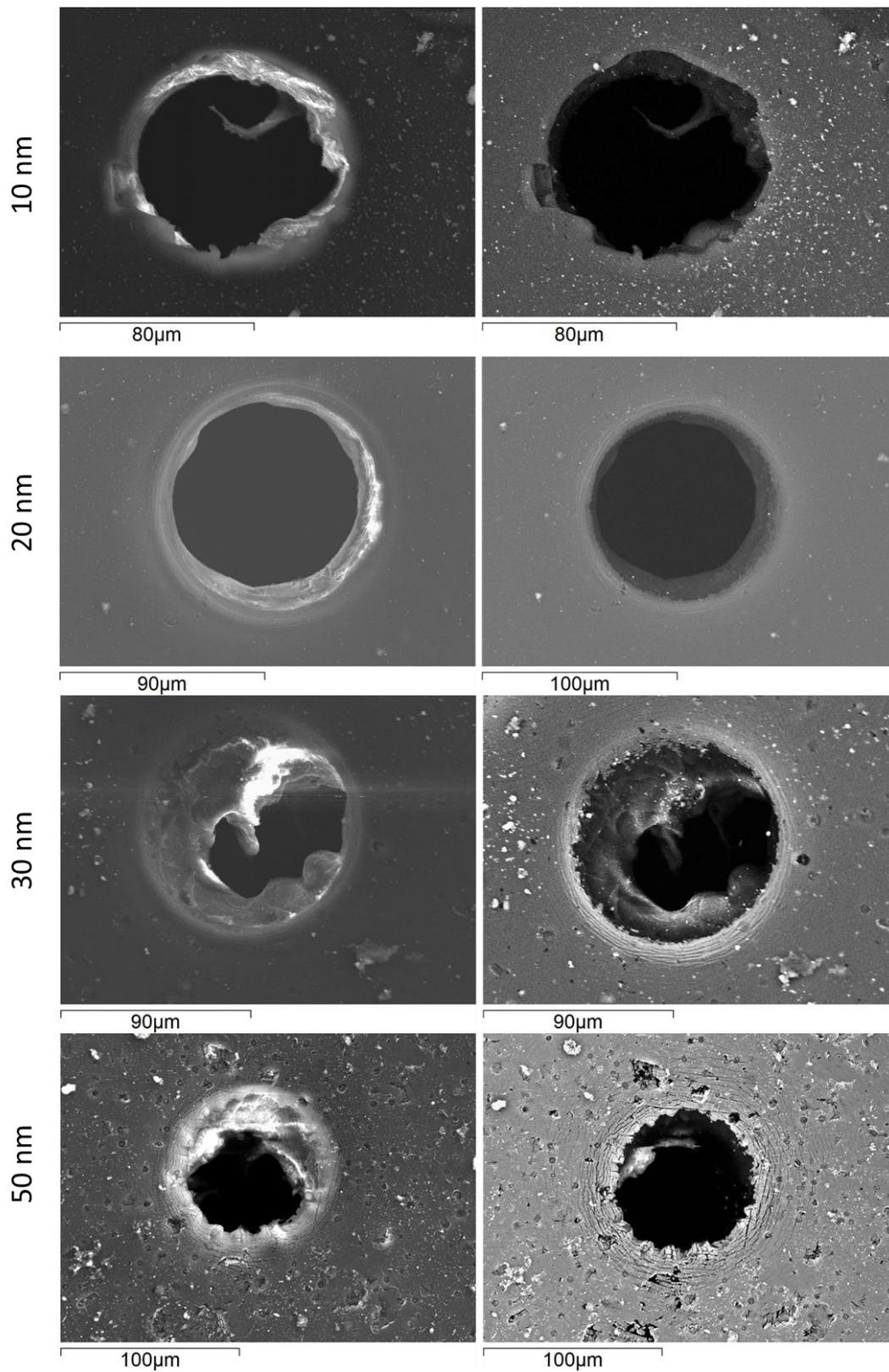
Figure 4.7. Holes created by 1 km/s impacts on various thicknesses of palladium coating imaged with SE (left) and BSE (right). There is a strong tendency towards concentric cracking after 30 nm in thickness.

4.1.3   Conclusion

The coatings showed similar preservation abilities at both speeds considered (1 and 5 km/s) but the thicker coatings experienced more damage and coating loss post-impact. Therefore thinner coatings of 10 nm or 20 nm would be recommended to prevent the loss of the coating so that the Kapton can remain protected from atomic oxygen.

Damage to the coating from hypervelocity impact appears in the form of cracks and delamination of the coating. The cracking of the coating has two main components: radial and concentric. The radial cracks are present on all features and are the dominant form of cracking on the smaller impact features ~10 µm and on the thinner coating thicknesses of 10 nm, 20 nm and 30 nm. The thicker coatings led to more concentric cracking which progressed to a severity such that the coating peeled back in chunks, delamination, and allowed for the petals forming around the impact holes to fall off as a result.

Ultimately, the palladium coating survived the hypervelocity impacts with different thicknesses showing varying degrees of damage post-impact. The loss of the palladium coating is to be avoided as best as is possible for ODIE to protect the detector in the destructive LEO environment and to preserve the feature dimensions. The most extreme damage occurred on the 100 nm coating where it peeled off in petals and the 50 nm coating experienced the same issue but to a lesser extent. Cracking occurred to a large extent in the range of 30 – 50 nm thick palladium coatings. The 30 nm and 40 nm coatings both showed more radial cracking around the features rather than the peeling. This is better with regards to the preservation of the coating but the amount of exposed polymeric material underneath is still a risk to the detector in atomic oxygen. Both the 20 nm and 10 nm coatings retained the majority of the coating with only small radial cracking occurring. The 10 nm coating is noted as having the least amount of damage but the 20 nm coating also showed good survivability.

Thus, for the purposes of ODIE, a coating thickness below 50 nm or the thinnest coating possible would be optimal as the thinner the coating the lower the risk of forming cracks that could hinder the function of the detector. and thus either the 10 nm or 20 nm coatings would be recommended for ODIE.

4.2   Performance of Palladium-Coating Under Atomic Oxygen Exposure

4.2.1   Method

The samples for the atomic oxygen exposure were prepared similarly to the targets for hypervelocity impact. The 25 µm thick Kapton foil was cut to 5 x 5 cm squares for mounting onto the photographic slides to be coated. Different thicknesses of palladium were applied to the samples: 10 nm, 25 nm, 50 nm, 75 nm and 100 nm. After the palladium coating was applied the samples were cut down to 2 x 2 cm, the size required for the atomic oxygen test holder. An additional sample of uncoated Kapton was

also cut to 2 x 2 cm. One sample that was coated with 10 nm of palladium was shot at 5 km/s for assessing the effect that a large bombardment of impacts would have on the protective qualities of the palladium coating. These samples were packaged and shipped to ESTEC for testing.

The sample mass was recorded and optical images were taken of the samples before and after atomic oxygen exposure. The samples were placed in the holder with a circular area of the sample exposed to the atomic oxygen beam and the corners of the square pinning the sample in place in the holder. An average atomic oxygen fluence of 2 x 10^{21} atoms/cm^2 across all the samples was targeted.

Upon return, the samples were imaged optically and by SEM. The circular exposure area created a boundary between the exposed and covered sections of the foil, hence when imaging the samples in SEM they were mounted such that this boundary was visible (Figure 4.8). Images were taken to illustrate the nature of any damage to the coating. A comparison was taken between the impact features greater than 80 µm in diameter from a 10 nm foil shot at 5 km/s and the same sample that was exposed to atomic oxygen to determine if the atomic oxygen had an effect on preserving the hole size.
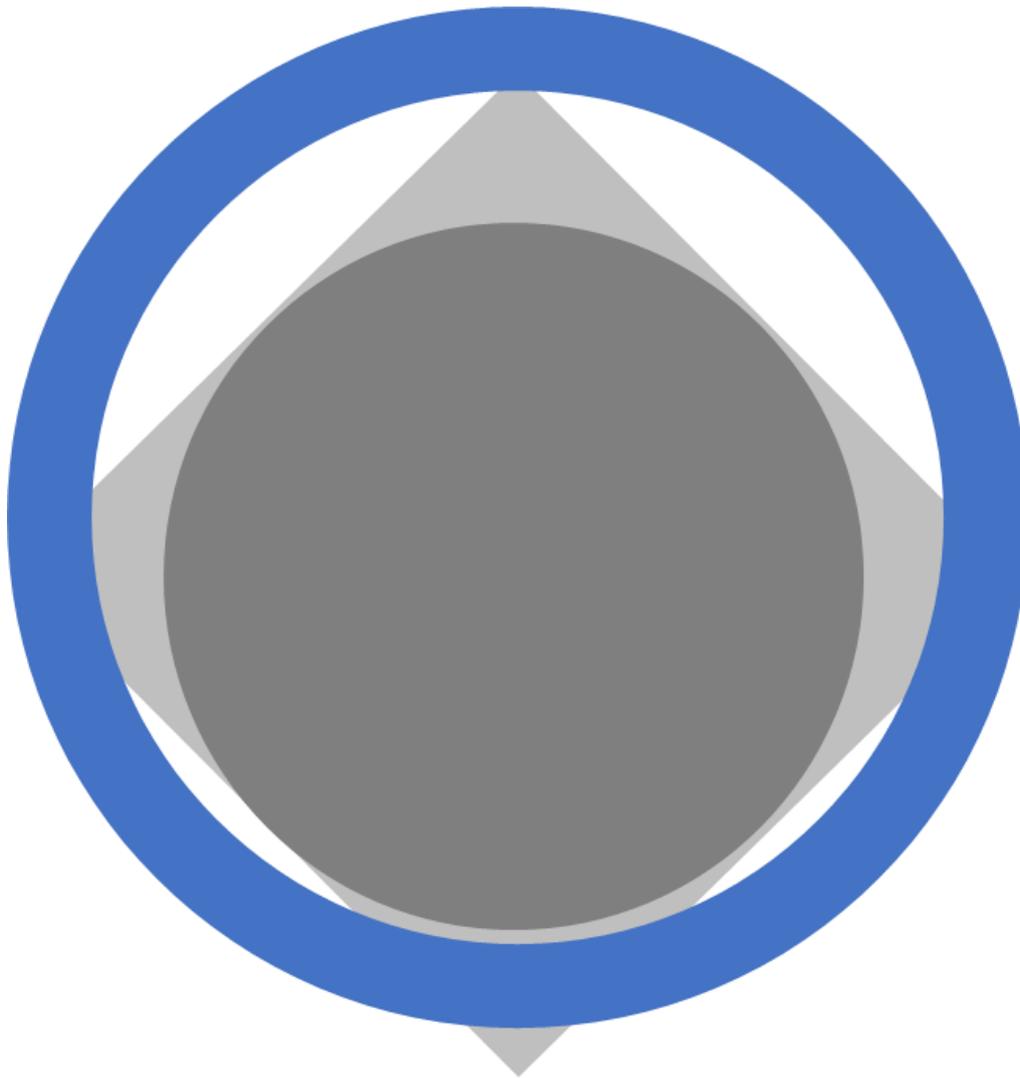
Figure 4.8. A schematic diagram of the mounting of the atomic oxygen samples. The outer blue ring represents the copper ring used to hold the foil in place and was taped down. The grey square is the sample to be analysed with the dark inner grey circle as the area previously exposed to atomic oxygen. The mounting was such that a boundary line between exposed and unexposed could be seen, the top corner shown here.

4.2.2   Results

4.2.2.1 Optical Assessment of All Kapton Foils

The uncoated Kapton sample was completely eroded, as to be expected for foils without a protective coating, with only the corners that were holding the sample in place remaining (Figure 4.9).

Figure 4.9. Photo of uncoated Kapton after exposure to atomic oxygen. The exposed area (central circle) has been completely eroded leaving behind only the four corners which pinned it in place within the holder and were therefore covered by a metal frame. Scalebar represents 1 cm.

All the samples with the palladium coating appeared intact after atomic oxygen exposure although all had a difference in their optical properties at the exposure boundary which created a visibly darker circular region where the sample was exposed (Figure 4.10).
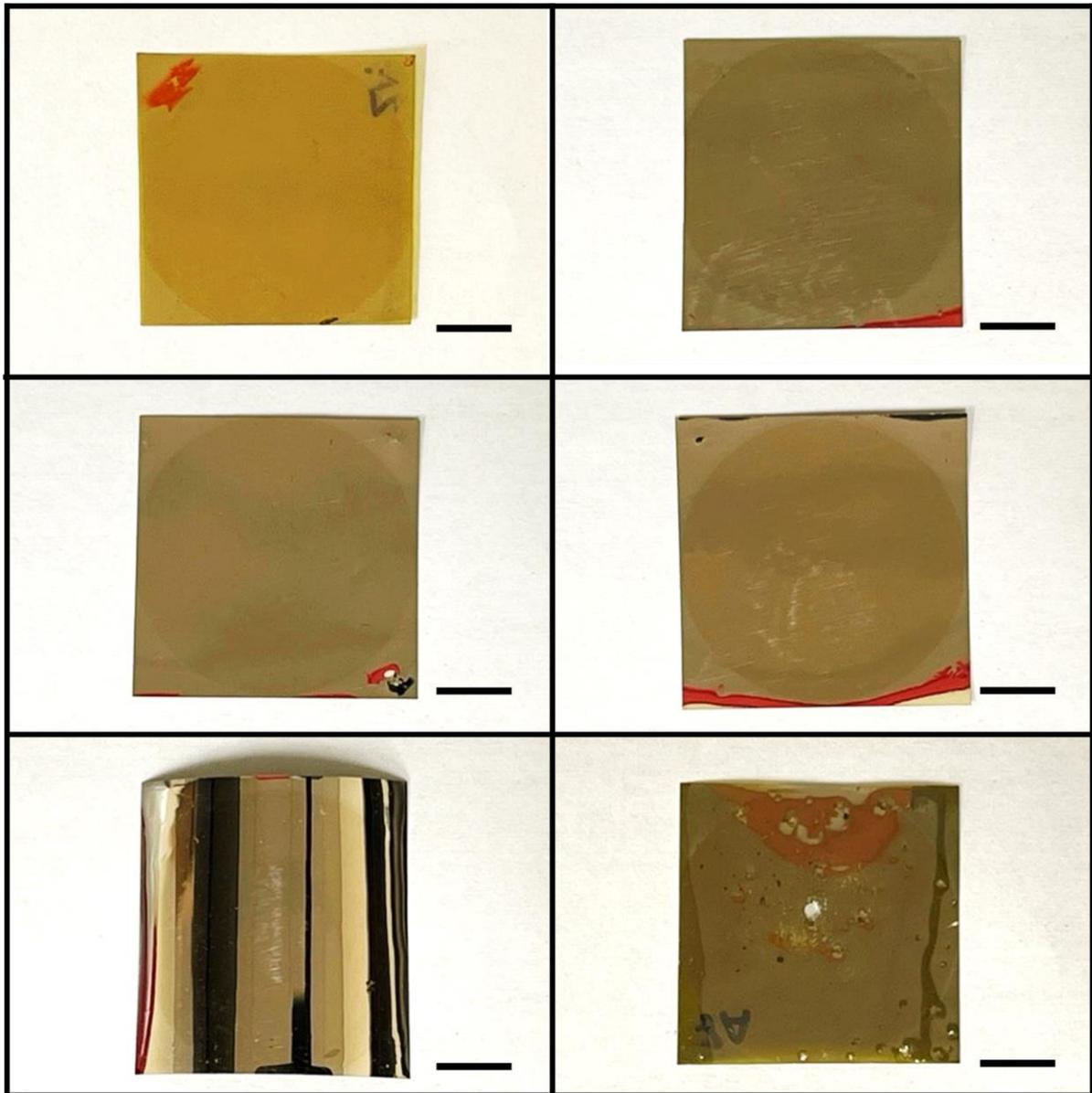
Figure 4.10. Optical images of the returned exposed palladium coated samples. The darkened ring in the centre is the area of the sample that was exposed to atomic oxygen. Scalebar represents 1 cm.

4.2.2.2 SEM Analysis of Palladium-Coated Foils that were not Impacted

The boundary line between atomic oxygen exposed and unexposed areas was visible in SEM images (for example, Figure 4.11). Such changes in brightness are not observed in the BSE images and indeed EDX spectra obtained from the exposed and covered regions exhibit no discernible differences between the two, suggesting the composition and chemistry of the two regions remain the same with no detectable (by this method/with this instrument) oxidation of the coating occurring.
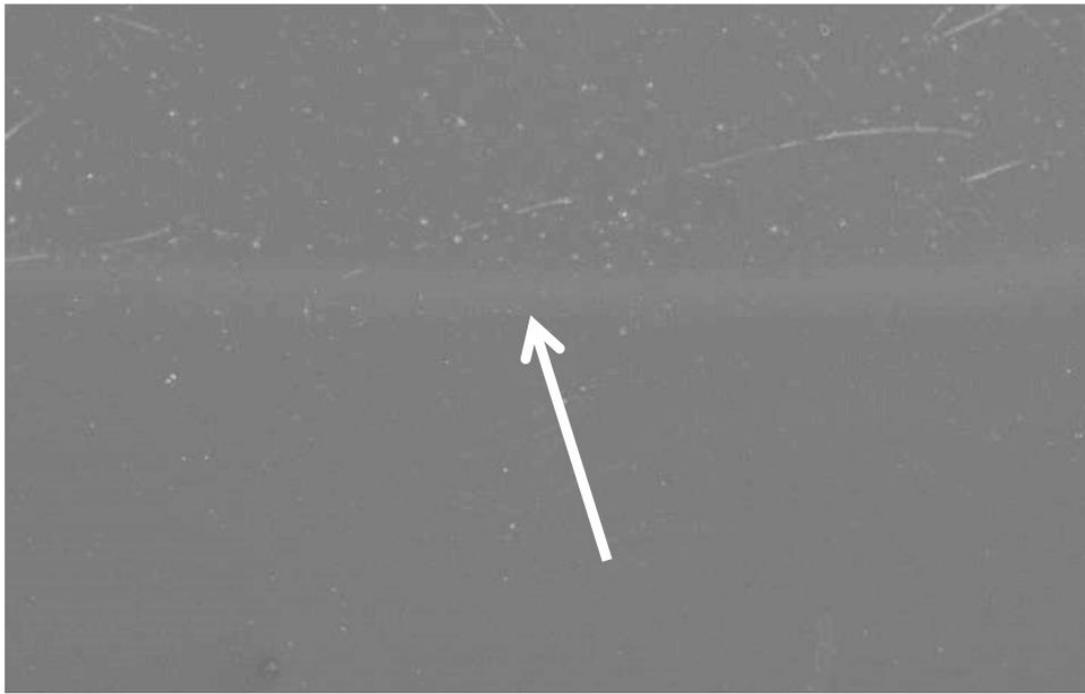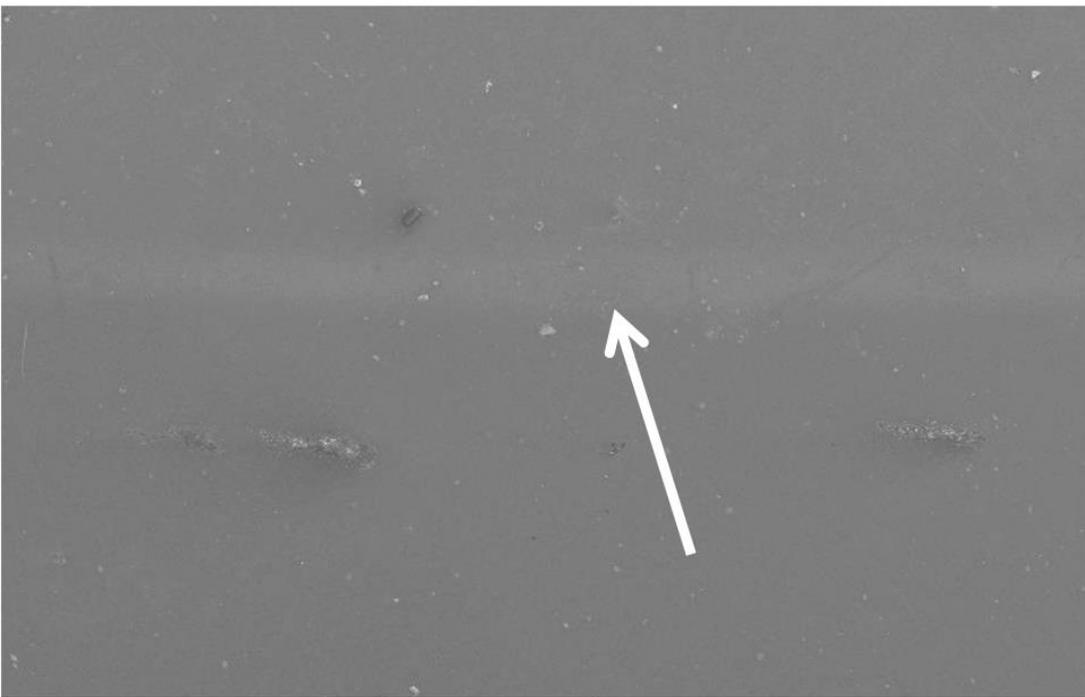
Figure 4.11. SE image showing the boundary line between atomic oxygen exposed and unexposed Kapton on the 10 nm and 100 nm Palladium-coated foils (location highlighted pointed by the white arrow).

The lack of oxidation found between the regions is consistent with the findings of Silverman et al. (1995) in which it was observed that there is no discernible difference between the exposed and covered regions of coatings on Kapton other than a dulling of the coating when exposed to atomic oxygen.

A more in depth analysis with SEM revealed differing extents of damage on the different coating thicknesses. The 10 nm palladium coating performed the worst out of the coated, unimpacted samples. There was widespread damage across the foil which likely exploited any imperfections in the coating (Figure 4.12).
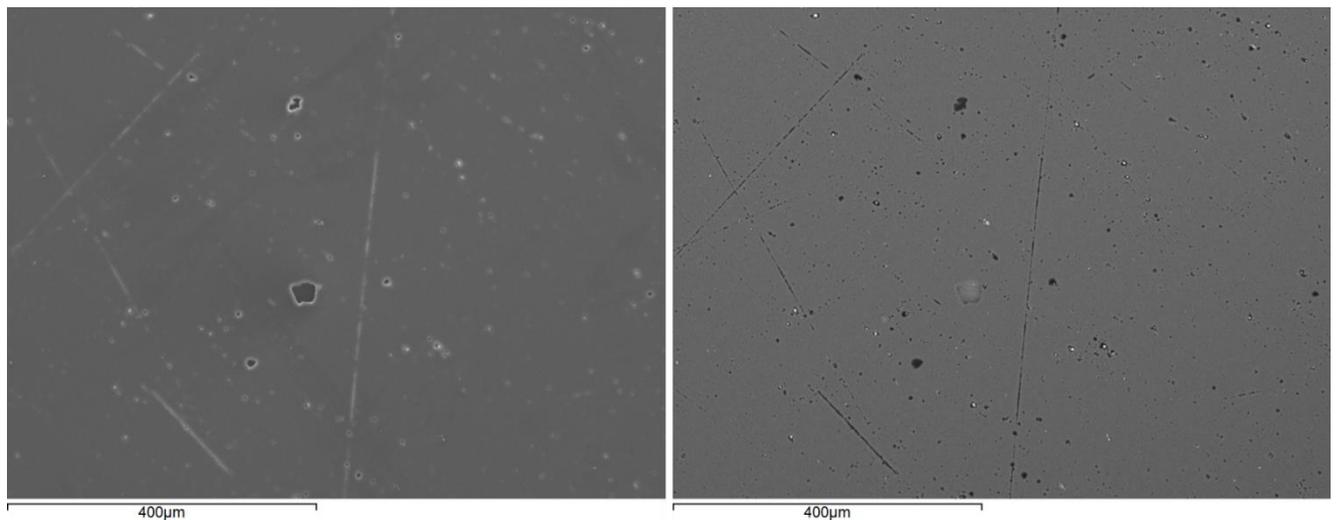
Figure 4.12. A wide view of the exposed area on the 10 nm coated foil. There are many different holes and line features visible on the foil.

The holes formed by the erosion do not have any rims and are non-circular in shape (Figure 4.13). The lack of a rim is a key indicator that the hole was not made by an impact and was created by atomic oxygen, although impacts at velocities of 1 km/s also do not have rims. It is highly unlikely that ODIE would experience any impacts in LEO that are at such low speeds but it may be possible if the particle was released from the body that ODIE is deployed upon and hence the relative velocities of the impactor and detector are low.
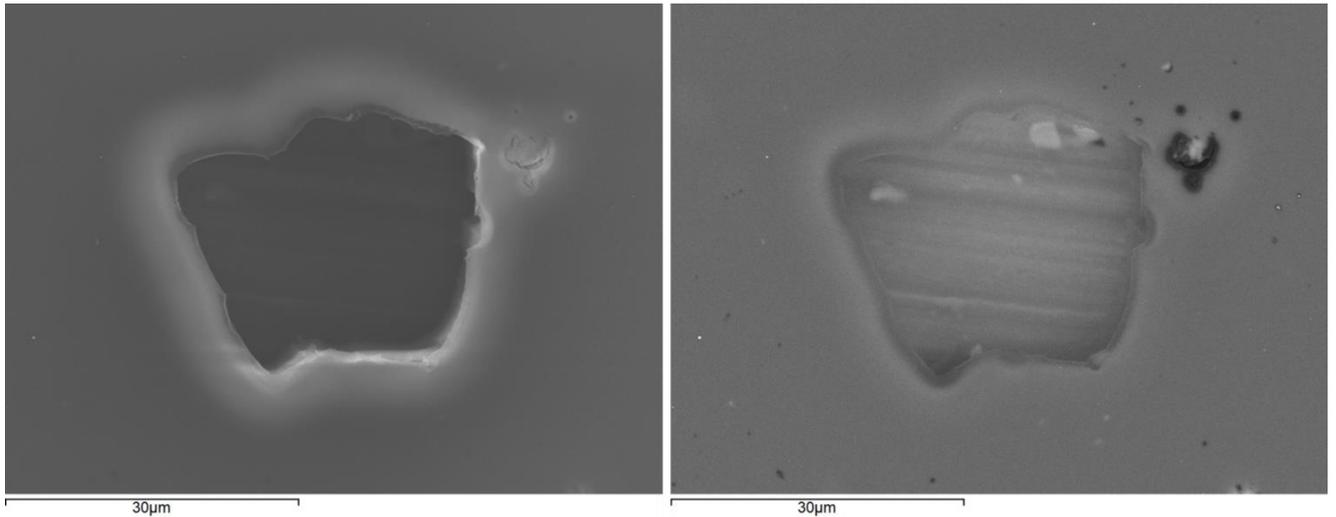
Figure 4.13. A hole created on the 10 nm coated foil by atomic oxygen. Notably, the hole is an irregular shape.

Features were found on the foil that were long, thin regions of erosion. These were not as a result of the small, straight channels that were characteristic of the coating as these are not linear in nature. Figure 4.14 shows a highly magnified image of the feature which shows that the Kapton remains intact through filaments that cross the chasm formed by erosion. These filaments are thin and fragile which resulted in them breaking due to the electron beam of the SEM, hence imaging them requires caution to preserve the feature. These long features are likely a result of undercutting where the atomic oxygen entered through a defect and then eroded the Kapton underneath the palladium. A feature like this occurring on ODIE would result in any impacts collected along or near this feature to be affected and potentially lead to the loss of data. As ODIE is modular in design, there are no major concerns with features such as this occurring occasionally as it would only damage a single module and not the entire detector.
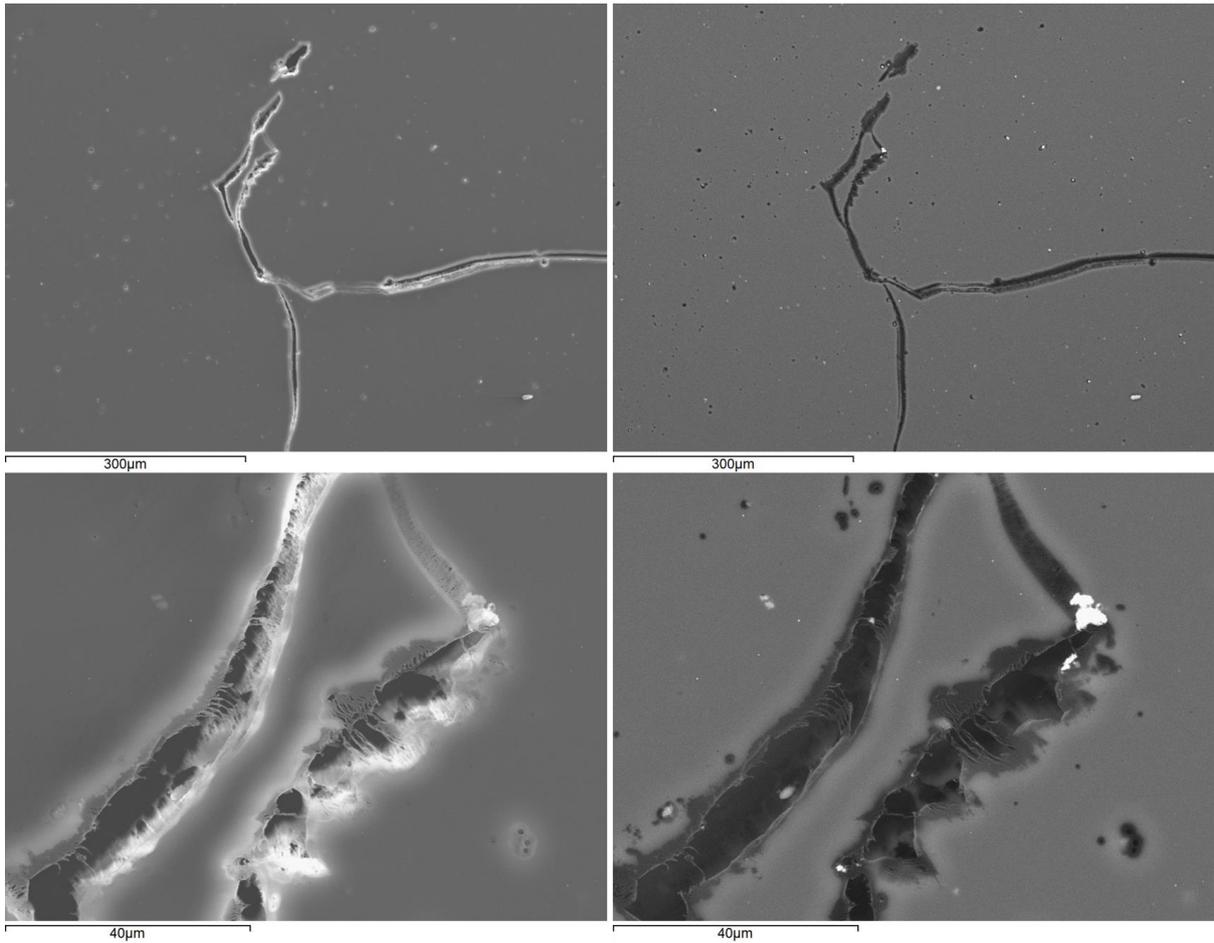
Figure 4.14. SEM SE (left) and BSE (right) images of long erosion features that spanned a large distance on the foil. Filaments can be seen in the lower images where the Kapton fibres are being eroded and some of these filaments broke under the SEM electron beam.

The boundary region shows the increase in damage on the exposed side versus the covered side of the foil. The BSE image shows no change across this boundary line leading to the conclusion that the chemical composition of the foil and coating remains unchanged after exposure. All thicknesses of coating showed the same result.
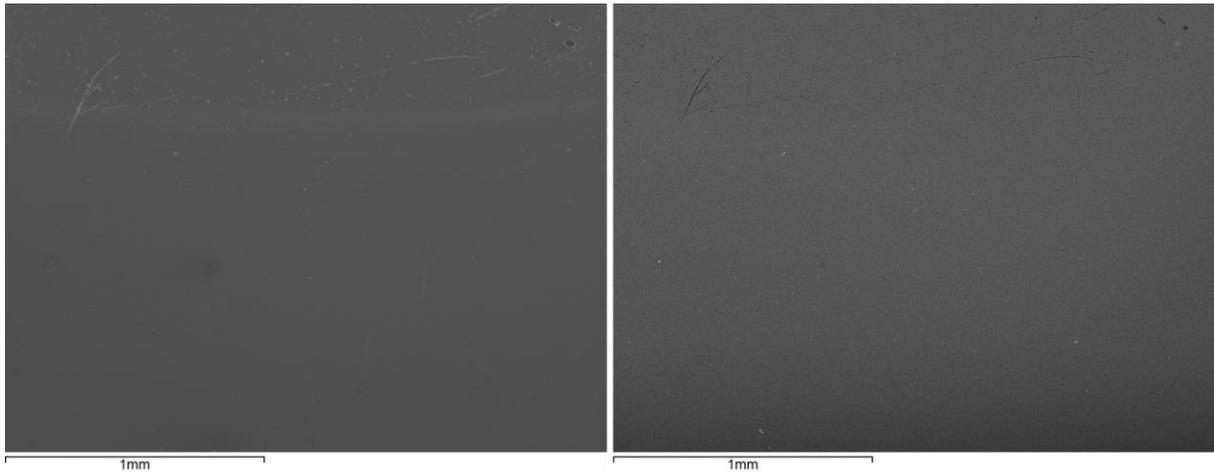
Figure 4.15. SE (left) and BSE (right) SEM images showing the boundary between the covered and exposed regions of the 10 nm palladium-coated foil. Only the boundary line can be seen clearly and the difference between the two sides is evident in the increased numbers of erosion features present on the upper exposed portion. The BSE image (right) show no change across the boundary.

There were some features present on the foil that were created through handling. As seen in Figure 4.16, there are two long straight lines with a build-up of palladium at one end of the lines. This indicated that this was potentially formed when the foil was being handled, maybe by tweezers as the two lines are parallel. Sputter coating can be removed by simply rubbing the coating gently and as such care must be taken when handling the samples. It is noted that in developing an analysis protocol for ODIE considerations must be made for the handling instrumentation that is to be used on the foils when constructing the detector as any defects in the coating creates a potential entry point for atomic oxygen to erode the foils. This feature was likely created post-exposure as there is no notable damage along the scrape that would be indicative of atomic oxygen erosion.
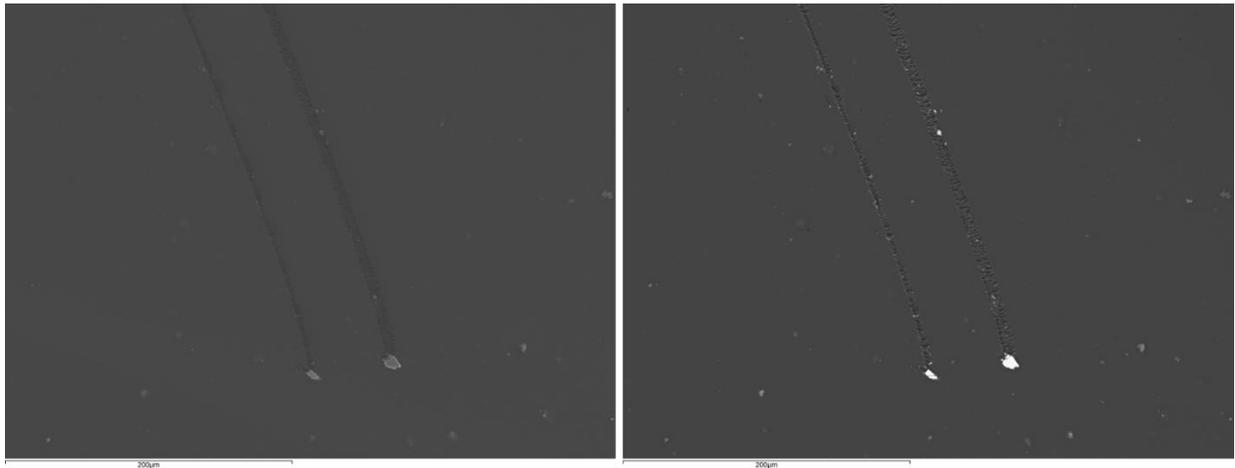
Figure 4.16. Two long scrapes present on the foil. These may be from tweezers or some other handling effect as there is a build-up of the coating that was removed at the bottom of the feature. This probably occurred before exposure as there is some atomic oxygen erosion of the exposed Kapton.

In general, the foils all looked similar, with some regions of damage on the foils and holes being easiest to spot with the BSE image as black spots. It appears that when the atomic oxygen creates an erosion feature, seemingly most common by exploitation of a coating feature, it tends to be an extended feature that is expanding across the surface. The BSE image in Figure 4.17 shows darker regions surrounding the feature which are regions where potentially the Kapton beneath the palladium has eroded away.

For the purposes of ODIE this general erosion mechanism could severely impact the impact features collected on the foils. This highlights that if there is a point that atomic oxygen can access the Kapton the extent of the damage can be much greater than it seems on the surface. In this study the back surface of the foils was not studied as we did not have a suitable mounting method such that the sputtered coating would not become rubbed off of the foil surface it were placed coating side down. This could be a line of investigation to be able to determine the exact extent of the damage on the back surface of the foil.
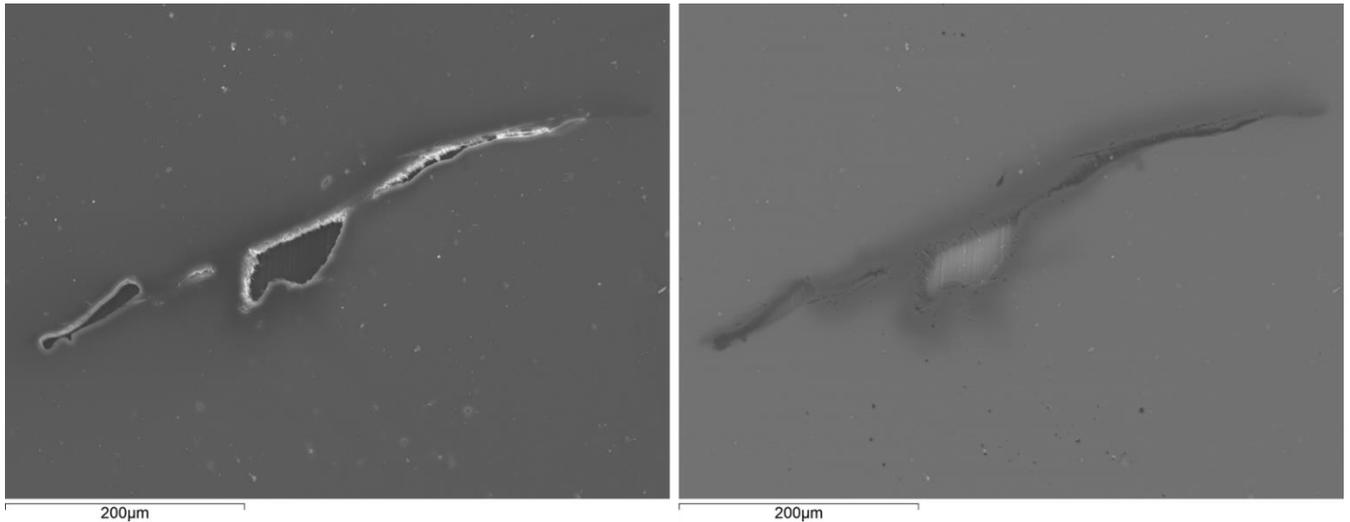
Figure 4.17. SE (left) and BSE (right) SEM images of a big, long feature that appears to have expanded into a hole in the centre of the feature. Dark regions may be undercutting, where the atomic oxygen has removed Kapton beneath the palladium coating in these regions.

4.2.2.3 SEM Analysis of 10 nm Palladium-Coated Foil (impacted prior to atomic oxygen exposure)

SEM images obtained of the impacted foil before and after exposure to atomic oxygen show clear evidence that this foil suffered greater erosion that the unimpacted foils (Figure 4.18): the penetration holes appear to have expanded, which is particularly evident for the large central hole generated by the 1 mm basalt where the edges of the central rim eroded to conjoin with the other nearby smaller impacts, although similar behaviour is observed for almost every other hole and impact feature. The post-exposure foil was difficult to image as there were many points on the foil where Kapton had become exposed as a result of the atomic oxygen. This led to charging across the foil with the minimal amount of disconnected palladium coating not being sufficient to dissipate the charge that built up across the foil.

The yellow arrows depict holes that initially were only just touching with the rims of these holes visible in image A (pre-exposure) that have had these rims eroded in image B (post-exposure) by the atomic oxygen. The impacts created avenues of entry for the atomic oxygen through the exposed edges of the Kapton within the centre of the holes but also in cracks in the coating around the impact features. This expansion of features occurred across the foil to every impact. The likelihood of having impacts in LEO that are this dense and closely located is low, hence this should not have a noticeable impact on the identification of individual impact features on the detector.

It is to be noted, however, that, as mentioned previously, the back surface of the foil was not examined. Therefore the effect of having impacts, especially a large central impact, where the impacts themselves create entry points for the atomic oxygen has not been quantified in this study. In future work this would be a key area of interest because, as noted above, any small defect can erode the underlying Kapton and hence, the rear side of the foils should be investigated to determine if there is any Kapton left or if it is predominately palladium that is holding the foil together.
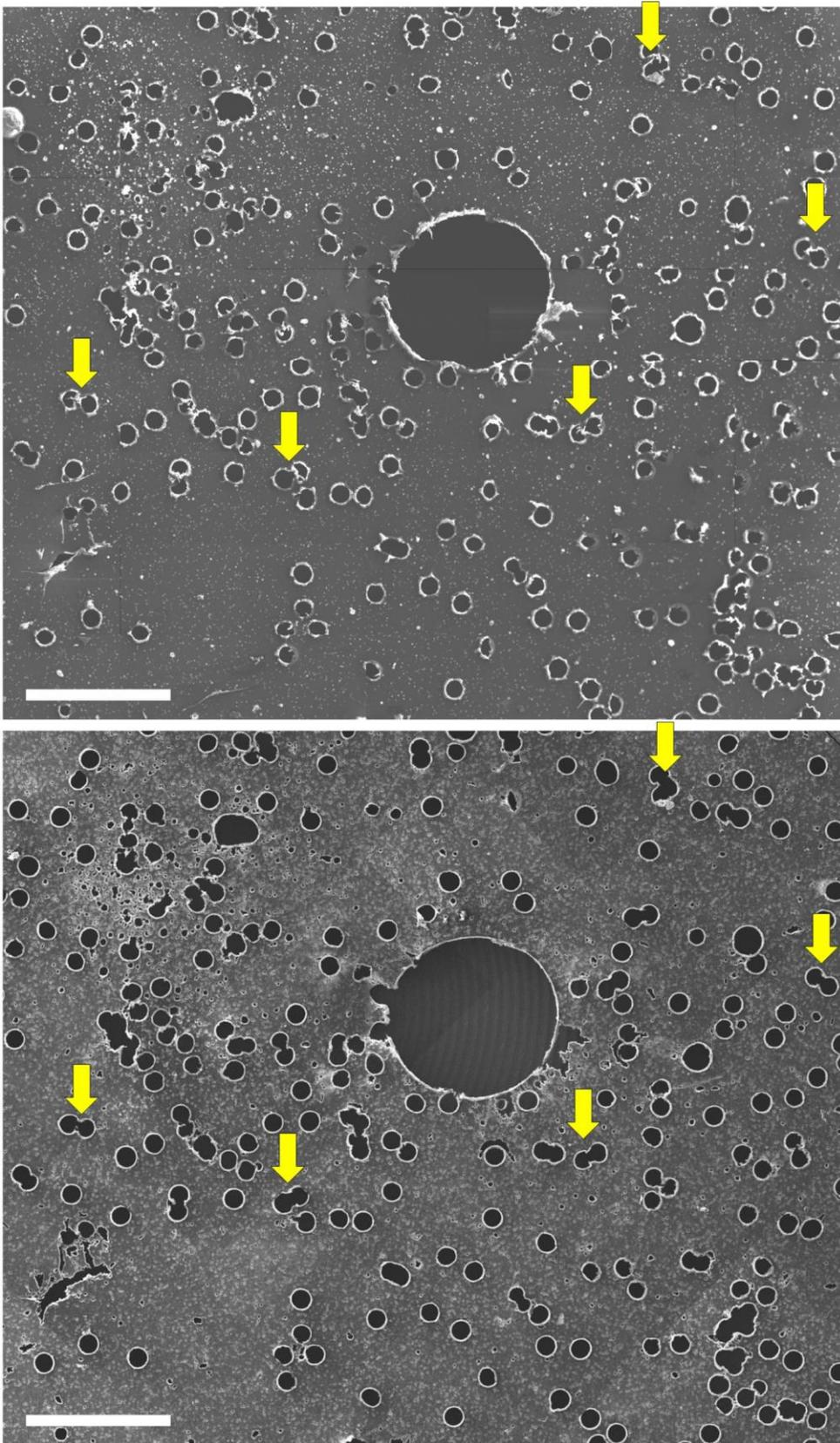
Figure 4.18. SEM images of the impacted 10 nm foil pre (top) and post (bottom) exposure to atomic oxygen. Yellow arrows highlight examples of holes that were, prior to exposure, touching but discrete, and post-exposure have had the boundary between them eroded.

The size difference between the pre and post-exposure impact features is predominately due to the exposed Kapton on the inner section of the hole being eroded. This alteration changes the measurement for the inner through hole although there are not notable consequences on the preservation of the hole size based upon the rim of the feature. It is thought that since the rim is comprised of folded over material that is much more dense than its surrounds this protects the rim from considerable erosion (Figure 4.19). Measurements of the hole diameters for impact features >80 μm in diameter and on the impacted 10 nm palladium coated foils that were and were not exposed to atomic oxygen revealed an average size of the central hole measurement of 130 ± 5 μm and 108 ± 1.1 μm in diameter respectively. Exposure to atomic oxygen therefore appears to result in a ~20% increase in impact feature diameter due to erosion of the underlying Kapton. Further work is needed to determine whether this size modification varies with the original impact feature dimensions. However, rim-to-rim measurements for the non-exposed features are 125 ± 12 μm and 134 ± 3.3 μm for the exposed features. These impact features differ by ~6% and thus may provide a better means for quantifying relationships between impactor and impact feature dimensions. This smaller difference implies that the diameter measurements to be taken from these impact features should be taken on the rim of the impact features as the size information is preserved more than that of the central hole
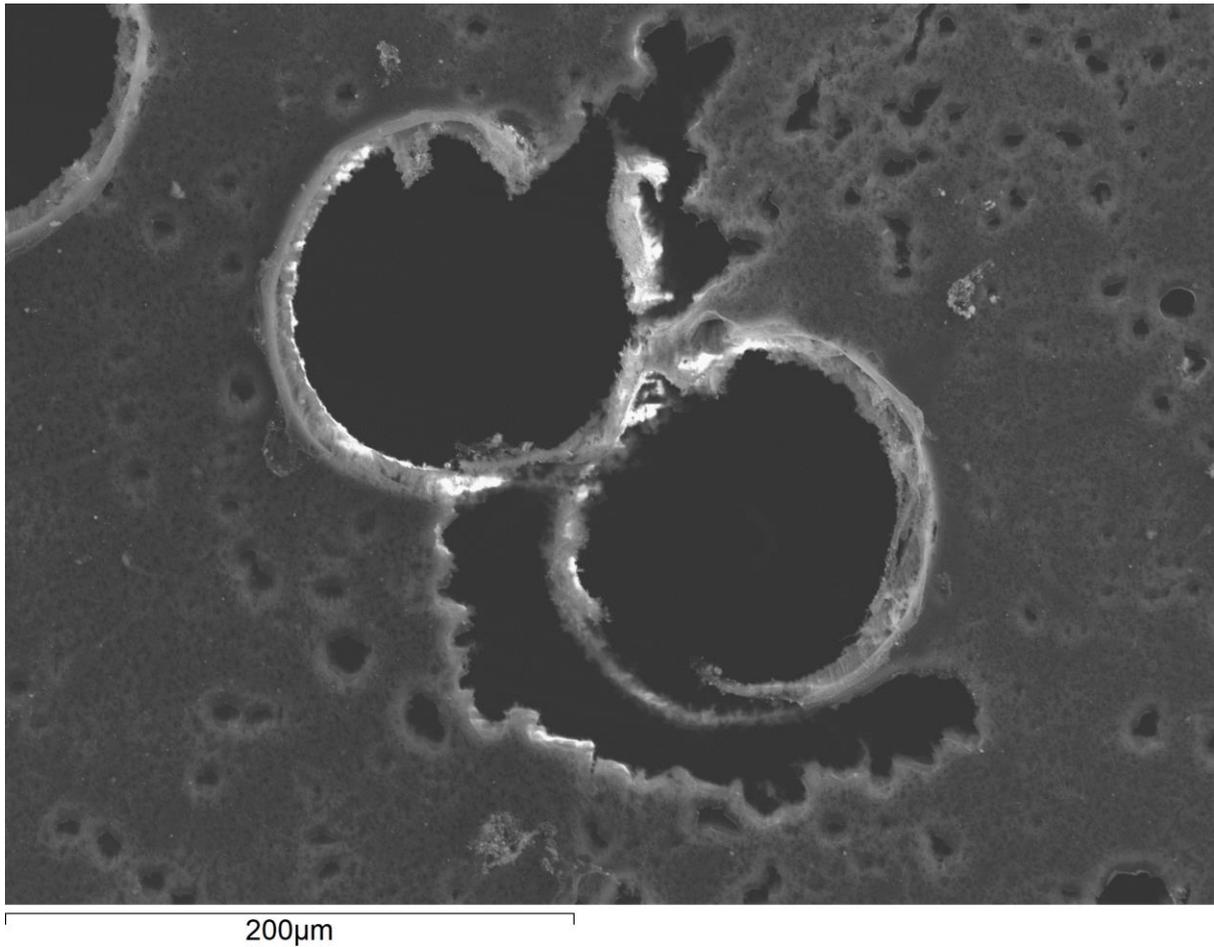
Figure 4.19. Eroded impact features showing that in parts only the rim remains whilst surrounding material has been destroyed.

On closer inspection at higher magnification, a large amount of pitting of the surface is observed, indicating undercutting visible across the entirety of the surface (Figure 4.20). This is characteristic of a surface that is being destroyed by atomic oxygen and is what the uncoated sample would have looked like midway through being annihilated. This type of damage occurring across the surface is highly destructive and indicates the foil wouldn't endure a much longer term exposure. Undercutting likely occurred due to vulnerabilities in the coating surface produced during the LGG shot.
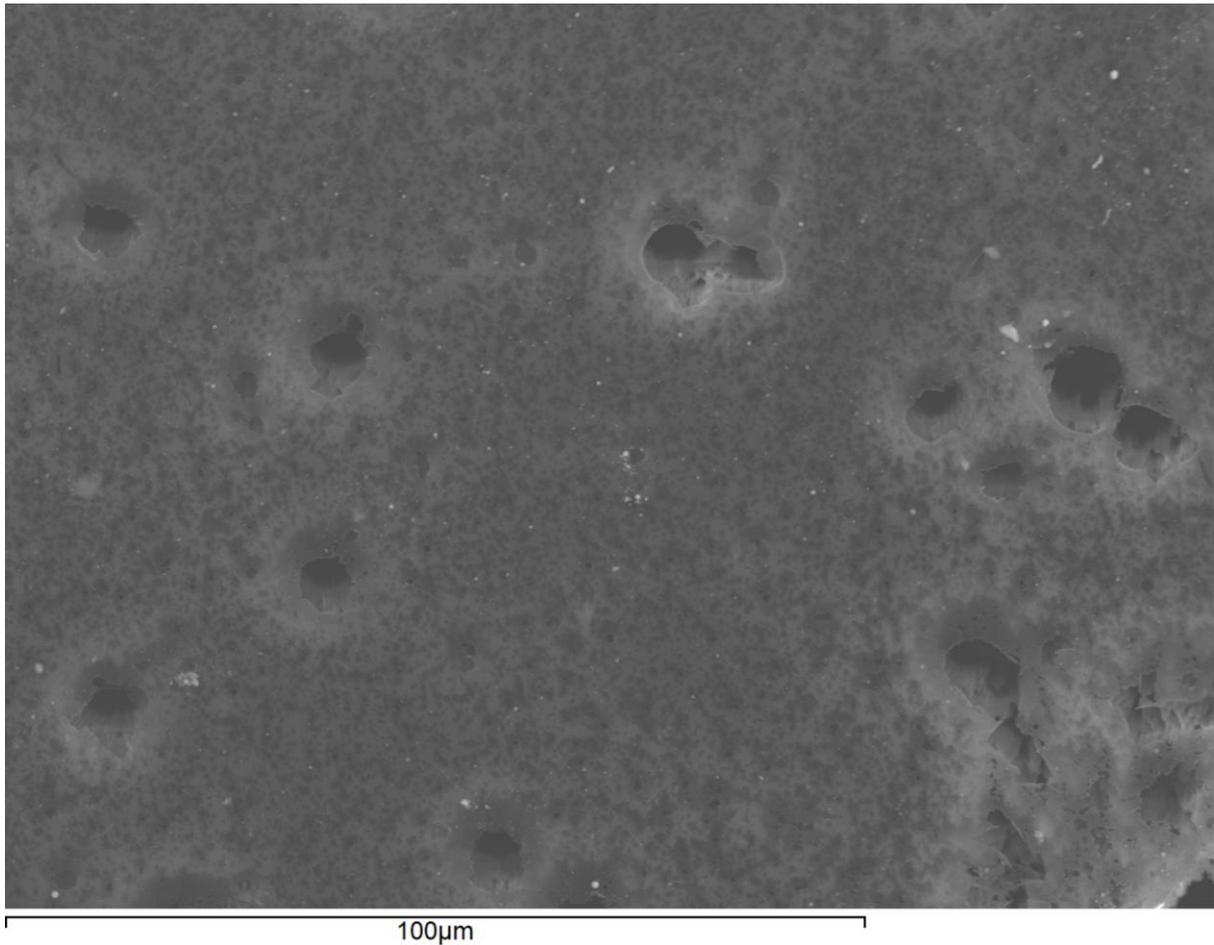
Figure 4.20. SEM image of atomic oxygen eroded surface of the impacted 10nm Palladium-coated Kapton foil. The small hole-like features are "pits" that have formed due to atomic oxygen undercutting.

The shots performed with the LGG are not optimal at reproducing the degree of impacting anticipated for our collected when exposed in LEO for ~1 year – projectiles are concentrated over a small impact region and are far more numerous. The outcome of this is that the entirety of the foil was riddled with impacts, which would exacerbate mass loss on exposure to atomic oxygen since every little crack, hole and crater creates an opportunity for the erosion of the underlying Kapton. In LEO, the number of impacts expected would be much less than what we have shot at our samples, thus the damage observed (and mass loss – see next section) of the impacted sample is a worse than worst case scenario for that foil.

4.2.2.4. Mass Loss Recorded for the Different Atomic Oxygen Exposed Foils

The mass loss of the samples was calculated from the recorded mass pre and post atomic oxygen exposure at ESTEC (see Table 4.2). These values represent the mass loss in the exposed circle of the foil as this was the section that actually experienced the atomic oxygen erosion, a circle of radius 2 cm. The fluence over the entire sample holder was normalised to one year exposure in LEO as the different locations on the holder were exposed to different levels of atomic oxygen due to the nature of the experiment (see method and Figure 4.21).
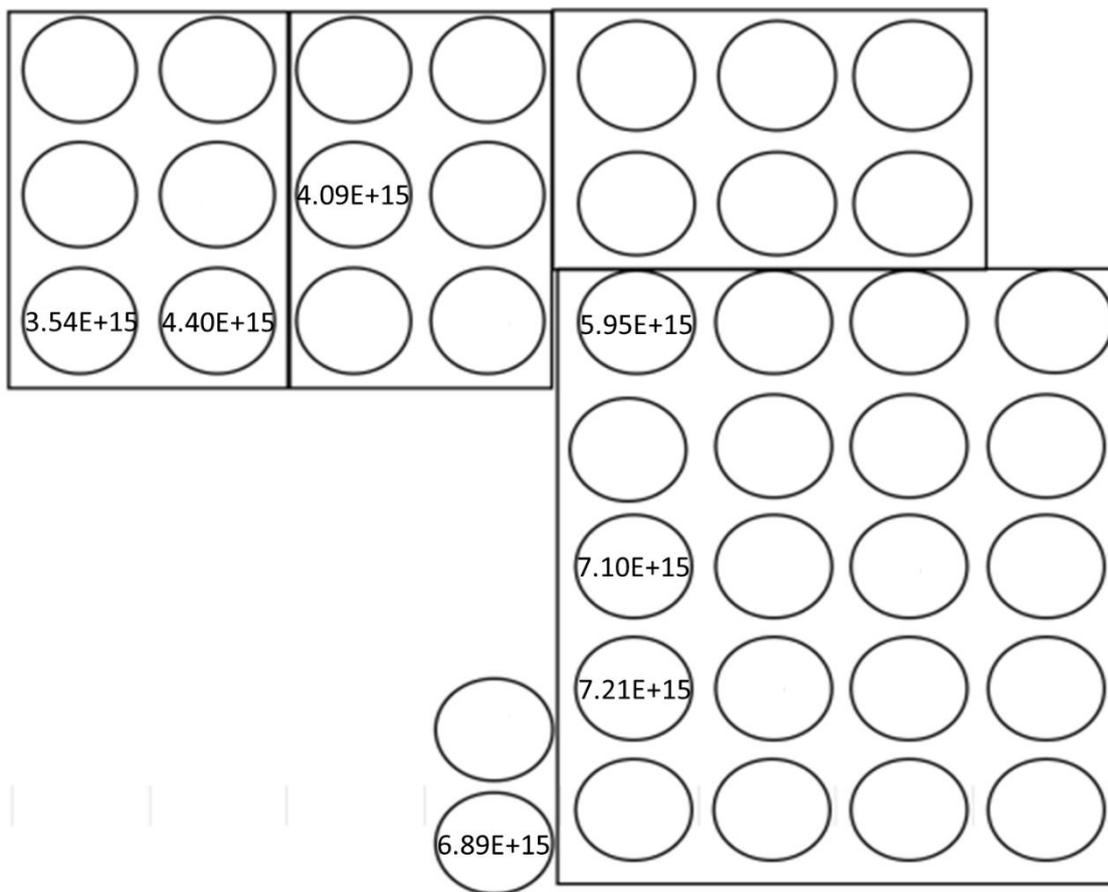
Figure 4.21. Diagram of the sample holder showing individual sample positions. Calculated fluence values are shown for the positions occupied by our samples.

The normalised fluence versus the mass loss per unit area is plotted in 4.20. The uncoated 25 μm Kapton sample is not plotted since it was completely destroyed. The sample that underwent hypervelocity impact prior to atomic oxygen exposure lost a significantly higher mass than the rest of the Palladium-coated samples – it lost twenty times more mass than its unimpacted counterpart and is also not present

as it is off the scale of the plot. Table 4.2 shows the initial and final mass of the foils that were exposed and the normalised fluence that each foil experienced. The percentage mass loss is shown with the uncoated Kapton mass only a result of the corners that were used to hold down the sample during the experiment.

Coating Thickness	Initial Mass (mg)	Final mass (mg)	Normalised Fluence (atoms/cm^3)	Percentage Mass Loss
Uncoated	12.99	2.17	0.33	83.26
10 nm	12.91	12.84	0.28	0.56
25 nm	13.89	13.87	0.21	0.09
50 nm	13.94	13.92	0.19	0.19
75 nm	14.80	14.78	0.32	0.10
100 nm	15.11	15.07	0.34	0.22
Impacted	13.68	12.26	0.17	10.38

Table 4.2. The mass loss for the different foils is shown with the normalised fluence that each foil experienced.

In contrast to these two, all other samples survived making it clear that palladium is suitable for protecting polymers against atomic oxygen erosion. Of these foils, the thinnest coating, 10 nm, suffered the most mass loss, as would be expected. However, the levels of protection provided by the other thicknesses of coating do not follow the expectation of a linear trend of the thicker the coating the better the protection. Based purely on the mass loss, the best protection of the underlying Kapton was by the 75 nm coating, then the 25 nm coating, the 100 nm and finally the 50 nm coating (Figure 4.22). This unexpected non-linear trend could possibly be explained by the quality of the coating. As noted in Section 2.1 the coating process was not done within the confines of a clean room, and therefore dirt, dust and other small particulates in the air could have settled on the surface of the Kapton prior to coating resulting in defects on the surface. Imperfect coatings have areas that are thicker, thinner and bumpier which can lead to varying amounts of erosion across the whole surface, especially with areas that are thinner, potentially due to some particulate under the surface. It is probable therefore, for example, that the 25 nm coating may have fewer imperfections than the 100 nm and 50 nm coating, leading to the improved protective ability.
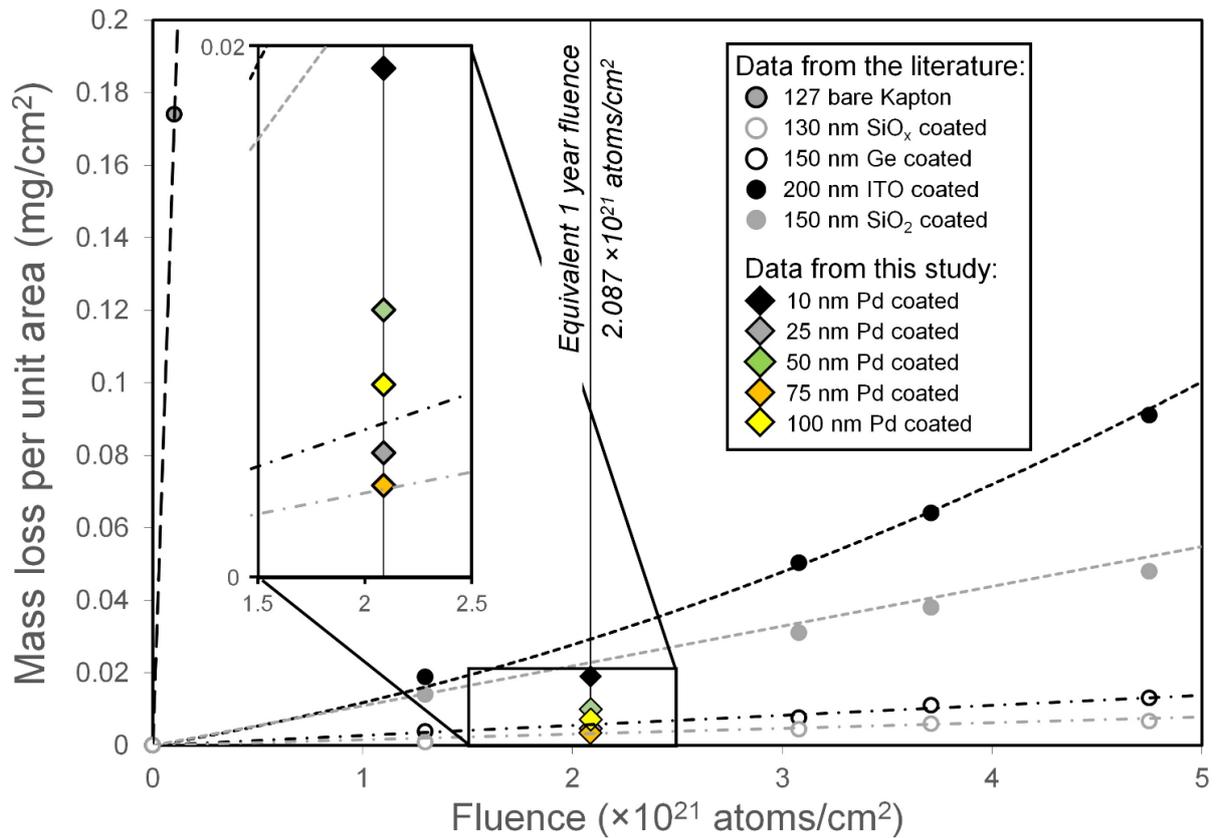
Figure 4.22. Plot of fluence versus mass loss with a vertical line representing the annual fluence that the material would experience in orbit. The Palladium coatings outperformed the indium titanium oxide and the SiO$_2$ coatings in protection of Kapton.

In Figure 4.22, data from this study are also plotted against data from the literature for different Kapton coatings as well as uncoated Kapton (Silverman, 1995). The uncoated Kapton performs the poorest as is evidenced by the near vertical line on the plot highlighting the vulnerability of the material to atomic oxygen. Other coating types have varying degrees of success in protecting the Kapton from erosion, least effective of which is 200 nm indium titanium oxide (ITO) showing almost direct proportionality between the increase in atomic oxygen fluence and the mass loss of the sample. Improving on this level of protection is the 150 nm SiO$_2$ coating, followed by the 150 nm Germanium coating and then the 130 nm SiO$_x$ ($1.9 < x < 2.0$) coating. These coatings are all commonly used on space-exposed surfaces, e.g. germanium coated black Kapton is used as a heat shield on antenna as it remains transparent in the radio wavelengths whilst protecting the Kapton against atomic oxygen erosion. It would be expected that SiO$_x$ would perform the best out of this sample group as, upon exposure to atomic oxygen, the oxidised portion of the coating performs a self-healing function with any gaps in the coating being filled in by this effect.

The data collected in our experiment is plotted along a line representing the fluence experienced in an orbit of 400 km for one year (Silverman, 1995). The data were normalised to this fluence as they all experienced different levels of exposure due to their placements in the sample holder. Figure 4.20 shows that the 10 nm palladium coating is the worst performing out of those plotted although all coatings show a better performance than that of the 200 nm ITO and 150 nm SiO_2 coatings. The 25 nm and 75 nm had a higher level of protection than 150 nm germanium, only being slightly worse than the 130 nm SiO_x coating.

Further, when comparing the atomic oxygen exposed, impacted 10 nm palladium coated foil to the 10 nm palladium coated foil that was exposed to atomic oxygen only, the degree of atomic oxygen damage is clearly much greater on the foil that was impacted, with abundant erosion pits visible across the surface. The impacted 10 nm coated foil shows complete erosion of Kapton beneath the palladium coating in areas and pitting across the exposed surface, facilitated by the large number of holes in the coating produced by impact, allowing entry of atomic oxygen. The undercutting effects on the surface are comparable to those observed by de Groh and Banks (1994) where there are pits and small channels created in the surface (de Groh and Banks, 1994). We note that the number of impact features produced on the foil in our laboratory by the light gas gun is far greater per unit area than would be anticipated during 1 year of exposure to atomic oxygen in Earth orbit and thus, this level of damage and mass loss should be regarded as an extreme upper limit. This result shows that palladium is a very effective coating for use in LEO in protection against atomic oxygen erosion; importantly, it is on par or better than many common coatings used today depending on the thickness employed.

4.3 Conclusion

The Palladium coating is resilient against hypervelocity impacts and atomic oxygen. The coating experiences cracking which becomes more noticeable for coatings above ~30 nm thick, and leads to delamination for coatings above ~50nm thick. Delamination is not ideal for ODIE as the residue that is deposited after impact would ideally stay on the detector rather than be lost with delaminating coating, and this exposes Kapton beneath to atomic oxygen which can erode and thus increase the apparent dimensions of the impact feature. Therefore, the recommended coating thickness would be less than 30 nm to preserve the coating after impact.

All coating thicknesses are effective at preventing atomic oxygen erosion with the 75 nm coating preserving the most mass. It was noted that the coating defects are highly susceptible to exploitation by atomic oxygen and consequently extreme care must be taken when making, handling and analysing the samples. The mass loss did not decrease linearly with the increase in coating thickness which may be a result of these coating defects. These results also suggest that a limitation on the thickness of the coating of less than 30nm is not a problem.

The impacted 10 nm Palladium-coated foil lost significantly more mass, twenty times more, than its unimpacted counterpart, but such a high impact density as produced in the LGG on this sample is extremely unlikely in orbit, hence represents a worst case scenario. Furthermore, since the impacted sample was still protected to a degree where the rims of the impact features were preserved and hole sizes could be determined, a particle flux would still be possible to determine even in such a worst case scenario. In conclusion, a palladium coating of less than 30 nm is recommended for use on ODIE.

Chapter 5: Initial Studies and Possible Further Work

5.1. Introduction

This chapter discusses the potential for further development of this project to encompass all impact scenarios possible on the ODIE detector, such as different velocities or impact angles, and to include the other analysis methods that can be used to study these foils. Each of these investigations were hindered in this study by limited laboratory access, finite resources with limitations on acquiring more materials and hence are only preliminary investigations. These are all cases that require further investigation before the ODIE detector would be suitable for deployment. The detector will likely be impacted by particles travelling at speeds much greater than the 5 km/s achievable with the LGG. This requires extrapolating our current results to higher velocities via modelling. The detector is also likely to be subjected to impacts at angles other than perpendicular impacts like the experiments we have previously conducted. This requires additional experiment with a variety of impact angles be conducted. There are also many other avenues for analysis that could be utilised in characterisation of the impact residues left on the foils. This could potentially be done with instruments other than SEM. There are also the other requirements of reaching a Technology Readiness Level (TRL) of 8 to be prepared for launch. Here, we discuss all these possibilities and the groundwork that has already been completed.

5.2. Modelling Impacts into Kapton Foils

Impacts in LEO take place at speeds much greater than those possible with the LGG at the University of Kent, typically taking place at about 60 km/s. These extremely high impact velocities pose a particular difficulty in calibrating materials and instruments for use in orbit as it is currently only possible to accelerate sub-millimetre particles to comparable speeds, as previously mentioned, with Van de Graff generators. Therefore, computational models are utilised in this regard to simulate the impacts at the high velocities experienced in LEO. One popular software for conducting these simulations is Ansys Autodyn which conducts dynamical simulations of impacts with hypervelocity capabilities. This software is designed for performing non-linear dynamics problems that are typically referred to as hydrocodes. Autodyn handles simulations of impacts, penetrations and explosions at various speeds and has a multitude of solution techniques and materials available in its libraries.

With this software it is possible to build material and projectile models to initiate impact scenarios. There are a multitude of modelling methods inbuilt within the software that can be used to simulate impacts that have benefits and drawbacks depending on the situation (Figure 5.1). Using the Smoothed Particle Hydrodynamics (SPH) model for the projectile within the simulation creates a more realistic

result for impacts in the hypervelocity regime versus traditional mesh or grid based Lagrangian and Eulerian methods as these methods suffer from mesh-tangling. This is a scenario where the mesh becomes ensnared upon itself and gives non-physical results, where SPH relies on nodes to perform its simulation and therefore has no mesh to entangle (Verma 2018). The following is an investigation into whether an Autodyn simulation can be built such that it would replicate the results observed in the LGG experiments for the different Kapton thicknesses, coating thicknesses and the two velocities of 1 km/s and 5 km/s. The models can then be used to increase the velocity of the impacting particle to ascertain the robustness of the relationship between projectile size and the size of the impact feature created at much higher velocities.
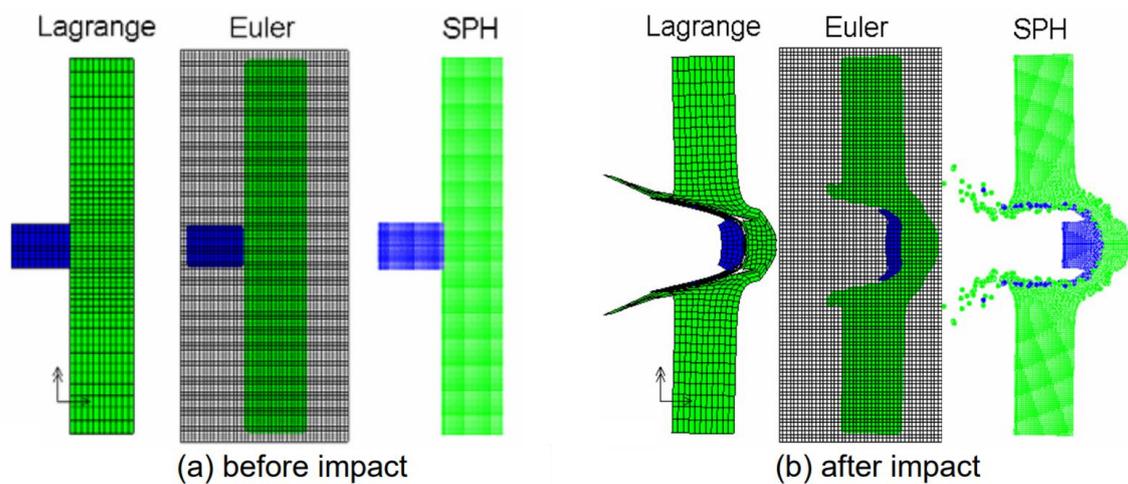
Figure 5.1. Examples of the different modelling techniques before (a) and after (b) impact using Autodyn (modified from Birnbaum et al., 2004). The projectile is in blue and the target is in green. In the Lagrangian method, the mesh is contained within the materials and behaves as a unit. The Eulerian technique has a fixed grid through which the material moves. The SPH method is comprised of nodes that contain the information on the dynamics of every particle a node represents at that point in time.

The Kapton foil is the target in these simulations and is modelled using Lagrangian techniques, which are commonplace for numerical simulations. These methods have efficient tracking of the interfaces of the materials and is capable of handling complex material models. The Lagrangian techniques use a grid based structure which can have the negative effect of becoming extremely warped and deformed if large deformations are caused to the grid relative to the grid size.

The projectile is modelled using SPH, with 956 nodes, which removes the grid from the Lagrangian method which is adaptable for complex material models. This method performs much like the Lagrangian method but allows for greater mobility of the internal nodes of the projectile rather than the

rigidity of the grid in the Lagrangian technique. This combination of the target using Lagrangian methods and the projectile using SPH is the common practice for performing hypervelocity impact simulations with Autodyn as it gives the most realistic results.

5.2.1 Method

The projectile was made of a 100 µm sphere of "floatglasb" which is a material in the Autodyn database. This uses a density of 2.53 g/cm^3, the Johnson-Holmquist strength and failure models. The target was comprised of the Teflon reference material in the database as Kapton was unavailable and thus this simulation relied upon the similarity between Teflon and Kapton. The density of the Teflon in the database is 2.16 g/cm3 and the von Mises strength model and Geometric Strain erosion model were used. The simulations were conducted using axial symmetry, which assumes the interaction to be symmetric as to be expected of a circular impactor into a target comprised of a singular material, to speed up computation time (Figure 5.2). The speeds of 1 km/s and 5 km/s were used along with investigating the thickness of the foil. The thicknesses used were 25 µm, 75 µm and 125 µm as it was necessary to compare to the shots performed with the LGG to validate the models and hence the 13 µm could not be validated against experimental data and was not included.
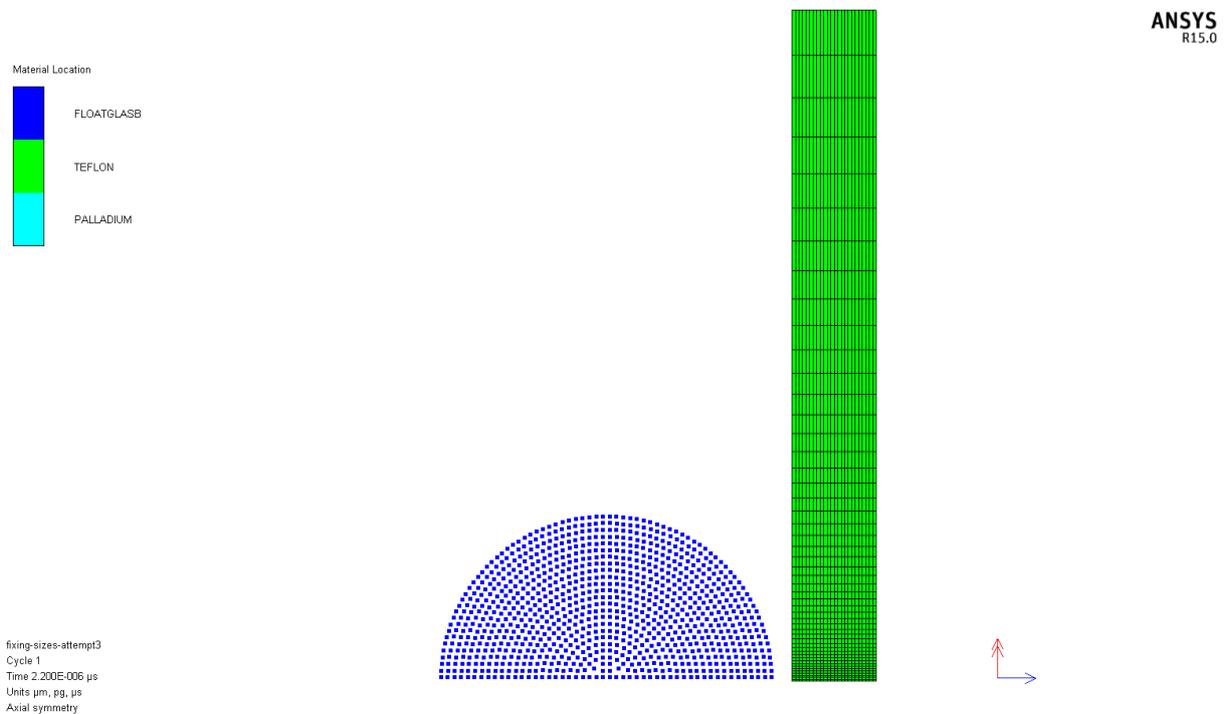
Figure 5.2. Initial setup of the simulation. The blue semicircle comprised of dots is the SPH projectile and the green rectangle is the Teflon target with the mesh grid visible in black.

5.2.2. Results

The measurements of the diameter of the impact features created on the Teflon in the simulation were measured from the hole location only and not the rim. The rim was not produced in these simulations to a satisfactory level as this would require much more computation time than was possible. The diameter measurements are similar for the 25 µm foil at 1 km/s and 5 km/s but the simulations give much different results for the thicker foils. Notably, the simulation of the 25 µm foil at 1 km/s also produces holes that are much smaller than that of the original impactor size, confirming that this is indeed a feature of this foil. The cause of this discrepancy could potentially be the result of the shear or strain models not representing the Kapton foil accurately. The cells are also not optimised for the failure mode of Kapton in this simulation and therefore are not calibrated for representing our LGG experiments accurately.

Kapton Thickness (µm)	5 km/s Experimental Diameter (µm)	5 km/s Simulated Diameter (µm)	1 km/s Experimental Diameter (µm)	1 km/s Simulated Diameter (µm)
25	106 +/- 1.1	107	65.1 +/-0.8	67.5
75	107 +/- 2.0	126	121 +/- 4.5	91.1
125	96.8 +/-1.3	117	101 +/- 0.6	93.2

Table 5.1. Comparison of the diameter measurements across the different thicknesses of Kapton in the LGG experiments and the simulated impacts. Only the simulated 25 µm Kapton foil showed a reasonable agreement with its experimental counterpart.

The simulations, overall, struggled with the erosion in the model where the foil became thinner as the projectile progressed through the material the foil did not break in a physical manner. This led to some difficulty in creating the models which was circumvented by changing the zoning on the target foil. Graded zoning was introduced to increase the number of cells in the centre of the foil where the projectile impacts, thus creating more cells and improving the erosion of the Teflon foil. This allowed the projectile to break through the foils but did not solve the problem of the erosion of elements, which would potentially lead to the production of a rim but currently only produced long, linear elements that remain attached to the foil as in Figure 5.3.
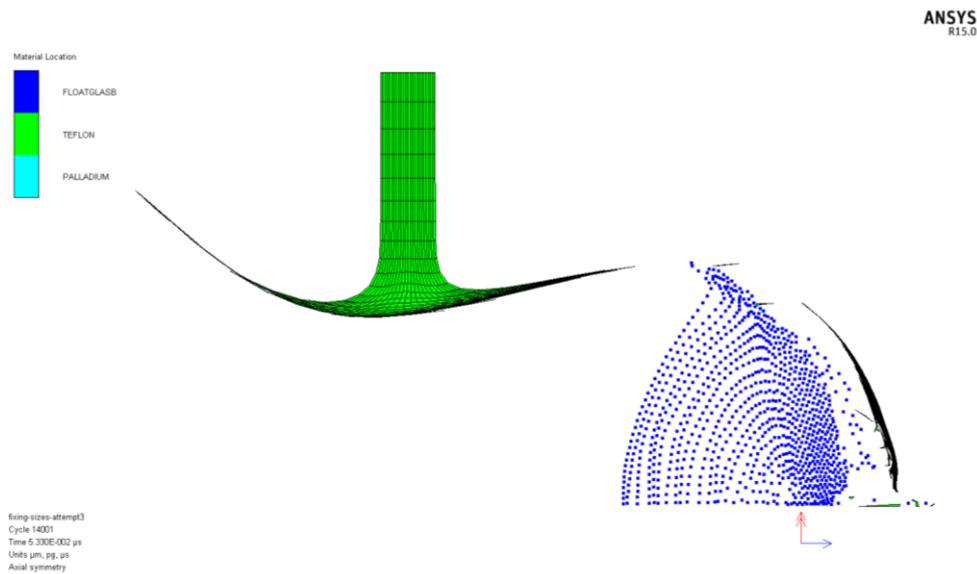
Figure 5.3. Post-impact of the simulation. The long straight segment to the left of the figure is the failure in erosion of the target material.

To accurately model the erosion of these elements to produce results analogous to the observed experimental data, an investigation into the erosion of the elements and nodes would be required for much higher resolution simulations than were achieved here. These simulations would also be required to run for extended periods of time on larger targets as it is unclear as to the exact moment the Teflon foil stops moving after the impact. The limitations on access to the LGG and SEM laboratories led to the slow acquisition of the diameter data to validate the model, therefore our simulations were limited by computational power and reference data.

The simulations were then accelerated to 60 km/s to ascertain if the results obtained at 5 km/s are similar to impacts at a much higher velocity. This resulted in the material behaving in a fashion where the edges of the impact hole reformed back into the middle of the hole, which is a result of using a Lagrangian model for the target leading to mesh entanglement. One solution may be to use SPH for the target as well as that does not suffer the same deformation problems. However, it would take a lot more computing time and power to model the simulation using SPH for both the projectile and the target.

Potentially other modelling software or the creation of a new simulation would improve the results found or comparison between Autodyn simulations and other software would yield useful simulations. Another avenue for investigation would be to acquire reference material information for Kapton and determine the similarities between Kapton and Teflon in the Autodyn software. This would allow for more direct comparison of the Teflon simulations and the previously mentioned studies of Teflon measurement investigations.

5.3. Studying Residues and Developing the Analysis Protocol

The ODIE detector has the aim of being able to distinguish between the OD and MM populations through the analysis of the residues left behind on the surfaces of the foils as the impacting particles travel through the detector with a view towards optimising this process. The analysis of these residues can be done by many instruments and in this thesis we focused on using SEM. With SEM and FEG-SEM it is possible to get EDX spectra of the sample and therefore deduce the composition of the sample such as in Figure 5.4. This was shown by Kearsley et al. (2006) to be possible on the SFU MLI that was returned from space and the MULPEX foils which were shot in LGG experiments. The residue present on both sets of foils was enough to determine the origin of the impacting particles.
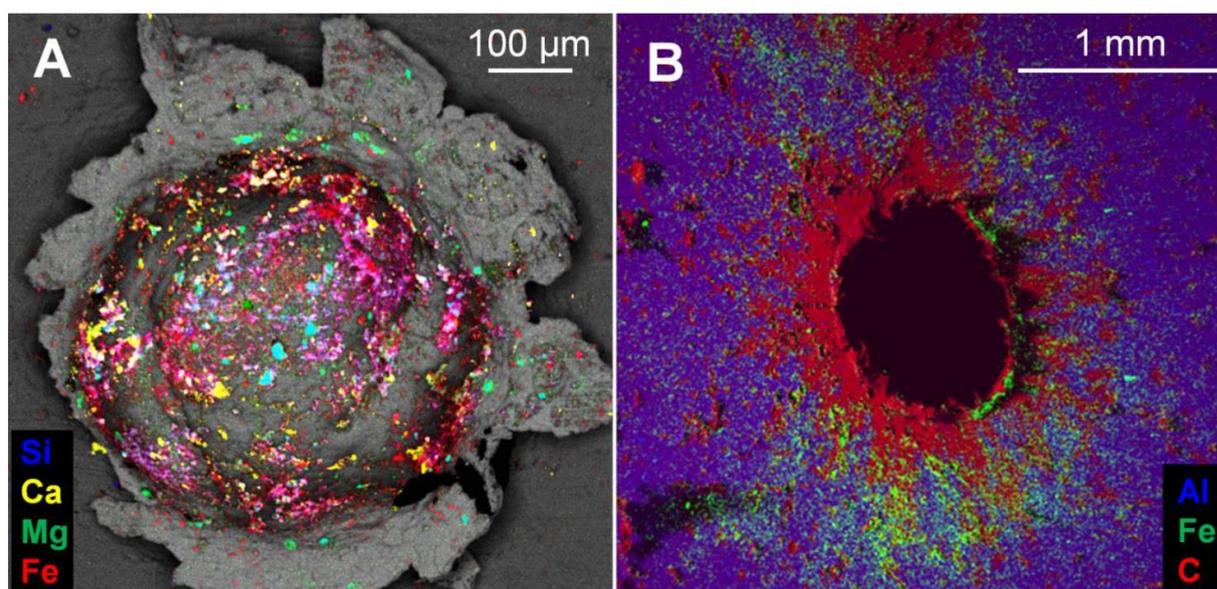
Fig. 1: Chemical map highlighting residue A: in a crater on LDEF Al clamp and B: around a penetration hole on MULPEX#1 foil.

Figure 5.4. Chemical maps on impact features from A) a crater on an LDEF aluminium clamp and B) a penetration hole in an impact experiment with the LGG (Wozniakiewicz et al., 2019).

The residue of OD is generally comprised of metallic elements such as aluminium or titanium, which is distinct to those of MM which are typically sulphur and silicon. The use of EDX on the samples can show the elemental composition of the residue on the impact site. Investigations into the residues could be performed using SEM or FEG-SEM, whereby the sample is mapped to obtain spectra of the sample, but this analysis for all impact features measured in this study would take a large amount of time to conduct. For significant residue to mapped takes a ~5 minute map on the FEG-SEM and over 20 minutes

for the equivalent map on the SEM. The limited laboratory access hindered progress in this area during the course of this project but showed that the FEG-SEM is capable of finding these residues.

The analysis of the small silica impacts was hindered by the resolution of the SEM with the effects of charging on the Kapton foil. An appropriate analysis method for these small impacts is required as the majority of impacts to ODIE in orbit are more likely to be in the smaller size regime. Initial investigations with the FEG-SEM proved to be capable of measuring the smallest diameters, although for the current impact samples it is unclear which features are created by debris or silica, thus necessitating cleaner shots to establish an analysis protocol for the smallest sizes.

Future studies to calibrate ODIE would require the determination of the optimum analysis protocol for the returned foils. This would involve improving on current methods used in this research for residue examination and identifying and measuring the diameters of impact features. The method used in this thesis was time consuming and slow for large quantities of impacts as it was all performed manually. There is potential for this to be automated using image processing now that the reference data base for the diameter sizes has been established. This data can be used in future to validate any image processing investigations into the automation of the diameter measuring process as Chapter 3 identified the optimum measurement location to be used. The hole measurement could be automated using an erosion filter to remove the frayed inner edges of the impact holes to then measure the hole diameter. Fine tuning this algorithm would enable the realisation of the easily identifiable feature goal of ODIE.

5.4. Further LGG Experiments

While many shots were conducted over the course of this study, more shots under different conditions would aid in calibrating the foils exactly for the swift identification of impact particles and features post-flight. This was not possible during this investigation as there were limitation on laboratory time and access.

5.4.1 Inclined Shots

In LEO, not all impacts would be occurring at a right angle. Depending on the pointing of the detector, there could be more impacts at a severe angle rather than perpendicular. Thus it is necessary to calibrate ODIE, or any detector for that matter, for impacts at an angle. To do this, an angled mount would be required for the LGG. This is not feasible currently to do within the blast tank of the LGG due to the small dimensions of the blast tank and would need to be placed in the blast chamber. As reported previously, the blast tank was chosen due to its generally minimal gun debris and as such if the mount for inclined shots were to be placed in the target chamber, there would need to be some sort of debris

mitigation in place, otherwise the shots would not be suitable for analysis. This could possibly be done with a valve that is currently in development at the University of Kent. The valve would allow the projectile to pass through the aperture into the target chamber and then shut to stop any following debris from entering.

An investigation into the angles impacts on the foil would need to be shot at many angles (10°, 20°, 30°, 40°, 50°, 60°, 70°, 80°) to create a relationship between the angle of the impact and the size and shape of the impact feature made. The resulting diameter measurements would require the definition of new measurement locations as the impact would not likely create circular features as those previously measured here. As mentioned previously, the lighting of the impact feature can have an effect on the diameter measured and as such a new standard method of illuminating the sample may need to be adopted. The analysis protocol determined in Section 5.3 would need refinement with regards to the precise locations to search for the residue remaining on the foils. The investigation of inclined impacts would require the acquisition of another coating machine, making more foils to be shot and analysing these foils and hence required more resources, such as time and coating capabilities, than we had for this study.

5.4.2 Ballistic Limit

In order to determine the ballistic limit of the palladium-coated Kapton foils, a set of experiments were designed using discrete sizes of soda lime glass projectiles from Whitehouse Scientific of sizes 11 µm, 26 µm, 35 µm, 42 µm, 53 µm, 63 µm, 70 µm, 83 µm, 91 µm and 100 µm with the aim of finding which size projectile just broke through the foil. All powders were imaged with SEM to ensure the range of diameters was well constrained. For efficiency, two different sizes were to be shot at once which would cut down on the amount of shots needed and sizes that were much different were grouped with the first attempt being with the 42 µm and 91 µm projectiles (Figure 5.5). The shots were at 5 km/s with the same set up of using the powders within the sabot although in this case there was no 1 mm basalt sphere present in the sabot.
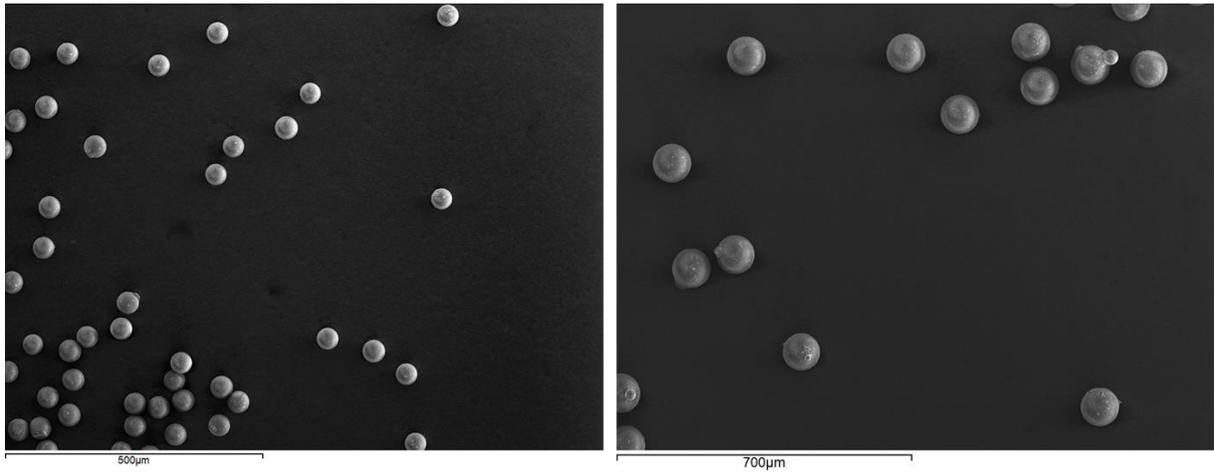
Figure 5.5. The 43 µm (left) and 91 µm (right) projectiles to be shot together imaged with SEM. There is a sphere in the top right of the 91 µm image that has a smaller sphere attached which may affect the diameter analysis.

There were impacts of all sizes found on the foil (Figure 5.6). This occurred identically for the repeat of the shot thus indicating that the broad range of sizes of impact feature that were seen on the two foils was not likely an occurrence of gun debris. All features were irregular in size, as shown in Figure 5.6, where there are only minimal circular impacts. In general, the soda lime glass spheres create circular features as discussed previously in this thesis and therefore the conclusion that the glass shattered during its flight was reached.
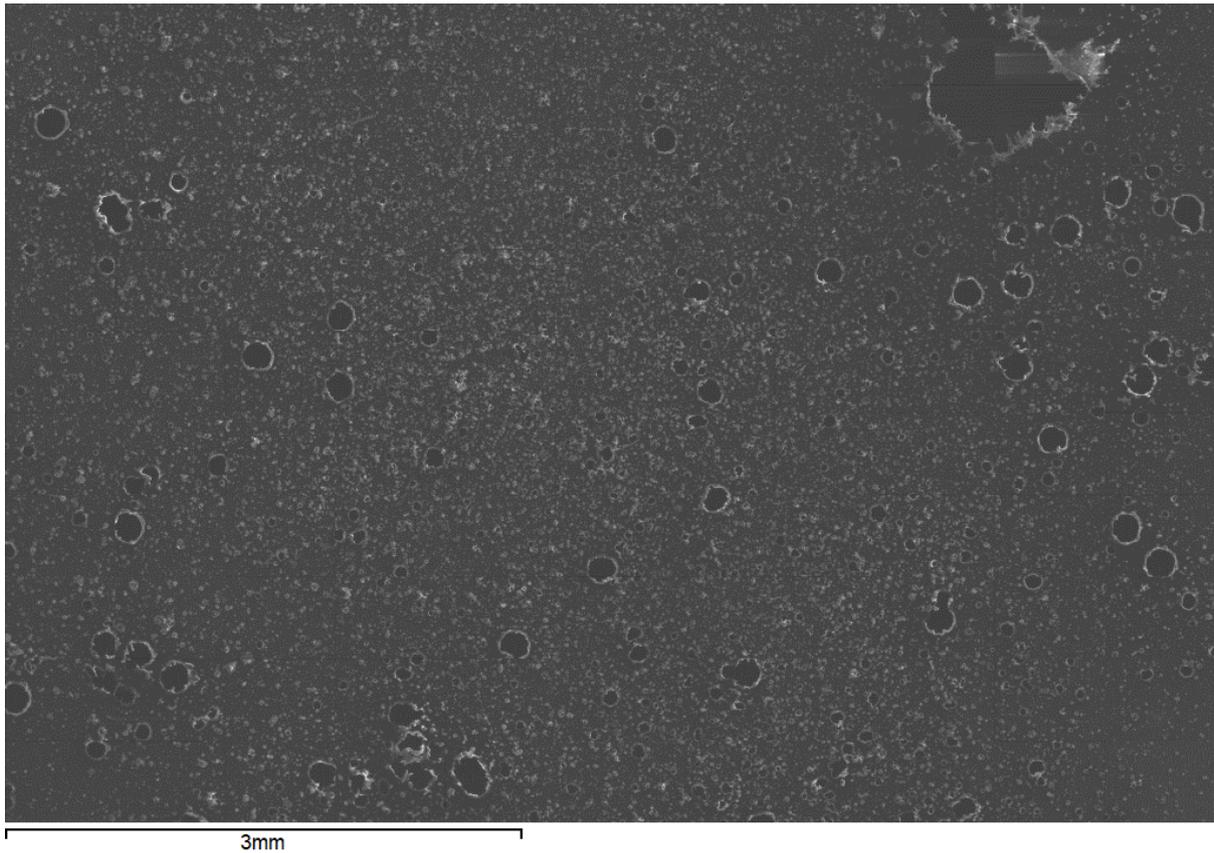
Figure 5.6. The 25 μm Kapton foil coated with 10 nm of palladium shot at 5 km/s with a projectile mix of 43 and 91 μm soda lime glass.

The investigation was repeated but with only the 11 μm soda lime glass to ascertain if this glass would also shatter with only one size of glass present. This shot was attempted 5 times but was not successful. The two main causes of this were that the powder was not travelling down the gun and that there was a large quantity of gun debris present. The gun debris was larger in size than the soda lime glass which made it difficult to determine which impact was debris and which was the glass with the gun debris being more numerous than the glass.

Therefore, in order for these shots to work in the future and determine the ballistic limit for the different foils, a method of shooting small powders reliably needs to be found. Improvements were made with the projectile quantity that reached the target foil when a 1 mm basalt sphere was included to hold the power in the sabot but the shattering of the glass still occurred. Potentially using a projectile that does not shatter would solve the issue experienced by soda lime glass. Once this is optimised, then the shots into the different thicknesses of foils with the varying size projectiles can be conducted to determine the size of projectile that just breaks through each foil, thus giving the ballistic limits for each.

5.4.3 Changing the Projectile Mix

The projectiles chosen in this study were based primarily on the size of the projectile with a secondary focus on the composition, hence why molybdenum was chosen as the representative projectile for the OD population and not the more common aluminium. To calibrate the ODIE detector appropriately, many different compositions of projectile should be shot into the foils to improve the analysis protocol for identifying the particle residue.

Another major difficulty encountered in this research was that the projectile constituents all had different problems associated with them, except for the basalt. The soda lime glass particles had a population of larger diameter particles that was unknown before shooting as the population is small and thus did not get detected in the initial assessment of the quality of the powder and only became evident after shooting. Additionally, as seen in Figure 5.5, there were some particles that had small globules present on the surface of the sphere. The irregularity in the particles produced features that were non-circular in size but could not be attributed to the glass projectile at first glance as the feature created is similar to that of the gun debris particulates due to their irregularity.

The molybdenum powder had a wide spread of particle sizes and also charged such that it attracted many silica spheres to adhere to it. It is unknown whether the silica remains adhered to the molybdenum during the flight of the particles but it introduces an uncertainty into potentially obtaining the molybdenum diameter measurements. Perhaps residue analysis of the impact features could determine if the silica and molybdenum impacted as one although there could be residual silica remaining on the molybdenum even if the silica spheres themselves were removed from the molybdenum during flight.

Components OD should be shot into the foils at the same size ranges as the MM analogues to investigate the effect that density (and composition) has on the features created in the impacts. The typically metallic nature of OD is more dense than the MM aggregates that would impact ODIE in orbit, thus there could be a difference between the two populations with regards to how the features form and potentially the quantity of residue left behind.

5.4.4 Full-scale ODIE Experiments

The foils used in our experiments were scaled down from the original size that ODIE would use as a detector. The ODIE detector is modular with each of these modules being 10 x 10 cm, whilst our experiments were with much smaller foils (Figure 5.6). This was for making the best use of the limited Kapton and palladium available in this project and for the ease of mounting in the LGG. Also, the sputter coater could not manage samples that were 10 x 10 cm with ease and hence smaller size samples were required. The Autodyn simulations showed an uncertainty in the exact termination of the

simulation with regards to the movement within the target material. This could have an effect on the experimental results and therefore requires experimentation with a full-size foil.
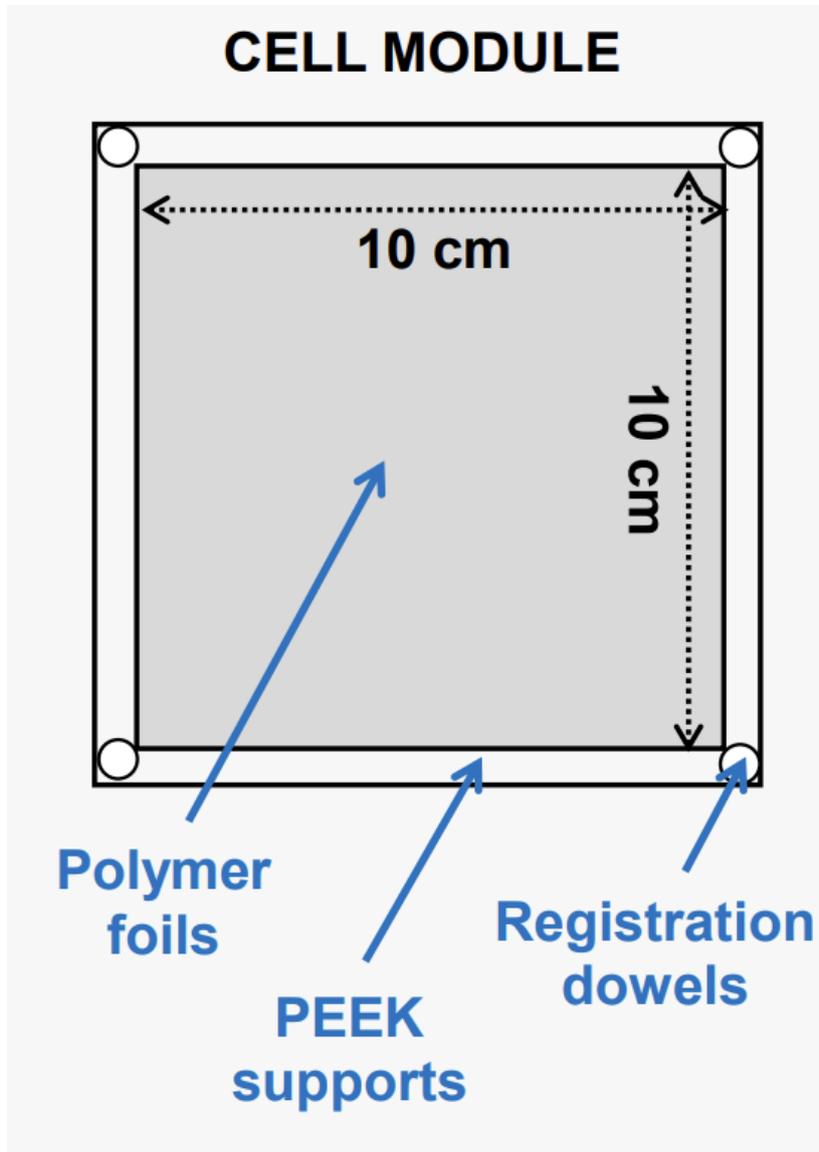
Figure 5.6. Construction of a cell module on ODIEs. Each module is 10 x 10 cm consisting of the polymer foils with PEEK as a frame supporting the modules.

The other aspect of ODIE that was not investigated here was the number of foils in the detector configuration and the spacing between these foils. The number of foils proposed for use in ODIE is four, with the back foil as a thick (potentially 125 µm) Kapton foil. The objective of this setup is to act as a Whipple shield to slow down the particles as they enter the detector with residues being deposited as they impact each layer. The optimum number of foils is also dependent on the separation of the foils.

With ODIE designed to be used on the outside of any spacecraft the detector must not have large distances between the foils. The initial spacing proposed is in the region of a centimetre, but this is subject to change as the spacing can change the amount of residue found on the foils.
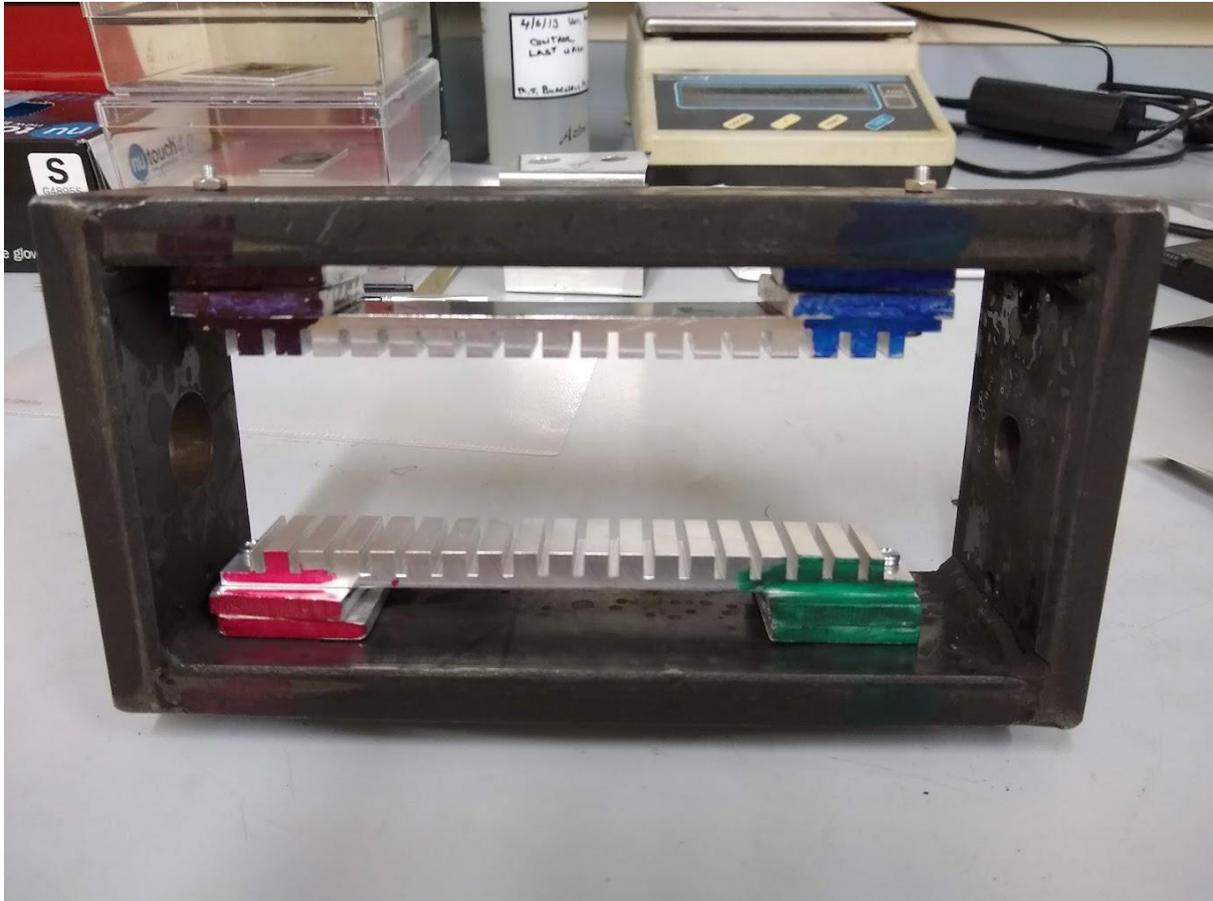
Figure 5.7. The target holder for the blast tank that was used for the LGG shots. This holder has many slots that can be used for the photographic slides at different locations.

Therefore, one set of experiments is required to determine the spacing between the foils to determine how this affects the residue obtained. This could be done with the mount currently built for the blast tank of the LGG as it consists of multiple slits that can house the photographic slides containing the foils (Figure 5.7). The spacing can be varied from the maximum to minimum positions available on this mount (~10 shots on the LGG) and the residue retention can be measured using the analysis protocol developed in Section 5.3.

The quantity of foils in the detector was originally to be four layers. This was on the premise that the front foil would be thinner than the middle two and back foils. In this thesis we have shown that the 75 µm Kapton foil shows the best retention of impact feature size and therefore should be the front foil of

the detector. This changes the original basis for the number of foils in the detector and thus different numbers of foils should be investigated. As shown previously, the MLI on the SFU has three layers and was sufficient to completely disrupt and stop an impacting particle. Hence both the three and four foil configurations should be studied to determine the formation that retains the most residue and also has the potential to stop impacting particles.

5.4.5 The 13 µm Foil

The inability to shoot the 13 µm foils using the LGG was due to a high number of impacts from gun debris. If this can be reduced or minimised then this foil could be studied to investigate the relationship between the impact features and projectiles formed on this foil. Potentially the valve in development at the University of Kent could solve the issue but it is currently unclear as to what degree this valve would remove the gun debris. Other accelerating methods, such as Van de Graff acceleration could be used but these are no longer commonplace.

5.5 Modelling the Ballistic Limit

The ballistic limit of the palladium-coated Kapton can be modelled with Autodyn as well as other modelling software. This would involve validating the previous issues the raised within in the model noted in the previous section. Following from a fully functional model, the ballistic limit equation is required to find the exact size of impactor that can just break through the Kapton foils. The reason for using modelling rather than conducting an experimental campaign to find the ballistic limit is due to the limitations on the availability of projectiles. Due to the nature of having to survey a large number of projectiles across a large size range, acquiring the exact sizes projectiles, such as 10 µm, 11 µm, etc., would not be feasible. It could potentially be possible to sieve the projectiles to measure and create the right sizes required for this investigation, however it would ultimately not be practical as the other issue encountered is shooting the powders.

As mentioned previously, there was no shooting method found that would successfully shoot the small powders reliably which presents difficulty as the ballistic limit is smaller than the 50 µm sized projectiles. Hence, simulations could be used to investigate this issue. Using simulations using different size ranging of projectile can determine the ballistic limit, although the simulations would require more time and computing power than was available within this project.

5.6 Expansion of Atomic Oxygen Testing

The atomic oxygen testing conducted in this thesis was greatly affected by the covid pandemic, the ESTEC facility closed for many months and when it reopened experiments were scaled down to accommodate the large backlog of samples to be tested and all experiments were changed to be operated remotely. Our initial number of samples to be tested with atomic oxygen exposure was 16, which was then reduced to the 7 samples that were used in Section XX. There is more testing that could take place to refine the effects that exposure to atomic oxygen has on Kapton but also other materials that could be used in similar detectors.

5.6.1 Compare with Other Materials

One of the original polymers to be exposed in the atomic oxygen testing was Mylar, a polymer that is similar to Kapton which is commonly used in MLI. Using Mylar as the main foil was to compare the difference between Kapton and Mylar with regards to the survival of the material as well as assessing the protection ability of the palladium coating for both materials. The original programme was as follows:

1. Dupont Kapton HN polyimide 125 µm bare IM301450

2. Dupont Kapton HN polyimide 125 µm 100nm Pd IM301450

3. Dupont Kapton HN polyimide 75 µm bare IM301400

4. Dupont Kapton HN polyimide 75 µm 100nm Pd IM301400

5. Dupont Kapton HN polyimide 25 µm bare IM301200

6. Dupont Kapton HN polyimide 25 µm 100nm Pd IM301200

7. Dupont Kapton HN polyimide 13 µm bare IM301130

8. Dupont Kapton HN polyimide 13 µm 100nm Pd IM301130

9. Mylar polyethylene terephthalate, clear, biaxial, 125 µm 100nm Pd ES301402

10. Mylar polyethylene terephthalate, clear, biaxial, 125 µm 100nm Pd ES301402

11. Mylar polyethylene terephthalate clear, biaxial, 75 µm 100nm Pd ES301300

12. Mylar polyethylene terephthalate, clear, biaxial, 75 µm 100nm Pd ES301300

13. Mylar polyethylene terephthalate, clear, biaxial, 23 µm bare ES301230

14. Mylar polyethylene terephthalate, clear, biaxial, 23 µm 100nm Pd ES301230

15. Mylar polyethylene terephthalate, clear, biaxial, 13 µm bare ES301130

16. Mylar polyethylene terephthalate, clear, biaxial, 13 μm 100nm Pd ES301130

5.6.2 Test 30 nm Coating

As noted in Section 4, the exposure of palladium coatings on Kapton foils showed that 75 nm thick palladium experienced the least mass loss after atomic oxygen exposure, followed by the 25 nm, 100 nm and 50 nm coatings. Each coating thickness showed varying survivability when impacted at hypervelocity, with the 30 nm coating showing the least damage. Therefore, exposing a foil with a 30 nm palladium coating to atomic oxygen would test the survivability of this thickness in atomic oxygen and could potentially yield the optimal coating thickness.

5.6.3 Impact Testing

The atomic oxygen exposure of the impacted 10 nm coated Kapton led to a large mass loss and showed undercutting features throughout the foil. This was a result of a large quantity of impacts, including the buckshot and gun debris, which led to many opportunities for atomic oxygen undercutting, pitting and erosion. This type of impact is unlikely to occur in orbit and hence it would be more appropriate if there were less impacts present on the foil.

The foils require further investigation with impacts that have reduced gun debris. The gun debris is the main cause of the erosion as there was a constant spread present on the foil. Future experiments need to have less gun debris, potentially using the valve once developed. Following this, the LGG projectiles used previously were susceptible to shattering during the shots. Therefore, for future atomic oxygen exposure experiments with impacted foils the number of projectiles used should be reduced so that it actually represents the likely number of impacts that the ODIE would experience.

5.6.4 Simulations of Atomic Oxygen Erosion

It is possible to simulate the erosion of atomic oxygen using ESABASE2, a software designed by etamax. The software is capable of modelling the effects on atomic oxygen on many different materials, satellites and experiments (although it is not open access software). Multiple different orbital locations are modelled with this software, which is something to be considered for ODIE as the detector can be practically placed on the outside of different spacecraft, thus could be placed in multiple different orbits which changes the quantity of atomic oxygen that the detector would experience.

ESABASE2 uses both meshed and unmeshed options with unmeshed running faster but is lower resolution. One feature of the software that would be ideal for ODIE is the ESABASE2/COMOVA application. The function of this application simulates the contamination, outgassing and venting experienced by the spacecraft, thus calculating the contamination on the surfaces of the exposed detector. This simulation could show potential impacts but, more specifically, the deposits on the surface and is optimised for satellites that generally intend to utilise this software to determine the amount of outgassing and venting that the satellite creates and hence how to minimise this to prevent the creating of more OD. This simulation would be highly beneficial for ODIE with regards to the likelihood of the detector experiencing mass loss due to atomic oxygen but also the different materials that may impact the foils. This analysis could then be compared with the observed data that ODIE will collect and the difference between data that is over 25 years old versus a modern dataset could be found and integrated into the model.

5.7 Simulation of Impacts

The number of impacts that will be experienced by ODIE in orbit depends on the deployment location of the detector. The original design based the expectations of impacts and the OD or MM populations to be experienced on the orbit of the International Space Station as the Columbus module was an identified potential location of the detector that would be optimal for deployment. The key factor taken into consideration is the passive nature of the detector, requiring deployment but also retrieval. Therefore, simulations of the impact flux at this location can be investigated using the two major Earth orbit environment models MASTER and ORDEM.

These simulations can be undertaken as simple surfaces or complex, full-scale models of ODIE. These models can also account for the impacts experienced with regards to the pointing of the surface. Therefore, to simulate the impacts appropriately, it is suggested to use a full-scale model, which has been created using CAD. The CAD model for ODIE requires adapting as the material for the frames, PEEK, has been identified as problematic. Functionality in both the MASTER and ORDEM models allows for the use of CAD models of spacecraft to be used in the simulations.

The different rendered models of the ODIE detector can be placed in different orbits and at different pointing to simulate the potential impacts it can experience with the different parameters in the different simulation software (Figure 5.8). It is necessary to complete this analysis to a high degree of accuracy as the quantity of impacts and how they react with the Whipple-shield like function of the detector can be effectively simulated with the models for the entire surface area and hence can inform the decision about the deployment location of ODIE. As the software is generally for identifying the locations at which additional shielding may be required for protecting instrumentation, it is ideal for highlighting the parts of ODIE that would experience the highest likelihood of impact.
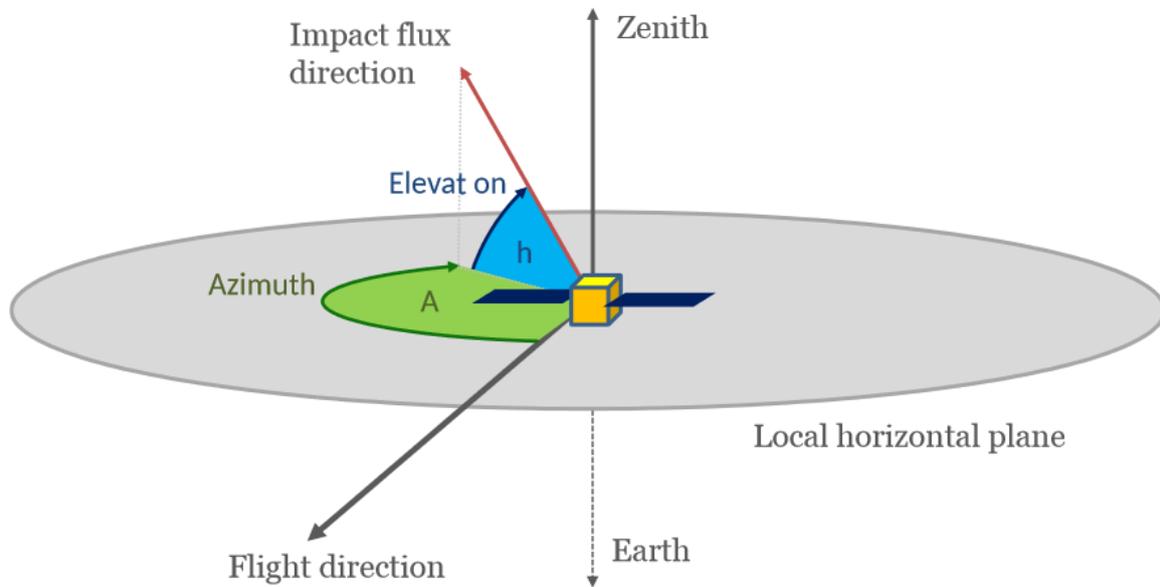
Figure 5.8. One example of a pointing configuration within the MASTER simulation. This is modelled for a satellite to maintain Earth pointing (ESA, 2022b).

Both simulations, as mentioned in the Introduction, have the OD and MM populations included in their simulations, albeit with different parameters and populations included for the MM population. At the altitude of 400 km (ISS) the likelihood that the difference between the MM models is notable would be minimal as this is a low altitude where the MM should be primarily due to the background population and seasonal streams.

Through these simulations it may be possible to identify the optimum deployment location for ODIE and the quantities of impacts that would be predicted to be OD and MM. As the input data for the smaller ranges of the simulations are both based on old, unreliable data that has not been obtained since before the increase of space traffic and the large debris generating event, ODIE may potentially not experience impacts in line with those predicted by either simulation.

5.8 TRL Advancement Testing

The TRL is a measure of the maturity of a technology for spaceflight. As such, the ODIE detector requires testing to advance the TRL of the technology so that it may one day be deployed for use as a

space dust detector and, hence, must reach TRL 8. The existence of the different levels is to perform a robust analysis of the reproducible survivability of the technology for use in space. The TRL of ODIE at the beginning of this project was potentially TRL 3.

TRL	Level Description
1	Basic principles observed and reported
2	Technology concept and/or application formulated
3	Analytical and experimental critical function and/or characteristic proof-of-concept
4	Component and/or breadboard functional verification in laboratory environment
5	Component and/or breadboard critical function verification in relevant environment
6	Model demonstrating the critical functions of the element in a relevant environment
7	Model demonstrating the element performance for the operational environment
8	Actual system completed and accepted for flight ("flight qualified")
9	Actual system "flight proven" through successful mission operations

Table 5.2. TRL level brief descriptions adapted from ISO 16290:2013.

TRL 1 is the lowest level on the scale and consists of having the basic principles of operation of the element being tested to be observed and reported. There must be a scientific foundation for the technology although it may only be in the early phases of testing and implementation. The second level, TRL 2, is the point at which the technology is being formulated and invented as the basic principles have already been established although there may not be a proof of concept made. Proof of concept is the basis for TRL 3 (ISO 16290:2013). This can be done using simulation, modelling or experimentation and as such, investigating how ODIE behaves at higher velocities can be justified with modelling.

To advance the TRL past the beginning point of TRL 3, the conditions for TRL 4 and 5 must be met. TRL 4 and 5 are both based on a demonstration of the function of the technology with TRL 4 based in a laboratory environment and TRL 5 based in a relevant environment. In the instance of TRL 4 this is designed to show that all the different elements of a technology, in ODIE's case the different layers of foils, frames to hold the foils and any other structural pieces, work together to demonstrate the function of the technology as a whole (ISO 16290:2013). Therefore, although in this thesis we have shown that the palladium coating on the Kapton foil works for the function of the detector, the entirety of the structure has not been assessed. Originally, this was to accounted for in the project with polyetherketone (PEEK) chosen as the material to act as a frame as it is lightweight and the elemental composition is similar to that of Kapton and so would not interfere with the residue analysis. Unfortunately, it was

difficult to obtain as a result of the times that this project spanned. Additionally, through the experiments at ESTEC, there was anecdotal evidence that PEEK performs poorly under atomic oxygen exposure and we were advised to reassess the choice of material for the frame. Thus only the element of the detector consisting of the Kapton foils coated with palladium has a TRL of 4. Therefore, for ODIE as a whole to obtain a TRL of 4 it would be necessary to find an appropriate material that could be used as the material for the frame without hindering the objective of minimal cross-contamination of the foils whilst also potentially being suitable to analyse for impact features much like what was done for the frames, clamps and other holders of experiments mentioned in Chapter 1.

To achieve TRL 5, ODIE must be proven to be functional within a relevant environment which would entail the survivability of the instrument through launch, exposure and retrieval (ISO 16290:2013). The critical function of ODIE, to detect dust and retain the impactor size and residue, must be achieved in all the environment conditions that it will experience. At this stage, full-scale resting is not required, but there must be an extrapolation protocol determined for the instrument. Two major tests would be required for ODIE to obtain TRL 5 as the effects of these tests could destroy the detector or render it non-functional; vibration testing and thermal testing. The thermal testing is highly relevant to the ODIE detector as Cooper et al. (2008) noted that thick (~100 nm) coatings are highly susceptible to producing cracks when undergoing thermal cycling. This would create opportunities for atomic oxygen to enter the ODIE configuration and erode the Kapton of the detector. For these tests the detector could be exposed to high vacuum, cold shroud and artificial solar rays. This would determine the reaction of the detector to the temperatures changes under extreme conditions. For ODIE it would be worthwhile to run these tests on pre and post impacted samples to determine if impact has a major effect on the thermal properties of the foils and coating.

Vibration testing for ODIE is necessary to assess how the detector will survive its transit to and from space. The vibrations experienced by payloads in a launch vehicle can damage the payloads inside and so requires testing to mitigate these risks. Depending on the launch vehicle, the vibrations differ, but generally remain sinusoidal in nature thus ODIE must be tested in a vibration testing facility to ascertain the survivability of the detector. As it is a passive detector, there are no concerns about electrical inputs or moving parts remaining functional after the test.

There are not many facilities in the world that offer thermal and vibrational testing and therefore these tests could not be performed during the course of this study. Hence, it is recommended that they are performed in any future developments of the ODIE technology.

Further TRL are dependent on the critical functions, for ODIE the preservation of size and residue detail for impactors, have been fully demonstrated within relevant environments and remain operational. It is at TRL 6 where a full-scale model of ODIE would need to be constructed with all final materials that have been tested during this process (ISO 16290:2013). At this point it would be possible to establish a

timeline of development of the detector such that determining the deployment location of ODIE and the launch possibilities can be taken as considerations in the development process.

TRL 7 is the point at which the technology is almost in its final form. The full-scale model is required to be tested in relevant environments as a whole unit as this will fully demonstrate the capability of ODIE to survive the environmental stressors and reliably collect data in orbit. This model used in the testing process is not considered to be the flight model as it may become over-tested throughout the course of the investigation and would not be the ideal form to be deployed (ISO 16290:2013).

The final stage that ODIE can reach before launch is TRL 8 where the detector is fully test and qualified to be flown. The operational environment, orbit and pointing, is determined and the detector is accepted for flight (ISO 16290:2013). This is the goal of the ODIE detector development process and, as can be seen here, would take a substantial amount of time and resources to reach this level of development. Although this process is not mandatory to launch instrumentation in orbit, it is highly recommended and increases the chances of obtaining a position on a mission.

The final TRL 9 is potentially what ODIE would be classified as post-retrieval. This level denotes a technology that has been previously used in orbit and has achieved all its objectives in a successful deployment in the intended orbital environment. As a result of obtaining TRL 9, the detector would be no longer required to conducted extensively testing in order to be deemed flight ready. This would potentially allow ODIE detectors to be constructed quickly and deployed on available surface that are part of retrieval or return missions, which would collect valuable data about the dust population in multiple orbits and locations.

5.9 Other Deployment Locations

As ODIE is a passive detector a condition of its deployment is that it must be returned to Earth for analysis. This requirement for a return mission is one major limitation of ODIE, and passive detectors, that prevents choosing any location for the placement of ODIE. That reasoning led to the initial identification of the ISS as an ideal location for ODIE as there are regular resupply missions to the ISS that could be used to transport the detector to and from the space station. Therefore, other locations must, similarly, have a return mission.

A future potential deployment location is the Lunar Gateway that is planned as a space station in orbit around the Moon. The Gateway is planned for construction to begin in the late 2020s and is a joint endeavour between many space agencies and independent companies. This has been identified as an ideal location for dust detectors including passive detectors as the planned space station is designed to be serviceable, i.e. return vehicles will be available to return samples. Shown in Figure 5.3, the Gateway is comprised of modules which are planned to be deployed at separate intervals to progressively build

up the space station (Wozniakiewicz et al., 2021). The opportunity to collect dust in the predominately uncontaminated Lunar orbit would offer information on the background MM population before the contribution of OD to this orbit begins as we expand space operations.

Figure 5.3. Model of the Lunar Gateway space station that is planned to be launched in the late 2020s which would present an ideal location for the deployment of ODIE.

The main calibration for ODIE that would need to occur for this location would be updated modelling on the quantity of impacts to be expected in the highly elliptical Lunar orbit that is planned. Therefore the results obtained from the Gateway exposure can be compared with our current estimations of the dust environment at this location.

It may be beneficial to perform LGG impact experiments into the palladium-coated Kapton foils with a Lunar regolith simulant. As the Gateway is planned to be inhabited for brief periods of time for expeditions to the lunar surface, there is a possibility that the dust on the surface of the Moon can become perturbed into orbit off of the various vehicles that may be used to conduct the surface expeditions. These expeditions could potentially increase the amount of Lunar dust in the orbit of Gateway and therefore it is necessary to calibrate the detector for these types of impacts.

The coting thickness required for ODIE in Lunar orbit is not dependent on the presence of atomic oxygen as it is a substantially large distance from the Earth atmosphere and hence there should be no atomic oxygen present. The coating was useful in the identification of impact features on the surface of the foils and therefore is recommended to be kept on the detector even when no atomic oxygen is present. The thickness can be 10 nm of palladium as this was effective in its adhesion to the surface without having an impact on the spread of the diameter size measurements, although a coating up to 30 nm is suitable.

The Lunar Gateway is not the only location beyond the ISS that could be used for ODIE. As mentioned previously, the detector can be placed on any body that has a return mission. Due to its modular design, the detector can be increased or decreased in size as required for the spacecraft upon which it resides. This is a major benefit in the design of ODIE such that it does not limit the potential bodies that can be used for deployment. Another location that ODIE could potentially analyse is that of interplanetary space. The detector could be placed onboard any of the missions to other bodies in the solar system that will return post-sampling. This is not generally performed as of yet but in the future could be a possibility for ODIE.

One consideration is that depending on the orbit the quantity of atomic oxygen varies. If ODIE were to be deployed in GEO, there is a negligible proportion of atomic oxygen present and therefore a thinner coating can be used. Thus, a suggestion for future work is to develop a relationship between the thickness of palladium coating required for optimum foil preservation in varying fluences of atomic oxygen while also maintaining a well-defined relationship between the impacting particle size and impact feature size. With such a relationship the development of ODIE detectors for every Earth orbit can be easily determined.

5.10 Conclusion

This project was severely limited with the time constraints imposed by limited laboratory access and data collection becoming delayed by one or two years. Therefore the preliminary investigations into many topics have been conducted. The TRL of ODIE at the beginning of this project was a level 3 and has advanced the technology of the palladium-coated foils for preservation of diameter data and retention of Kapton post exposure to atomic oxygen to TRL 4, achieving a major aim of this project to advance the TRL in any capacity.

Further experimentation with LGG facilities is required to address the number of foils required for ODIE, the optimum spacing between these foils, the ballistic limit of the foils and to determine if using a full-scale module would have an effect on the impacts. To determine all these parameters would take a substantial amount of LGG shots which was not feasible within the scope of this project.

The modelling of the hypervelocity impacts yielded the same result that at 1 km/s the 25 µm foil creates impact features that are much smaller in diameter than those observed in the original projectiles. This necessitates further experimentation using LGG shots and experimental methods to improve the model to a point at which it can quantify the cause of this phenomenon.

Simulations can be used to identify the ideal locations and points of deployment for ODIE. Using both MASTER and ORDEM could develop an analytical testbed to compare with post-retrieval. These simulations have limited capabilities in differentiating between OD and MM populations and therefore would be useful comparisons to ODIE; e.g. the detector may collect and provide data that could be used for the improvement of these models. Thus accurate simulations are required including all ODIE material to create exact reference simulations.

As the atomic oxygen testing campaign was cut short due to the shutdown of the facility and restrictions on access, the original intended broad range of experiments was not conducted and hence we recommend investigating the original plan but also now have another line of inquiry based off the results in this thesis. It would be ideal to test the 30 nm coating in atomic oxygen as this was the thickest foil that showed retention of the coating with minimal cracking after hypervelocity impact. Another set of exposure experiments would be run with ideally singular impact features on the foils. This would be difficult to achieve as the gun debris can have random effects on the impacts, making it difficult to create a foil with a singular impact that would be wholly analogous to impacts in LEO.

ODIE, being a modular, passive detector, has the capability to be adapted to fly on any spacecraft that would be returning or having components returned to Earth. This opens up many deployment capabilities for ODIE once the technology is flight ready. One such location is the Lunar Gateway which would be an ideal location for sampling the cis-Lunar environment before the introduction of any human debris as a result of space activities. This would require calibrating the detector for Lunar dust by investigating the residues deposited on impact features created by LGG shots of Lunar simulant into

the detector. This was not calibrated in our previous investigations and thus is necessary if ODIE were to be deployed on Gateway.

The ODIE detector has showed promising preliminary results which have led to a clear calibration plan of the detector forming using both analytical and experimental methods. Within the University of Kent it would be possible to advance the TRL of ODIE to 5 then requiring further external testing. This detector has the potential to validate the environment models that are currently in use with updated data and thus these recommendations would advance the technology to a point at which this would be possible.

Chapter 6: Conclusions

The ODIE detector was developed and calibrated throughout the course of this project using hypervelocity impact experiments conducted with the LGG at the University of Kent and atomic oxygen exposure experiments performed at ESTEC. The main aim of this thesis was to advance the technology of the ODIE detector to a TRL of 6. Ultimately, the technology with regards to the palladium coating on Kapton foils for use in protection of the Kapton and preservation of the impactor size and residue under hypervelocity impact and atomic oxygen exposure was advanced from a TRL 3 to TRL 4.

6.1 Studying the Size Relationships between Impactors and Impact Features

The relationships between the impact features created on the foils with the sizes of the original projectiles was investigated using a series of LGG experiments shot at 1 and 5 km/s. These experiments were to change the thickness of the Kapton foil and the thickness of the palladium coating to ascertain what impact this has on impact features found on the foils

Initial results showed that the 13 µm foil tore on every impact, creating long shears that affected all the impact features present on the foils. The tears also impeded studying the holes due to the shading that was created from the uneven surface of the foil. The foil could not be held down as the sputter coating is very susceptible to being wiped off the surface if care is not taken when handling. Thus the 13 µm foil could not be investigated with the LGG as the extreme amount of gun debris that impacts the foil causes a large number of impacts in such close proximity to one another that the foil tears. It was also difficult to handle due to the thinness of the film. Therefore, the 13 µm foil needs to be investigated through another method of acceleration.

The 25 µm, 75 µm and 125 µm foils were analysed with SEM to determine the spread of the impact features and which foil retained the original size of the glass projectiles. This led to the conclusion that the 25 µm and 125 µm foils shot at 5 km/s had reliable relationships with the original projectile sizes although the hole diameters on all foils at 5 km/s are within 98% of the mean projectile diameter

It was found that the 1 km/s shot into 25 µm Kapton produced a phenomenon where the impacts that occur are on average 38% smaller in diameter than the average glass projectile size. The investigations into the different thicknesses of palladium coating and their effect on the impact features were all conducted using 25 µm Kapton and thus acted as repeat experiments for this occurrence. All foils exhibited the 38% reduction in size from the glass average. This was not observed in any other literature and the cause could not be identified. Further investigations of increasing the speed of the shots or the thickness of the foils to determine the exact conditions that create this phenomenon would be advisable.

In determining the effect that coating thickness had on feature diameters it was found that the quality of the relationship, i.e. the standard deviation of the measurements, was greatly affected by the number of impacts the shots imparted and the size distribution of projectiles within that particular shot. It was noted that the Hörz et al. (2005) study was conducted with projectiles that had been measured with high precision to mitigate this effect. The different coating thicknesses did not have an effect on the relationships and the variation is attributed to the variation in each LGG shot.

It was found that the rim measurement location on these foils was consistently much larger and more spread than the hole measurements with no apparent trend present and thus the rim measurement is not suggested as a measurement location for ODIE.

The 75 µm foil had a relationship of 0.99 D_P and performed best for the preservation of the original impactor size and hence is a recommendation for the front foil of the detector.

6.2 Investigating Palladium Coating Performance

The palladium coating was exposed to hypervelocity impact and atomic oxygen with its reaction to these studied for defects and damage. The coating was found to be resilient to both impacts and atomic oxygen with most coating thicknesses surviving both investigations.

The hypervelocity impacts induced cracks and delamination in the coatings to varying extents, the thicker coatings suffering the most damage. The cracking becomes severe at coating thicknesses greater than ~30 nm and above ~50 nm the coatings exhibited delamination where the coating peels away from the Kapton surface. This delamination would not be ideal for ODIE as any exposure of the Kapton to atomic oxygen can lead to erosion and loss of any impact features collected.

All thicknesses of the coating were shown to be effective at protecting the Kapton from atomic oxygen erosion. It was found that the 75 nm coating had the lowest mass loss of all samples. In the SEM analysis it was seen that any defect in the coating was exploited to become an entry point for the atomic oxygen to attack the Kapton and thus the differing quantity of defects on the coatings could have had an impact on the coating integrity and thus should be prepared within a clean room in future. The results also suggest that a 30 nm coating thickness, to prevent delamination upon impact, would be sufficient to protect the Kapton although the impacted foil did suffer extensive mass loss. This was likely a result of gun debris creating imperfections across the coating surface and therefore this should be taken into account if impacted shots are to be exposed to atomic oxygen.

6.3 Initial Studies and Possible Future Work

The limitations placed on this projects as a result of laboratory restrictions hindered the advanced of some studies past the preliminary stages. This leaves many opportunities for further work on this project to prepare ODIE for use in orbit.

Ansys Autodyn was used to simulate the hypervelocity impacts conducted in the lab with some degree of success in replicating the impacts for 25 μm foils. This also showed the production of features at 1 km/s that are smaller than the size of the projectiles. This preliminary investigation relied on using the LGG diameter data to validate the model and was therefore limited in time due to the delays in collecting the data. More time and computing power would be required to create a higher fidelity simulation that could explain the 25 μm phenomenon and could be used to extrapolate to high velocities more akin to those experienced in LEO.

With more LGG experimentation the ballistic limit of the foils could be determined, which would be instrumental in calibration of the detector. Inclined shots are required to calibrate the detector for the highly likely probability that it will experience impacts at non-perpendicular angles. The quantity and spacing of foils for optimal residue retention is also an aspect to be investigated further.

Simulations of the orbital environment would be useful in creating a dataset of what impacts are to be expected that can be compared against post-flight. These simulations can also be used in determining the orbit and pointing that could provide the most impacts. There is also software that can be used to simulate the erosion of the surfaces due to atomic oxygen, a tool that may be useful for modelling foils that have impacts as these samples are difficult to create without the introduction of a large quantity of gun debris.

More atomic oxygen exposure experiments are required to pinpoint the exact coating thickness that performs best in both hypervelocity impact and atomic oxygen exposure. This would involve investigating the 30 nm thickness coating and other coatings thicknesses that have been impacted. Different materials could also be investigated to compare Kapton to Mylar and Teflon which are more commonly reported.

The TRL of ODIE has a clear trajectory as a result of this thesis. The beginning of the analytical studies and experimental studies have been investigated and have led to the advancement of one element of ODIE by a level. The palladium coated Kapton is now of a higher level but the rest of ODIE still requires advancements. The suggestions in this chapter are all to improve the calibration of the detector and advance the TRL levels so that the detector can be used in orbit.

6.4 Final Conclusions

The ODIE detector calibration and development has been advanced as a result of this project. The detector has the potential to be deployed on any body with a return mission, making ODIE a versatile instrument to be used for dust detection. The TRL of the palladium-coated Kapton foils that comprise the majority of ODIE has been increased from TRL 3 to TRL 4, achieving the main goal of this thesis.

The optimal Kapton thickness for defining a relationship between the impact feature diameter and the original projectile diameter has been found as the 25 μm foil and it has been shown that the coating thickness has a negligible impact on the sizes of impact features created.

The palladium coating has been found to be effective at remaining intact after hypervelocity impact and exposure to atomic oxygen. Coatings thicker than 30 nm showed signs of severe delamination and are hence, not recommended for ODIE. The 75 nm coating performed best in the atomic oxygen testing although all coatings provided substantial protection. Therefore, a coating thickness of ~30 nm is recommended.

In conclusion, a Kapton thickness of 25 μm coated with 30 nm of palladium has been found to give optimum performance with regards to the survivability of the coating in hypervelocity impacts and atomic oxygen environments. This is the configuration that is recommended to be used as the front foil of the ODIE detector. Further work is required for the detector to the reach flight readiness of TRL 8 with more computational modelling of impacts and erosion, LGG experiments and atomic oxygen exposure testing needed to refine and completely calibrate the detector. These investigations will enable ODIE to finally address the data gap in the sub-millimetre dust population and determine the flux of the individual OD and MM populations.

7. Appendix

	1 km/s		
	25 μm	75 μm	125 μm
Crater number		Hole Measurement (μm)	
1	74.8	101.0	101.1
2	62.7	81.9	103.3
3	64.4	113.3	105.3
4	63.1	110.7	104
5	58.7	106.3	95.4
6	54.8	117.7	101.3
7	49.7	107.7	92.1
8	73.3	111.3	96.4
9	60	108.3	98
10	68.4	97.6	101.2
11	72.3	105.6	104.2
12	64.7	99.9	105.3
13	65.1	103.7	98.7
14	59.7	107.3	105.3
15	64.2	110.0	100.6
16	64.5	173.3	80.5
17	48.6	112.7	104.3
18	60.6	115.0	94.4
19	62.8	115.3	98.2
20	57.7	112.3	104.7
21	63.8	199.0	100.1
22	58.7	105.6	102.4
23	67.4	245.3	97.4
24	67.3	101.3	107
25	66.1	108.0	100.7
26	51	97.0	95.5
27	50.7	154.0	103.7
28	66.6	99.6	104

29	63.9	99.9	106.3
30	60.2	101.9	103.3
31	58	109.0	103
32	56.9	239.0	102.7
33	69.8	112.0	102.3
34	67.8	109.7	105.7
35	75.3	111.0	103.7
36	69.5	109.7	103
37	53.6	117.3	102.6
38	72.5	117.3	103
39	70.1	249.0	101.3
40	58.2	217.0	103.3
41	53.1	100.1	104
42	68.7	108.0	105
43	64.2	245.7	102
44	70.7	108.0	105.3
45	65.5	95.6	103.6
46	68.4	112.7	93.1
47	69.2	114.0	105.4
48	61.7	115.3	101
49	58.5	102.9	102.4
50	72.4	114.3	101
51	61.8	112.0	101.3
52	55.3	102.0	99.5
53	61.3	111.0	105.7
54	62.6	101.5	101.6
55	68.3	110.0	87
56	64.4	117.0	95.3
57	65.3	101.8	97
58	50.4	106.3	97.2
59	63.3	112.7	101.7
60	62.1	117.0	98.6
61	80.6	103.3	
62	61.9	107.0	

63	65.4	106.0	
64	73.5	105.7	
65	77.7	167.3	
66	72.5	109.1	
67	70.1	109.7	
68	50.3	105.3	
69	77.4	116.3	
70	73		
71	76.8		
72	72.6		
73	59.7		
74	70.1		
75	69		
76	77.5		
77	73.1		
78	71.7		
79	67		
80	64.5		
81	73.6		
82	71.7		

Table 1. Diameter measurement data for the 1 km/s shots

	1 km/s			5 km/s			
	25 μm	75 μm	125 μm	25 μm		75 μm	125 μm
		Hole Measurement		Hole	Rim	Hole Measurement	
Crater number		(μm)		(μm)	(μm)	(μm)	
1	74.8	101.0	101.1	93.6	105.9	111	86
2	62.7	81.9	103.3	80.8	97.4	96	113.3
3	64.4	113.3	105.3	110.7	127.3	109.3	100.2
4	63.1	110.7	104	106.3	132.3	111.3	89.6
5	58.7	106.3	95.4	107.3	123	243.7	100.3

6	54.8	117.7	101.3	186	209.3	105.3	120.3
7	49.7	107.7	92.1	80.1	93.4	116	235.7
8	73.3	111.3	96.4	95.1	107	193	103.8
9	60	108.3	98	179	212	113	106.4
10	68.4	97.6	101.2	112.7	128	113	90.8
11	72.3	105.6	104.2	108.7	125.3	112.3	101.5
12	64.7	99.9	105.3	111.7	127.3	107.5	217
13	65.1	103.7	98.7	180.3	203.7	110	198
14	59.7	107.3	105.3	108.7	127.7	112.7	93
15	64.2	110.0	100.6	107.3	129.3	97.4	91.5
16	64.5	173.3	80.5	108	127.7	104.7	222.7
17	48.6	112.7	104.3	108.3	131.3	103	225
18	60.6	115.0	94.4	113.7	134.3	81.7	94.9
19	62.8	115.3	98.2	112.7	142.7	114	92.7
20	57.7	112.3	104.7	179.7	210	106.9	95.6
21	63.8	199.0	100.1	109.7	133.3	99.4	94.2
22	58.7	105.6	102.4	108	126	247.3	95.9
23	67.4	245.3	97.4	104.6	127.7		79.5
24	67.3	101.3	107	105.7	125.3		214
25	66.1	108.0	100.7	107	124		219
26	51	97.0	95.5	98.1	114.7		95.5
27	50.7	154.0	103.7	110.7	132		99.3
28	66.6	99.6	104	112	130.3		99.1
29	63.9	99.9	106.3	120.3	140.3		233.7
30	60.2	101.9	103.3	104.3	123		94.5
31	58	109.0	103	107	123.7		90
32	56.9	239.0	102.7	109	129.3		91.6
33	69.8	112.0	102.3	95.5	109.3		93.5
34	67.8	109.7	105.7	94.4	113		224.3
35	75.3	111.0	103.7	103.4	125.3		76.7
36	69.5	109.7	103	111	137		225.7
37	53.6	117.3	102.6	112.3	135.7		100.2
38	72.5	117.3	103	108	126.3		97.5
39	70.1	249.0	101.3	109.3	130.3		94.8

40	58.2	217.0	103.3	103.8	126.7	81.1
41	53.1	100.1	104	108.7	124.3	90.2
42	68.7	108.0	105	113	131.7	96.9
43	64.2	245.7	102	112	135.7	98.1
44	70.7	108.0	105.3	109.7	129	99.7
45	65.5	95.6	103.6	108	129	87.7
46	68.4	112.7	93.1	97.1	109.7	95.9
47	69.2	114.0	105.4	79	91.5	41.8
48	61.7	115.3	101	130.3	162	92.6
49	58.5	102.9	102.4	108	132.7	103.6
50	72.4	114.3	101	115	134.3	93.1
51	61.8	112.0	101.3	106.3	125.7	209
52	55.3	102.0	99.5	110.7	131.7	222.3
53	61.3	111.0	105.7	174.7	203	143.7
54	62.6	101.5	101.6	108	131.3	93
55	68.3	110.0	87	110.3	128.7	221
56	64.4	117.0	95.3	173.7	205.3	98.6
57	65.3	101.8	97	101.7	121.7	93.7
58	50.4	106.3	97.2	180	206.7	96.5
59	63.3	112.7	101.7	106.3	125	109
60	62.1	117.0	98.6	96.1	120.3	
61	80.6	103.3		103.7	127.7	
62	61.9	107.0		108.7	129	
63	65.4	106.0		105.5	123.3	
64	73.5	105.7		91.4	106	
65	77.7	167.3		100.7	110	
66	72.5	109.1		91	108.3	
67	70.1	109.7		111.3	134	
68	50.3	105.3		109.7	132.3	

Table 2. Diameter measurement data for the 5 km/s shots

	1 km/s		
	20 nm	30 nm	40 nm
Crater number		Hole Measurement (µm)	
1	80.3	77.2	75.9
2	78.1	75	77.4
3	78.8	83.1	71.8
4	66.8	68.1	66.7
5	71.9	72.6	63.2
6	64.9	82.9	64.5
7	79.9	75.6	66.7
8	75.4	73.8	75.2
9	72.1	81.1	62.5
10	63.9	75	77.7
11	62.5	74	60.6
12	71.9	67	71.2
13	67	64.1	66.8
14	69.4	77.5	70.5
15	74.1	64.6	73.7
16	61.3	70.4	76.6
17	61.5	62.2	71.4
18	65.4	61.8	71
19	60.8	69.9	63.7
20	68.6	67.3	54.2
21	60.3	68.3	67.6
22	80.6	58.9	69.8
23	75.8	57.5	45.9
24	74.6	71.9	70.9
25	75	53.4	69.6
26	76	66.6	64.7
27	77	55.8	69.8
28	70.9	59.2	60.4
29	72.8	68.1	65.3
30	62.2	69.2	51.3

31	69.3	55.7	60.7
32	71.1	87.9	70
33	75.2	81.4	63.3
34	64.4	84	73.4
35	60.6	63.4	72.7
36	52.9	63.6	75
37	60.5	65.2	71.6
38	69	65.7	70.6
39	60.4		61.8
40	51.7		51.3
41	46.2		68.8
42	63.6		52.8
43	62.4		43.7
44	67.3		68.1
45	49.3		71.8
46	70		68.7
47	61.3		64.3
48	68.9		67.6
49	64.9		75.9
50	73.6		65.1
51			70.6
52			69.5
53			64
54			55.4
55			58.4
56			43.2
57			59.6
58			55
59			51.9
60			65.1
61			25.3
62			55.4
63			55.7
64			68.5

65	65.9
66	64.3
67	73.6
68	57
69	71.8
70	65.4
71	66.9
72	62.6
73	58.1
74	55.4
75	65.3
76	65.1
77	61.3
78	65.9
79	55.6
80	64.6
81	65.5
82	78.1
83	65.1
84	69.1
85	67.7
86	63.5
87	74.1
88	73.6
89	61
90	55
91	54.8
92	67.4
93	63.3
94	52.5
95	60.1
96	63.3
97	67.2
98	72.2

| | | | 99 | | | 59.4 | | | |
| | | | 100 | | | 64 | | | |

Table 3 Diameter measurement data for the different coating thicknesses at 1 km/s.

		5 km/s							
20 nm		30 nm		40 nm		50 nm		100 nm	
Hole	Rim	Hole	Rim	Hole	Rim	Hole	Rim	Hole	Rim
(µm)	(µm)	(µm)	(µm)	(µm)	(µm)	(µm)	(µm)	(µm)	(µm)
108.3	149	117.3	143.3	135.7	155.7	119	146.7	94.2	109.7
174.3	212.3	117.3	144.3	113.3	142.7	141	168.7	112	141.3
103	128.3	117.3	145.3	142	160	173	208.3	113	151.3
80	99.8	116.7	143.3	111.7	138	113.7	145.7	118.3	153.3
69.1	83.3	114.3	140.7	180.7	203.7	180.7	213.7	118.7	147
93.7	117.3	127	152.7	176	195	117	149.7	113.3	148.7
126.7	157.7	111.3	141.7	174	197.7	117.3	142.3	112.3	142.7
83.6	106.6	117	144.7	147	167.3	90.8	113.3	86.9	101.5
82	105.5	117	140.7	177.7	197.3	109.3	142	113.7	142.7
92.3	110.6	112.3	135.3	179	210	125.7	155.7	118.3	148
92.2	119.3	120.3	148	113.7	136.7	114.3	146	186.3	213.3
176	204.7	189	211	180.3	196.7	120	148.7	126.3	154
98.7	119.3	120.7	145	119.7	135.7	113.3	130	113	137.7
118	141.3	190.7	219.7	109.3	124	88.1	105.7	111.7	140.7
106.7	124.7	111.3	134	113	129	110.7	133	113.7	138.3
97.3	126.3	188.7	219.7	112.3	138	107.3	130	113.7	150.7
104.3	124.7	124.7	149.7	106.7	129.3	110.3	129.7	141.7	173
81.8	101.8	114.3	138	115.7	141	86.8	101.7	119.3	145.7
99.4	122.7	114.7	139.7	109.7	134.3	100.2	120.3	116.3	155.3
110.3	138.3	116	143.7	182	201	110	129.7	118.3	145
85	103.3	119.7	149.7	114	137.3	108.3	126.3	116.7	144.7
97.3	120	117.3	140.3	180.7	206	168	198.7	94.5	123.3
112.3	134.3	117	145	137.3	153.7	112.7	133	121	155
108.3	130.7	112.3	131.3	177.7	201.7	118.3	133.3	120	140

91.7	114	89.6	110.3	179.3	189.7	112.3	141	197.7	217.3
78.9	99	118.3	146	116	136.3	115.7	140.3	189.3	215.3
74.4	89.5	114	151	111	126.3	90.2	103.3	115	146.3
105	130.7	112.7	145	182.3	199.7	108.7	134.7	113	133.3
89.8	113.3	119.3	150	202	219	113.7	128	125	151.7
98	120	186.3	214	183.7	200.7	115.7	141.3	181.7	215.7
81.6	93.6	119.7	145.3	102.3	121.7	183	208.7	121	153.7
83.3	95.6	114.3	130	115	134	184.7	210.3	114.3	150
99.1	129.3	118	151	174	194.7	105.3	127.7	95.7	112.3
95	113.3	109.3	130.7	179	196.3	112.7	138	116.3	150.7
75.2	88	124	151	182.3	196.7	78.3	89.9	111.3	147.7
93.3	114.3	117.7	149	116	130.3	116	135.3	116	151.3
99	124	111.3	138.3	113.3	126.7	106.3	127.7	114.3	142.7
139.3	168	112	144	114.7	136.7	110	126	113	138
76.8	95	115.7	136.3	113	128.3	112.3	133.3	120.3	149.7
101.2	128.7	185	205	178	191.7	116.7	143.7	112.3	132.3
84	96.6	114.7	146			94.7	111	114.7	151.7
97.7	124.3	184.7	214.7			177	204.7		
105	129.3	112.7	145			101.6	116.7		
100.7	124	117	147			105	121		
75.5	89.6	111.3	137.3			118	138		
102.7	124	109.7	140.3			112.7	132.7		
95.1	115.7	113.7	138			180.7	206		
112	129	112.7	135.7			121	138.7		
106	121.3	113.3	140.7			108.3	129.3		
98.8	113.3	114	147			117.7	137.7		
96	112	116.3	150			113.3	142		
112.3	127.3	116.7	156			111	135		
107.3	123.7	119	144.3			74.4	87.2		
102.7	119.7	115.3	147.3			112.7	132.7		
77.7	91.2	109	138			79.8	98.4		
112.7	128.7	115	148.7			107.6	126.7		
104.7	121.7	112.7	146.3			112	146.3		
97.1	112	114	148.3			114.3	131.7		

81.1	92.5	110.7	138		145.7	167.7
100.8	121	116.3	149.7		186.3	211
105.7	122.3	112.7	141.3		113	137
110.7	133.3	98.1	116		123	147.7
		109.3	136			
		114.7	148			
		114.7	137.3			
		115.7	143.3			
		180	211			
		108.7	137.7			
		109	143			
		118.3	154			
		187.7	210			
		106.3	136			
		113.7	145.3			
		113	144			
		183	214.7			
		116.3	146			
		116	145.7			
		185	217			
		118	147			
		112	141.3			
		105	132			
		110	144.3			
		121.7	145.7			
		117.7	151.7			
		111.7	141			
		115.7	150.7			
		113.3	150.7			
		112	150.3			
		110	147.3			
		115.7	137			
		112.7	147.3			
		114.7	147.7			

119.7	153.7
109.7	141.3
112	147.7
113.3	141.3
112.3	144.3
109.3	142.3
112.3	141.7
173.7	210.3

Table 4 Diameter measurement data for the different coating thicknesses at 5 km/s.

Shot Date	Target Speed	Final Speed
20-Jul-20	5	5.192
21-Jul-20	5	4.9
21-Jul-20	5	4.72
22-Jul-20	5	5.412
21-Oct-20	1	0.964
21-Oct-20	1	0.924
18-Nov-20	1	0.895
29-Jan-21	5	4.653
03-Feb-21	5	4.495
09-Feb-21	5	4.34
16-Feb-21	1	0.889
24-Feb-21	1	0
03-Mar-21	1	0.945
26-Mar-21	1	0
30-Mar-21	1	0.968
20-Apr-21	5	4.227
20-Apr-21	5	4.656
20-Apr-21	5	3.313

04-May-21	5	3.912
14-May-21	5	4.223
19-May-21	5	4.397
28-May-21	5	4.481
02-Jun-21	1	0
02-Jun-21	1	0.9756
02-Jun-21	5	0
25-Jun-21	1	0.72
26-Jun-21	1	0.471
28-Jun-21	1	0.684
30-Jun-21	5	5.136
13-Jul-21	5	4.69
20-Jul-21	5	5.088
30-Jul-21	5	4.402
08-Oct-21	5	4.716
13-Oct-21	5	5.166
25-Oct-21	5	4.933
02-Nov-21	5	4.426

Table 5. Shot information.

8. References

Alby, F., Lansard, E., Michal, T., 1997. Collision of Cerise with Space Debris. Presented at the 2nd European Conference on Space Debris, ESA, Darmstadt, Germany.

Anselmo, L., Pardini, C., 2008. Space debris mitigation in geosynchronous orbit. Adv. Space Res. 41, 1091–1099. https://doi.org/10.1016/j.asr.2006.12.018.

Anz-Meador, P., Ward, M., Manis, A., Nornoo, K., Dolan, B., Claunch, C., Rivera, J., 2019. The Space Debris Sensor Experiment 10.

Anz-Meador, P.D., Opiela, J.N., Shoots, D., 2018. History of On-orbit Satellite Fragmentations, 15th Edition 637.

ARES Orbital Debris Program Office Optical Measurements [WWW Document], 2019. . ARES Orbital Debris Program Off. Opt. Meas. URL https://orbitaldebris.jsc.nasa.gov/measurements/optical.html (accessed 7.3.22).

Barrows, S.P., Swinerd, G.G., Crowther, R., 1995. The cascade fragmentation of a satellite constellation. Adv. Space Res. 16, 119–122. https://doi.org/10.1016/0273-1177(95)98761-C.

Bernhard et al., R.P., 1993. Composition and frequency of impact residues detected on LDEF surfaces. Presented at the Proceedings of the First European Conference on Space Debris, Darmstadt, Germany.

Birnbaum, N.K., Cowler, M.S., Gerber, B.I., & Clegg, R.A. (2004). Numerical simulation of structural deformation under shock and impact loads using a coupled multi-solver approach.

Bogner, A., Jouneau, P.-H., Thollet, G., Basset, D., Gauthier, C., 2007. A history of scanning electron microscopy developments: Towards "wet-STEM" imaging. Micron 38, 390–401. https://doi.org/10.1016/j.micron.2006.06.008.

Burchell, M.J., Cole, M.J., McDonnell, J.A.M., Zarnecki, J.C., 1999. Hypervelocity impact studies using the 2 MV Van de Graaff accelerator and two-stage light gas gun of the University of Kent at Canterbury. Meas. Sci. Technol. 10, 41–50. https://doi.org/10.1088/0957-0233/10/1/011.

Celestis, 2022. Featured Participants. About. URL https://www.celestis.com/about/featured-participants/# (accessed 7.5.22).

Cooper, R., Upadhyaya, H.P., Minton, T.K., Berman, M.R., Du, X., George, S.M., 2008. Protection of polymer from atomic-oxygen erosion using Al2O3 atomic layer deposition coatings. Thin Solid Films 516, 4036–4039. https://doi.org/10.1016/j.tsf.2007.07.150.

Cour-Palais, B.G., 1974. The current micrometeoroid flux at the moon for masses <10E-7 g from the Apollo window and Surveyor 3 TV camera results. Presented at the Proceedings of the Fifth Lunar Conference (Supplement 5. Geochimica et Cosmochimica Acta), pp. 2451–2462.

Crozier, W.D., Hume, W., 1957. High-Velocity, Light-Gas Gun. J. Appl. Phys. 28, 892–894. https://doi.org/10.1063/1.1722882.

de Groh, Banks, B.A., 1994. ATOMIC OXYGEN UNDERCU'ITING OF LDEF ALUMINIZED-KAPTON MULTILAYER INSULATION. J. Spacecr. Rockets 31, 656–664.

Divine, N., 1993. Five populations of interplanetary meteoroids. J. Geophys. Res. 98, 17029. https://doi.org/10.1029/93JE01203.

Doolan, C.J. 2001. A Two-Stage Light Gas Gun for the Study of High Speed Impact in Propellants. Engineering Physics.

Douglas Caswell, R., McBride, N., Taylor, A., 1995. Olympus end of life anomaly — a perseid meteoroid impact event? Int. J. Impact Eng. 17, 139–150. https://doi.org/10.1016/0734-743X(95)99843-G.

Drolshagen, G., McDonnell, J.A.M., Stevenson, T.J., Deshpande, S., Kay, L., Tanner, W.G., Mandeville, J.C., Carey, W.C., Maag, C.R., Griffiths, A.D., Shrine, N.G., Aceti, R., 1996. Optical survey of micrometeoroid and space debris impact features on EURECA. Planet. Space Sci. 44, 317–340. https://doi.org/10.1016/0032-0633(95)00140-9.

Drolshagen, G., Svedhem, H., Grün, E., Grafodatsky, O., Prokopiev, U., 1999. Microparticles in the geostationary orbit (GORID experiment). Adv. Space Res. 23, 123–133. https://doi.org/10.1016/S0273-1177(98)00239-7.

ESA (2022). Lunar Gateway. Retrieved 14 September 2022, from https://www.esa.int/Science_Exploration/Human_and_Robotic_Exploration/Exploration/Gateway.

ESA, 2022a. ESA'S Annual Space Environment Report (No. 6).

ESA, 2022b. Software User Manual - MASTER Revision 1.3.

ESA, 2009. ESA Image Gallery.

Esther, A.C.M., Dey, A., Sridhara, N., Yougandar, B., Bera, P., Anandan, C., Rangappa, D., Sharma, A.K., 2015. A study on degradation of germanium coating on Kapton used for spacecraft sunshield application: Study on degradation of germanium coating on Kapton. Surf. Interface Anal. 47, 1155–1160. https://doi.org/10.1002/sia.5867.

Fernholz, T., 2018. What happens when astronauts drop their tools in space. Quartz. URL https://qz.com/1318450/a-recent-history-of-nasa-astronauts-dropping-things-from-the-space-station/.

Giannuzzi, L., Goldstein, J.I., Newbury, D.E., Michael, J.R., Ritchie, N.W.M., Scott, J.H.J., Joy, D.C., 2018. Scanning Electron Microscopy and X-Ray Microanalysis, 4th Edition. ed. Springer.

Goldstein, R.M., Goldstein, S.J., Kessler, D.J., 1998. Radar observations of space debris. Planet. Space Sci. 46, 1007–1013. https://doi.org/10.1016/S0032-0633(98)00026-9.

Hamilton, J., Matney, M., Christiansen, E., 2017. DEVELOPMENT OF THE SPACE DEBRIS SENSOR. Presented at the 7th European Conference on Space Debris, ESA Space Debris Office, p. 11.

Herbert et al., M.K., 1997. Morphological classification of impacts on the eureca & hubble space telescope solar arrays. Presented at the Second European Conference on Space Debris, ESA-SP, ESOC, Darmstadt, Germany, p. 169.

Hoppe, P., Zinner, E., 2000. Presolar dust grains from meteorites and their stellar sources. J. Geophys. Res. Space Phys. 105, 10371–10385. https://doi.org/10.1029/1999JA900194.

Horstmann, A., Stoll, E., 2017. INVESTIGATION OF PROPAGATION ACCURACY EFFECTS WITHIN THE MODELING OF SPACE DEBRIS 5.

Hörz, F., Cintala, M.J., Bernhard, R.P., See, T.H., 1995. Cratering and penetration experiments in teflon targets at velocities from 1 to 7 km/s. Int. J. Impact Eng. 17, 419–430. https://doi.org/10.1016/0734-743X(95)99867-Q.

Hörz, F., Cinatala, M., Bernhard, R.P., Cardenas, F., Davidson, W., Haynes, G., See, T.H., Winkler, J., Knight, J., 1994. Cratering and Penetration Experiments in Teflon Targets at Velocities from 1 to 7 km/s.

ISO 16290:2013. 2013. ISO standard 16290 Space systems – Definition of the Technology Readiness Levels (TRLs) and their criteria assessment. 49.140 Space systems operations, 1, 12.

Jenniskens, P., 1993. Meteor Stream Activity. Astron. Astrophys. 280, 24.

Johnson, N.L., 2012. A new look at the GEO and near-GEO regimes: Operations, disposals, and debris. Acta Astronaut. 80, 82–88. https://doi.org/10.1016/j.actaastro.2012.05.024.

Jones, J., 2004. Modeling the sporadic meteoroid complex 48.

Kearsley, A.T., Drolshagen, G., McDonnell, J.A.M., Mandeville, J.-C., Moussi, A., 2005a. Impacts on Hubble Space Telescope solar arrays: Discrimination between natural and man-made particles. Adv. Space Res. 35, 1254–1262. https://doi.org/10.1016/j.asr.2005.05.049.

Kearsley, A.T., Graham, G.A., Burchell, M.J., Taylor, E.A., Drolshagen, G., Chater, R.J., McPhail, D., 2005b. MULPEX: A compact multi-layered polymer foil collector for micrometeoroids and orbital debris. Adv. Space Res. 35, 1270–1281. https://doi.org/10.1016/j.asr.2005.03.030.

Kearsley, A.T., Burchell, M.J., Hörz, F., Cole, M.J., Schwandt, C.S., 2006. Laboratory simulation of impacts on aluminum foils of the Stardust spacecraft: Calibration of dust particle size from comet Wild-2. Meteorit. Planet. Sci. 41, 167–180. https://doi.org/10.1111/j.1945-5100.2006.tb00201.x.

Kessler, D.J., 1993 A Partial History of Orbital Debris: A Personal View 13.

Koschny, D., Soja, R.H., Engrand, C., Flynn, G.J., Lasue, J., Levasseur-Regourd, A.-C., Malaspina, D., Nakamura, T., Poppe, A.R., Sterken, V.J., Trigo-Rodríguez, J.M., 2019. Interplanetary

Dust, Meteoroids, Meteors and Meteorites. Space Sci. Rev. 215, 34. https://doi.org/10.1007/s11214-019-0597-7.

Krag, H., Serrano, M., Braun, V., Kuchynka, P., Catania, M., Siminski, J., Schimmerohn, M., Marc, X., Kuijper, D., Shurmer, I., O'Connell, A., Otten, M., Isidro Muñoz, J. Morales, M. Wermuth, D. McKissock, A 1 cm space debris impact onto the Sentinel-1A solar array, Acta Astronautica, Volume 137, 2017, Pages 434-443, ISSN 0094-5765, https://doi.org/10.1016/j.actaastro.2017.05.010.

Krisko, P.H., Flegel, S., Matney, M.J., Jarkey, D.R., Braun, V., 2015. ORDEM 3.0 and MASTER-2009 modeled debris population comparison. Acta Astronaut. 113, 204–211. https://doi.org/10.1016/j.actaastro.2015.03.024.

Krueger, H., Landgraf, M., Altobelli, N., Gruen, E., 2007. Interstellar Dust in the Solar System. Space Sci. Rev. 130, 401–408. https://doi.org/10.1007/s11214-007-9181-7.

Lederer, S.M., Hickson, P., Cowardin, H.M., Buckalew, B., Frith, J., Alliss, R., 2017. NASA's Optical Program on Ascension Island: Bringing MCAT to Life as the Eugene Stansbery-Meter Class Autonomous Telescope (ES-MCAT) 13.

Luo, H., Mao, Y.-D., Yu, Y., Tang, Z.-H., 2019. FocusGEO observations of space debris at Geosynchronous Earth Orbit. Adv. Space Res. 64, 465–474. https://doi.org/10.1016/j.asr.2019.04.006.

Matney, Mark, Anz-Meador, P., Murray, J., Miller, R., Kennedy, T., 2019. The NaK Population: A 2019 Status. Presented at the International Orbital Debris Conference, Sugar Land, TX.

Matney, Manis, A., Anz-Meador, P., Gates, D., Seago, J., Vavrin, A., 2019. The NASA Orbital Debris Engineering Model 3.1: Development, Verification, and Validation 10.

Menicucci, Alessandra ; Drolshagen, Gerhard ; Kuitunen, Juha ; Butenko, Yuriy ; Mooney, Cathal. 6th European Conference on Space Debris, Proceedings of the conferencje held 22-25 April 2013, in Darmstadt, Germnay. Edited by L. Ouwehand. ESA SP-723, ISBN 978-92-9221-287-2, 2013, id.16. In-Flight and Post-Flight Impact Data Analysis from DEBIE2 (Debris In-Orbit Evaluator) on Board of ISS.

Moorhead, A.V., Kingery, A., Ehlert, S., 2019. NASA's Meteoroid Engineering Model (MEM) 3 and its ability to replicate spacecraft impact rates. ArXiv190905947 Astro-Ph.

Neish, M.J., Kibe, S., 2001. Hypervelocity impact damage equations for kapton multi-layered insulation and teflon second-surface mirrors. Proc. Third Eur. Conf. Space Debris 19 - 21 March 2001 Darmstadt Ger. Ed Huguette Sawaya-Lacoste ESA SP-473 Vol 2 Noordwijk Neth. ESA Publ. Div. 2.

Nesvorný, D., Jenniskens, P., Levison, H.F., Bottke, W.F., Vokrouhlický, D., Gounelle, M., 2010. COMETARY ORIGIN OF THE ZODIACAL CLOUD AND CARBONACEOUS

MICROMETEORITES. IMPLICATIONS FOR HOT DEBRIS DISKS. Astrophys. J. 713, 816–836. https://doi.org/10.1088/0004-637X/713/2/816.

Oliver, J P, Singer, S F, Weinberg, J L, Simon, C G, Cooke, W J, Kassel, P C, Kinard, W H, Mulholland, J D, Wortman, J J, POD Associates, Inc., Albuquerque, NM, and North Carolina State Univ., Raleigh, NC. 1995. "LDEF Interplanetary Dust Experiment (IDE) results". United States.

Pardini, C., 2005. Survey of past on-orbit fragmentation events. Acta Astronaut. 56, 379–389. https://doi.org/10.1016/j.actaastro.2004.05.065.

Pardini, C., Anselmo, L., 2016. Characterization of abandoned rocket body families for active removal. Acta Astronaut. 126, 243–257. https://doi.org/10.1016/j.actaastro.2016.04.035.

Pardini, C., Anselmo, L., 2011. Physical properties and long-term evolution of the debris clouds produced by two catastrophic collisions in Earth orbit. Adv. Space Res. 48, 557–569. https://doi.org/10.1016/j.asr.2011.04.006.

Pardini, C., Anselmo, L., 2009. Assessment of the consequences of the Fengyun-1C breakup in low Earth orbit. Adv. Space Res. 44, 545–557. https://doi.org/10.1016/j.asr.2009.04.014

Portree, D., Loftus, J., 1999. Orbital Debris: A Chronology (No. 19990041784).

Prajwal, K., Carmel Mary Esther, A., Dey, A., 2018. RF transparent vanadium oxide based single and bi-layer thin films as passive thermal control element for satellite antenna application. Ceram. Int. 44, 16088–16091. https://doi.org/10.1016/j.ceramint.2018.05.204.

Reddy, M.R., 1995. Effect of low earth orbit atomic oxygen on spacecraft materials. J. Mater. Sci. 30, 281–307. https://doi.org/10.1007/BF00354389.

Rex, D., 1997. SPACE DEBRIS MITIGATION AND SPACE SYSTEMS DESIGN. Acta Astronaut. 41, 311–316.

Rogers, J.A., Bass, N., Mead, P.T., Mote, A., Lukasik, G.D., Intardonato, M., Harrison, K., Leaverton, J.D., Kota, K.R., Wilkerson, J.W., Reddy, J. N. , Kulatilaka, W.D and Lacy Jr., T.E. , 2022. "The Texas A&M University Hypervelocity Impact Laboratory: A modern aeroballistic range facility", Review of Scientific Instruments 93, 085106 https://doi.org/10.1063/5.0088994.

Rossnagel, S.M., 2003. Thin film deposition with physical vapor deposition and related technologies. J. Vac. Sci. Technol. Vac. Surf. Films 21, S74–S87. https://doi.org/10.1116/1.1600450.

Schneider, E., Schäfer, F., 2001. Hypervelocity impact research - acceleration technology and applications -. Adv. Space Res. 28, 1417–1424. https://doi.org/10.1016/S0273-1177(01)00448-3.

Schwanethal et al., J.P., 2005. Analysis of impact data from the DEBIE (debris in-orbit evaluator) sensor in polar low earth orbit. Presented at the Proceedings of the 4th European Conference on Space Debris (ESA SP-587), ESA/ESOC, Darmstadt, Germany.

Silverman, M., 1995. Space Environmental Effects on Spacecraft: LEO Materials Selection Guide 504.

Simon, A.H., 2012. Sputter Processing, in: Handbook of Thin Film Deposition. Elsevier, pp. 55–88. https://doi.org/10.1016/B978-1-4377-7873-1.00004-8.

Skinner, M.A., Russell, R.W., Kelecy, T., Gregory, S., Rudy, R.J., Kim, D.L., Crawford, K., 2014. Observations in the thermal IR and visible of a retired satellite in the graveyard orbit, and comparisons to active satellites in GEO. Acta Astronaut. 105, 1–10. https://doi.org/10.1016/j.actaastro.2014.08.016.

Stabroth, S., Homeister, M., Oswald, M., Wiedemann, C., Klinkrad, H., Vörsmann, P., 2008. The influence of solid rocket motor retro-burns on the space debris environment. Adv. Space Res. 41, 1054–1062. https://doi.org/10.1016/j.asr.2006.12.024.

The Sydney Morning Herald, 2016. Piers Sellers, astronaut who warned of global warming risks. Syd. Morning Her. URL https://www.smh.com.au/national/piers-sellers-astronaut-who-warned-of-global-warming-risks-20161224-gthld1.html (accessed 7.4.22).

Trigo-Rodríguez, J.M., Blum, J., 2021. Learning about comets from the study of mass distributions and fluxes of meteoroid streams. Mon. Not. R. Astron. Soc. stab2827. https://doi.org/10.1093/mnras/stab2827.

Verma, P.N., Dhote, K.D. Characterising primary fragment in debris cloud formed by hypervelocity impact of spherical stainless steel projectile on thin steel plate, International Journal of Impact Engineering (2018), doi: 10.1016/j.ijimpeng.2018.05.003.

Ward, M.A., Anz-Meador, P.D., 2019. MLI Impact Phenomenology Observed on the HST Bay 5 MLI Panel 10.

Warren et al., J.L., 1989. The detection and observation of meteoroid and space debris impact features on the solar max satellite. Presented at the Proceedings of the 19th Lunar and Planetary Science Conference, Lunar and Planetary Institue, Houston, TX, USA, pp. 641–657.

Williams, D. R. (2022). Cosmos 1408. Available at: https://nssdc.gsfc.nasa.gov/nmc/spacecraft/display.action?id=1982-092A (Accessed April 26, 2022).

Wired, 2009. Lost in Space: 8 Weird Pieces of Space Junk. URL https://www.wired.com/2009/02/spacestuff/ (accessed 7.5.22).

Wozniakiewicz, P.J., Bridges, J., Burchell, M.J., Carey, W., Carpenter, J., Della Corte, V., Dignam, A., Genge, M.J., Hicks, L., Hilchenbach, M., Hillier, J., Kearsley, A.T., Krüger, H., Merouane, S., Palomba, E., Postberg, F., Schmidt, J., Srama, R., Trieloff, M., van-Ginneken, M., Sterken, V.J., 2021. A cosmic dust detection suite for the deep space Gateway. Adv. Space Res. 68, 85–104. https://doi.org/10.1016/j.asr.2021.04.002.

Wozniakiewicz, P.J., Kearsley, A.T., Bridges, J., Holt, J., Price, M.C., Hicks, L., 2019. Orbital Dust Impact Experiment (ODIE) – A Passive Dust Collector Designed to Address the Dust Flux Data Gap 10.

Yano, H., Kibe, S., Deshpande, S.P., Neish, M.J., 1997. The first results of meteoroid and debris impact analyses on Space Flyer Unit. Adv. Space Res. 20, 1489–1494. https://doi.org/10.1016/S0273-1177(97)00423-7.